FEEDBACK-CONTROLLED TRANSITION-EDGE SENSOR BOLOMETERS IN A FAR-INFRARED DOUBLE-FOURIER INTERFEROMETER

CHRIS S. BENSON
Master of Science, University of Lethbridge, 2020

A thesis/project submitted
in partial fulfilment of the requirements for the degree of

DOCTOR OF PHILOSOPHY

in

EARTH, SPACE, AND PHYSICAL SCIENCE

Department of Physics and Astronomy
University of Lethbridge
LETHBRIDGE, ALBERTA, CANADA

© Chris S. Benson, 2024

FEEDBACK-CONTROLLED TRANSITION-EDGE SENSOR BOLOMETERS IN A FAR-INFRARED DOUBLE-FOURIER INTERFEROMETER

CHRIS S. BENSON

Date of Defence: December 20, 2023

Dr. Locke D. Spencer Thesis Supervisor	Associate Professor	Ph.D.
Dr. David A. Naylor Thesis Examination Committee Member	Professor	Ph.D.
Dr. Brant Billinhurst Thesis Examination Committee Member Canadian Light Source, Staff Scientist	Adjunct Professor	Ph.D.
Dr. Adam D. Hincks External Examiner University of Toronto Toronto, Ontario	Assistant Professor	Ph.D.
Dr. Chad Povey Chair, Thesis Examination Committee	Instructor	Ph.D.

Abstract

The far-infrared Universe provides substantial insights into the formation of stars and planetary systems, the assembly history and evolution of galaxies, the origins of the Universe, and the search for life. Despite its great scientific potential, the far-infrared Universe remains relatively unexplored with the degree of spatial resolution that is available in observations at other wavelengths. Double-Fourier spatial-spectral interferometry provides a promising path to achieve transformative spatial resolution in far-infrared observations. To further study this technique and improve on its technology readiness, we have constructed a far-infrared double-Fourier interferometry testbed that is coupled to a unique detector array of feedback-controlled transition-edge sensor bolometers.

To fully understand measurements made with the interferometry testbed and ensure that these are well-calibrated, the detector system must be understood and characterised at a technical level. The detector array itself is a bespoke system with a substantial parameter space that can be optimized for different use-cases which has made this a daunting task. This thesis centres on the experiments I have conducted to characterise, calibrate, and optimise the detector system both in a general sense and in the context of the double-Fourier instrument. Through this investigation of the detector system, I have reduced the spectral noise of the double-Fourier interferometry testbed by 70%.

Throughout this work, I review the concepts and theory related to measurements made with Fourier transform spectrometers and double-Fourier interferometers (Chapter 2). Additionally, I discuss transition-edge sensor bolometers and introduce the feedback-controlled bolometer system (Chapter 3). I have included a detailed discussion of my experiments to chracterise the measurement process of the detector array, optimise its noise performance,

and tune its response to optical modulation (Chapter 4). I also provide a similar discussion of experiments I conducted to optimise and spectrally characterise the detector system as an integrated component of the interferometer assembly (Chapter 5).

Acknowledgments

Primarily, I need to thank Prof. Locke Spencer for the opportunity to work in the Lethbridge Astronomical Instrumentation Group (AIG) and the projects that he has supported me in pursuing. These several years of mentorship and guidance have been extraordinarily rewarding and led to opportunities far beyond my musings as a young student enjoying the lectures he delivered (these being riddled with obscure movie references). It has been an absolute privilege to be his first doctoral graduate and it is difficult to find the words to express my thanks. His insistence that his first job was programming binary load-lifters will be sorely missed.

I must also thank my dear wife, Anna, who has stood with me and supported me through this effort. I think she may have been prepared to survive life with someone writing their dissertation, but I do not think she had planned on having to do so while preparing for us to move overseas to continue my work in an ideal postdoctoral position. Thank you for your patience, kindness, and the incredible things you do to make every part of life that much better. I also must thank my parents, Lawrence and Deborah Benson for the love and counsel they have given me throughout my life and for their constant encouragement. I owe them many thanks for teaching me how to work a problem, the value of considering multiple perspectives, cultivating my creativity, and allowing me to make important life decisions from an early age. Additionally, I would like to thank Judy and Eric Dumouchel for their kindness and understanding as my work has often meant distance.

Thank you to Prof. David Naylor for his guidance and for providing a significant portion of the test equipment for my experiments. Thank you to Dr. Berke Ricketti and to Prof. Locke Spencer for your help in proofreading this thesis and throughout the editing process.

I am particularly thankful in this as I know you have both been working on sizeable grant proposals and papers simultaneously.

I also wish to thank members of the AIG group, past and present, and other graduate students within the department. Research is a collaborative process, and discussing big-picture ideas together has always been rewarding.

This research has been funded in part by the Natural Sciences and Engineering Research Council of Canada (NSERC), Alberta Innovates (AI), the Canadian Foundation for Innovation (CFI), the University of Lethbridge, and the Institute for Space Imaging Science.

Contents

Contents vii

List of Tables xi

List of Figures xii

List of Abbreviations xxi

Notes on Format xxv

1 Introduction 1
- 1.1 The scientific potential of far-IR astronomy . . . 2
- 1.2 The case for a far-IR spatial interferometer . . . 6
- 1.3 The University of Lethbridge DFI . . . 11
- 1.4 Thesis Summary . . . 12

2 Fourier Spatial-Spectral Interferometry 14
- 2.1 Fourier transform spectroscopy . . . 14
  - 2.1.1 Fourier Analysis . . . 14
  - 2.1.2 The Michelson Interferometer . . . 17
  - 2.1.3 Instrumental Line Shape . . . 21
  - 2.1.4 Phase considerations . . . 22
  - 2.1.5 Consequences of Digitisation . . . 25
- 2.2 The Michelson stellar interferometer . . . 26
- 2.3 Coherence theory of light . . . 29
  - 2.3.1 The mutual coherence function and complex degree of coherence . 29
  - 2.3.2 The van Cittert-Zernike Theorem . . . 31
- 2.4 Double-Fourier interferometry . . . 34
- 2.5 Design and alignment of the DFI testbed . . . 35
  - 2.5.1 Full double-Fourier configuration . . . 35
  - 2.5.2 Single FTS configuration . . . 37
  - 2.5.3 Alignment configuration . . . 37
- 2.6 Conclusion . . . 39

3 Feedback-controlled Far-IR TES Bolometers 40
- 3.1 Bolometer theory . . . 41
  - 3.1.1 Principles of operation . . . 42
  - 3.1.2 Sources of noise . . . 45

3.1.3 Modern TES focal planes . . . 48
3.2 The QMC feedback-controlled TES bolometer array . . . 48
3.2.1 Operation . . . 50
3.2.2 Cryostat performance . . . 54
3.2.3 Control electronics . . . 54
3.3 Detector array operation . . . 57
3.3.1 Detector measurements and adjustable parameter summary . . . 58
3.3.2 Detector output data structure and control software . . . 62
3.3.3 Detector units . . . 63
3.3.4 Initialisation decay . . . 64
3.3.5 DMA communication errors . . . 67
3.4 Conclusions . . . 71

4 The Characterisation of a Feedback-Controlled Array of Far-IR TES Bolometers 72
4.1 General detector performance . . . 73
4.1.1 Superconducting transition measurements . . . 74
4.1.2 Thermal behaviour . . . 87
4.1.3 Output variable bit structure . . . 91
4.1.4 Measurement timing . . . 94
4.1.5 Measured noise performance . . . 108
4.1.6 PID tuning . . . 113
4.2 Considerations of low-frequency detector noise . . . 122
4.3 Effective detector time constants . . . 123
4.3.1 Measurement techniques . . . 124
4.3.2 Near-saturation response . . . 129
4.3.3 Detector timing . . . 132
4.3.4 PID effects . . . 136
4.4 Conclusions . . . 140

5 Performance of the Double Fourier Interferometery (DFI) and Detector Assembly 142
5.1 The DFI testbed as a spectrum analyser . . . 143
5.1.1 Fourier Transform Spectrometer (FTS) modes of measurement . . . 144
5.1.2 Processing rapid-scan interferograms . . . 147
5.2 Beamsplitter performance . . . 153
5.2.1 Spectral bandpass . . . 153
5.2.2 Phase effects and phase correction . . . 159
5.3 Relative Spectral Response of the DFI . . . 167
5.3.1 Maximum spectral stage scanning speed . . . 173
5.4 Spectral noise characterisation . . . 174
5.5 Conclusions . . . 176

6 Future characterisation and Conclusions **179**
6.1 Conclusions . . . 179
6.1.1 Double Fourier Interferometry . . . 180
6.1.2 Feedback-controlled TES bolometers . . . 181
6.1.3 Integration of the detector array in the DFI testbed . . . 181
6.1.4 Detector performance summary . . . 182
6.2 Future Characterisation . . . 182
6.2.1 Extending optimisation to the full array . . . 183
6.2.2 Multimoded detector behaviour . . . 183
6.2.3 Detector system beam-mapping . . . 192
6.2.4 Detector cross-talk . . . 192
6.2.5 Forward and reverse scanning of the spectral stage . . . 195
6.2.6 Performance at multiple baselines . . . 196
6.3 Advancing far-IR interferometry in the next decade . . . 197
6.4 KIDS and the forward path for FIR detectors . . . 198
6.5 Final thoughts . . . 199

Bibliography **201**

A Derivations **220**
A.1 Phonon noise . . . 220
A.1.1 Ballistic transmittance . . . 220
A.1.2 The scattering, absorption, and/or emission limit . . . 222
A.2 Photon noise . . . 223
A.3 Spectral representation of the mutual coherence function . . . 224
A.3.1 A note on Fourier analysis . . . 224
A.3.2 Equation 2.37 . . . 224
A.4 Normalisation of the mutual coherence function . . . 225
A.4.1 Normalisation . . . 225
A.5 FTS NEP . . . 226

B Alignment of the Lethbridge DFI **227**
B.1 Motivations for the second design . . . 227
B.1.1 Beamsplitters . . . 229
B.2 Incorporating the primary mirror . . . 229
B.3 Aligning the first cavity flats . . . 230
B.4 Refining the alignment of the first cavity . . . 232
B.5 Aligning the second cavity . . . 232
B.6 Introducing the double-rooftop assembly . . . 232
B.7 Rotating the beamsplitters . . . 234

C Alternate Beamsplitter Construction **236**
C.1 Introduction . . . 236
C.2 Method 1 . . . 238
C.3 Method 2 . . . 238

C.4 Method 3 242

D Additional Software Info. 245
D.1 Custom readout modes 245
D.2 Metadata encoding 249
D.3 Detector control software 249
D.4 LabVIEW PID implementation 249
D.5 DMA mitigation routine 252

E Additional Detector Response Measurement Techniques 253

List of Tables

1.1 A list of science cases that stand to benefit from far-Infrared (IR) interferometry from a space-based platform and their required angular resolution. . 9

3.1 A selection of far-IR, Sub-Millimetre (sub-mm), and Millimetre (mm) instruments that employ Transition Edge Sensor (TES) bolometers. 49
3.2 The default Proportional-Integral-Derivative (PID) parameters of the detector array set by QMC Instruments. For all detectors, the derivative term is not used and has a gain value of 0. 62
3.3 The fitted time constants from the initialization decays shown in Figure 3.11. 67

4.1 The short (τ_s) and long (τ_l) time constants extracted from a least-squares fit of a dual decay model (see Equation 3.23) to the switching noise in channels A and C shown in Figure 4.3. 78
4.2 The steepness of the superconducting region of the TES on the central detector for each segment in Figure 4.12. 87
4.3 The detector activity and full-frame heater duty cycle (D.C.) when operating in TES profiling mode without multiplexing at different pulse widths (P.W.). 98
4.4 The -3 dB cutoff frequency of the response curves at different detector pulse widths as shown in Figure 4.48. 133
4.5 The -3 dB cutoff corresponding to each frequency response measurement in Figure 4.50. 134

5.1 The atmospheric model for the laboratory environment calculated with `am` . 170
5.2 The detector parameters required to fully sample the spectral bandpass of the DFI at the minimum and maximum scanning speed of the spectral stage. 174
5.3 Detector parameters that I have selected to provide a better optimised detector central detector for the DFI testbed are shown with the default parameters. Selected detector performance metrics are also shown. 175

6.1 A summary of the central detector characterisation determined in this work. 182
6.2 Parameters extracted from a least-squares fit of the rapid and slow response features to a large change in the heater state on the central detector. See Figures 6.8 and 6.9. 195

List of Figures

1.1 The spatial resolution of several current and legacy world-class observatories across the Electromagnetic (EM) spectrum. 7
1.2 The Space Infrared Interferometric Telescope (SPIRIT)/Space Interferometer for Cosmic Evolution (SPICE) mission concept. 10
1.3 The DFI testbed developed at the University of Lethbridge. 11

2.1 The first five terms of the Fourier composition of a square wave. 16
2.2 Optical diagram of a Michelson interferometer. 18
2.3 The consequences of a limiting Optical Path Difference (OPD) on the line profile of an FTS in both the measured interferogram and its Fourier reciprocal spectral domain. 23
2.4 Optical diagram of a spatial interferometer with two apertures separated by a baseline b. A focusing optic behind the apertures combines the light passing each aperture on a viewing screen or detector array. 27
2.5 Optical diagram of the Michelson stellar spatial interferometer. 28
2.6 The arrangement of source plane ($\mathcal{S}$), aperture plane ($\mathcal{A}$), and image plane ($\mathcal{B}$) in the discussion of the mutual coherence function and derivation of the van Cittert-Zernike Theorem. 28
2.7 An optical diagram of the Lethbridge DFI instrument. 36
2.8 The DFI testbed in a modified arrangement to serve as a single Mach-Zehnder FTS. See Figure 2.7 for additional details. 37
2.9 The DFI testbed in its alignment configuration. The optical layout has been modified from Figure 2.8 to form two resonant cavities. 38

3.1 An electrical and thermal diagram of a bolometer. 44
3.2 The cryostat that houses the detector array. Detector control electronics are housed in the room temperature electronics boxes external to the red cryostat vacuum can. 50
3.3 A schematic diagram of internal cryostat assembly (left) with a cross-sectional view (right). 51
3.4 A detailed schematic diagram showing the location of the detector array within the cryostat assembly. 52
3.5 A photograph of the niobium TES detector array and readout wiring board which has been mounted inside the cryostat behind the feedhorn assembly (see Figure 3.4). 53
3.6 A thermal diagram (left) and electric diagram (right) of a single TES detector in the QMC feedback-controlled TES array. 54

3.7 A full cycle of the detector cryostat measured by its three internal thermometers. 55
3.8 The order in which detectors are multiplexed by the Field-Programmable Gate Array (FPGA) readout system is shown in the left panel. The colour convention for each detector is also shown. The right panel shows a zoomed-in view of the detector array for reference. 56
3.9 An example of a single detector measurement pulse. 59
3.10 The decaying detector signal that results from uncontrolled detector initialisation for the central detector. 65
3.11 The initialisation decay in the detector signal of the first row of detectors. . 66
3.12 The frequency of Direct Memory Access (DMA) errors while operating the detector array with a lower specifications computer (left) and a higher specifications computer (right). the rate at which DMA errors occur in each case is also shown. 69
3.13 The time the FPGA remains inactive while detectors are operated by a lower specifications local computer (left) and a higher specifications computer (right). 70

4.1 The detector block thermometer diode calibration profile for a 10 μA bias. . 75
4.2 Detector block (left) and TES state (right) timelines of the central detector are shown while the cryostat was allowed to warm with detector heaters switched off. 76
4.3 The switching noise in two channels of multiplexed measurements of the TES state with all detector heaters switched off (left). 77
4.4 The increase in temperature during four partial warming cycles of the detector cryostat. 78
4.5 Multiple measurements of the superconducting transition of the central TES (A0) while operating in multiplexing mode and while the detector environment is warmed. 79
4.6 Multiple measurements of the superconducting transition of the central TES while the detector environment is allowed to cool. 80
4.7 Transition measurements of the central detector while the cryostat environment was warmed (left) and cooled (right) aligned to the start of their transition. 81
4.8 Multiplexed measurements of the central detector's superconducting transition for a variety of Pulse Widths (PWs) during a warming of the cryostat environment. The maximum width of the distribution of co-aligned curves when the pulse width is varied and when it is held constant is also shown. . 82
4.9 The superconducting transition for each detector in the array. Each panel represents a channel of the detector array. Detectors are marked and coloured following the convention introduced in Figure 3.8. 83
4.10 The superconducting transition for each detector in the array as in Figure 4.9 aligned at the point on the transition where the process variable is 9 415 data units. Again, the convention introduced in Figure 3.8 is employed. 84

4.11 The steepness of the superconducting transition of the central detector measured in multiplexing mode. 85
4.12 Breakpoint analysis of the superconducting transition of the central detector. 86
4.13 The response of the TES to optical modulation as it is heated through its superconducting transition. 89
4.14 Measurements of the dynamic thermal conduction of the central detector in internal data units (left) and calibrated into physical units (right). 91
4.15 A bit-level histogram for a detector observation with a flat mirror at the entry window to the cryostat. Detector markers and colours follow the convention introduced in Figure 3.8. 92
4.16 The distribution of output variable values is shown for each detector corresponding to the data from Figure 3.8 93
4.17 The bit-level histograms of the anomalous B4 and C3 detectors corresponding to the signal distributions shown in the right panel of Figure 4.16. . . . 93
4.18 Output variable distributions for detectors B4 (left) and C3 (right) under a variety of integral-term PID weights (I) while viewing a mirror. 94
4.19 Central detector measurement pulses with different readout structures corresponding to different versions of the TES profiling readout mode (see §3.3.2). 96
4.20 Central detector output variable signals with different readout structures corresponding to the measurement pulses and software versions outlined in Figure 4.19. 97
4.21 The top panels show the average process variable signal throughout a single measurement of the central detector in nominal Multiplex (MUX) operation in TES profiling mode and unmultiplexed operation with pulse widths of 89, 60, and 74 loop counts (left) and the corresponding distribution of process variable values at the read index (right). 99
4.22 The calibrated blackbody source used in detector to provide optical loads for the detector array while studying detector timing parameters. 101
4.23 The average process variable profile for measurements of a 343 K black body source modulated at 40 Hz by a chopper (left) and the distribution of process variable values at the read index (right) for a variety of blanking times with a fixed read index. 102
4.24 The average process variable profile for measurements of a chopped blackbody source and the distribution of process variable values at the read index as in Figure 4.23. 103
4.25 Average process variable measurement curves (left column) and the associated distributions of output variable values (right column) while viewing a static optical load provided by a room temperature mirror. 105
4.26 The average TES state profile during a detector measurement for a variety of heater times, with the TES read index spaced 40 loop counts from the heater switch-off. 106
4.27 The detector signal distribution widths for various blanking times and delays (in loop counts) between the heater switch-off and the TES read index. 107

4.28 The $A\Omega$ product is shown for a multimoded beam (blue line) model with the detector filter transmission (dashed black line) in the left panel. The detector signal variation while measuring a static 40°C blackbody source is shown in the right panel. 110
4.29 Noise Equivalent Power (NEP) measurements of the central detector using a static optical load from a blackbody source at differing temperatures. . . . 111
4.30 An example of a measured (blue) and fitted power spectral peak (orange) from the central detector signal while viewing a 50°C blackbody source chopped at ∼90 Hz. 113
4.31 The NEP of the entire detector array measured using chopped optical loads and an $A\Omega$ product consistent with single-mode coupling (left) and multi-mode coupling (right). 114
4.32 The average central detector output signal while viewing a chopped blackbody source under a variety of PID conditions. 115
4.33 The distribution of the central detector's TES voltage at the read index corresponding to the output signals in Figure 4.32. 115
4.34 The effect of increased derivative-term weighting in the PID loop on the central detector while viewing a static optical load. Results are shown for a variety of proportional and integral term weights. 116
4.35 The standard deviation of the output signal from the central detector while viewing a static optical load throughout the PID parameter space. 116
4.36 The effects varying proportional and integral-term gains on the Signal-to-Noise Ratio (SNR) of central detector measurements of a 90°C blackbody source chopped at 40 Hz. 117
4.37 Distributions of the output signal from detector A0 while viewing a static optical load. Over the range of P-term and I-term gains shown, these distributions show multimodal behaviour. 118
4.38 The output signal from the central detector while viewing a static optical load and operating with PID parameters for which the signal is found to be multimoded. 119
4.39 The χ^2_{red} value obtained from single-Gaussian least-squares fits to detector signal distributions and example histograms where the detector signal distributions appear to be single-moded and multimoded. 121
4.40 The effects varying proportional and integral-term gains on the SNR of central detector measurements of a 90°C blackbody source chopped at 40 Hz as in Figure 4.36. 121
4.41 Detector noise spectra corresponding to a central and an off-axis detector are shown over a linear (left) and logarithmic (right) axes. 123
4.42 The central detector's frequency response measured using optical modulation from the FTS and a coherent source for two PID gain conditions. A nominal bolometer response model is shown as a dashed black line. 126
4.43 A detector response model fit to the frequency response of the central detector with default operational parameters measured with modulation from the FTS. measurements of the central detector's response made with the FTS and with the chopped photomixer source are also shown. 127

4.44 The central detector signal while viewing a photomixer source and a physical chopper (left) and the corresponding peak in its power spectrum (right). 128
4.45 The central detector's signal while viewing a high-power VDI source as it nears detector saturation and the photomixer source are shown in the left panel. These have been modulated with a mechanical chopper. The spectral peak corresponding to the modulation frequency is shown for each case in the right panel. 129
4.46 The response of the central detector to a high-power source and an optical chopper. 130
4.47 The simulated effect of "clipping" an interferogram measured with the DFI as would be experienced by a typical photodetector reaching the limits of its dynamic range. The filtering effect of a feedback-controlled TES bolometer approaching its saturation limit is also shown. 131
4.48 The signal (left) and SNR (right) response of the central detector to optical modulation at pulse widths of 10, 15, 20, 30, and 40 loop counts (i.e., increasing the time required for detector measurements) 133
4.49 The response of the central detector to low-frequency optical modulation from the FTS with a pulse width of 30 (green) and 40 (yellow). As in Figure 4.48, the -3 dB cutoff of each response measurement is shown by the vertical line in the respective colour. 134
4.50 The frequency response of the central detector operating with a variety of detector timing parameters (top) and the associated SNR (bottom). 135
4.51 The response of the central detector to optical modulation from the chopped photomixer source in a variety of PID conditions. 137
4.52 The effective time constant (left) and associated uncertainty (right) of the central detector under different P and I term weighting in its PID control. . 138
4.53 The value of χ^2_{red} as a goodness of fit metric for the time constant measurements of the central detector. The -3 dB cutoff frequency associated with the response profile in each P and I gain condition is also shown. 138
4.54 The response of the central detector corresponding to particular P and I gain conditions of interest denoted in Figures 4.52 and 4.53. 139
4.55 The SNR of the central detector signal while responding to the modulated optical load provided by the photomixer and chopper at the -3 dB cutoff frequency. 140

5.1 The high-temperature blackbody used as a broadband source for the FTS. . 145
5.2 Three interferograms corresponding to a blackbody at 1 200°C measured from the FTS using the central detector and the Step-and-Integrate (S&I) technique. 146
5.3 The low-frequency correction of an S&I interferogram presented in Figure 5.2 and the corresponding spectrum. 148
5.4 The interpolation of a single interferogram measured by the central detector for Rapid Scan (RS) averaging. 150

5.5 The location of the Zero Path Difference (ZPD) fringe throughout 3 000 bidirectional scans of the FTS before (left) and after (right) the positional axis of each scan has been interpolated to a common positional vector. . . . 151
5.6 A linear fit to the phase measured with a single scan of the FTS. 152
5.7 An interferogram from a single scan of the FTS and the average interferogram from 1 500 scans while viewing a 950°C blackbody source are shown in the left panel. The right panel shows the corresponding spectra. 152
5.8 The arrangement of the Toptica photomixer and receiver for measuring beamsplitter transmission spectra. 154
5.9 The transmission (left) and efficiency (right, see Equation 5.5) spectra of the beamsplitter at 45° of incidence over all three photomixer bands. Each band is separated by colour. 154
5.10 The transmission (left) and efficiency (right) spectra of the beamsplitter over two photomixer bands at 22° and 45° angles of incidence. These measurements correspond to the parallel polarisation orientation of the beamsplitter. 156
5.11 The transmission (left) and efficiency (right) spectra similar to those in Figure 5.10 with the beamsplitter in the perpendicular polarisation orientation. 156
5.12 The beamsplitter efficiency at an incidence angle of 22° (left) and 45° (right) at orthogonal polarisation angles. These measurements correspond with the orange and green curves in Figures 5.10 and 5.11. 158
5.13 Beamsplitter efficiency is shown for when opposing sides are first in the optical path at incidence angles of 22° (right) and 45° (right). 158
5.14 An example interferogram (left) and phase spectrum (right) measured by the central detector of the FTS while viewing 1 200°C blackbody source from a single spectral scan. 160
5.15 The symmetric (blue) and antisymmetric (red) inputs of the FTS. 161
5.16 The measured phase from an FTS measurement of a 1 200°C blackbody in three FTS configurations. 161
5.17 The fitted phase in the region of the spectrum that has high amplitude corresponding to corresponding to a source at each input of the FTS is shown. The phase difference between each port is also shown. 162
5.18 The phase correction of a spectral measurement of a 1 200°C blackbody source from the central detector corresponding to 1 800 scans of the FTS. . 163
5.19 A measured interferogram from the central detector while viewing a blackbody source at 1 200°C is shown with the beamsplitters arranged in their opposing configuration in the FTS. 165
5.20 The phase correction of an FTS measurement of a 1 200°C blackbody with the FTS beamsplitters in their opposing configuration. 166
5.21 The profiles of known sources of optical filtering in the FTS and detector assembly compared to a measured blackbody spectrum from the FTS. . . . 169
5.22 The Relative Spectral Response Function (RSRF) of the FTS and detector assembly determined from spectral measurements of a blackbody source at a temperature of 950°C (T_1) and 1 200°C (T_2). 171

5.23 A theoretical 950°C blackbody spectrum as it would be measured by the FTS if it had an RSRF of unity. 172
5.24 The spectral noise measured by the FTS while viewing a blackbody source with the default parameters set by QMC Instruments and with the optimised parameters I have determined. 176
5.25 The spectral NEP of the central detector in the DFI testbed using default and optimised detector parameters. 177

6.1 The spectral peak of detector signals while the full detector array views a photomixer source modulated by a physical chopper at ∼20 Hz. The layout of panels in the figure matches the convention of Figure 3.8. It should be noted that there are significant differences in detector calibration across the array. 184
6.2 The interferograms viewed by each detector of the array corresponding to 100 spectral scans of the FTS while viewing the Pegasus blackbody source at 1 200°C. 185
6.3 Measurements made with the central detector while viewing a static optical load and operating under PID conditions that result in a multimodal signal distribution. 187
6.4 The distribution of the the TES thermometer state at each loop count of a measurement pulse for the three steady state regions identified in Figure 6.3. 188
6.5 A time-stream of data from the central detector that experiences several abrupt changes to its steady-state. 189
6.6 The time between transitions in the central detector's steady state (corresponding to the 10 minutes of detector measurements in Figure 6.5) and the distribution of the amplitudes of steady-state changes in the central detector signal under a variety of PID conditions are shown. 190
6.7 An interferogram measured by the central detector of the DFI testbed from a single spectral scan is compared against the average of 25 forward scans. The PID gain conditions of the detector are such that rapid changes to the detector's steady state signal can be seen. 191
6.8 The response of detectors B0, C0, and D0 to a significant change in the power dissipated in the heater on detector A0. 193
6.9 The response of detector B0 to a significant change in the power dissipated in the heater on detector A0 (as shown in Figure 6.8). Each feature of the detector's response was fit with a decay model. 194
6.10 Average interferograms determined from 1 500 forward and reverse scans of the DFI testbed operating as an FTS and viewing a 1 200°C blackbody source. 196

B.1 The DFI testbed in its alignment configuration. This image matches Figure 2.9. 228
B.2 The first DFI optical design while in its alignment configuration. In this design there is one less folding mirror, however the focal point of the primary collimator is not on the optics bench. 228

B.3 The incorporation of the primary mirror in the alignment of the interferometer using two alignment lasers. 229
B.4 An optical diagram demonstrating the alignment of the first resonant optical cavity of the DFI (top) and a corresponding photograph of the testbed (bottom). Note that a cube beamsplitter is shown in the photograph, this was later replaced with a Mylar beamsplitter. 231
B.5 The spot pattern from the output of the first resonant cavity while it is poorly aligned. The arrow demonstrates that subsequent passes of the beam through the cavity move down and to the right. 233
B.6 The introduction of the right single-rooftop portion of the double-rooftop assembly. In this diagram there is no reverse beam passing through the interferometer and bottom mirror does not receive an alignment beam. . . . 234
B.7 The DFI in its final alignment phase in which it operated a single FTS. See Figure 2.8 for additional details. 235

C.1 Technical diagram of the top (upper panel) and bottom (lower panel) pieces of the ring mounts that clamp the beamsplitter membrane. The non-circular holes on the bottom piece allow self-wrenching of the M4 nuts. 237
C.2 The first method employed to make beamsplitters. In this method an embroidery hoop was used to tighten the aluminised polyester. 238
C.3 Significant modifications are employed in the second method. The three optical posts and lab jack are clearly seen. The wooden embroidery hoop shown in this image was replaced by the metal ring shown in Figure C.5. . . 239
C.4 A diagram of the layers of different parts of the mounting apparatus that are clamped together. 240
C.5 The beamsplitter manufactured using the second method (left) and the beam quality after 3 m of optical path once it has reflected from the membrane surface (right). 241
C.6 In method 3, four optics posts are used as clamping points and the membrane is held between two larger outer diameter rings. 243
C.7 The beam quality after 3 m of optical path after it has reflected from the membrane surface of a Mylar beamsplitter manufactured with the third method. 244

D.1 The output of the detector array to the DMA First In, First Out (FIFO) when operating in the default readout mode for a measurement pulse width of n. . 246
D.2 The output of the detector array to the DMA FIFO when operating in the custom TES profiling readout mode for a measurement pulse width of n. . . 247
D.3 The output of the detector array to the DMA memory space when operating in additional TES output mode for a measurement pulse width of n. 248
D.4 The bit structure of the 32-bit metadata integer prior to modifications in April 2022 (left) and after (right). 250
D.5 The response of the central detector to 24 separate DMA errors under nominal operation (left) and a single DMA error with PID control limiting operation (right). 252

E.1 The signal amplitude from the central cluster (left) and outer ring (right) of detectors measured using an illuminated small aperture and a chopper. . . . 254
E.2 The signal amplitude from the central detector while the photomixer antenna bias frequency was changed. 254
E.3 The chopped signals measured by the central detector corresponding to all four techniques included in this work. 256

List of Abbreviations

ADC Analogue-to-Digital Converter

AIG Astronomical Instrumentation Group

ALMA Atacama Large Millimetre Array

BETTII Balloon Experimental Twin Telescope for Infrared Interferometry

BLAST-TNG Next-Generation Balloon-borne Large-Aperture Submillimeter Telescope

CMB Cosmic Microwave Background

CO Carbon monoxide

CPU Central Processing Unit

DAC Digital-to-Analogue Converter

DFI Double Fourier Interferometery

DMA Direct Memory Access

ELT Extremely Large Telescope

EMI Elecromagnetic Interference

EM Electromagnetic

ESA European Space Agency

FISICA Far Infrared Space Interferometer Critical Assessment

FET Field-Effect Transistors

FFT Fast Fourier Transform

FIFO First In, First Out

FWHM Full Width at Half Maximum

FIRI Far Infrared Interferometer

FOV Field Of View

FPGA Field-Programmable Gate Array

FTS Fourier Transform Spectrometer

GUI Graphical User Interface

ILS Instrument Line Shape

IR Infrared

IRQ Interrupt Request

ISM Interstellar Medium

JWST James Webb Space Telescope

KID Kinetic Inductance Detector

LIGO Laser Interferometer Gravitational-Wave Observatory

mm Millimetre

MUSCAT The Mexico UK Sub-mm Camera for Astronomy

MUX Multiplex

NASA National Aeronautics and Space Administration

NEP Noise Equivalent Power

NI National Instruments

OPD Optical Path Difference

PID Proportional-Integral-Derivative

PRIMA Probe far-Infrared Mission for Astrophysics

PSO Pulse Synchronized Output

RAM Random Access Memory

RSRF Relative Spectral Response Function

RS Rapid Scan

SED Spectral Energy Density

SNR Signal-to-Noise Ratio

SPECS Submillimetre Probe of the Evolution of Cosmic Structure

SPIRIT Space Infrared Interferometric Telescope

SPIRE Spectral and Photometric Imaging Receiver

SPICE Space Interferometer for Cosmic Evolution

sub-mm Sub-Millimetre

SQUID Superconducting Quantum Interference Device

S&I Step-and-Integrate

TES Transition Edge Sensor

TMT Thirty-meter Telescope

TRL Technology Readiness Level

USB Universal Serial Bus

UV Ultraviolet

VLA Very Large Array

YSO Young Stellar Object

ZPD Zero Path Difference

Notes on Format

The following style conventions were selected:

Colours: To improve the accessibility of this thesis, colour conventions that are friendly to those with colour vision deficiencies have been used where possible. Of particular note is the use of the colour conventions suggested by Bang Wong in their 2011 Nature, Methods article [1]. These are:  .

Reference: Parenthetic citation was utilized for references to external works by other authors (e.g., [1,7] refers to citations 1 and 7). Internal references to different chapters/appendices and sections are denoted by *chapter/appendix.section.subsection*. References to subsections make use of the section symbol such that a reference to subsection 3.3.1 is denoted §3.3.1. Figure, table and equation numbers are denoted by *chapter/appendix.value*, where value is the incremental numerical value of the figure, table or equation.

Equations: Units are provided for every numbered equation, presented in square brackets (e.g., $[\mu m\, s^{-1}]$ indicates micrometres per second). If the units are not provided for a numbered equation, the equation is unitless unless it is otherwise explained in the text of the thesis. Particular equations and mathematical expressions within the body of text that are not numbered will occasionally include units in square brackets for emphasis, e.g. $P_0 + P_1 e^{i\omega t}\,[\mathrm{W}]$. If units do not appear in these equations and expressions, they are not assumed to be unitless. Units are provided in the standard International System of Units (SI), unless otherwise noted. In this thesis, the real and imaginary parts of a complex number or function z are denoted $\Re[z]$ and $\Im[z]$, respectively.

Frequency and Wavelength: In far-infrared astronomy it is fairly common to use both

wavelength (λ) and frequency (ν) to represent the spectral content of electromagnetic radiation. Both are related by $c = \nu\lambda$ where c is the speed of light in vacuum. Additionally, I will note that wavenumbers ($\sigma = 1/\lambda = \nu/c$) provide a natural frequency unit in Fourier transform spectroscopy. As these representations will be used throughout this thesis, I have noted them explicitly here.

Variables: The Greek letter σ is used in this thesis to both represent wavenumber, $\sigma = 1/\lambda$, and the statistical quantity, standard deviation. To distinguish between both cases, standard deviation will be represented by a $\boldsymbol{\sigma}$ character while wavenumber will use the σ character. Also throughout this thesis, the Greek character, ν, is used to represent frequency while the Latin character v is used for speed/velocity. In some fonts these characters are very similar, here I note the difference.

Spelling: British/commonwealth-standard spelling has been used throughout this this.

Acronyms and Abbreviations: The first letter in each word of an acronym has been capitalized to help provide clarity in the choice of acronym letters as was done in my Master's thesis. Additionally, the first occurrence of each acronym in a chapter has been spelled out explicitly to aid the reader when reviewing a chapter of this thesis in isolation.

Chapter 1

Introduction

> An object is frequently not seen *from not knowing how to see it*, rather than from any defect in the organ of vision.
>
> –John. F. W. Herschel (1792–1871) [2, 3]

As an undergraduate student, I was privileged to have a particularly astute lab instructor that made a remark to the effect of the following:

> Many people believe they enjoy the scientific process. After all, our understanding of the natural world and our place in it has seen radical changes informed by both scientific experiment and theory. However these changes in our understanding, are not the scientific process, rather *they are the results of scientific endeavors*. It is rare to find someone who actually has a desire to spend countless hours in a dark windowless room performing the repeated measurements that make and reinforce these discoveries.
>
> –Mark Tipper, M.Sc.

It was a sentiment I do not believe I fully appreciated until, at the commencement of my doctoral program, I left the comforting pulses of the cryostat and my repeated measurements of what is effectively a hot brick to begin my studies without access to laboratory or equipment in the relative isolation necessitated by a global pandemic. In spite of the lofty end goals held by any researcher focused on instrumentation, I feel I must warn the reader that the work I present and discuss in this thesis, which to my knowledge is unique, is unlikely to fundamentally change one's understanding of their place in the Universe. It is much more likely that it will be as dull an experience (if not more so) as reading countless other doctoral theses. That said, it is my sincere hope that this work is not only of

some use to others but that it may also instill in some small part the sense of purpose (and what I may dare even call beauty) that comes from the rigorous examination and profound understanding of a scientific instrument.

To contextualise the motivations for the instruments that I will discuss throughout this thesis, this chapter will consider the scientific promise of far-Infrared (IR) astronomy with a particular emphasis on that which could be achieved by observations with improved spatial resolution. I will introduce and discuss Double Fourier Interferometery (DFI) from a space-based platform as a promising path to overcome the challenges faced by far-IR observatories in achieving imaging with an acute spatial resolution at long wavelengths. Accompanying these, I will also provide a brief introduction to the concept of spatial interferometry and the development of a laboratory-based DFI testbed instrument. I will also provide a summary of the following chapters of this thesis.

1.1 The scientific potential of far-IR astronomy

Approximately half of the total energy density of Electromagnetic (EM) radiation emitted by stars and accreting objects in the Universe throughout cosmic time is observed in the far-IR regime (loosely defined as encompassing $\sim$30 to 1 000 μm or 10 to 0.3 THz) [4, 5]. Astronomy at these wavelengths is vital in furthering our understanding of our cosmic origins. In their review of the modern technology landscape of far-IR astronomy, Farrah et al. (2019) [6] outline four salient areas of astrophysical research that are uniquely addressed by the far-IR regime: (1) planetary systems and the search for life, (2) the early lives of stars, (3) the assembly history of galaxies, and (4) the origins of the Universe. For these reasons, there has been substantial interest in far-IR observatories throughout the past decade and most recently with the United States calling for proposals for a potential far-IR probe mission (approximate budget of $1B) as the second greatest priority in its 2020 decadal survey of astronomy and astrophysics report, *Pathways to Discovery in Astronomy and Astrophysics for the 2020s* [7, 8, 9].

The far-IR regime is home to many molecular and atomic spectral features, including water, that are of particular interest in understanding planetary systems and their capability to support life [5, 6, 10, 11]. Spatially resolved measurements of far-IR water features would provide a probe of protoplanetary disc structure and indicate where the water-snow line is located near Young Stellar Objects (YSOs) [12]. The abundance and phase of water near YSOs can notably be used to measure the efficiency of dust grain clumping, trace the flow of volatile elements, determine the composition of early atmospheres, and measure water's ultimate incorporation into potential biospheres [10, 12, 13]. Additionally, far-IR emission from rotational and low-lying vibrational features of organic molecules provide measurements of potential building blocks for life [5]. The Spectral Energy Densities (SEDs) of proto-stellar, proto-planetary, and debris discs are measured at or near their peak brightness in the far-IR, and their evolution in Galactic stellar nurseries can be traced through far-IR continuum measurements [5, 6, 10]. Far-IR continuum observations are also useful in measuring trans-Neptunain objects and zodiacal dust to provide powerful constraints on the early formation stages of our Solar System [14, 15]. With sufficient spatial resolution, observations of this type could potentially be extended to other solar systems as well [6].

A wealth of molecular and atomic fine-structure spectral lines that provide powerful probes of Interstellar Medium (ISM) composition, structure, and dynamics fall within the far-IR. These spectral diagnostics also provide potent tracers of star formation. The low-lying rotational transitions of Carbon monoxide (CO) (being the second most abundant molecule in interstellar clouds [16, 17]) provide an important tracer of the warm molecular ISM as they are the dominant source of cooling in these diffuse regions [11, 12]. Observations of CO emission combined with observations of atomic fine structure emission in the far-IR from CI, CII, OIII, and NII provide powerful tools for studying the energetic regions of molecular clouds in the ISM that are ionised by stellar Ultraviolet (UV) radiation, accretion flows, outflows, jets, and associated shocks [6, 11, 12, 18, 19]. Additionally,

water emission provides an important tool for studying star formation as a tracer of shocks as well as the accretion and infall of matter close to protostars [12]. Complementing the information provided by far-IR spectral lines, far-IR continuum measurements are useful in determining the luminosity and evolutionary stages of protostars as the SED of early-stage protostars peak in the far-IR [6, 20, 21]. Far-IR continuum measurements are also powerful tools in tracing ISM structures and measuring their dust temperatures [5, 6, 10].

The insights provided by far-IR observations on ISM physics are not limited to the Milky Way, as measurements of the energy balance of the ISM can also be determined in nearby galaxies [6, 12, 22]. Additionally, the redshift experienced by the light from distant galaxies is such that half of the observed flux from galaxies resides in the far-IR [4, 10, 23, 24]. The far-IR provides access to measurements of the star formation rates and black hole accretion rates of galaxies up to redshifts of $z \gtrsim 7$ and are essential in understanding the steady rise of star formation rates after $z \sim 6$ and their peak in $z \sim 1$–3 before strongly declining [6, 10, 12, 25]. Although CO rotational features, the lowest transitions of which can be observed by ground-based Sub-Millimetre (sub-mm) observatories, are often used as a proxy tracer of H_2, 20-80% of the molecular gas in galaxies may be "CO-dark" [12, 26]. Emission measurements of the rotation lines of HD at 28 and 122 μm enable direct observations of H_2 that are not reliant on surrogate gas tracers [10, 12].

In addition to the above, it must be noted that far-IR observations play an important role in B- and E-mode observations of the Cosmic Microwave Background (CMB) which provide the most powerful observational constraints on the early universe [6]. These rely on the subtraction of polarised dusty foregrounds that require far-IR measurements for isolation and removal [27, 28].

In spite of the promising science it affords, the far-IR Universe remains relatively unexplored due in significant part to technological limitations that have only been alleviated to some measure in the past 40 years [29, 30, 31, 32]. Farrah et al. (2018) [6] state "far-infrared astronomy has more of the 'wild west' about it" when compared to the maturity of

optical and near-IR astronomical technology. They make particular note that far-IR observing platforms range widely in maturity and that all modern far-IR technology areas have development paths by which enormous increases in observing capabilities are possible.

The major technology hurdles faced by far-IR astronomy can largely be attributed to three challenges: (1) the capabilities of suitable detectors, (2) attenuation from Earth's atmosphere, and (3) the need for the cryogenic cooling of optical systems and detectors [6]. The foundations of far-IR astronomy as a field were laid in the 1960s through the development of far-IR bolometers sensitive enough to serve as suitable direct detectors (see Low, 1961 [29]) and the field experienced significant maturation after this time through the increased sensitivity of far-IR detectors and the development of far-IR observatories to employ the advancing detector technologies [6, 32]. In spite of impressive advances, the pixel count and sensitivities of direct far-IR detectors are still modest compared to optical and near-IR focal planes in which millions of near photon noise limited detectors can be fielded in a single chip [6, 33]. I provide a discussion and history of bolometers as far-IR detectors in Chapter 4 of this thesis. Earth's atmosphere, which is almost entirely opaque in the far-IR regime, results in attenuation in far-IR observations that is a significant challenge for far-IR astronomy and limits the most effective far-IR observatories to space-based platforms [6, 34, 35, 36]. In addition to these two challenges, thermal emission from components in the optical path at temperatures higher than a few Kelvin are a significant source of contaminate light in far-IR telescopes [37]. Attempts to balance all three of these technical challenges have divided the legacy of space-based far-IR observatories as of the time of writing into two design camps: small, cold telescopes or large, warm telescopes. This division in designs has led to observatories with severe limitations in either spatial resolution (small telescopes) or sensitivity (warm telescopes) [8].

1.2 The case for a space-based far-IR spatial interferometer

The minimum on-sky angle between two objects, $\Delta\theta$, that can be spatially resolved as physically distinct by a single aperture telescope is given by the Rayleigh criterion [38],

$$\Delta\theta = 1.22\frac{\lambda}{D} \quad [radians], \tag{1.1}$$

where λ is the wavelength of observed light and D is the diameter of the telescope's aperture (nominally its primary mirror). The factor of 1.22 corresponds to the radius of the first dark fringe in an Airy-disk pattern which is the diffraction pattern corresponding to a circular aperture (e.g., a telescope with a circular primary mirror) [38, 39]. From this relationship, we see that a larger telescope is required at longer wavelengths to achieve a similar degree of spatial resolution that can be obtained at shorter wavelengths. To overcome this limitation, astronomy at sub-mm and longer wavelengths has turned to multi-aperture solutions employing spatial interferometry. It is common to refer to using multiple apertures or telescopes (i.e., an array of telescopes) to decode the spatial information of an astronomical source simply as interferometry. As the optical instrument discussed in this thesis measures both the spectral and spatial information of a target through optical interference, I will make the explicit distinction between *spatial* interferometry and *spectral* interferometry throughout this thesis.

Figure 1.1 demonstrates the spatial resolution of multiple world-class ground-based and space-based observatories. Unfettered access to the mid-IR to UV regimes of the spectrum with sub-arcsecond spatial resolution have been obtained through space-based single-aperture observatories such as the Hubble Space Telescope and the James Webb Space Telescope (JWST). Additionally, the next generation of extremely large ground-based telescopes (e.g., the Extremely Large Telescope (ELT) and the Thirty-meter Telescope (TMT)) aims to significantly improve the spatial resolution of observations in these wavelengths in the coming decade. Through interferometry from ground-based platforms in the previous

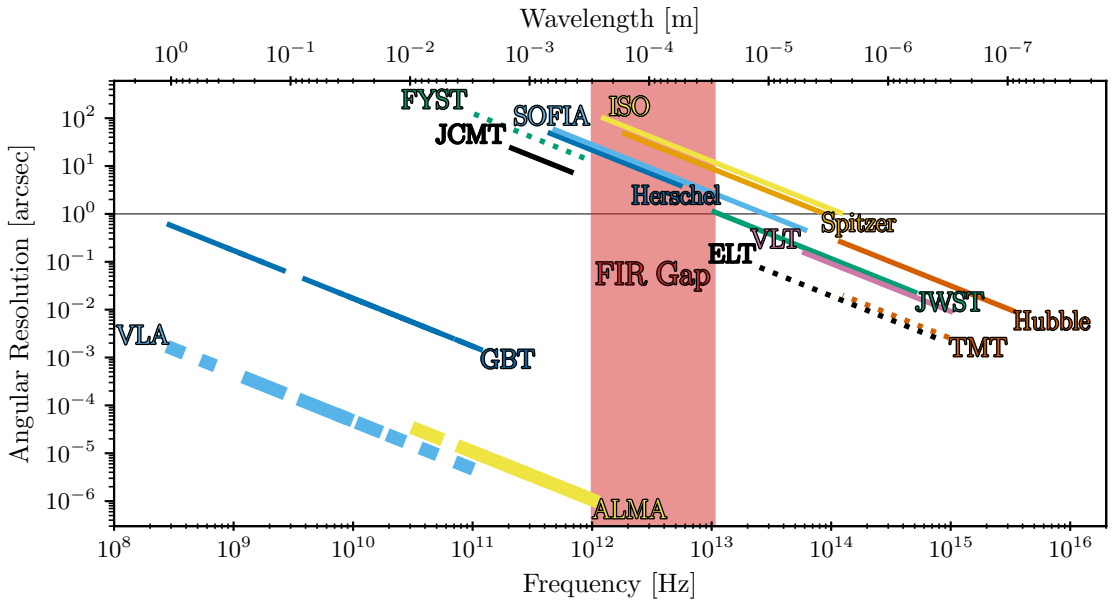


Figure 1.1: The spatial resolution of several current and legacy world-class observatories across the EM spectrum (see Equation 1.1). Selected facilities that are under construction but have not achieved first light are also included as dashed lines. The interferometer observatories Atacama Large Millimetre Array (ALMA) and Very Large Array (VLA) are denoted by a thicker line width. A resolution of one arcsecond is marked by the horizontal black line and the far-IR regime where sub-arcsecond resolution observations have not been achieved is shaded in red.

decade and earlier, sub-mm and radio astronomy have seen observations with better than milli-arcsecond spatial resolution. Due to the limited size of space-based single-aperture telescopes, the spatial resolution of observations in the far-IR from 1 to 10 THz lag those at other frequencies by several orders of magnitude.

To achieve a spatial resolution of 0.2 arcsecond (i.e., a similar resolution to what can be achieved at radio, mid-IR, optical, and UV wavelengths) at the longest wavelength band of the far-IR gap would require an observatory with a $\sim$38 m diameter mirror. A mirror of this size is nearly a factor of 6 larger than the primary mirror of JWST and nearly a factor of 11 larger than that of *Herschel*. A far-IR spatial interferometer from a space-based platform has been identified by the astronomical community as having substantial potential that far exceeds the capabilities of any single-aperture facility [6, 40]. For this reason, investigations into the development of a space-based far-IR interferometer have been recommended

in the United States astronomy community's decadal reporting process (2000), *Astronomy and Astrophysics in the New Millennium* [41], the National Aeronautics and Space Administration (NASA) Origins Probe Mission Concept Study (2004) [10], the European Space Agency (ESA) Far-Infrared Interferometer Technology Reference Study (2006) [42], the ESA Cosmic Vision long term plan (2015) [7], the Far Infrared Space Interferometer Critical Assessment (FISICA) (2015) [43], and a white paper in the ESA Voyage 2050 Long-term plan (2020) [44].

Many of the far-IR science cases outlined in §1.1 cannot be fully addressed by ground-based observatories and require spatial resolution beyond that of a single-aperture space telescope [10, 12]. Additionally, nearly all of these science cases would experience transformative progress with the dramatic increase in spatial resolution that would be achieved with the implementation of a space-based far-IR interferometer [6]. Of particular note are studies of protoplanetary and debris discs, ISM structures that lead to star formation, the structure of star formation in nearby galaxies, and spatially resolving redshifted galaxies at the cosmic peak of star formation. Table 1.1 highlights a selection of science cases identified by the global astronomy community that would see significant benefits from the implementation of a space-based far-IR interferometer.

DFI has received substantial attention as a promising technique/instrument concept for space-based far-IR spatial interferometry leading to mission proposals by both the NASA and ESA communities, the launch of a balloon-born DFI instrument to serve as a pathfinder, and a number of laboratory-based DFI instruments to further study the technique and improve on DFI technology readiness. DFI couples a spatial interferometer to the spectral interferometry techniques familiar to Fourier Transform Spectrometers (FTSs) through the inclusion of two or more separable apertures. I discuss this technique and instrument type more fully in Chapter 2. Through NASA, the ambitious Submillimetre Probe of the Evolution of Cosmic Structure (SPECS), and its smaller pathfinder the Space Infrared Interferometric Telescope (SPIRIT), have been studied since the early 2000's [10, 48, 49]. SPECS

Table 1.1: A list of science cases that stand to benefit from far-IR interferometry from a space-based platform and their required angular resolution. These are a selection of cases identified in far-IR community workshops held in Madrid (2004), Leiden (2005), and Obergurgl (2006) [5] with additions from cases identified by Linz. et al. (2020) [12], Benford and Leisawitz (2004) [45], Rinehart et al. (2016) [46], and Rinehart et al. (2020) [47].

Science Case	Resolution Needed (arcsecond)
ISM Star formation feedback	1
ISM Turbulent Dissipation Regions	0.7
Water abundance in protostellar cores	1
Protoplanetary discs:water	0.02–0.1
Protoplanetary discs:dust	<0.01
Debris discs: dust	<0.01
HD/CO-dark gas	0.01-0.1
Protostellar outflows	0.05
Luminoscity function in clusters	0.01
Water tracing infall	<0.1
Giant planets in protoplanetary discs	0.001
Solar system science	0.1
Photodissociation Regions	0.1
Asymptotic giant branch shells	0.01–0.1
Turbulent ISM	0.1
Ultra-luminous IR galaxies: Dust	<0.05
Ultra-luminous IR galaxies: Gas	<0.05
Merging active galactic nuclei	<0.02
Interstellar gas evolution	0.3-1
Interstellar dust evolution	0.3-1
Active galactic nuclei line diagnostics	<0.05
Planetary formation in nearest protostars	0.01
Deep field targets for cosmology	0.02

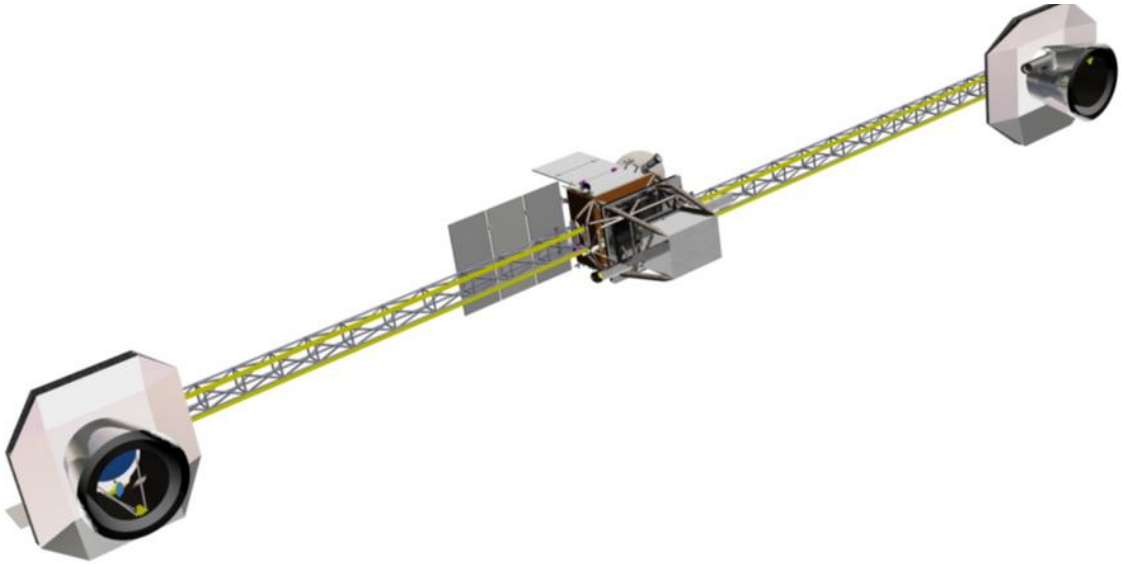


Figure 1.2: The SPIRIT/SPICE mission concept. Two telescopes are connected by a deployable boom feed light to a central beam combiner. Image credit: Leisawitz, D., Mundy, L., and the SPICE Instrument Team.

sought to achieve a maximum baseline of a kilometre through a tethered formation of three telescopes while SPIRIT was to achieve a maximum baseline of 36 m with two telescopes connected by a deployable boom [10, 49]. Most recently, the Space Interferometer for Cosmic Evolution (SPICE) has been considered for a proposal to the most recent NASA astrophysics probe announcement of opportunity (2023) and builds on the design of SPIRIT [50]. Through ESA, the Far Infrared Interferometer (FIRI) mission was studied (2009 and 2012) and considered in detail through the FISICA report [5, 43]. As a pathfinder for the SPIRIT mission, the Balloon Experimental Twin Telescope for Infrared Interferometry (BETTII) had its first flight in 2017 which unfortunately ended with the destruction of the payload and was only successful as an engineering flight [51, 52]. Laboratory testbed DFI instruments have been developed by NASA Goddard (U.S.A.) [53, 54], a collaboration between Cardiff University, University College London, and the Rutherford Appleton Laboratory (U.K.) [55, 56, 57], the National Astronomical Observatory (Japan) [58], and now the University of Lethbridge (Canada) [59, 60, 61, 62].

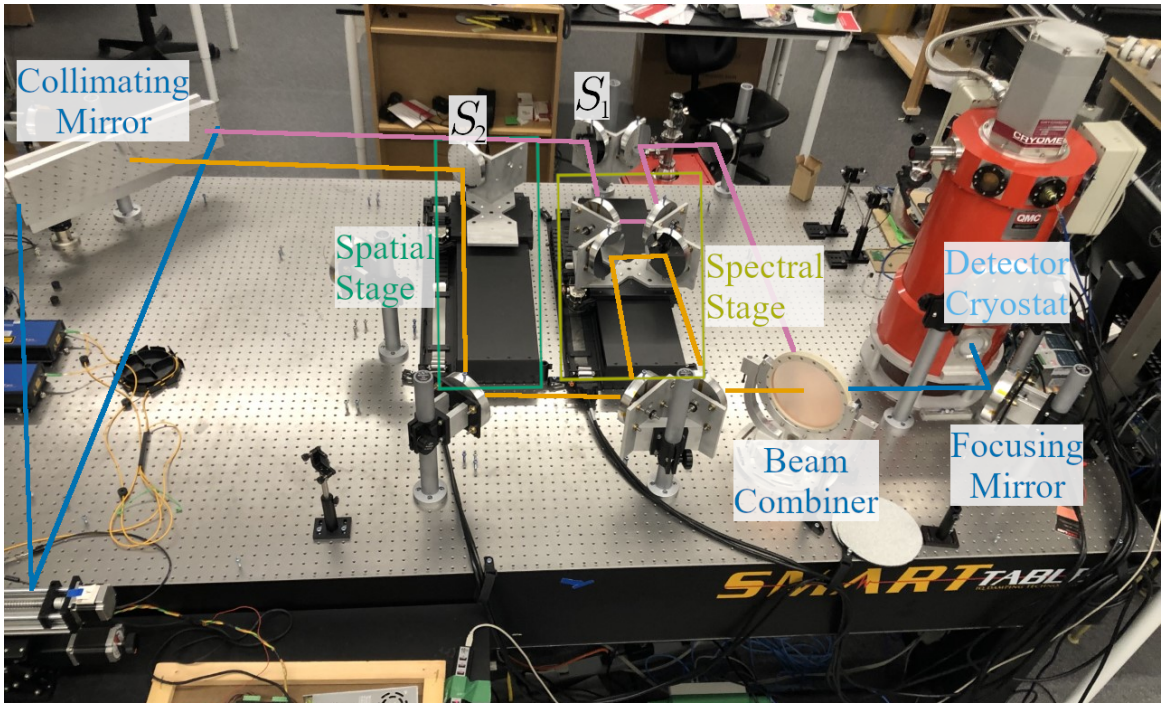


Figure 1.3: The DFI testbed developed at the University of Lethbridge. Entrance apertures are marked as S_1 and S_2.

1.3 The University of Lethbridge Double-Fourier Interferometer

As a part of the University of Lethbridge Astronomical Instrumentation Group (AIG), I have been part of the development and construction of a laboratory-based DFI testbed. The Lethbridge DFI stands unique among DFI testbeds as it operates within a spectral band of ∼200–2,200 GHz and is coupled to an array of bolometric detectors. Figure 1.3 shows a photograph of the DFI testbed. The design is similar to that of a Michelson spatial interferometer [63] that has been coupled to a Mach-Zehnder-like FTS spectral interferometer (similar to the *Herschel* Spectral and Photometric Imaging Receiver (SPIRE) FTS [37, 64]). The interferometer makes use of two linear translation stages: the spatial stage is used to separate the two input apertures of the interferometer (S_1 and S_2) while the spectral stage scans to introduce optical path delays between each beam path through the interferometer (shown in pink and orange in Figure 1.3).

As the development of the DFI testbed has been a collaborative effort within the AIG, here I detail my particular contributions to the development of the DFI testbed. My pri-

mary contribution has been the characterisation and optimisation of the unique array of Transition Edge Sensor (TES) bolometers that serve as detectors for the DFI. Additionally, my work has included aligning the interferometer, measuring the spectral performance of the beamsplitters, constructing alternative broadband beamsplitters to aid in interferometer alignment, and characterising the spectral performance of the interferometer assembly and detectors. As a collaborator, I have contributed to the optical design of the interferometer and the optical performance testing of assembly mirrors.

In Chapter 2, I fully present the optical design of the DFI testbed and detail the theory of operation of the DFI. Additionally, the alignment of the optical system is detailed in Appendix B. The Lethbridge DFI testbed measured its first far-IR spectral interference fringes in September 2022 and early spatial results in the following month. The first spatial interference fringes were measured with the DFI testbed in May 2023 [62].

1.4 Thesis Summary

This thesis centres on the characterisation and optimisation of the unique array of TES bolometers which serve as detectors for the DFI testbed. Before an optical instrument can be used for science, a detailed understanding of the performance and systematics of the detector system that is employed is crucial. In Chapter 2, I present the underlying physics of FTS and DFI with a particular emphasis on the optical signals that are output from DFI and FTS instruments. The chapter provides the necessary theoretical framework to understand the performance requirements and considerations for optimising the detector system in the context of DFI and FTS instruments.

Chapter 3 discusses far-IR detectors focusing on TES bolometers. Fundamental equations to measure the performance of TES bolometers as far-IR detectors are presented and discussed as is a brief overview of modern observatories with TES bolometer focal planes. The unique array of feedback-controlled TES bolometers that serve as a detector array for the DFI are presented and discussed in the chapter. The operational principles, the ad-

justable parameter suite, general communication performance, and the measurement process of the unique TES detector array employed by the DFI testbed are also detailed.

The technical characterisation and optimisation of the detector array that is largely independent of additional considerations from operating the detector array in a DFI are presented and discussed in Chapter 4. This includes a discussion and overview of experiments to determine the thermal properties of the detectors and to determine the optimal configuration of adjustable detector parameters. Additionally, I study the results of detector characterisation experiments to determine performance and experiment design considerations for the optimal coupling of the DFI testbed and detector array.

I present and discuss the measurements of the DFI testbed optical assembly necessary to fully characterise the spectral and noise performance of the detector array in the assembly in Chapter 5. The chapter includes measurements of the spectral behaviour of other pieces of the optical assembly some of which are directly coupled to the detectors within the cryostat unit. I provide further detector performance characterisation with the full context of the detectors as an integrated part of the interferometer assembly.

In Chapter 6, I summarise detector performance and characterisation measurements made throughout this thesis. In addition, I have included avenues of additional investigation to further understand the performance of the detector array.

I have provided an overview of control software, test equipment, additional details on experimental procedures, and the derivation of key equations within this thesis in the appendices that follow.

Chapter 2

Fourier Spatial-Spectral Interferometry

> It always seems odd to me that the fundamental laws of physics, when discovered, can appear in so many different forms that are not apparently identical at first, but, with a little mathematical fiddling you can show the relationship.
>
> –Richard Feynman (1918–1988) [65]

To introduce the experimental considerations required to optimally integrate a detector array into a Double Fourier Interferometery (DFI) system, I will introduce the theory of Fourier transform spectroscopy and spatial interferometry and how these are combined in a DFI instrument.

2.1 Fourier transform spectroscopy

Using a prism or another dispersive element to divide "white" light into an array of colours is a fairly simple but informative experiment to illustrate that light is composed of a spectrum of different frequencies. Though approximating light with simple monochromatic representation can be informative, it is through Fourier decomposition that we may obtain a powerful mathematical representation of polychromatic light [38, 66, 39].

2.1.1 Fourier Analysis

The technique of Fourier analysis was initially developed by Jean Baptiste Joseph Fourier (1768–1830) in his study of heat flow in solids and has since developed into a robust and widely used tool for signal analysis [67]. Fourier's theorem states that a function, $f(t)$ of

some temporal duration, T_0, (e.g., an electromagnetic wave varying in time) can be represented by an infinite series of harmonic functions with periods that are integer sub-multiples of T_0 (i.e., T_0/n where $n = 1,2,3\ldots$). An example of this Fourier composition of a square wave is shown in Figure 2.1. We can see this in the trigonometric form as,

$$f(t) = \frac{a_0}{2} + \sum_{n=1}^{\infty} \left[a_n \cos\left(n\omega_0 t\right) + b_n \sin\left(n\omega_0 t\right)\right], \tag{2.1}$$

where,

$$\omega_0 = \frac{2\pi}{T_0} \tag{2.2}$$

is the fundamental frequency in the series and a_n and b_n are the amplitudes, or weighting factors, of each sinusoid's *nth* frequency [68]. These coefficients are determined as,

$$a_n = \frac{2}{T_0}\int_t^{t+T_0} f(t)\cos(n\omega_0 t')dt' \quad n = 1,2,3\ldots, \tag{2.3}$$

and

$$b_n = \frac{2}{T_0}\int_t^{t+T_0} f(t)\sin(n\omega_0 t')dt' \quad n = 1,2,3\ldots, \tag{2.4}$$

for some function with periodicity T_0. In Equation 2.1, the series of $\cos\left(n\omega_0 t\right)$ and $\sin\left(n\omega_0 t\right)$ terms form a mutually orthogonal basis set [68].

It is common to see the Fourier series written in exponential form,

$$f(t) = \sum_{n=-\infty}^{\infty} d_n e^{in\omega_0 t}, \tag{2.5}$$

where

$$d_n = \frac{1}{T_0}\int_t^{t+T_0} f(t)e^{-in\omega_0 t'}dt', \tag{2.6}$$

and the weights of each frequency component are split between negative frequencies ($n < 0$) and positive frequencies ($n > 0$), while $n = 0$ provides d_0, the zero frequency offset term. It is important to note that there exist Dirichlet conditions for which a convergent

Fourier series representation of $f(t)$ exists [68, 69]. With a sufficient number of Fourier components, periodic waveforms that can be generated in a laboratory environment may be described by a Fourier series [70, 71].

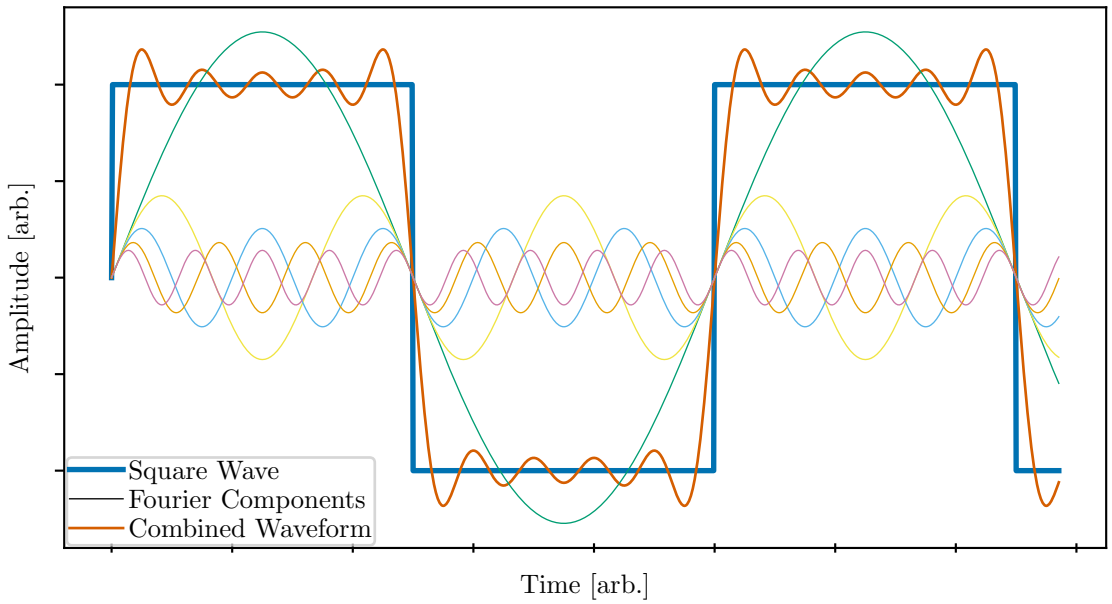


Figure 2.1: The first five terms of the Fourier composition of a square wave. Each discrete frequency sinusoid is shown as a thin waveform and the sum of these components is shown in the thicker orange line. A perfect square wave of the same period is shown by the thickest blue line.

Let us now consider the situation where the spacing between harmonic frequencies becomes infinitesimally small and the limits of the Fourier series extend out to infinity. As we approach this limit, Equation 2.5 takes the form,

$$f(t) = \int_{-\infty}^{\infty} F(\nu) e^{i2\pi\nu t} d\nu. \tag{2.7}$$

This is known as the reverse (or inverse) complex Fourier transform (note $2\pi\nu = \omega$). Instead of a set of discrete weighting coefficients or amplitudes for each harmonic frequency, we now have a smooth and continuous spectrum. This spectrum of Fourier coefficients is given

by the forward complex Fourier transform (or simply the complex Fourier transform),

$$F(\nu) = \int_{-\infty}^{\infty} f(t) e^{-i2\pi\nu t} dt. \tag{2.8}$$

It must be noted that measured data are a sampling of the theoretically smooth continuous analytical functions that have been discussed. The Fourier transform of a discrete signal comprised of N samples can be written as

$$F(\nu_k) = \sum_{m=0}^{N-1} f(t_k) e^{-i2\pi\nu_m t_k}, \tag{2.9}$$

where $t_k = k\,\delta t$ and $\nu_m = m\,\delta\nu$ are finitely sampled measurements that are spaced δt apart in the measured domain resulting in samples spaced $\delta\nu$ apart in the Fourier domain [68, 72]. The similarities between Equations 2.9 and 2.5 should be noted. Fourier analysis with discretely sampled data is more fully discussed in §2.1.5.

2.1.2 The Michelson Interferometer

The Michelson (spectral) interferometer has been a particularly effective measurement tool that has applications ranging from the historical evidence against the theory of a luminiferous ether to the detection of gravitational waves by the Laser Interferometer Gravitational-Wave Observatory (LIGO) [73, 74]. The Michelson interferometer provides a useful starting example of an Fourier Transform Spectrometer (FTS) and how it can be used to extract spectral information from a light source [72]. An experimental design of a simple Michelson interferometer is shown in Figure 2.2.

Though cost-effective and straightforward in its design, the Michelson interferometer has a disadvantage over other interferometer designs in that one of its outputs is co-aligned with the input making it challenging to exploit the full throughput of the interferometer. Improvements to the design have been made by tilting the light path so that it enters and exits the interferometer off-axis from the beamsplitter and stationary mirror or through the

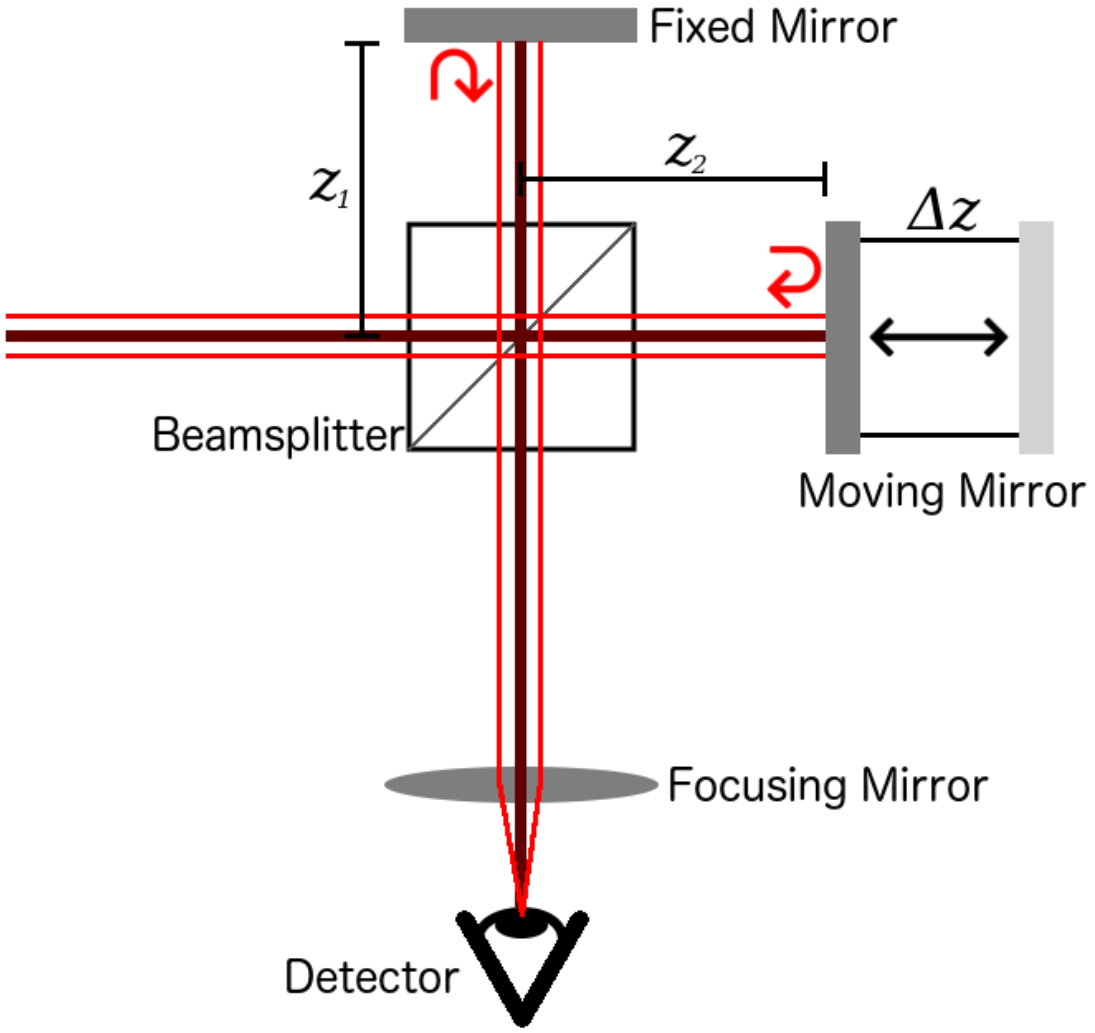


Figure 2.2: Optical diagram of a Michelson interferometer [39, 73]. Adapted from Spencer (2009) [71]. Light enters the interferometer (1) and is directed to a beamsplitter (2). Light reflects off of a stationary mirror (3a) and a moving mirror (3b) and is recombined at the beamsplitter (4). Light from the output is then focused onto a detector (5).

use of the Mach-Zehnder configuration [37, 64, 75, 76].

Let us begin by considering a quasi-monochromatic source of wavenumber $\sigma_0\,[\mathrm{cm}^{-1}]$ illuminating the input of the interferometer. Here I note that in the field of FTS, wavenumbers provide a natural frequency unit defined as $\sigma = 1/\lambda = \nu/c$, where ν is the optical frequency of light (with c being the vacuum speed of light). Once this input beam is divided by the beamsplitter, the electric fields describing each beam can be written as,

$$\begin{array}{ll} E_1\left(z_1,t'\right) = E_0 r e^{i\rho} r_m e^{i2\pi(\sigma_o z_1 - \nu t')} t e^{i\tau} & [\mathrm{V/m}] \\ E_2\left(z_2,t'\right) = E_0 t e^{i\tau} r_m e^{i2\pi(\sigma_o z_2 - \nu t')} r e^{i\rho} & [\mathrm{V/m}] \end{array}, \tag{2.10}$$

where E_0 is the amplitude of the initial electromagnetic wave with an angular frequency $\omega_0 = 2\pi\sigma_0$, $te^{i\tau}$ is the beamsplitter transmission, $re^{i\rho}$ is the beamsplitter reflection, r_m is the reflection coefficient of each folding mirror, and t' is the travel time [71, 77]. Variables z_1 and z_2 are the optical path lengths of each arm, respectively. The electric field of the waves interfering at the detector, E_D, is simply the superposition of both waves (i.e., $E_D = E_1 + E_2$). The detectors under study measure the total intensity, $I_0 = \langle E_D^* E_D \rangle$, from both waves once they are recombined (see Chapter 4) which is given by,

$$I_o(z) = \frac{c\varepsilon_o}{2}\left|E_D\right|^2 = c\varepsilon_o E_0^2 R_m R T\left[1+\cos\left(2\pi\sigma_o z\right)\right] \quad \left[\mathrm{W/m^2}\right], \tag{2.11}$$

where c is the speed of light, ε_o is the permittivity of free space, $z = z_1 - z_2$ is the Optical Path Difference (OPD), $R_m = r_m^2$ is the reflectance of the mirrors, and $R = r^2$ and $T = t^2$ are the reflectance and transmittance of the beamsplitter, respectively. For an ideal interferometer, the beamsplitter reflects and transmits 50% of incident light and the mirrors are perfect reflectors. The constant term in Equation 2.11 is typically ignored since it contains no spectral information [71, 72]. With the substitution, $B(\sigma_0) = c\varepsilon_o|E_0|^2$ which represents

the intensity of the quasi-monochromatic source, Equation 2.11 can be written,

$$I_o(z) = R_m RTB(\sigma_o)\left[\cos\left(2\pi\sigma_o z\right)\right] \quad \left[\mathrm{W/m^2}\right]. \tag{2.12}$$

Here we see that as z varies by scanning the movable mirror, the detector will observe alternating intensity maxima and minima (i.e., spectral interference fringes measured in the temporal/OPD domain). Taking the Fourier transform of Equation 2.12, two Dirac delta functions are obtained at $\pm\sigma_0$ [71]. The spectrum is zero for all other frequencies.

Due to the linearity of the Fourier transform, the detector responds to a superposition of interference fringes when viewing a polychromatic source [71, 72] which can be written as

$$I(z) = R_m RT \int_{-\infty}^{\infty} B(\sigma)\cos(2\pi\sigma z)\, d\sigma \quad \left[\mathrm{W/m^2}\right]. \tag{2.13}$$

For an ideal interferometer, when $z = 0$ all frequency components exhibit zero phase difference and constructive interference occurs simultaneously for all wavelengths. This point is commonly referred to as the point of Zero Path Difference (ZPD).

We see that, neglecting the leading constant $R_m RT$ for the moment, Equation 2.13 is the even, or cosine, Fourier transform of the spectrum $B(\sigma)$ [72]. The spectrum is then recovered by the inverse transform,

$$B(\sigma) = \frac{1}{R_m RT} \int_{-\infty}^{\infty} I(z)\cos(2\pi\sigma z) dz \quad \left[\mathrm{W/m^2}\right]. \tag{2.14}$$

Also note that just as time (t [s]) and frequency (ν [Hz]) make a reciprocal Fourier domain pair, OPD (z [cm]) and wavenumber (σ [cm^{-1}]) do as well. The distinction between the Fourier transform and its inverse is further discussed in Appendix A.3.

2.1.3 Instrumental Line Shape

Up to this point our discussion of FTS has been based around an "ideal" instrument. In Equation 2.14, we have considered a system in which OPD can be infinite. Real-world instruments experience some finite maximum OPD that can be achieved resulting in an Instrument Line Shape (ILS) that deviates from a Dirac delta function.

Consider the interferogram for a quasi-monochromatic source:

$$I(z) = I_0 \cos(2\pi\sigma_0 z) \quad \left[\mathrm{W/m^2}\right]. \tag{2.15}$$

The interferogram is limited to some finite path where $-L \leq z \leq +L$, which is the equivalent of multiplying an infinitely long interferogram (Equation 2.15) by a box-car function,

$$\begin{aligned} I_{obs}(z) &= I(z)u\left(\frac{z}{2L}\right) \quad \left[\mathrm{W/m^2}\right], \\ \text{where} \quad u\left(\frac{z}{2L}\right) &= \begin{cases} 1 & -L \leq z \leq +L, \\ 0 & \text{otherwise.} \end{cases} \end{aligned} \tag{2.16}$$

To understand the effect this has on the spectral domain, we must consider the convolution theorem for Fourier transforms. We begin by considering any two functions $f(z)$ and $g(z)$ that have the Fourier transform pairs $\mathcal{F}\{f(z)\} = F(\sigma)$ and $\mathcal{F}\{g(z)\} = G(\sigma)$. Here, $\mathcal{F}$ is the Fourier transform operator (i.e., $\mathcal{F}\{f(z)\} = \int_{-\infty}^{\infty} f(z)e^{-i2\pi\sigma z}\,dz$). The convolution theorem is,

$$\mathcal{F}\{f(z)g(z)\} = F(\sigma) * G(\sigma), \tag{2.17}$$

where $F(\sigma) * G(\sigma)$ is the convolution of $F(\sigma)$ and $G(\sigma)$ [68]. The convolution theorem shows us that multiplication in one (interferogram) domain is equivalent to convolution in the reciprocal Fourier (spectral) domain [68].

If we now consider the interferogram observed by the spectrometer in Equation 2.16,

the observed spectrum takes the form,

$$B_{\text{obs}}(\sigma) = B(\sigma) * 2L\text{sinc}\,(2L\sigma) \quad \left[\text{W/m}^2\right], \tag{2.18}$$

where

$$\text{sinc}\,(2L\sigma) = \frac{\sin(2\pi L\sigma)}{2\pi L\sigma}, \tag{2.19}$$

is the Fourier transform of the box-car function $u\left(\frac{z}{2L}\right)$ (Equation 2.16). Due to the finite optical path, the ILS of a real world FTS is a sinc profile. The Full Width at Half Maximum (FWHM) of this sinc profile is given by,

$$\text{FWHM} = 1.207\,\delta\sigma = 1.207\left(\frac{1}{2L}\right) \quad [\text{cm}^{-1}]. \tag{2.20}$$

The width, $\delta\sigma$, of the feature in Equation 2.20 is the resolution width or the distance between statistically independent samples in a spectrum. We see that in order to increase the spectral resolution of an FTS we must increase the maximum possible OPD that is scanned.

The maximum OPD constraints of a physical FTS instrument are described by an ILS function, $O(\sigma)$. The observed spectrum is the ideal spectrum, $B(\sigma)$, convolved with the ILS, $O(\sigma)$ (see Figure 2.3). To reduce the magnitude of sidelobes from spectral lines (or 'ringing') at the cost of increasing the FWHM of the line, from the ILS in an FTS spectrum, it is common to multiply the measured interferogram by an apodising function [72, 77, 78, 79, 80].

2.1.4 Phase considerations

Equation 2.13 shows the Fourier relationship between a real positive spectrum and a symmetric interferogram. The sine term representing the imaginary portion of the transform is zero and there is no phase term. In reality, an interferogram that is physically measured with digital sampling will likely have asymmetries that give rise to a complex spectrum [72]. These are often referred to as phase errors [81]. Systematic asymmetries may arise from:

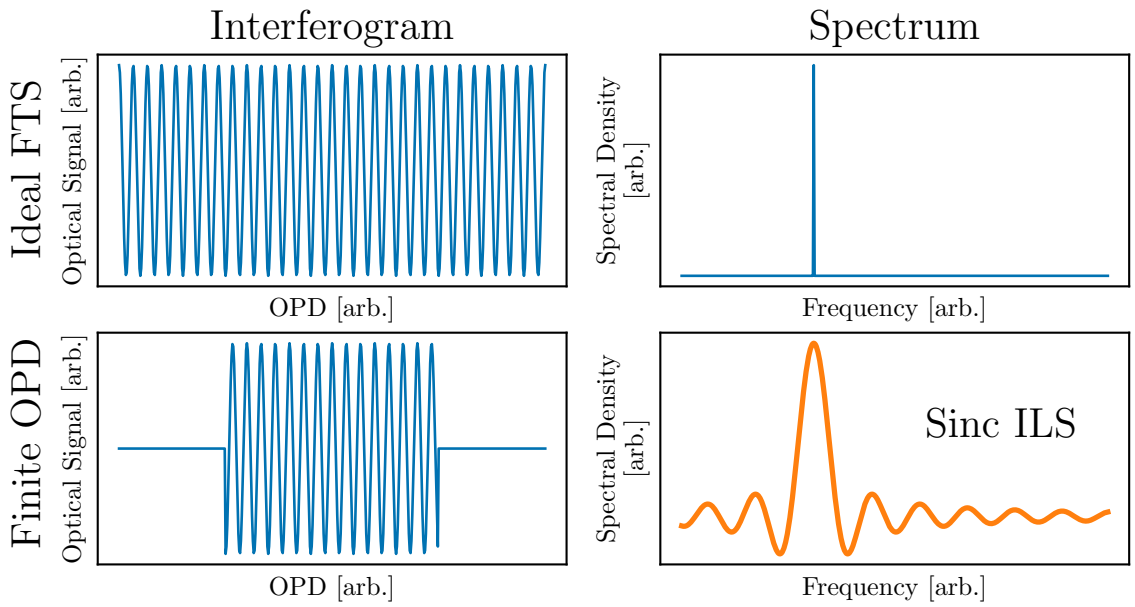


Figure 2.3: The consequences of a limiting OPD on the line profile of an FTS in both the measured interferogram and its Fourier reciprocal spectral domain.

the centre of the ZPD fringe not coinciding with a sampled point of the interferogram; changes in the source intensity during the measurement of an interferogram; phase effects from data acquisition electronics (inverting amplifiers, etc.); and dispersive effects causing OPD to be frequency dependant [72]. To fully recover the real spectrum from an FTS measurement, a complex Fourier transform is required to determine the necessary phase information.

With phase errors, we can write Equation 2.13 in its complex form as (neglecting the initial multiplicative terms),

$$I_{\text{asym}}(z) = \int_{-\infty}^{\infty} B(\sigma) e^{i[2\pi\sigma z + \phi(\sigma)]}\, dz \quad [\text{W/m}^2], \tag{2.21}$$

where $\phi(\sigma)$ represents any phase errors. Equation 2.21 represents an interferogram that is real, but asymmetric. As a result, the spectrum recovered from the Fourier transform is split between a real component with an even symmetry, and an imaginary component with an

odd symmetry [81, 82],

$$\int_{-\infty}^{\infty} I_{\text{asym}}(z) e^{i2\pi\sigma z}\, dz = B(\sigma) e^{\phi(\sigma)} = B_r(\sigma) + B_i(\sigma) \quad [\text{W}/(\text{m}^2\,\text{Hz})]. \tag{2.22}$$

The total phase error can be considered to be the sum of multiple components [81, 83],

$$\phi(\sigma) = \phi_{\text{offset}} + \phi_{\text{lin}}(\sigma) + \phi_{\text{NL}}(\sigma) + \phi_R(\sigma). \tag{2.23}$$

In Equation 2.23, ϕ_{offset} represents a phase offset which can be the result of inverting amplifiers and filters in the detector readout electronics [81, 83]. The linear phase term, $\phi_{\text{lin}}(\sigma)$, is a result of ZPD not being sampled in the interferogram [72]. Non-linear phase components, $\phi_{\text{NL}}(\sigma)$ may arise from detector signal processing and can also be the result of non-linear optics in the interferometer such as a dispersive beamsplitter or filter [72, 81]. In addition, there is a random component to phase errors, $\phi_R(\sigma)$, due to noise.

To retrieve the real measured spectrum, phase errors must be corrected. Various phase correction methods can be employed and the choice of phase correction method largely depends on how one chooses to measure an interferogram [81]. It is a common practice to preferentially measure an interferogram to a greater OPD on one side of ZPD. Measuring in this way effectively increases the maximum OPD that can be measured by an FTS and thereby the resolution (provided it has an appropriate optical design) [72, 81, 84]. Since phase errors from all sources apart from noise are often slowly varying over frequency, measurements of a preferentially-sided interferogram are often sufficiently corrected by a low-resolution phase measurement. This is obtained by measuring a small portion of the interferogram on the shorter side of ZPD [81, 83]. In this work, interferograms are not measured in this way and "single-sided" interferograms will not be fully discussed. For the interested reader, there is a comprehensive treatment of preferentially "sided" interferograms by Spencer (2005) [81]. When an interferogram is not preferentially measured on one side of ZPD, $\phi(\sigma)$ has the same resolution as $B(\sigma)$ and phase correction is easily

computed as $B_{\text{corr}}(\sigma) = B_{\text{complex}} e^{-i\phi(\sigma)}$ (or equivalently, $I_{\text{corr}}(\sigma) = I_{\text{asym}} * \mathcal{F}\{e^{-i\phi(\sigma)}\}$). It is a common practice to determine a fit to the measured phase and use the fitted representation of $\phi(\sigma)$ for phase correction to reduce the introduction of phase noise into the real spectrum [81]. Additionally, there is large uncertainty in phase measurements outside the spectral band of an FTS instrument due to low spectral amplitude. To avoid undesirable effects in phase correction, the fitted representation of $\phi(\sigma)$ should smoothly transition to zero at the edges of the spectral band [81].

2.1.5 Consequences of Digitisation

Our considerations of the Fourier relationship between interferogram and spectrum up to this point have only included smooth and continuous functions. The measured data in an FTS instrument is in reality a *digital sampling* of some theoretically smooth continuous interferogram. Ideally, the sampling of the mirror's movement provides evenly spaced OPD intervals with width δz. The Nyquist-Shannon (or simply Nyquist) sampling theorem states the required conditions for a discrete signal to be mathematically equivalent to the continuous interferogram [85, 86]. The theorem as stated by Claude Shannon is as follows [86]:

> If a function $f(t)$ contains no frequencies higher than W counts per second, it is completely determined by giving its ordinates at a series of points spaced $1/(2W)$ seconds apart.

The consequence of this theorem in the spectral domain limits the spectrum to a maximum frequency equal to $1/(2\delta z)$, often called the *Nyquist frequency*, σ_{nyq}. The sampling theory can be thought of as sampling in time or distance [72]. If a spectral feature with a frequency greater than the Nyquist frequency is present in the interferogram, it will be aliased [72].

Measuring the interferogram in equal increments of δz allows for the use of the Fast Fourier Transform (FFT) algorithm [87]. The FFT algorithm performs the computation of the discrete Fourier transform of N data points on the order of $N \log_2 N$ operations requiring

at least one unique sampling of ZPD. Failure to properly sample ZPD results in unwanted phase errors in the spectrum that can be handled in post-processing (as noted in §2.1.4).

We have already considered the effects that a finite maximum OPD, L, has on the ILS in the spectrum. As a consequence of performing the Fourier transform on a discrete signal, independent spectral data points are spaced over a finite interval $\delta\sigma = 1/(2L)$. Again we see that the spectral resolution of an FTS instrument is improved by increasing the maximum OPD that can be measured [72].

2.2 The Michelson stellar interferometer

The application of spatial interferometry in astronomy traces its heritage back to 1920 with the Michelson stellar interferometer [63]. This instrument serves as a useful introduction to the physics of spatial interferometry. We begin by considering two small apertures of equal size S_1 and S_2 separated by a distance b each viewing two quasi-monochromatic point sources, S and S', each with a wavelength of λ_0 and separated on the sky by angle θ (see Figure 2.4). If both are incoherent sources, the combined interference pattern at a given point in space is the sum of these two patterns. The OPD between light from S passing through each aperture to a point on the image plane P is given by,

$$\Delta z = \overline{SS_2P} - \overline{SS_1P} = \overline{NS_2} + \overline{S_2P} - \overline{S_1P} \quad [\mathrm{m}], \tag{2.24}$$

where $\overline{NS_2}$ is the OPD between $\overline{SS_1}$ and $\overline{SS_2}$. Similarly, the OPD from light passing each aperture to P from S' is given as,

$$\Delta z' = \overline{S'S_2P} - \overline{S'S_1P} = \overline{N'S_2} + \overline{S_2P} - \overline{S_1P} \quad [\mathrm{m}]. \tag{2.25}$$

Since $\overline{N'S_2} - \overline{NS_2} = b\theta$ in the small angle approximation ($\sin\theta \approx \theta$), the interference patterns from each source experience a phase difference of $2\pi b\theta/\lambda_0$ or a time delay of $d\theta/c$.

The separation of fringes from each interference pattern, which in principle defines

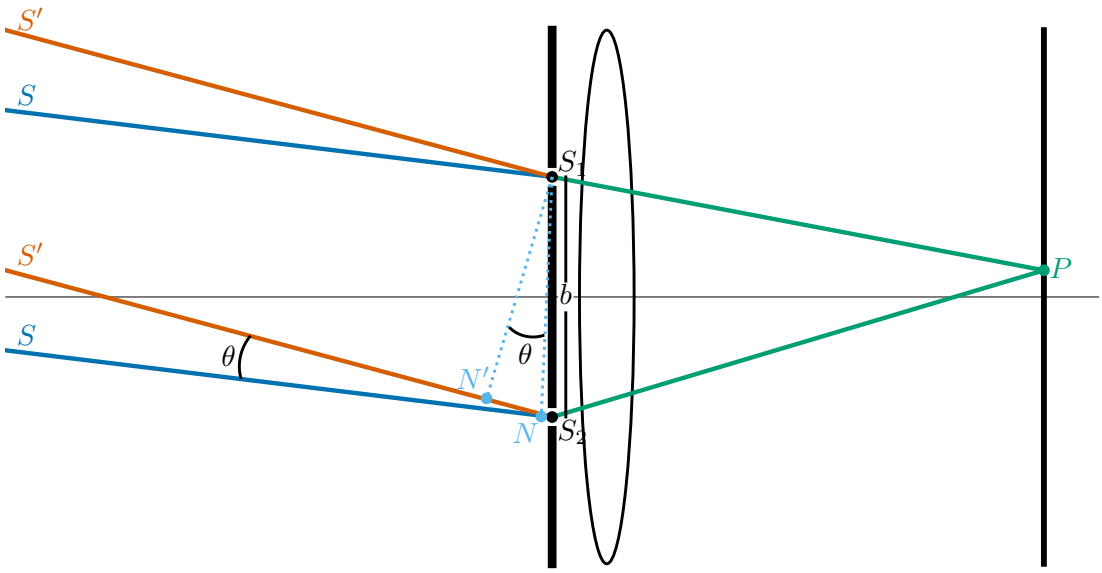


Figure 2.4: Optical diagram of a spatial interferometer with two apertures separated by a baseline b. A focusing optic behind the apertures combines the light passing each aperture on a viewing screen or detector array.

the spatial resolution of such an instrument, *relies on the separation, or baseline between the apertures*, b [38, 39]. When $2\pi b\theta/\lambda_0 = 2\pi m$ where $m = 0, 1, 2, \ldots$ intensity maxima from S and S' align and the fringing patterns from the spatial separation of the sources are most distinct. Conversely, the fringes are least distinct when the interference patterns are completely out of phase, i.e., $2\pi b\theta/\lambda_0 = \pi m$. This treatment can be broadened to extended sources which can be considered as a collection of mutually incoherent point sources. Michelson used this arrangement of a spatial interferometer that was capable of aperture separations up to 6.1 m (see Figure 2.5) and successfully measured the angular diameter of the star Betelgeuse (α Orionis) as 0.047 arcseconds [38, 63, 39]. In principle, an aperture mask is not required for such an interferometer as the collecting mirrors can serve as apertures for the instrument [39].

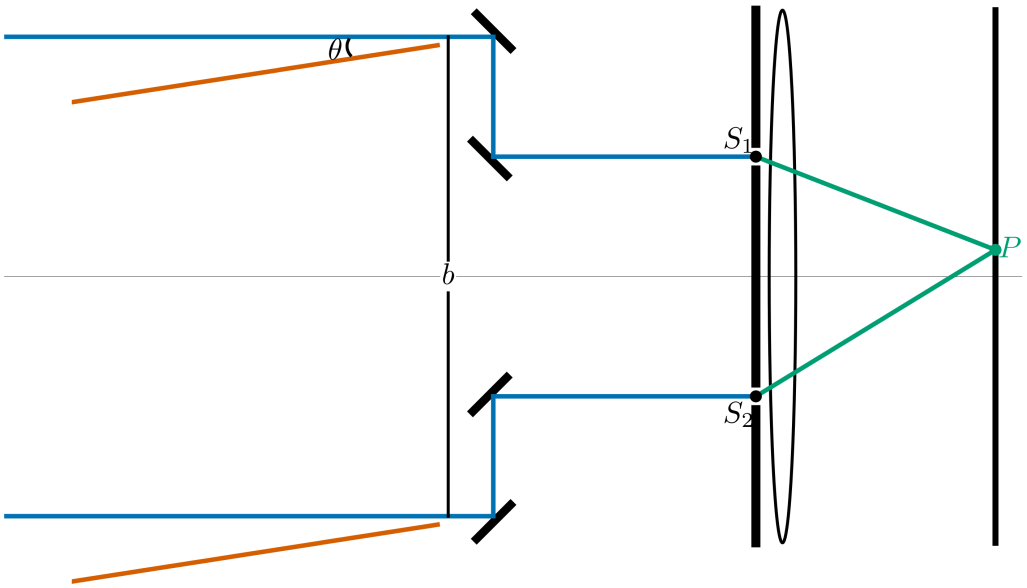


Figure 2.5: Optical diagram of the Michelson stellar spatial interferometer.

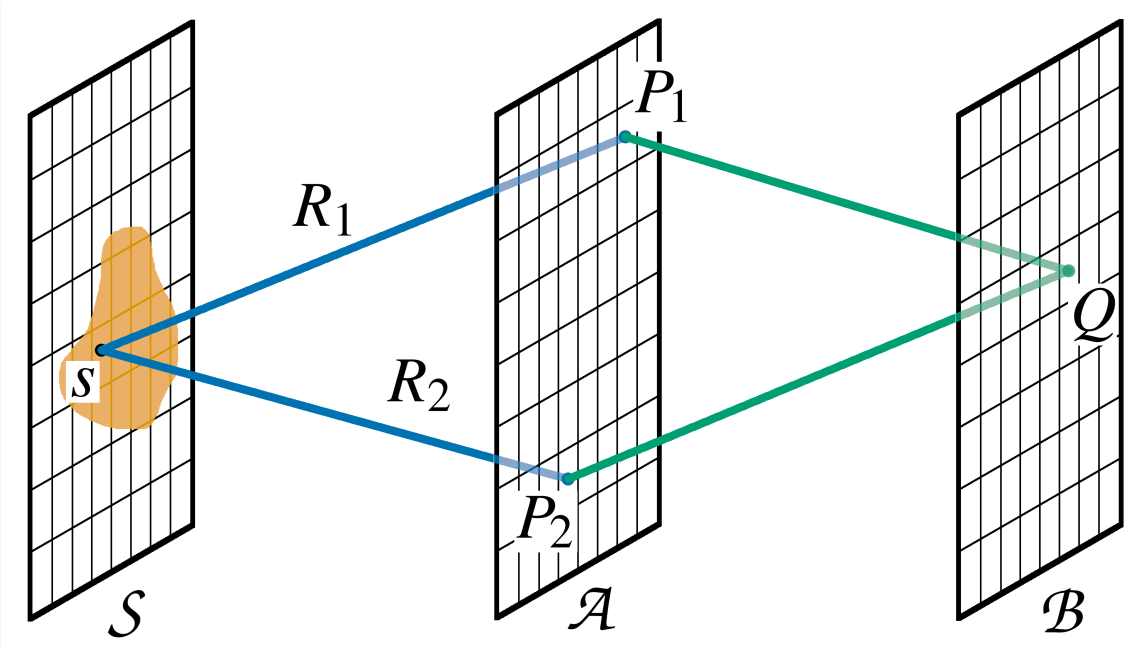


Figure 2.6: The arrangement of source plane ($\mathcal{S}$), aperture plane ($\mathcal{A}$), and image plane ($\mathcal{B}$) in the discussion of the mutual coherence function and derivation of the van Cittert-Zernike Theorem.

2.3 Coherence theory of light

2.3.1 The mutual coherence function and complex degree of coherence

The example of the Michelson stellar interferometer can be expanded to a more general treatment of how spatial information is encoded in light. To consider the interference arising between the vibrations from two points on a wavefront, P_1 and P_2, again we imagine an aperture mask $\mathcal{A}$ with two apertures at P_1 and P_2 and we consider the intensity distribution on a viewing screen $\mathcal{B}$ placed some distance from the mask (see Figure 2.6). For some arbitrary point Q on the screen $\mathcal{B}$, the distance to P_1 and P_2 is represented by s_1 and s_2, respectively. The disturbance at Q is thus given by,

$$E(Q,t) = K_1 E_1(t-t_1) + K_2 E_2(t-t_2) \quad [\mathrm{V/m}] \tag{2.26}$$

where $E_n(t-t_n)$ is the complex representation of the stochastic light field from the point S_n and K_n is the propagator associated with the aperture n. Note that this treatment overlooks any polarisation effects which may warrant further consideration for optical systems with moving mirrors. The representation in Equation 2.26, however, is sufficient for the scope of this work. The propagators K_1 and K_2 in Equation 2.26 are inversely proportional to s_1 and s_2 and depend on the size of the apertures and their relative location with respect to Q. Additionally, they can be used to account for attenuation effects along the path of travel and can account for phase changes from traversing the apertures [38, 39]. As light from the source traverses the apertures P_1 and P_2, these can be treated as the source of secondary wavelets following from the Huygens-Fresnel principle [39, 88, 89]. These wavelets are out of phase from the primary wave by a quarter period and we will take K_1 and K_2 to be fully imaginary. Also in Equation 2.26, $t_1 = s_1/c$ and $t_2 = s_2/c$, represent the time needed for light to travel from the respective aperture to Q. The intensity measured at Q is then

given by,

$$I(Q) = \langle E_Q(t)\, E_Q^*(t)\rangle = K_1K_1^*\langle E_1(t-t_1)\, E_1^*(t-t_1)\rangle + K_2K_2^*\langle E_2(t-t_2)\, E_2^*(t-t_2)\rangle + K_1K_2^*\langle E_1(t-t_1)\, E_2^*(t-t_2)\rangle + K_2K_1^*\langle E_2(t-t_2)\, E_1^*(t-t_1)\rangle \quad [\mathrm{W/m^2}], \quad (2.27)$$

where the angular bracketed terms denote a time average over an interval that is long compared to the period of the disturbance (as would be measured by some physical detector system). With the assumption that the wave does not alter its statistical nature with time (i.e., that the wave is stationary), the time average is independent of whatever time origin we select. As a result,

$$\langle E_n(t-t_n)\, E_n^*(t-t_n)\rangle = \langle E_n(t)\, E_n^*(t)\rangle = I_n \quad [\mathrm{W/m^2}] \quad (2.28)$$

and with the introduction of $\tau = t_2 - t_1$, the last two terms of Equation 2.27 can be shifted by t_2 which become

$$K_1K_2^*\langle E_1(t+\tau)\, E_2^*(t)\rangle + K_2K_1^*\langle E_2(t+\tau)\, E_1^*(t)\rangle = 2\Re\left[K_1K_2^*\langle E_1(t+\tau)\, E_2^*(t)\rangle\right] \quad [\mathrm{W/m^2}]. \quad (2.29)$$

Since the propagators are purely imaginary, $K_1K_2^* = |K_1||K_2|$, we now write Equation 2.27 as,

$$I(Q) = |K_1|^2 I_1 + |K_2|^2 I_2 + 2|K_1K_2|\,\Re[\Gamma_{1,2}(\tau)] \quad [\mathrm{W/m^2}] \quad (2.30)$$

where the cross correlation function,

$$\Gamma_{1,2}(\tau) \equiv \langle E_1(t+\tau)\, E_2^*(t)\rangle \quad [\mathrm{W/m^2}] \quad (2.31)$$

is referred to as the *mutual coherence function* of the light field at S_1 and S_2. Note that when $\tau = 0$ the mutual coherence function simplifies to $\Gamma_{n,n}(0) = I_{S_n}$. Also, note that $|K_1|^2 I_1$ is

the observed intensity at Q if only the aperture P_1 was open (and likewise for $|K_2|^2 I_2$). It becomes natural to normalise $\Gamma_{1,2}(\tau)$ such that,

$$\gamma_{1,2} = \frac{\Gamma_{1,2}(\tau)}{\sqrt{\Gamma_{1,1}(0)}\sqrt{\Gamma_{2,2}(0)}} = \frac{\Gamma_{1,2}(\tau)}{\sqrt{I_1}\sqrt{I_2}}. \tag{2.32}$$

$\gamma_{1,2}$ is often referred to as the *complex degree of coherence* or the *normalised mutual coherence* (see Appendix A.4) [39, 38]. The modulus of $\gamma_{1,2}$ can be shown to be the fringe visibility from the spatial interference pattern [39]. Defining $I^{(1)}(Q) = |K_1|^2 I_1$ and $I^{(2)}(Q) = |K_2|^2 I_2$, Equation 2.30 can be expressed as,

$$I(Q) = I^{(1)}(Q) + I^{(2)}(Q) + 2\sqrt{I^{(1)}(Q)}\sqrt{I^{(2)}(Q)}\,\Re[\gamma_{1,2}(\tau)] \quad [\mathrm{W/m^2}]. \tag{2.33}$$

Equation 2.33 is the *general interference law for stationary optical fields* [38, 39] which provides a clear method by which the real part of the mutual degree of coherence can be measured. By measuring the intensity of light behind the aperture mask $I(Q)$ at a point Q such that $P_2Q - P_1Q = c\tau$ and alternately covering each aperture such that $I^{(1)}(Q)$ and $I^{(2)}(Q)$ are determined,

$$\Re[\gamma_{1,2}] = \frac{I(Q) - I^{(1)}(Q) - I^{(2)}(Q)}{2\sqrt{I^{(1)}(Q)}\sqrt{I^{(2)}(Q)}}. \tag{2.34}$$

2.3.2 The van Cittert-Zernike Theorem

Figure 2.6 demonstrates the coordinate arrangement I will employ to determine the mutual coherence of a polychromatic extended source. The source plane, $\mathcal{S}$ is considered to be sufficiently far away such that incident wavefronts on the aperture plane, $\mathcal{A}$, are planar. The image plane, $\mathcal{B}$ is taken to be at a distance from $\mathcal{A}$ sufficient to be in the far-field diffraction limit. Coupled with these distances is the assumption that the angle between all light rays can be assumed to be small.

Through Fourier synthesis, mutual coherence can be expressed spectrally. We now

represent the electric field from a polychromatic light source that has a spectrum of optical frequencies as,

$$\Psi(P,t) = \int_{-\infty}^{\infty} \psi(P,\nu) e^{-2\pi i \nu t}\, d\nu \quad [\mathrm{V/m}], \tag{2.35}$$

where $\psi(P,\nu)$ is the Fourier component of the electric field with a frequency ν at a point P. The mutual coherence function (see Equation 2.31) is then given by,

$$\Gamma_{1,2}(\tau) = \lim_{T\to\infty} \frac{1}{2T} \int_{-\infty}^{\infty} \Psi(P_1, t+\tau)\Psi^*(P_2,t)\, dt \quad [\mathrm{W/m^2}]. \tag{2.36}$$

Replacing $\Psi(P_1, t+\tau)$ with its spectral domain representation and considering the integration over t of $\Psi^*(P_2,t)$ with the $e^{-2\pi\nu t}$ portion of the exponent term, Equation 2.36 can be written (see Appendix A.3),

$$\Gamma_{1,2}(\tau) = \lim_{T\to\infty} \frac{1}{2T} \int_{-\infty}^{\infty} \psi(P_1,\nu)\psi^*(P_2,\nu) e^{-2\pi i \nu \tau}\, d\nu \quad [\mathrm{W/m^2}]. \tag{2.37}$$

This expression allows us to easily represent the mutual coherence of the polychromatic source.

If we consider the distant extended source as being comprised of a collection of point source elements, the disturbance at a point P_j from a single source m is,

$$\Psi_m(P_j,t) = \int_{-\infty}^{\infty} \psi_m(P_j,\nu) e^{-2\pi i \nu t}\, dt \quad [\mathrm{V/m}] \tag{2.38}$$

with the total disturbance given by,

$$\Psi(P_j,t) = \sum_m \Psi_m(P_j,t) \quad [\mathrm{V/m}]. \tag{2.39}$$

The mutual coherence function is then given by,

$$\Gamma_{1,2}(\tau) = \sum_m \sum_n \langle \Psi_m(P_1, t+\tau)\, \Psi_n^*(P_2,t) \rangle \quad [\mathrm{W/m^2}]. \tag{2.40}$$

Again we introduce propagation effects similar to Equation 2.26 which are frequency dependant such that $\psi_m(P_j,\nu) = a_m(\nu)K(S_m,P_j,\nu)$ and with Equation 2.37,

$$\Gamma_{1,2}(\tau) = \sum_m \sum_n \int_{-\infty}^{\infty} A_{m,n}(\nu)\kappa(S_m,S_n;P_1,P_2;\nu)e^{-2\pi i\nu\tau}\,d\nu \quad [\mathrm{W/m^2}], \tag{2.41}$$

where

$$A_{m,n}(\nu) = \lim_{T\to\infty}\frac{1}{2T}\left[a_m(\nu)a_n^*(\nu)\right] \quad \text{and} \tag{2.42}$$

$$\kappa(S_m,S_n;P_1,P_2;\nu) = K(S_m,P_1,\nu)K^*(S_n,P_2,\nu). \tag{2.43}$$

In Equations 2.41–2.43, S_m, and S_n, represent pairs of source points on the source plane, $\mathcal{S}$. Note that $A_{m,n}$ contains the information concerning the source intensity distribution while $\kappa(S_m,S_n;P_1,P_2;\nu)$ relates to attenuation effects through the propagation medium. The light vibrations arising from different elements in the source are assumed to be statistically independent and $A_{m,n} = 0$ when $m \neq n$ (a fair assumption for non-monochromatic sources; see Born and Wolf, 1999 [38]). Additionally, as we approach the limit at which individual point sources are a continuous intensity distribution over the extended source,

$$\sum_m A_{mm}(\nu) = \int_{\mathcal{S}} B(s,\nu)\,ds \quad [\mathrm{W/m^2}], \tag{2.44}$$

where $B(s,\nu)$ is the spectral intensity function of the source with units [$\mathrm{W\,m^2\,Hz^{-1}}$]. Equation 2.41 is now written,

$$\Gamma_{1,2}(\tau) = \int_{\mathcal{S}}\int_{-\infty}^{\infty} B(s,\nu)\kappa(s;P_1,P_2;\nu)e^{-2\pi i\nu\tau}\,d\nu\,ds \quad [\mathrm{W/m^2}]. \tag{2.45}$$

For propagation in a medium in which there is no significant attenuation from absorption

and/or scattering effects,

$$\Gamma_{1,2}(\tau) = \int_{\mathcal{S}} \int_{-\infty}^{\infty} \frac{B(s,\nu)}{R_1 R_2} e^{-2\pi i \nu \left[\tau - \frac{R_1 - R_2}{c}\right]} d\nu\, ds \quad [\mathrm{W/m^2}], \tag{2.46}$$

where R_1 is the distance from the source element to the first aperture and R_2 is the distance to the second. Equation 2.46 is the *van Cittert–Zernike* theorem and demonstrates that the mutual coherence between two points at the aperture plane and the spectral intensity of the source are related through a three-dimensional Fourier transform [39, 38, 90, 91]. Through this arrangement, the spectral information of the source is determined through an inverse Fourier transform in time (similar to a nominal FTS) and spatial information is determined through a two-dimensional inverse Fourier transform over *spatial* frequencies [39].

2.4 Double-Fourier interferometry

Chapter 1 details the interest in DFI as a pathway to dramatically increase the spatial resolution of astronomical observations of the far-Infrared (IR). Recalling Equations 2.33 and 2.46, DFI provides an effective way to measure the spectral content of a source through modulations in time, and the spatial intensity distribution of the source through its complex degree of coherence.

Recalling Equation 2.32, with $\overline{\nu}$ representing the mean frequency of light we can write the complex degree of coherence in a more convenient form,

$$\gamma_{1,2}(\tau) = |\gamma_{1,2}| e^{i[\alpha_{1,2}(\tau) - 2\pi\overline{\nu}\tau]}, \tag{2.47}$$

where

$$\alpha_{1,2}(\tau) = 2\pi\overline{\nu}\tau + \arg\gamma_{1,2}(\tau). \tag{2.48}$$

Equation 2.33 can now be written,

$$I(Q) = I^{(1)}(Q) + I^{(2)}(Q) + 2\sqrt{I^{(1)}(Q)}\sqrt{I^{(2)}(Q)}|\gamma_{1,2}|\cos[\alpha_{1,2}(\tau) - \delta] \quad [\mathrm{W/m^2}], \tag{2.49}$$

where

$$\tau = \frac{s_2 - s_1}{c} \quad [s] \quad \text{and} \quad \delta = 2\pi\bar{\nu}\tau = \frac{2\pi}{\bar{\lambda}}(s_2 - s_1). \tag{2.50}$$

If we now consider the polychromatic output from a Michelson type FTS coupled with a Michelson stellar interferometer, the interferogram as a function of optical path difference, $I(z)$, measured at a given separation between apertures b, is given by

$$I(z) = \int_{-\infty}^{\infty} I(\sigma)|\gamma_{1,2}(\tau)|\cos[2\pi\sigma z + \Phi_{1,2}(\tau)]\,d\sigma \quad [\mathrm{Wm}^2], \tag{2.51}$$

where $I(\sigma)$ is the source spectrum and $\Phi_{1,2}(\tau) = \arg\gamma_{1,2}(\tau)$ [92, 93]. Equation 2.51 is of a similar form as Equation 2.13 and demonstrates *that the output of a DFI is the Fourier transform of the source spectrum attenuated by the baseline-dependent complex degree of coherence*. Note that unlike Equation 2.13, there is an inherent phase term in spatial-spectral measurements made by a DFI. This phase term should not be confused with the phase errors discussed in §2.1.4.

2.5 Design and alignment of the DFI testbed

The Lethbridge DFI testbed [59, 60, 61, 62] has been constructed to provide further study and validation of the DFI technique for the future generation of far-IR space-based spatial interferometers (see Chapter 1). The optical layout of the DFI testbed has been designed to easily incorporate three configurations. Two of these configurations are used for measurement purposes while the third is to aid in the alignment procedure of the interferometer.

2.5.1 Full double-Fourier configuration

The Lethbridge DFI employs a Mach-Zehnder FTS design [64] that is coupled to a moving aperture and a static aperture in its full DFI configuration. Each aperture receives light from the large primary collimating mirror. Figure 2.7 shows an optical diagram of the

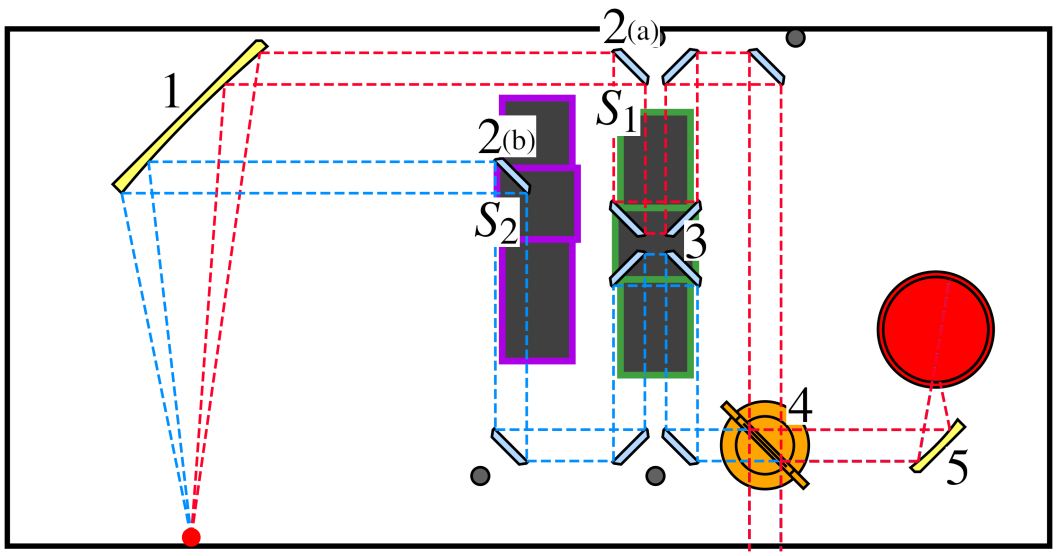


Figure 2.7: An optical diagram of the Lethbridge DFI instrument. Off-axis parabolic mirrors are shown in yellow, optical flats are drawn in grey, the beam-combiner is coloured in orange, the detector system is drawn in red, and the spatial and spectral stages are outlined in purple and green, respectively. Both optical paths (shown in blue and red) are traced through the interferometer in the text of this section. See the photograph in Figure 1.3 for reference.

DFI, the optical path of which follows:

1. the large off-axis parabolic primary mirror is illuminated by a source positioned at its focus;

2. collimated light illuminates the static aperture S_1 (a) and the dynamic aperture S_2 which is mounted on the spatial linear translation stage (b);

3. through a series of optical flats, each path of the interferometer is relayed to the double-rooftop mirror arrangement mounted on the spectral linear translation stage;

4. using another series of optical flats, each path of the interferometer is sent to the beam-combiner;

5. the combined beams are focused onto the detector array by a smaller off-axis parabolic mirror.

Measurements are made by first setting a baseline between apertures S_1 and S_2 using the spatial stage, after which the spectral stage scans through different OPDs between each arm of the interferometer (as in a nominal FTS). A single step of the spectral stage results in a factor of 4 increase in OPD such that $z_{\mathrm{OPD}} = 4z_{\mathrm{mech}}$.

2.5.2 Single FTS configuration

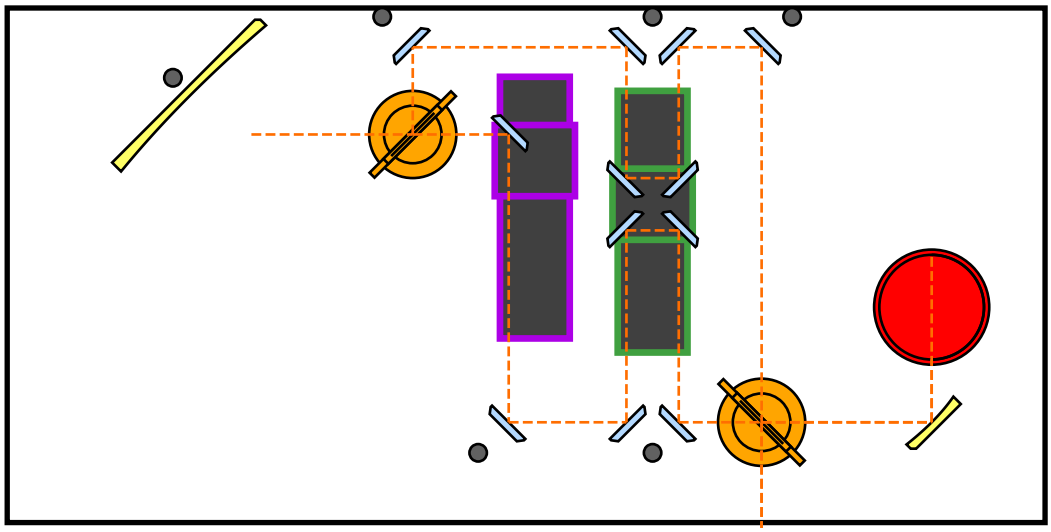


Figure 2.8: The DFI testbed in a modified arrangement to serve as a single Mach-Zehnder FTS. See Figure 2.7 for additional details.

Through the introduction of a second beam-splitting element and a folding mirror, the DFI testbed can be operated as a nominal Mach-Zehnder single-FTS as shown in Figure 2.8 [64, 37, 94]. Operating in this mode, the DFI testbed serves as a spectrum analyser that I have used to characterise the spectral performance of the detector array and interferometer assembly (see Chapter 5).

2.5.3 Alignment configuration

The alignment of an optical system comprised of 2 off-axis parabolic mirrors, 9–10 optical flats, and 1–2 beamsplitters and the two axes defined by the translation stages is not

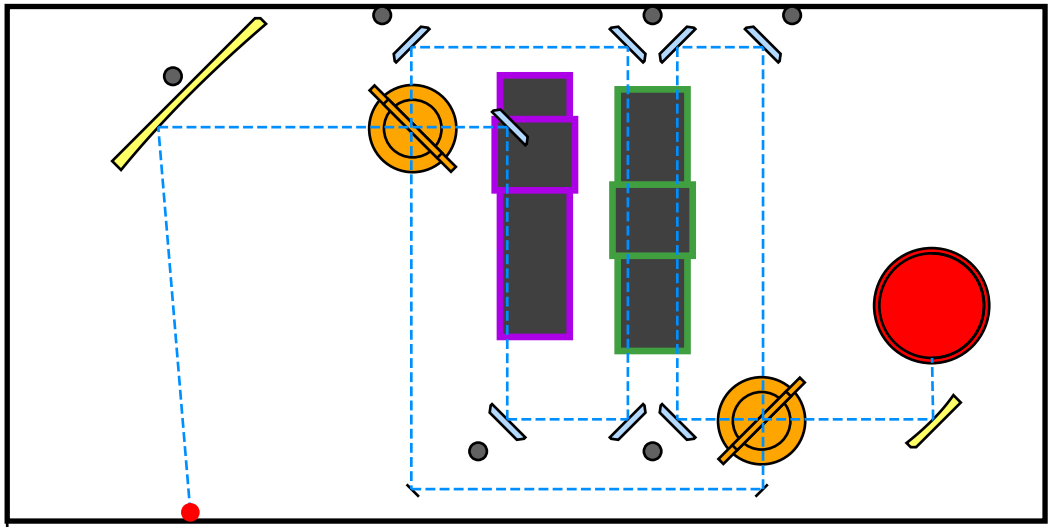


Figure 2.9: The DFI testbed in its alignment configuration. The optical layout has been modified from Figure 2.8 to form two resonant cavities.

a trivial task. We have designed the DFI testbed with this challenging optical alignment in mind. Starting with the single-FTS optical alignment, two resonant cavities can be formed by removing the double-rooftop mirror arrangement from the spectral stage, rotating each beamsplitter, and introducing two small relay optical flats (see Figure 2.9). These cavities allow for the alignment of the majority of interferometer components to be tested and verified over a substantial optical path as the alignment beam experiences multiple passes through each cavity.

I achieved the initial alignment of the interferometer visually using an optical wavelength helium-neon laser. Alignment with a visible laser required the use of optical wavelength beamsplitters that I designed and constructed to make use of the existing mounts for the far-IR beamsplitters employed by the testbed. The details of my work to build these broadband Mylar beamsplitters are detailed in Appendix C. The alignment and construction of the DFI was one of my primary responsibilities within the project and is fully detailed in Appendix B.

2.6 Conclusion

In this chapter, I have introduced the theoretical principles by which FTSs and spatial interferometers operate. This has provided the necessary context for the operation of DFI instrument. I have discussed the spectral consequences of practical FTS measurements including phase correction, digital sampling, and finite spectral resolution. I have detailed the van Cittert-Zernike theorem as the fundamental theory by which spatial information of a source can be determined through measurements of its mutual coherence function. In addition, I have presented and discussed the optical design of the Lethbridge DFI and my efforts to construct and align the interferometer as both a DFI testbed and FTS. Through the discussions in this chapter, I have provided a foundation for the physical interference of Electromagnetic (EM) radiation from the DFI testbed to provide context for the detector array we have used to measure the testbed output.

Chapter 3

Feedback-controlled Far-IR TES Bolometers

> The experiment left no doubt that, as far as accuracy of measurement went, the resistance disappeared. At the same time, however, something unexpected occurred. The disappearance did not take place gradually but abruptly. From 1/500 the resistance at 4.2 K, it could be established that the resistance had become less than a thousand-millionth part of that at normal temperature. Thus the mercury at 4.2 K has entered a new state, which, owing to its particular electrical properties, can be called the state of superconductivity.
>
> –Heike Kamerlingh Onnes (1853–1911) [95]

Advancements in far-Infrared (IR) astronomy have been closely linked to the capabilities and availability of suitable detectors. The bolometer, developed by Langley in 1881, has been particularly successful in this respect [30]. Consisting of an electric thermometer and an absorbing element that converts IR radiation to heat, the bolometer has seen both legacy and modern use in space-based and ground-based far-IR and Sub-Millimetre (sub-mm) observatories [6, 37, 96, 97].

In spite of the current widespread use of cryogenic bolometers as detectors for far-IR observations, the detection of IR radiation throughout the 1950s favoured other room temperature technologies [98, 99]. Though it was noted by Andrews, Milton, and DeSorbo in 1942, that cryogenic detectors held great promise for increased sensitivity,

> During the last few years a number of measuring devices have been built which have pushed sensitivity to the limit imposed by Brownian movement . . . If the sensitivity were to be increased beyond this limit, it would be necessary to lower the temperature of essential parts of receiving elements [100].

Building on this work by Andrews, Milton, and DeSorbo, the landmark development of a low-noise gallium-doped germanium bolometer by Low in 1961 achieved sufficiently sensitive semiconducting bolometers for use in far-IR and sub-mm astronomy after which they were rapidly adopted [32, 29, 98].

In modern applications, the bolometer has further developed toward increased sensitivities and faster responses by looking back to the work of Andrews, Milton, and DeSorbo with the development of superconducting Transition Edge Sensor (TES) bolometers [100, 101]. In their original article (1942) they present, "... bolometers of superior sensitivity operating in the temperature range where superconducting transitions could be found" [100]. While operating in this superconducting region where a small change in temperature in the thermometer results in a drastic electrical response is attractive, the low impedance of the superconducting thermometer results in poor impedance matching to traditional Field-Effect Transistors (FET) amplifiers [101]. Additionally, operating TES bolometers within their narrow superconducting region is difficult due to the Joule heating from the bias circuitry through the TES thermometer [101]. These two challenges have largely been overcome by constant-voltage biasing the TES and the use of Superconducting Quantum Interference Device (SQUID) amplifiers [98, 101].

Here, I will present the theoretical principles of TES bolometer operation and sources of noise in TES bolometers along with key equations for characterising bolometer performance as far-IR detectors. Additionally, I discuss the operation of the unique feedback-controlled detectors examined in this thesis and the adjustable parameter space associated with the operation of the detector array.

3.1 Bolometer theory

There are numerous reviews concerning the physical principles of bolometer operation with varying degrees of rigour. Of particular note among these are: a review of bolometers in general including early work with TES bolometers paired with SQUID am-

plifiers by Richards [98], a review focused on TES bolometers in particular by Irwin and Hilton [101], and a review on both TES bolometers and Kinetic Inductance Detectors (KIDs) by Mauskopf [102]. Since the detectors coupled to the Double Fourier Interferometery (DFI) testbed, which are the focus of this thesis, do not operate under constant voltage bias and do not employ SQUID amplifiers, the overview of bolometer physics contained in this section will most closely follow the treatment in the review by Richards.

3.1.1 Principles of operation

In its simplest form, a cryogenic bolometer can be modelled as an absorbing element thermally coupled to a variable resistor, $R(T)$, which serves as a thermometer for the detector (see Figure 3.1). The whole detector assembly is assumed to have a lumped heat capacity, $C_a = C_{\text{absorber}} + C_{\text{thermometer}} + C_{\text{substrate}}$. The detector is then coupled to a surrounding cryogenic bath of temperature T_b through a weak thermal link such that thermal conduction internal to the detector is large compared to the thermal conduction to the bath (i.e., the absorber, thermometer, and other components are thermalised on shorter time scales than heat is conducted to the surrounding environment). The thermal response of the bolometer is written,

$$C_a \frac{dT}{dt} = P_{\text{elec}} + P_{\text{opt}} - P_{\text{bath}} \quad [\text{W}], \tag{3.1}$$

where P_{elec} is the heating supplied by the bias circuity to the thermometer, P_{opt} is the absorbed optical power, and P_{bath} is the heat dissipation to the cryogenic bath. When under an optical load, the bolometer receives an optical power of the form $P_0 + P_1 e^{i\omega_s t}$ [W] which is comprised of a steady-state portion P_0 and a time-varying part with amplitude P_1 and frequency ω_s (as would be measured from a Fourier Transform Spectrometer (FTS) or a mechanical chopper; see Appendix E). This optical load causes the temperature of the bolometer to vary as,

$$T_a = T_0 + T_1 e^{i\omega_s t} \quad [\text{K}]. \tag{3.2}$$

If the thermometer is under a constant-current bias, I, the electrical heat added to the detector is written to first order as,

$$P_{\text{heat}} = I^2 R(T) = T^2[R(T_0) + (dR/dT)T_1 e^{i\omega_s t}] \quad [\text{W}]. \tag{3.3}$$

The bolometer dissipates thermal energy to the surrounding bath through the thermal link as $\overline{G}(T_a - T_b)$ where T_b is the temperature of the thermal bath and $\overline{G}$ is the average thermal conductance. The average thermal conductance for a wire of length l and cross sectional area A can be written,

$$\overline{G} = \frac{(A/l)}{(T_b - T_0)} \int_{T_0}^{T_b} \kappa(T) dT \quad [\text{W/K}], \tag{3.4}$$

where $\kappa(T)$ is the thermal conductivity of the bolometer material [98]. The thermal power balance of the bolometer is then written,

$$P_0 + P_1 e^{i\omega_s t} + I^2 R(T_0) + I^2 (dR/dT) T_1 e^{i\omega_s t} = \overline{G}(T_0 - T_b) + G T_1 e^{i\omega_s t} + i\omega_s C_a T_1 e^{i\omega_s t} \quad [\text{W}], \tag{3.5}$$

where $G = dP/dT$ is the dynamic thermal conductance at temperature T_0. Equating the steady state and time-varying parts of Equation 3.5 gives,

$$P_0 + I^2 R(T_0) = \overline{G}(T_0 - T_b) \quad [\text{W}], \tag{3.6}$$

and,

$$\frac{P_1}{T_1} = G + i\omega_s C_a - I^2 \left(\frac{dR}{dT} \right) \quad [\text{W}], \tag{3.7}$$

respectively. Note that approximating the time-varying expression for electrical heat from the thermometer to first order is equivalent to the small signal approximation in Irwin and Hilton (2005) and Mauskopf (2018) provided that in each power expression in the above equations, the time-varying portion is small with respect to the steady state power [101,

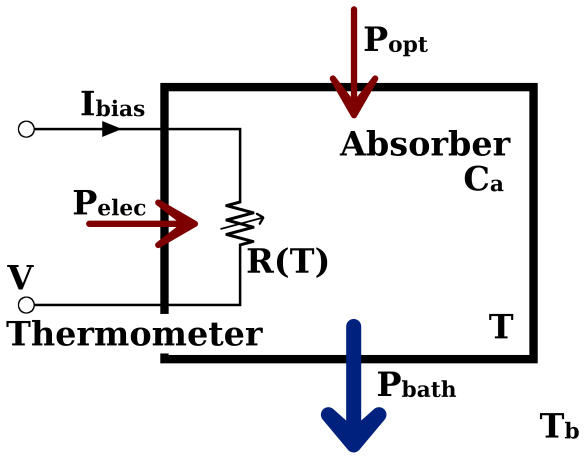


Figure 3.1: An electrical and thermal diagram of a bolometer.

102].

The voltage signal response of a bolometer can be defined as the change in voltage for each watt of incident optical power, $S_V = dV_1/dP_1 = I(dR/dT)T_1/P_1$ [V/W]. Equation 3.7 gives this as,

$$S_V = I\left(\frac{dR}{dT}\right)\frac{1}{G - I^2(dR/dT) + i\omega_s C_a} \quad [\mathrm{V/W}]. \tag{3.8}$$

Under optical loading, P_1, there is an expected rise in the bolometer temperature, $T_1 = P_1/\overline{G}$, resulting in a change in thermometer resistance, $R(T)$, and therefore a change in the electrical heating from the thermometer bias. This process is known as electrothermal feedback and can be expressed as an effective thermal conductance $G_e = G - I^2 R\alpha/T$ [98]. Here the parameter $\alpha = (T/R)dR/dT$ has been introduced as a unitless measure of the steepness of the thermometer's temperature-dependant resistance evaluated at $T = T_0$. For a superconducting bolometer, α has a large positive value (from about 10 to 50 [102]) while α is negative for semiconducting bolometers (from about -5 to -10 [103]). Here we see that for a constant-current biased TES bolometer, the Joule heating from the bias to the TES increases as the resistance of the thermometer increases. It is possible that for a large enough current bias, the bolometer can reach a state where $G_e = 0$ resulting in thermal runaway [98, 101, 102]. With the introduction of these parameters the responsivity of the

bolometer is written as,

$$S_V = \frac{IR\alpha}{TG_e}\frac{1}{1+i\omega_s\tau_e} \quad [\mathrm{V/W}]. \tag{3.9}$$

where $\tau_e = C_a/G_e$ is the effective time constant of the bolometer. It should be noted that the effective time constant relates to the physical thermal time constant, $\tau \equiv C_a/G$, as,

$$\tau_e = \tau\left(1 - \frac{P_{\mathrm{elec}}\alpha}{GT}\right) \quad [\mathrm{s}], \tag{3.10}$$

where $P_{\mathrm{elec}} = I^2R$ is the electrical power through the thermometer.

3.1.2 Sources of noise

TES bolometers are subject to a number of noise sources that limit their sensitivity as direct detectors. It is common to represent the noise performance of these detectors as a Noise Equivalent Power (NEP), defined as the incident signal power required to obtain a signal power equal to that of the noise in a one Hz bandwidth (expressed in $\mathrm{W}/\sqrt{\mathrm{Hz}}$) [98, 101, 102]. TES detectors are subject to fundamental noise sources including Johnson-Nyquist noise, photon noise, and thermal fluctuation noise as well as additional noise sources that result from the imperfect manufacturing of the detectors [98, 101, 102, 104, 105].

Johnson-Nyquist noise in a TES bolometer can be written to first order as,

$$(\mathrm{NEP}_J)^2 \simeq \frac{4k_BTR}{|S_V|^2} = 4k_BT^2G_e\frac{G_eT}{I^2R}\frac{1+\omega^2\tau_e^2}{\alpha^2} \quad [\mathrm{W^2/Hz}], \tag{3.11}$$

where k_b is Boltzmann's constant. Note that in Equation 3.11 if $G_eT \simeq P_{\mathrm{elec}}$, or equivalently, $GT/P_{\mathrm{elec}} - \alpha \simeq 1$, Johnson-Nyquist noise is suppressed relative to $4k_BTR$ by approximately $1/\alpha^2$ [98, 102, 106].

Thermal fluctuation noise in a bolometer is the result of random fluctuations in the heat flow between the bolometer and its environment. This heat flow can be calculated from the variations in the flow of phonons (quantised lattice vibrations within a solid state device) between the bolometer and its surrounding environment via its thermal link [98, 102]. As

such, this noise source can also be referred to as phonon noise. Phonons crossing the thermal link emitted by either the bolometer or surrounding bath are either absorbed, scattered, or transmitted [102]. If all phonons are transmitted across the thermal link ballistically (i.e., unimpeded), the phonon noise contribution is,

$$\mathrm{NEP}^2_{\mathrm{phonon}} = 2k_B T_a^2 G(T_a) + 2k_B T_b^2 G(T_b) \quad [\mathrm{W}^2/\mathrm{Hz}]. \tag{3.12}$$

The phonon noise in the opposing limit of dominant phonon scattering or absorption/emission across the thermal link can be expressed as,

$$\mathrm{NEP}^2_{\mathrm{phonon}} = 4k_B T_a^2 G(T_a) \frac{n}{2n+1} \frac{T_a^{2n+1} - T_b^{2n+1}}{T_a^{n+1}\left(T_a^n - T_b^n\right)} \quad [\mathrm{W}^2/\mathrm{Hz}], \tag{3.13}$$

where n represents a parameter related to the mode structure dimensionality of thermal propagation that is obtained from a power law fit. These expressions are derived and further discussed in Appendix A.1 (also see Mauskopf, 2018 [102]).

Photon noise results from the Poisson-statistical arrival of photons absorbed by the detector. Thermal emissions from all components of an optical assembly that are absorbed by the detector contribute to photon noise. The absorbed power, P_i, from a given source (e.g., a blackbody/greybody source i) within a frequency band from ν_1 to ν_2 can be written,

$$P_i = \int_{\nu_1}^{\nu_2} \varepsilon_i(\nu) B(\nu, T_i) t_i(\nu) \eta_i(\nu) A\Omega(\nu)\, d\nu \quad [\mathrm{W}], \tag{3.14}$$

where $t_i(\nu)$ is the transmission through the optical path to the detector, $\eta_i(\nu)$ is the net efficiency of the optical system, and $A\Omega(\nu)$ [m^2 sr] is the throughput of the optical system (which is the product of detector area, A, and beam solid angle $\Omega(\nu)$). In Equation 3.14, $\varepsilon_i(\nu)B(\nu, T_i)$ represents the blackbody spectral radiance of the source with temperature

T_i [K] and emissivity $\varepsilon_i(\nu)$. This can be written,

$$B(\nu,T) = \left(\frac{2h\nu^3}{c^2}\right)\frac{1}{\exp\left(\dfrac{h\nu}{k_B T_i}\right)-1} \quad [\mathrm{W\,m^{-2}\,Hz^{-1}\,sr^{-1}}], \tag{3.15}$$

where h is Planck's constant and c is the speed of light. The photon NEP of such a source can be written [71, 98, 106],

$$(\mathrm{NEP}_i)^2 = \frac{4h^2}{c^2}\int_{\nu_1}^{\nu_2}\frac{\eta_i\varepsilon_i t_i A\Omega\nu^4}{\exp\left(\dfrac{h\nu}{k_b T_i}\right)-1}\left[1+\frac{\eta_i\varepsilon_i t_i}{\exp\left(\dfrac{h\nu}{k_b T_i}\right)-1}\right]d\nu \quad [\mathrm{W^2/Hz}] \tag{3.16}$$

The total NEP from incoherent sources is obtained from the quadrature sum of the contributions from each source,

$$(\mathrm{NEP}_{\mathrm{photon}})^2 = \sum_{i=0}^{n}(\mathrm{NEP}_i)^2 \quad [\mathrm{W^2/Hz}]. \tag{3.17}$$

A derivation of these expressions is provided in Appendix A.2.

Excess noise from a variety of sources internal to a TES can also degrade detector performance. Irwin and Hilton (2005) [101] detail many of these excess sources of noise and divide them into four general categories: internal thermal fluctuation noise, excess electrical noise, telegraph noise, and excess low-frequency noise. These are also mentioned in Mauskopf's (2018) review of TES detectors in astronomical instruments with reference to experimental attempts to characterise them [102]. Excess low-frequency noise is of particular relevance to the development of a DFI paired to TES detectors in which spectral measurements are probed through optical modulation in the time domain (see Chapter 2). This excess low-frequency noise is often referred to as $1/f$-noise (though often dependent on frequency with a different negative exponent). Excess $1/f$-noise has been found to correlate with particularly high values of excess electrical noise, which can be reduced by operating at a higher temperature on the TES transition [101].

3.1.3 Modern TES focal planes

TES bolometers have seen widespread adoption in far-Infrared and sub-mm astronomy and as a result have seen significant maturation and a high Technology Readiness Level (TRL). Table 3.1 details a selection of modern sub-mm and far-IR astronomical instruments that employ TES bolometers. Challenges inherent in TES readout electronics limit the size of TES focal planes, particularly when multiplexed in the time domain. For an array with N readout columns each containing M rows of detectors, the required readout wire count scales as $N+M$ which can result in significant thermal conduction to the cold stages of the detector array at large pixel counts [6, 102]. This can be substantially alleviated through frequency domain multiplexing, in which up to 64 detectors have been read out with a single co-axial line with an additional 3 wires for the SQUID amplifier [107].

The sensitivity goal of TES detectors employed in astronomical instruments is such that detector NEP is approximate to or less than the photon noise of its observing background [6, 114, 115, 116]. For ground-based observatories, detector NEPs of a few $10^{-16}\,\mathrm{W}/\sqrt{\mathrm{Hz}}$ are required to be limited by emission from sky, telescope, and instrument while NEPs lower than a few $10^{-20}\,\mathrm{W}/\sqrt{\mathrm{Hz}}$ are required for space-based observatories for observations to be limited by the background from zodiacal light, galactic cirrus, and the microwave background [6, 8, 116].

3.2 The QMC feedback-controlled TES bolometer array

The detector array investigated in this thesis, provided by QMC Instruments Ltd. (Queens Buildings, The Parade Cardiff, Wales, CF24 3AA, UK), is comprised of 25 niobium TES bolometers housed within a cryostat. The feedhorn-coupled TES detectors each have an $f/4$ Field Of View (FOV) with the image plane located $\sim$60 mm behind the cryostat window. Figures 3.2, 3.3, and 3.4 show a photograph of the cryostat that houses the detectors and two schematic diagrams of the cryostat assembly. The location of the detectors within the assembly is shown in 3.4. Figure 3.5 shows a photograph of the detector

Table 3.1: A selection of far-IR, sub-mm, and Millimetre (mm) instruments that employ TES bolometers.

Instrument	Detector Count [/waveband]	NEP [W/$\sqrt{\text{Hz}}$]	Waveband [μm]	Platform
JCMT-SCUBA2	5 120	2.0×10^{-16}	450/850	Ground
APEX-ZEUS-2	555	4.0×10^{-17}	200–600	Ground
SPT-3G[a]	5 380	–	1 360/2 000/3 160	Ground
SOFIA-HAWK+	2 560	6.6×10^{-17}	20–250	Aircraft
SOFIA-HIRMES	1 024	2.2×10^{-17}	25–122	Aircraft
BETTII	81 / 81	2.2×10^{-16}	38 / 67	Balloon
SPIDER[a]	512 / 512 / 1 024 / 576	–	1 090 / 1 332 / 2 068 / 2 998	Balloon
EBEX	140 / 280 / 560	(62 / 88 / 160) $\times 10^{-18}$	731 / 1 199 / 1 999	Balloon
SPICA-SAFARI [b]	3 721 / 1 156 / 324	2.0×10^{-19}	35–60 / 60–110 / 110–210	Space

[a] In cosmic microwave background experiments, it is common for the sensitivity of bolometers to be characterised with a noise equivalent temperature which makes use of an on-sky target as a calibration source. For more information, see Bender et al. (2018) [108], Crill et al. (2008) [109], and The EBEX Collaboration (2018) [110].
[b] Though SPICA–SAFARI was not selected for its proposed European Space Agency (ESA) mission, much of the detector development was successfully completed. For more information, see Mauskopf et al. (2010) [111], Ridder et al. (2016) [112], and Khosropanah et al. (2016) [113].

array.

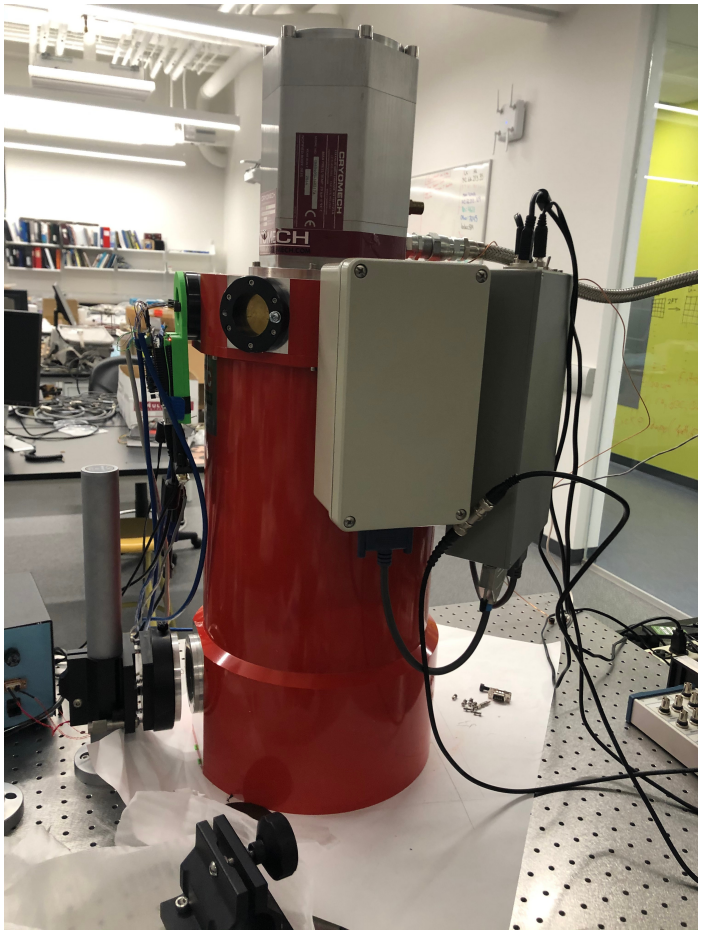


Figure 3.2: The cryostat that houses the detector array. Detector control electronics are housed in the room temperature electronics boxes external to the red cryostat vacuum can.

3.2.1 Operation

The TES detectors operate in an approximately constant-current biased state and make use of an actively controlled heating element and a Proportional-Integral-Derivative (PID) feedback loop to maintain the operating point of the detector [117]. Thermal and electrical model diagrams of a single detector in the array are shown in Figure 3.6. The detector maintains operation about a set temperature on the superconducting transition of the TES within a precisely timed multiplexing loop by balancing the thermal conduction to the surrounding environment of the cryostat, the optical loading on the detector, the Joule heating

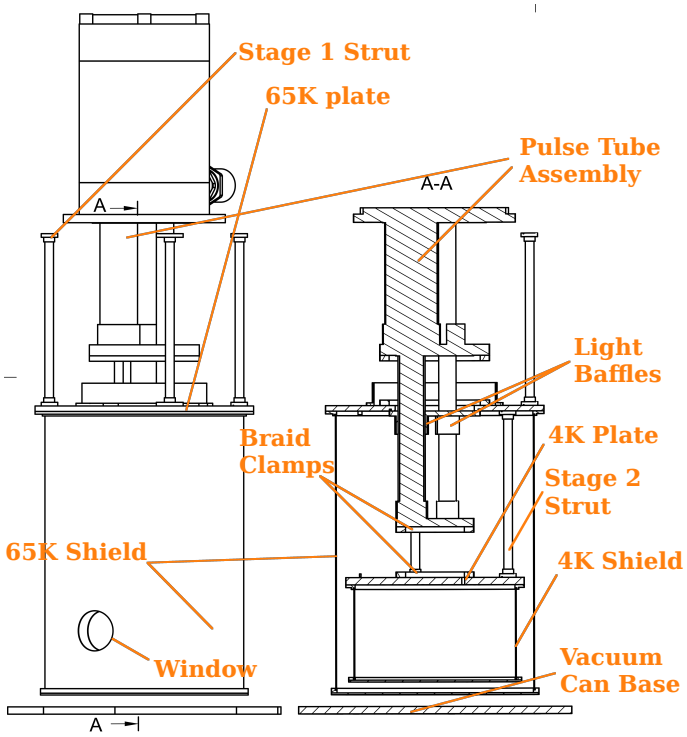


Figure 3.3: A schematic diagram of internal cryostat assembly (left) with a cross-sectional view (right).

from the bias circuitry of the TES, and the feedback-controlled heating element. Under an increase in incident optical power, there is a change in the TES temperature state that is measured by the voltage across the TES ($\mathbf{V_{TES}}$) under an approximately constant-current bias. In response, the PID feedback loop calculates the necessary reduction in heater power to maintain the setpoint on the superconducting transition (within the multiplexing loop). In this way, the heater power provides a measure reciprocal to the optical loading on the TES detector. The power balance of a detector follows that of Equation 3.1 with the addition of the heater power,

$$C_a \frac{dT}{dt} = P_{\text{elec}} + P_{\text{opt}} + P_{\text{heat}} - P_{\text{bath}} \quad [\text{W}]. \tag{3.18}$$

Through the large suite of parameters associated with the PID feedback control, the TES array provides a versatile detector system that can be used with a variety of room temperature FIR optical systems [118]. Though this thesis focuses on the optimisation of the detector array for use in a DFI testbed, this general versatility should be noted. Additionally,

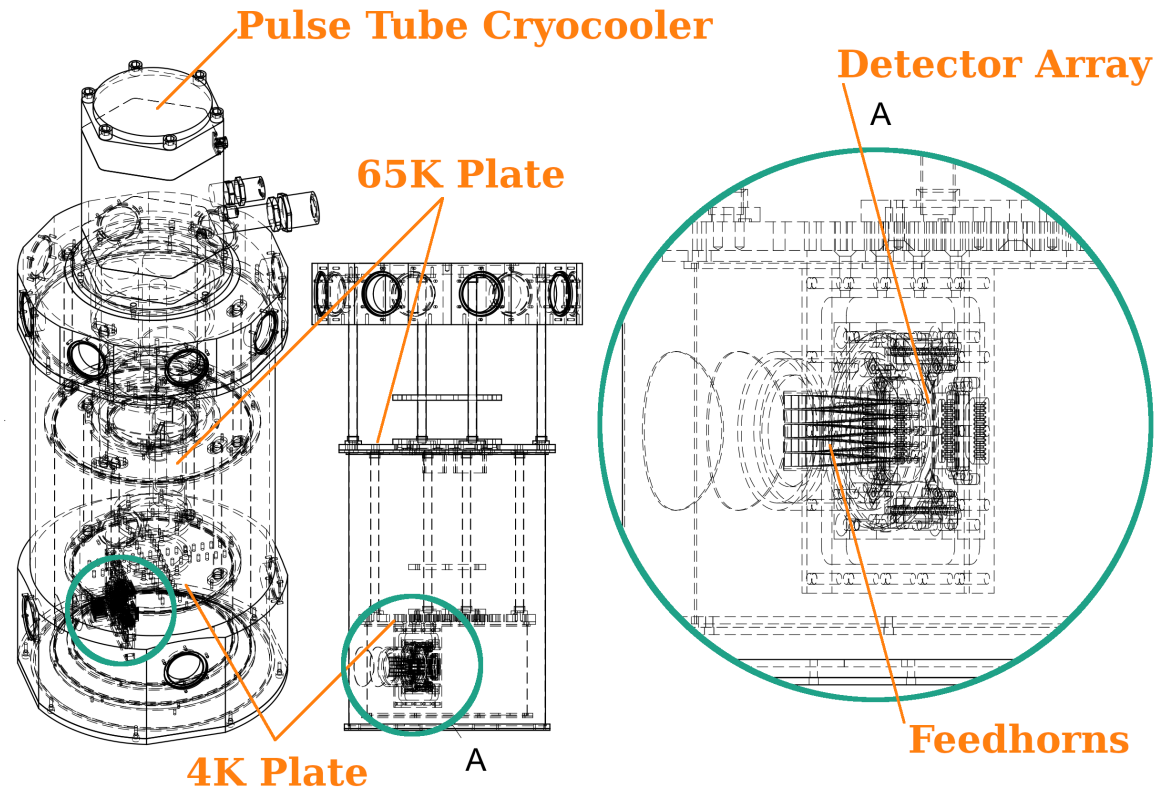


Figure 3.4: A detailed schematic diagram showing the location of the detector array within the cryostat assembly. The left image shows the entire assembly while the central image shows the detector block and internal cryostat stages with the shielding removed. The image on the right shows the detector, feedhorn, and filter assembly. In each case, the detector block is marked by the teal circle.

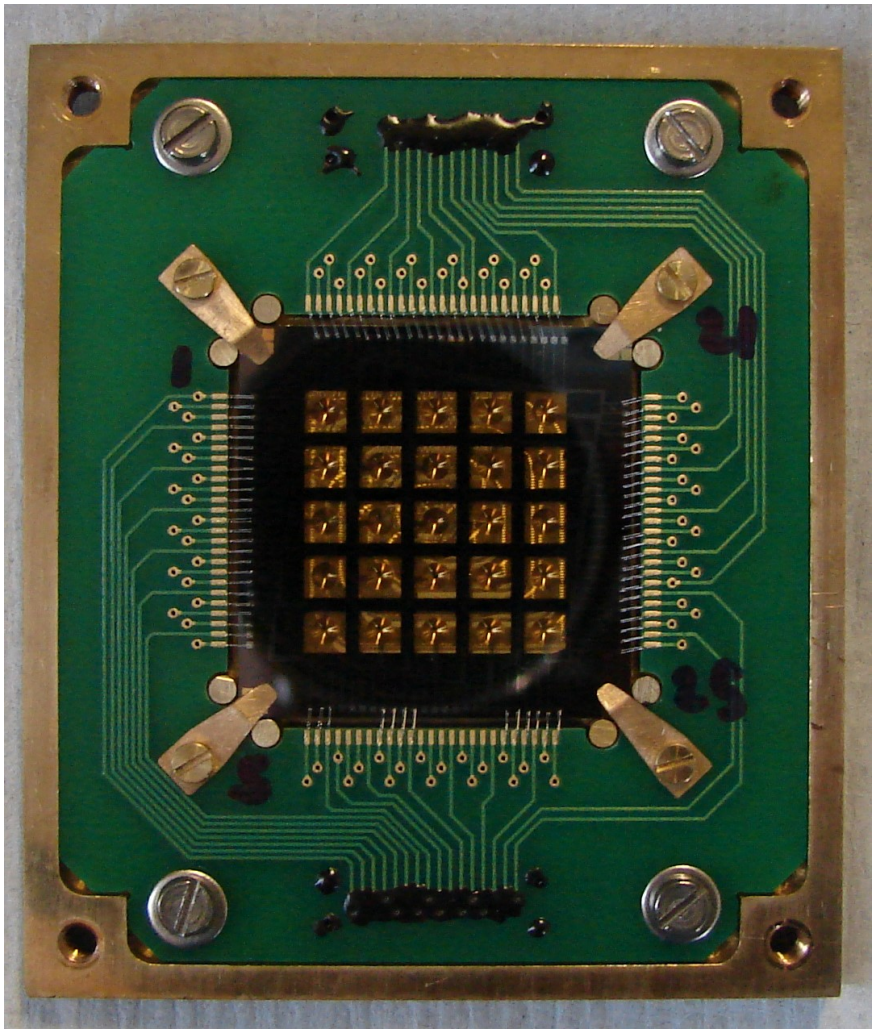


Figure 3.5: A photograph of the niobium TES detector array and readout wiring board which has been mounted inside the cryostat behind the feedhorn assembly (see Figure 3.4).

operating the detectors in this way allows for the use of TES thermometers with sufficient impedance to facilitate direct voltage measurements with traditional amplifiers. Typically, SQUID amplifiers are used to probe changing current across the TES. This simplification at the electronics level also significantly reduces the cost of the detector system and allows effective operation within a 4 K environment without the need for a lower temperature ^{3}He/^{4}He dilution refrigerator. In contrast to the benefits of relatively simple electronics and versatile detector tuning, characterising the performance of such a detector system and optimising the extensive parameter space for a specific use case is no small task.

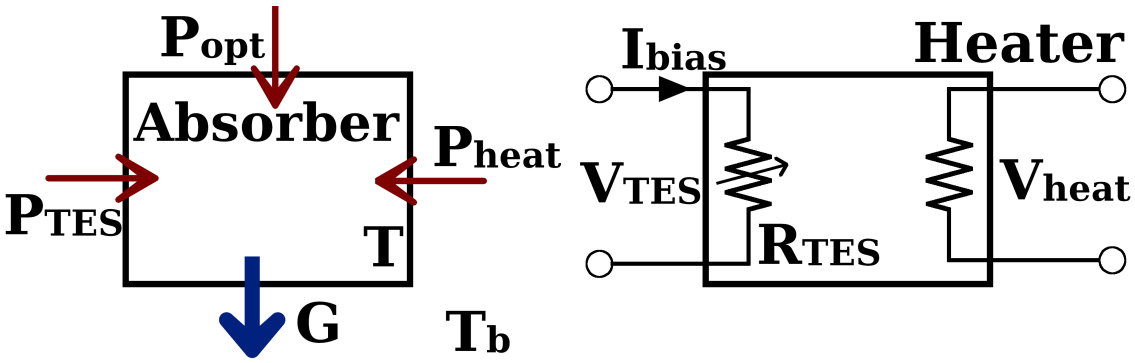


Figure 3.6: A thermal diagram (left) and electric diagram (right) of a single TES detector in the QMC feedback-controlled TES array. The absorber receives heat from the bias circuitry of the TES thermometer ($\mathbf{P_{TES}}$), optical loading ($\mathbf{P_{opt}}$), and a heating element ($\mathbf{P_{heat}}$) while conducting heat to the surrounding thermal bath via a thermal link (**G**).

3.2.2 Cryostat performance

The cryostat that houses the detectors is shown in Figure 3.3. The detector array (not shown) is housed beneath the cold plate in a 2 500 cm^3 enclosure at $\sim$4K. The internal temperatures of the cryostat are monitored by 3 diodes, one located on the $\sim$65 K first stage shielding, one on the $\sim$4 K cold plate, and one on the detector block. The cryostat environment is maintained and cooled by a PT405 cryocooler and a Cryomech CP2800 helium compressor.

Figure 3.7 shows a full cycle of the cryostat environment measured by all 3 internal diodes. It takes $\sim$7 hours for the cryostat to fully cool to operating temperature and $\sim$45 hours to warm to room temperature. The temperature calibration of the internal cryostat thermometers is further discussed in §4.1.1.

3.2.3 Control electronics

The PID control loop for each detector is managed, measured, and maintained by a National Instruments Field-Programmable Gate Array (FPGA) (NI USB-7856R OEM) operating with an 80 MHz system clock. This operation is time-domain multiplexed as four detector channels are maintained at their desired temperature bias and read out simultaneously (labelled A–D) and switched through seven rows in time (0–6). This 4×7 multiplex-

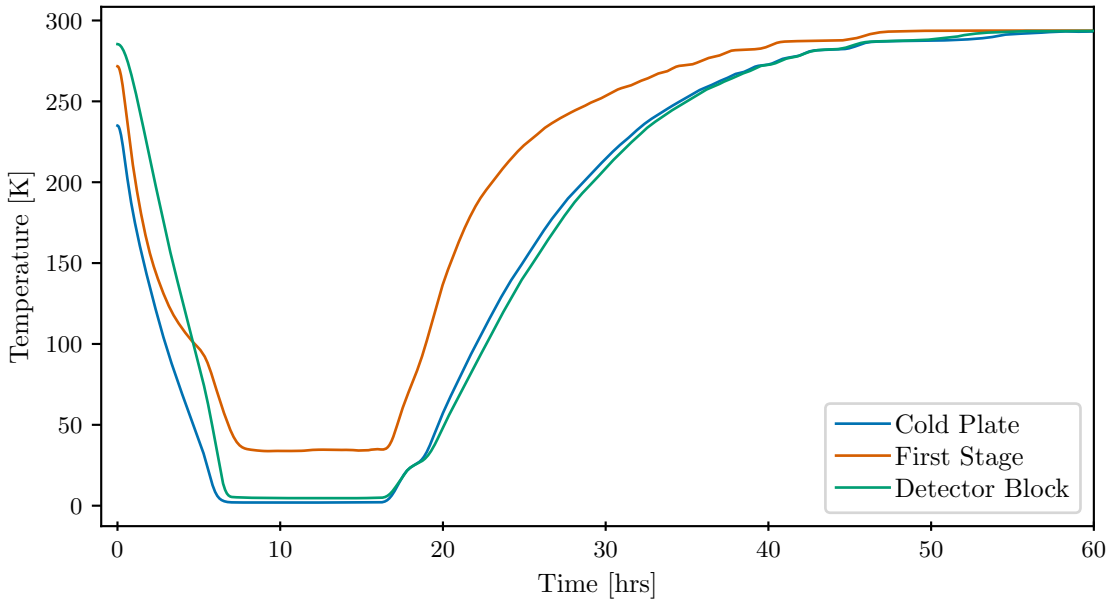


Figure 3.7: A full cycle of the detector cryostat measured by its three internal thermometers.

ing scheme results in 28 detector sites, with 3 remaining empty as they do not physically correspond to detectors on the array. The relation between the multiplexing scheme and the physical layout of the detector array is shown in Figure 3.8 which also introduces the colour and marker convention for the detector array that will be employed in this thesis unless otherwise specified.

A PID control loop is comprised of a proportional term (P), an integral term (I), and a derivative term (D) which can be written for a given point in time, t, as,

$$u(t) = K_P e(t) + K_I \int_0^t e(t')dt' + K_D \frac{d}{dt} e(t) \quad \text{[a.d.u]}, \tag{3.19}$$

where $u(t)$ is the output signal from the PID loop calculation and $e(t)$ represents an error signal from the desired state or setpoint. In Equation 3.19 the proportional, integral, and derivative terms (sometimes called "actions") of the equation have an associated gain factor (K_P, K_I, and K_D, respectively) that determines the weight that the term has in the calculation. Additionally, Equation 3.19 has been expressed in arbitrary data units (a.d.u) as PID

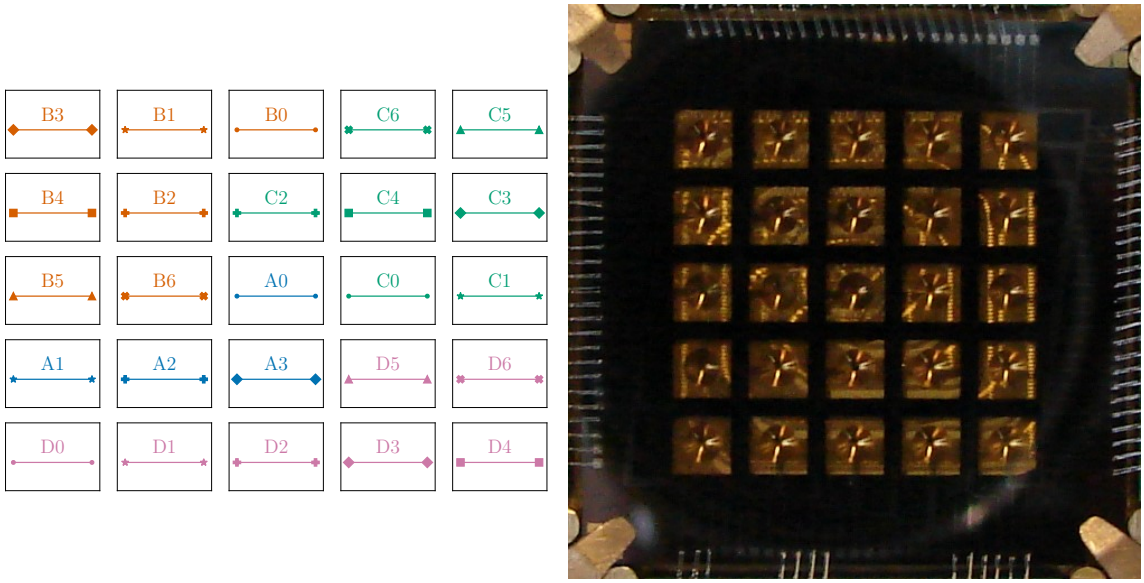


Figure 3.8: The order in which detectors are multiplexed by the FPGA readout system is shown in the left panel. The colour convention for each detector is also shown. The right panel shows a zoomed-in view of the detector array for reference.

calculations are often performed internal to the control electronics and physical quantities are represented by values read from an Analogue-to-Digital Converter (ADC). In the PID loop for a single detector, the voltage that represents the temperature state of the TES is measured by a 16-bit ADC. This 16-bit number is used as a state/process variable within the loop making the error signal $e(t) = V_{\text{setpoint}} - V_{\text{TES}}(t)$, where the desired TES position on its superconducting transition has been represented by the setpoint value, V_{setpoint}. In the detector measurement loop, the 32-bit value calculated by Equation 3.19 is sent to a Digital-to-Analogue Converter (DAC) that controls the heating element. In this thesis, detector signal will often be represented in units of squared volts as the heating element provides Joule heating to the detector that is proportional to the square of the voltage across the heating element. In this arrangement, when a detector is under an increased optical load, less heater power is required to minimise the error signal of the PID loop. In summary, the internal state variable of the PID feedback is the 16-bit ADC reading representative of the TES voltage and the detector signal is the output from the PID feedback loop that is sent as a 32-bit value to the DAC that controls the voltage of the heating element. It is then the

square of the 32-bit DAC signal that is linearly related to the optical power incident on the detector (see Equation 3.18).

Detector signal measurements and housekeeping metadata concerning detector operation are represented by a series of 32-bit integers which are kept on a First In, First Out (FIFO) buffer that interfaces with a Direct Memory Access (DMA) space on a local personal computer through a Universal Serial Bus (USB) connection. The data from the DMA space can be saved locally to the computer disk as binary files, or data packets, containing a chosen number of frames of detector measurements (nominally 15 000).

The circuitry that maintains the bias of the TES detectors and heating elements of the detector array occurs on two room-temperature electronic boards that also contain the multiplexing circuitry (channels A/B on one board, C/D on the other). The measured voltage from each TES is augmented by a low noise ($\sim$1 nV/$\sqrt{\text{Hz}}$ at 1 kHz) amplifier on each board.

3.3 QMC detector operation

The operation of normal TES detectors employs intrinsic electrothermal feedback to maintain constant operation within the transition region of the superconducting detector element. *The TES system under study does not operate in this manner*. Owing to the timing of the multiplexing and feedback processes involved in a detector measurement, the detectors under study do not maintain constant operation on their superconducting transition. Instead, a detector's thermal state switches between superconducting and normal conducting states throughout a single measurement and remains within its superconducting state while other detectors in the array are measured. The unique feedback control of the TES under study results in a wide variety of user-adjustable parameters to change the responsiveness of the feedback loop, the speed of detector measurements, and the noise performance of the system. In this section, I will present and discuss the nominal control and readout processes of the detector system.

Figure 3.9 provides an example of the processes involved in a single detector measure-

ment pulse. A detector measurement starts with the TES in its superconducting state (at which point its voltage is measured as $\sim$9 900 data units due to the impedance from leads to the thermometer). The heater is turned on at the start of the pulse and is switched off after the specified duty cycle. There is a delay in the TES response as it must be heated from its equilibrium state with the thermal bath in which it behaves as a superconductor before reaching its transition. Measurement(s) of the TES state to be used in the PID loop are made after a chosen delay. At the last loop count in the measurement pulse, the heater value required to maintain the setpoint (at the chosen delay) is calculated by the PID controller. After a detector measurement pulse is completed, the detector remains inactive as the FPGA switches through the other rows. In the example shown in Figure 3.9, an average of three TES state measurements is used in the PID calculation.

As a result of manufacturing defects, detectors B2 and B3 are unable to be stabilised by the PID feedback and do not provide useful observational data in their current state. Throughout this thesis, these detectors are treated as dead pixels with the heater switched off unless otherwise specified.

3.3.1 Detector measurements and adjustable parameter summary

The timing of the feedback loop involved in each detector measurement is controlled by a set of adjustable parameters that are ubiquitous across each detector in the array. These parameters are used to define the following: (1) the length of a measurement pulse, (2) the heater duty cycle within a measurement pulse, (3) when within a measurement pulse the TES state is measured for use in the PID feedback, and (4) how many TES state measurements internal to a measurement pulse are used in a detector measurement.

Pulse Width: The pulse width parameter defines the total time that is taken by the feedback loop in a single detector measurement. This number is given as the number of loop counts in a detector measurement *pulse*, which are referenced by a loop counter. At each loop count, the TES state can be measured and/or the heater can be switched off. The

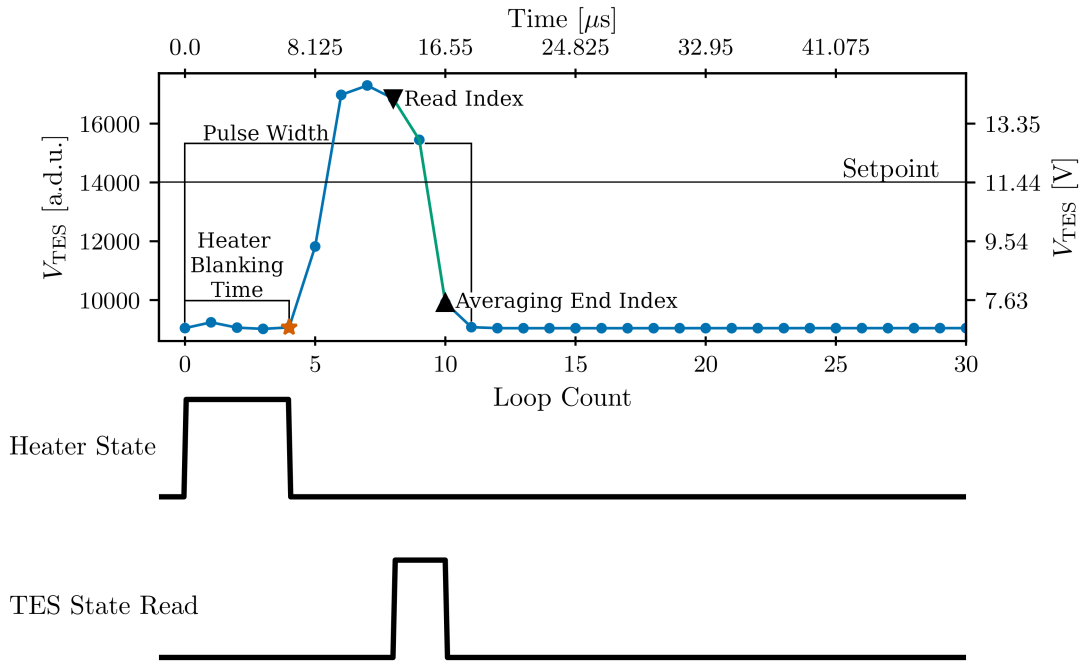


Figure 3.9: An example of a single detector measurement pulse when operating as an optical detector. The TES heater is active for the first 5 loop counts of the measurement pulse, the TES state is measured for use in the PID from loop counts 8–10 (inclusive), and the detector is inactive and no longer biased after loop count 11 having completed a full detector measurement pulse. The PID setpoint is marked by the horizontal line. The heater switch-off point is marked by a star while the start and end of TES state measurements for PID calculations are marked by triangles. The arbitrary data units representing TES voltage are the internal 16-bit representations measured by the ADC. A subset of the parameters outlined in §3.3.1 that affect detector measurement timing are also marked.

heater is switched on at the start of the detector measurement pulse (loop count 0) and the PID calculation occurs at the end (the last loop count in the pulse).

Heater Blanking Time: The blanking time parameter selects the time that the heater remains active within a detector measurement. The heater is switched on at the start of a detector measurement pulse and switched off at the loop count equal to the blanking time.

Read Index: Though the measurements of the TES can be made at every loop count within a detector measurement pulse (as in Figure 3.9), a single measurement of the TES state is nominally used in the PID calculation to determine the heater output of the detector. The defined read index is the loop count on which the TES state is read from the ADC for use in the PID calculation (or the loop count on which measurements of the TES state

start being read when multiple measurements are used). Nominally, this read index is used to introduce a delay between when the heater is switched off and when the TES state is measured for the PID calculation (i.e., the read index is set to be larger than the blanking time). Even though the read index dictates which TES state measurements within the pulse are input to the PID calculation, the FPGA performs the PID output calculation on the final loop count of the pulse.

In-pulse Averaging: The average of multiple TES state measurements within a detector measurement pulse can be used for the PID output state calculation. If this in-pulse averaging is used, an ending index needs to be specified such that TES measurements ranging from the read index to the end index, inclusively, are used in the average. E.g., during an observation using a pulse width of 14 loop counts, a blanking time of 4 loop counts, a read index of 9, with in-pulse averaging enabled and an end index of 11, the heater will turn off on a loop count of 4 (counting from loop count 0) and measurements from loop counts 9–11 will be averaged and used in the PID calculation.

Time Penalty/ADC delay: The time required for the FPGA to measure the TES state measurements can be probed through the use of the timing penalty parameter which has a Boolean value. When the time penalty is active, the TES state is measured from the ADC at each loop count though only the measurement at the chosen read index(ices) is(are) used in PID calculation. When the time penalty is inactive, the TES state is only measured on the specified read index(ices) and is otherwise assigned a value of zero. To provide greater clarity when referencing the time penalty, I have referred to this as the ADC delay throughout this work.

Multiplexing: The multiplexing of the detector array controlled by the FPGA can be limited to a single row (thus avoiding any time domain multiplexing). The unmultiplexed row can be selected by the user and all other rows of detectors remain inactive.

The default timing operation of the detector array, as designed by QMC Instruments, is to operate in multiplexed mode, with a pulse width of 10, a blanking time of 4, and a read

index of 9 (in-pulse averaging, $n = 1$). The detector array does not nominally employ the TES measurement ADC delay (time penalty).

In addition to the parameters that modify the timing of the detector measurement process, the PID calculation can be modified on a per-detector basis. Though the TES state is read by the ADC as a 16-bit integer and the heater power is represented by a 32-bit value sent to the DAC, the PID calculation implemented in LabVIEW operates with single precision floating point numbers (see Appendix D). As such, all selected PID parameters are of this data type.

PID gains (See Equation 3.19): The gains (weights) associated with the three terms of the PID loop can be adjusted for each detector in the TES detector array.

Setpoint: The setpoint that the PID feedback loop tries to maintain is an adjustable parameter for each detector. The setpoint is represented by a 32-bit floating point number in the same arbitrary data units employed by the 16-bit ADC representation of the TES voltage.

Output range: The allowable output range from the PID calculation is explicitly controlled to be within a minimum value and a maximum value both given as 32-bit floating point numbers. Nominally, these limits are not used.

Manual Detector Control: The heater power calculated by the PID feedback can be replaced with a static value set manually by the user. Manual control mode can be toggled on or off.

The default PID parameters of the detector array, as set by QMC Instruments, are outlined in Table 3.2. Section 4.1.1 demonstrates that there are variations in the shape of the superconducting transition of the TES from detector to detector as a consequence of fabrication tolerance. As a consequence, the PID parameters of the detector array should be chosen on a per-detector basis as reflected in the default parameters set by QMC Instruments. This is further discussed in §6.2.1.

Table 3.2: The default PID parameters of the detector array set by QMC Instruments. For all detectors, the derivative term is not used and has a gain value of 0.

	A	B	C	D
0	$P = 1\,000$, $I = 200$ Setpoint: 10 000	$P = 1\,000$, $I = 150$ Setpoint: 10 000	$P = 1\,000$, $I = 120$ Setpoint: 10 000	$P = 1\,000$, $I = 120$ Setpoint: 10 000
1	$P = 1\,000$, I=200 Setpoint: 10 000	$P = 1\,000$, $I = 100$ Setpoint: 10 000	$P = 1\,000$, $I = 150$ Setpoint: 10 000	$P = 1\,000$, $I = 300$ Setpoint: 10 000
2	$P = 1\,000$, $I = 200$ Setpoint: 10 000	Unstable	$P = 1\,000$, $I = 100$ Setpoint: 10 000	$P = 1\,000$, $I = 100$ Setpoint: 10 000
3	$P = 1\,000$, $I = 110$ Setpoint: 10 000	Unstable	$P = 1\,000$, $I = 550$ Setpoint: 12 000	$P = 1\,000$, $I = 150$ Setpoint: 10 000
4	Empty Channel	$P = 1\,000$, $I = 700$ Setpoint: 10 000	$P = 1000$, $I = 100$ Setpoint: 10 000	$P = 1\,000$, $I = 200$ Setpoint: 12 000
5	Empty Channel	$P = 1\,000$, $I = 100$ Setpoint: 10 000	$P = 1\,000$, $I = 100$ Setpoint: 10 000	$P = 1\,000$, $I = 80$ Setpoint: 10 000
6	Empty Channel	$P = 1\,000$, $I = 300$ Setpoint: 10 000	$P = 1\,000$, $I = 150$ Setpoint: 10 000	$P = 1\,000$, $I = 150$ Setpoint: 10 000

3.3.2 Detector output data structure and control software

Data from the detector array are output to the DMA space on the local computer as a series of 32-bit integers, which can be saved to the computer's hard drive. These data includes a 32-bit frame counter which increments once a full frame (all 7 rows of 4 channels) has been read out and a 32-bit metadata integer which includes the state of the FPGA's triggering pin, measurement timing (counted as ticks of the 80 MHz clock), and an error flag.

The control software, adjustable parameters, and data readout of the detector array were developed through collaboration with, and under the supervision of, the manufacturer, QMC Instruments. Two additional custom readout modes were developed without direct oversight from QMC Instruments. The first of these operating modes was designed to profile the TES behaviour throughout a measurement pulse. When operating in this mode, the TES voltage is measured and reported at each loop count of a detector measurement pulse. The TES measurements are sent to the DMA FIFO at each loop count as two 32-bit integers with the 32-bit metadata integer increasing the data rate by 3 times the loop count.

Additionally, the ADC delay must be enabled in this mode for the TES to be measured on each loop count.

The second custom readout mode provides the measured TES voltage at the read index used in PID calculation in addition to the standard output from the detector array (or the average of TES voltage measurements when in-pulse averaging is turned on). Operating in this mode allows the TES state to be monitored without the significant increase in the data rate to the DMA FIFO when operating in TES profiling mode. However, it should be noted that only a single TES value is reported for each detector measurement when operating in this additional output mode. A full overview of the reported data structure in each operating mode, the bit structure of the metadata bit, and LabVIEW implementation of PID control is given in Appendix D.

3.3.3 Detector units

Throughout this thesis, measurements of a TES voltage (the process variable of the PID loop) and measurements of a heater power (the output variable of the PID loop) are presented in different forms which often can be seen by the use of different units. Here I wish to disambiguate these numerical representations.

The output variable is calculated by the PID loop and sent across a resistor network (which includes the impedance of the leads) which sets the bias of the actual heating element on a detector. When represented in data units, the output variable is the 32-bit integer sent to the DAC which controls heater power. The heater power/detector signal is presented in squared volts which relates to DAC values as,

$$P_{\text{detector}} = \left((v_{\text{heat}}\,[\text{a.d.u.}])\,\frac{10}{2^{32}-1} \right)^2 \quad [\text{V}^2]. \tag{3.20}$$

Note that the DAC has a 10-volt reference. Though this is the value reported by the detector system, the actual power across the heating element has been attenuated by the resistor

network. This is then given by

$$P_{\text{heat}} = \left((v_{\text{heat}}\,[\text{a.d.u.}])\,\frac{10}{2^{32}-1}\left(\frac{30.8}{3\,630.79}\right)\left(\frac{6.5}{44.5}\right)\right)^2 /6.5$$
$$\approx \left(0.001239\,(v_{\text{heat}}\,[\text{a.d.u.}])\,\frac{10}{2^{32}-1}\right)^2 /6.5 \quad [\text{W}]. \tag{3.21}$$

The process variable (or V_{TES}) is measured after being amplified and passed through a resistor network that includes the impedance of the leads to the TES. When represented in data units, the TES voltage corresponds to the 16-bit measurement from the ADC,

$$V_{\text{TES}} = \left((v_{\text{TES}}\,[\text{a.d.u.}])\,\frac{5}{2^{16}-1}\right)^2 \quad [\text{V}]. \tag{3.22}$$

Note that the 16-bit ADC has a 5-volt reference.

3.3.4 Initialisation decay

When detector array operation is initialised, the detectors are below their operating temperature of $\sim$8.3 K and the TES thermometers are in a superconducting state (see §4.1.1). The PID process variable value does not change while a detector TES state is below its superconducting transition despite the increasing heater value. The accumulation of the integral weighting of the error signal causes the PID loop calculation to overshoot the setpoint requiring a significant time period for the detector to decay to the desired thermal state. Figure 3.10 shows this initialisation effect while operating in multiplexed TES profiling mode and with a mirror placed at the cryostat input to provide a minimal static optical load. For the first 10 detector samples, the TES is in its superconducting state and the heater ramps up and begins to slow just before the setpoint is reached.

Figure 3.11 shows an example of the initialisation decay in the detector signal for the first row of detectors. Using a Levenberg–Marquardt least squares fitting algorithm [119], a decay model has been fit to the data. A better fit to the data was obtained using the sum of a high-amplitude decay curve with a fast time constant and a low-amplitude decay curve

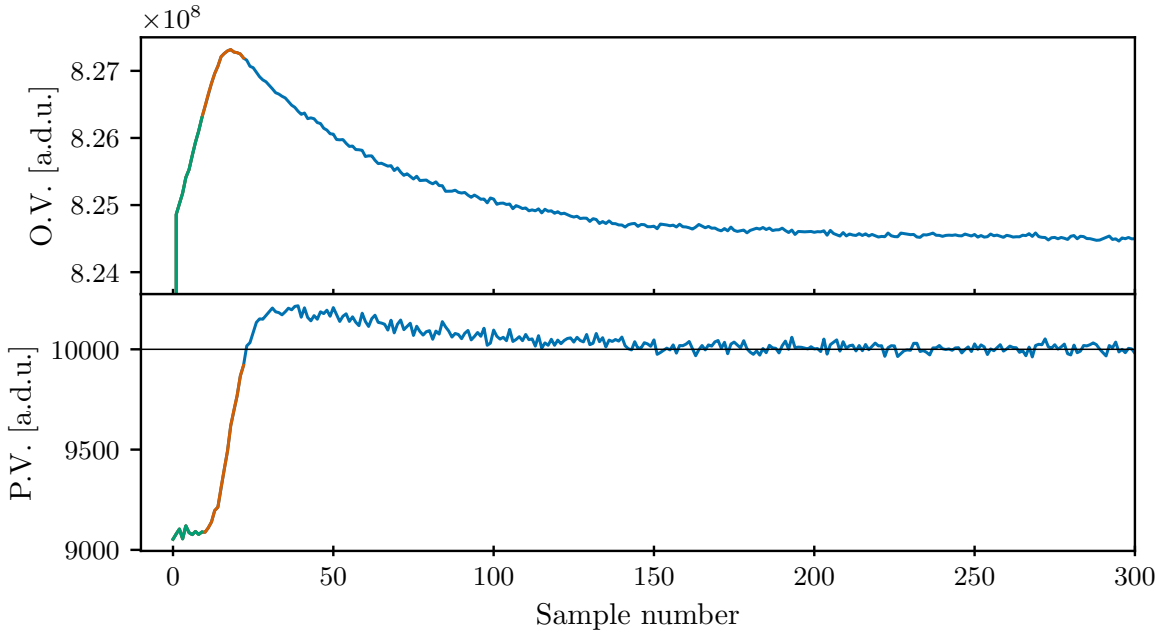


Figure 3.10: The decaying detector signal that results from uncontrolled detector initialisation for the central detector. The output variable (O.V.) is shown in the top panel and the process variable (P.V.) at the chosen read index is shown in the bottom panel. The sample points in which the detector TES is in its superconducting state are marked in green while samples that are below the chosen setpoint are marked in orange.

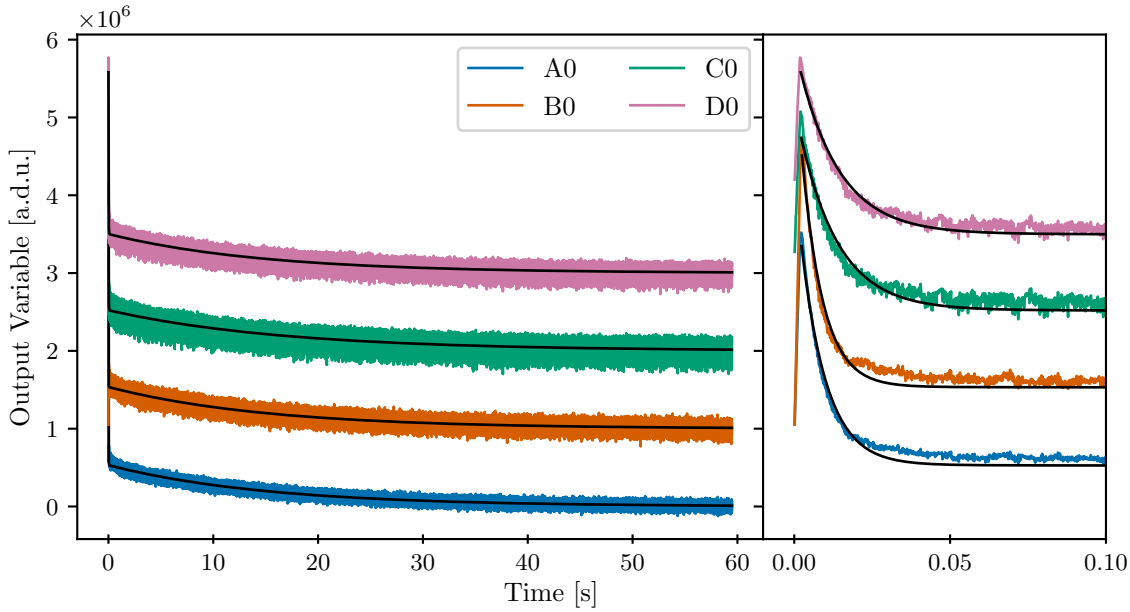


Figure 3.11: The initialisation decay in the detector signal of the first row of detectors. Decay models have been fit to each curve (shown in black) following the point at which the heater value begins to decrease to determine time constants for the relaxation from overshooting the setpoint. A zoom-in on the initial overshoot is shown in the right panel. An artificial offset has been applied to each curve to improve readability. Fitted time constants are reported in Table 3.3.

with a slower time constant rather than a single decay function (see Figure 4.3). This model is given as,

$$D(t) = A_s e^{-\frac{t}{\tau_s}} + A_l e^{-\frac{t}{\tau_l}} + D_{\text{steady}} \quad [\text{data units}], \tag{3.23}$$

where $\tau_s < \tau_l$ are the two decay time constants, $A_s > A_l$ are the respective amplitudes, and D_{steady} is the steady state of the signal. Though these fits to the data are poor over small time scales (resulting in values of $\chi^2_{\text{red}} > 30$), they do provide useful estimates as to the duration of the initialisation decay. The values of the longer of the two time constants for the four curves are found to range from 8.50 to 17.04 seconds (corresponding to ∼200 000 detector samples; see Table 3.3). After turning on the system, ∼1 minute (i.e., 4 time constants) should be waited to ensure that the detectors have settled prior to any science measurements.

In an effort to reduce the effects of this initialisation overshoot, I attempted to develop

Table 3.3: The fitted time constants from the initialization decays shown in Figure 3.11.

Detector	τ_l [s]	τ_s [s]
A0	15.20 ± 0.01	$0.008\,10 \pm 0.000\,03$
B0	15.89 ± 0.02	$0.006\,75 \pm 0.000\,04$
C0	17.04 ± 0.04	$0.012\,3 \pm 0.000\,1$
D0	8.50 ± 0.02	$0.008\,50 \pm 0.000\,08$

a custom set of "startup" PID gains in which the weight of the integral term is reduced. I found that an increased weighting of the proportional term is required for the detector to rise into its superconducting transition upon initialisation due to the reduction in the integral term. Unfortunately, the substantial increase in proportional gain is such that the thermal runaway of the TES cannot be controlled in a stable fashion. Instead, this causes the TES to rapidly jump between normal conducting and superconducting states.

3.3.5 DMA communication errors

While the FPGA FIFO is monitored by the local computer, we have found that communication errors intermittently occur. In data processing and control software, we refer to these as DMA errors. If the FPGA encounters a DMA error in passing data to the host computer's DMA FIFO, an Interrupt Request (IRQ) is thrown and the FPGA hangs until the IRQ is acknowledged. When this occurs, the host program checks the FIFO size and determines that the FIFO is not growing. The current FIFO contents are then saved to a packet on the local computer, the IRQ is acknowledged, and normal operation resumes. Due to the halt in the FPGA control of the detectors, the heater is inactive and the temperature of the detectors cools below the nominal operating temperature deeper into the superconducting state. As a result, a large spike in the calculated heater value occurs immediately following a DMA error. This behaviour is similar to when the detectors are initialised often affecting the next several detector measurements. I developed a custom operation mode designed to limit the effects of DMA errors on detector behaviour. This was not used in the analysis discussed in this thesis and is discussed in Appendix D.5.

The frequency of DMA errors has a dependency on the resource usage of the host computer. Figure 3.12 shows the distribution of the time between DMA errors with the detectors operating in their default mode while hosted by a local computer with an Intel Core i5-2500 Central Processing Unit (CPU) operating at 3.30 GHz with 24 GB of Random Access Memory (RAM) with Windows 10 as an operating system (left panel). Results are shown in which running processes on the local computer have been minimised and when the computer is under a heavy resource load. To occupy local computer resources, the host program monitoring the detectors was executed while (1) a virus scan and defragmentation program was used to increase communication with the local storage media, (2) multiple web browsers were active and a large number of files were transferred across the network to increase network communication, (3) several programs which have significant CPU usage were active, (4) a large array of random numbers was being created and deleted in a loop through a Python script to occupy communication with RAM and occupy a significant portion of the memory, and (5) the Windows operating system was commanded to look for and download updates to increase the number of processes specific to the operating system. When operating with light computer resource usage, 38 DMA errors were encountered while the detectors operated for $\sim$5.5 hours and 536 errors were encountered in the same duration while the detectors operated with heavy resource usage on the local computer. When operating with minimal resources, DMA errors occur over a wide range of time scales from less than 2.5 minutes to 36 minutes with the majority occurring on time scales of less than 6 minutes. All DMA errors occurred within 6 minutes of each other with heavy computer resource usage.

The time between DMA errors, while the detectors are hosted by a computer with better specifications, is shown in the right panel of Figure 3.12. This computer makes use of an Intel Xeon E5-2620 CPU at 2.40 GHz with 32.0 GB of RAM and Windows 10 as an operating system. While operating the computer with low-resource usage, only a single DMA error occurred in 18.6 hours of detector observation and 6 DMA errors occurred

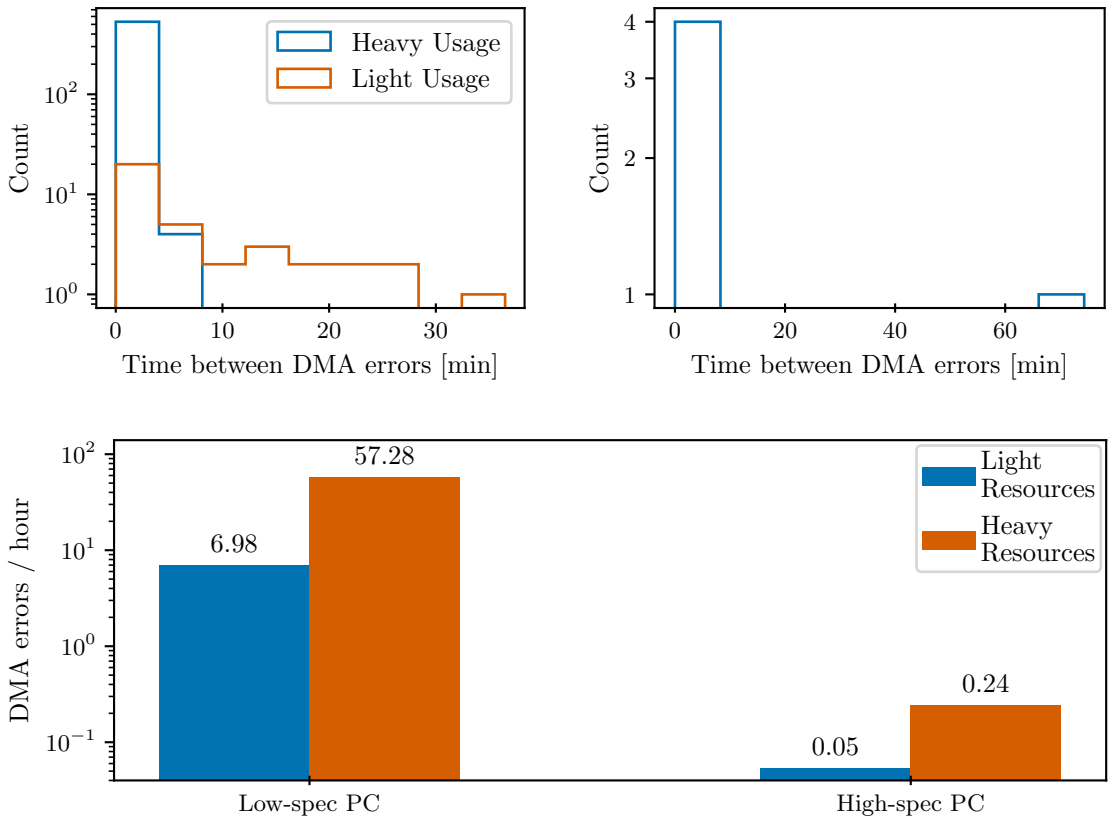


Figure 3.12: The frequency of DMA errors while operating the detector array with a lower specifications computer (left) and a higher specifications computer (right) is shown in the top panel. Results are shown for the lower specifications computer operating the detectors while under low and high resource usage. Only a single DMA error occurred in measurements made with the higher specifications computer while operating under low resource usage. The lower panel shows the rate at which DMA errors occur in each case.

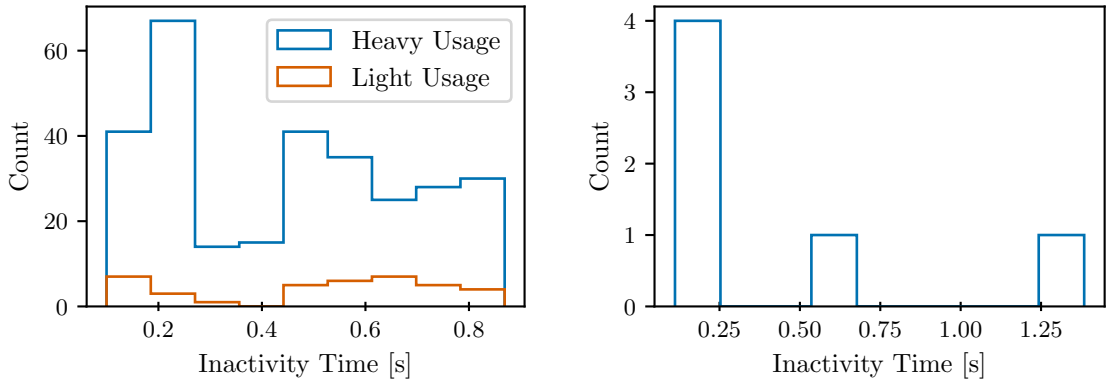


Figure 3.13: The time the FPGA remains inactive while detectors are operated by a lower specifications local computer (left) and a higher specifications computer (right). As in Figure 3.12 these distributions are shown while the lower specifications computer operates under high and low resource usage. Since the higher specifications computer experienced a single DMA error during which the FPGA was inactive for 8.26 seconds, it is not shown with the other distributions.

while operating under heavy resource usage in the same time span. With the exception of the final DMA error, all DMA errors that occurred while operating this computer under a heavy resource load occurred within 10 minutes of each other.

The time the FPGA remains inactive after a DMA error is shown for the same cases presented in Figure 3.12 is shown in Figure 3.13. The resource load of the local computer does not have an appreciable effect on how long the FPGA remains inactive following a DMA error. With the higher-specification computer, the FPGA was only ever inactive for less than 0.25 seconds with the exception of the final 2 DMA errors encountered in the observation under a heavy resource load.

Operating the detectors with a computer that has more RAM resources and a non-consumer grade processor dramatically reduces the frequency of DMA communication errors during detector operation. Additionally, reducing the resource load of the computer operating the detectors has been shown to reduce DMA errors by as much as 96%.

3.4 Conclusions

Throughout the chapter, I have provided a brief introduction to the history, theory, and sources of noise in TES bolometers to provide context for the bespoke feedback-controlled TES bolometer system that we have employed with the DFI testbed introduced in Chapters 1 and 2. I have also detailed the operation of this unique detector system and its accompanying array of adjustable parameters. In addition, I have summarised the control software that accompanies the detector system and discussed the deleterious effects of communication errors on the operation of the detector array. I have found that using a computer with sufficiently high specifications and minimal resource loading can reduce communication errors by as much as 96%.

Chapter 4

The Characterisation of a Feedback-Controlled Array of Far-IR TES Bolometers

> Outside our consciousness there lies the cold and alien world of actual things. Between the two stretches the narrow borderland of the senses. No communication between the two worlds is possible excepting across the narrow strip. For a proper understanding of ourselves and of the world, it is of the highest importance that this borderland should be thoroughly explored.
>
> –Heinrich Hertz (1857–1894) [120]

The multiplexed feedback-controlled Transition Edge Sensor (TES) system is a bespoke detector array with an extensive parameter space and both its optimisation and its characterisation is a substantial challenge. This task, which serves as the primary focus for my work, is not only necessary for a full understanding of the measurements made with the Double Fourier Interferometery (DFI), but is also something that has been bestowed upon us by the manufacturer, QMC Instruments, who have a particular interest in this endeavour and continue to collaborate with me in it. This has led to a unique situation in which I, as an end-user, have conducted various *in situ* characterisation experiments in an attempt to have a more complete technical understanding of the system without full access to its isolated components or the intellectual property that has led to its development.

I have conducted substantial experimental investigations into the detector system's thermal, electrical, and optical behaviour. Since all of these behaviours are coupled, it is difficult to chart a direct course through my characterisation of the system. In this chapter, I aim

to address three main aspects of the detector system: sensitivity, noise performance, and response speed. I discuss the general performance of the detector array largely independent of consideration as an integrated part of the DFI assembly at the start of the chapter (investigating thermal behaviour and broadband noise performance). I then move to topics and experiments that address the ability of the detectors to measure optical modulation in the latter portion of the chapter (excess low-frequency noise and detector time constants). The performance of the detector array at different frequencies of optical modulation is of particular importance for its integration in the DFI testbed as the detectors must be well-equipped to measure the modulated output from the interferometer.

Much of my investigation in this and the subsequent chapter focuses on a thorough characterisation and performance optimisation of the central detector. While my efforts and methodology can be applied to all working detectors in the array, the time required is considerable as a full characterization of any additional single detector may require repeated experiments with a variety of test equipment. Additionally, differences in the fundamental behaviour of each detector (see §4.1.1) suggest that the values of specific detector parameters should be determined on a per-detector basis. In the effort of extending this investigation to the entire array of detectors, much of the preliminary data necessary is in-hand. The extension of the measurements presented in this work to optimize the remaining detectors in the array is more fully discussed in §6.2.1.

Through my efforts characterising the central detector, I show that the performance of the detector can be improved over default parameters by a factor of $\sim$3. However, these must be balanced with a cost to the speed of the detector.

4.1 General detector performance

Much of the general performance of the detector array can be characterised with metrology internal to the detector system itself and relatively simple test equipment. This section details and builds on my specific contributions to the work presented in Spencer et

al. (2022) [121] in which we have presented early efforts to characterise the detector system.

4.1.1 Superconducting transition measurements

I have made measurements of the superconducting transition of the TES detectors by monitoring the TES state, as mentioned in §3.3.2. To obtain these measurements, the TES state was monitored through the Proportional-Integral-Derivative (PID) process variable with the PID feedback control turned off while the environment of the cryostat was partially cycled thermally. Through these partial cycles, the TESs are heated from their operating temperature (with the cold plate at $\sim$4 K) to a temperature at which the detectors have fully passed through their superconducting transition (usually with the detector block at $\sim$10 K) through passive conduction to the environment with the cryocooler off. The cryocooler is then turned back on and the detectors cool back through their transition as the cryostat cools. To reduce optical loading on the TES, I placed a room temperature mirror at the window to the cryostat. These experiments were achieved with the detector array operating in TES profiling mode and the heating element on each detector manually set to 0 power. In this operation, the detector array effectively provides a measurement time stream of the TES state (i.e., temperature or voltage under a $\sim$constant-current bias) for each detector. The temperature of the detectors is taken to be the temperature of the cryostat monitoring diode on the detector block assuming good thermalisation between detectors in the array and the rest of the detector block.

To synchronise detector measurements and measurements of the internal cryostat diodes, an external triggering pulse was sent to both the detector Field-Programmable Gate Array (FPGA) and the microcontroller that reads the detector block's temperature sensor (i.e., the voltage of the diode with a 10 μA current bias). The temperature calibration for the diode voltage is sparsely sampled over the relatively small temperature gradient of the detector block during a partial cycle (see the left panel of Figure 4.1). To provide a suitable

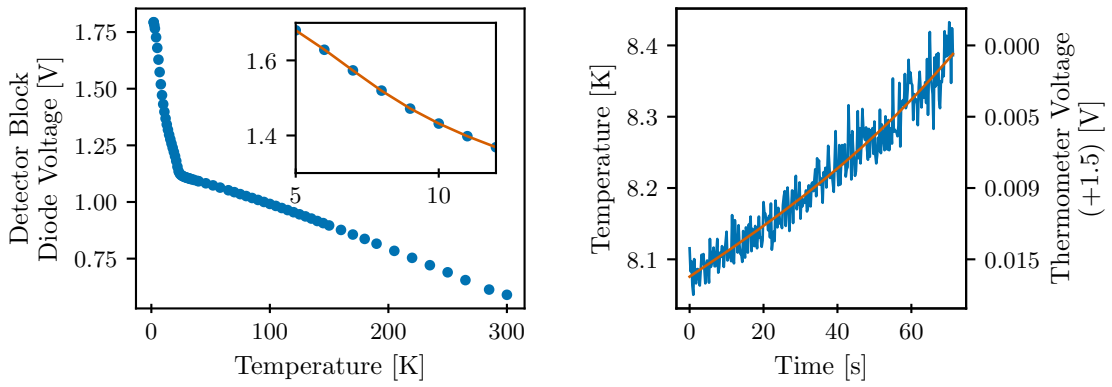


Figure 4.1: The detector block thermometer diode calibration profile for a 10 μA bias is shown in the left panel. A zoomed-in view of the region in which the TESs experience their superconducting transition is shown in the inset axis with a third-order polynomial fit to this region. The right panel shows an example temperature time stream measured by the microcontroller monitoring the detector block thermometer with a third-order polynomial fit. In both panels, the polynomial fit is shown by the orange line.

temperature axis for the microcontroller measurements, a third-order polynomial is fit to the calibration curve from 5 to 12 K and evaluated at the recorded voltage. Since the voltage measurements from the diode are subject to a substantial amount of noise (corresponding to $\sim$0.2 K) and temperature changes are expected to be smoothly varying over the timescales of a few minutes, another third-order polynomial is fit to the temperature time series (see the right panel of Figure 4.1). As a result of Direct Memory Access (DMA) errors, it is possible for data recorded from the detector to miss triggering pulses (see §3.3.5). To aid in synchronising the two timelines when trigger pulses are missed, time stamps are given by the microcontroller at each change in the trigger signal state. Once detector and diode temperature timelines are matched, a low-order polynomial is fit to the temperature data to remove noise from the temperature axis (see Figure 4.2).

Figure 4.2 demonstrates measurements of the superconducting transition taken with the detectors operating in both multiplexed and unmultiplexed modes (see §3.3.1). Each measurement timeline has been coaligned to the steepest point in the transition curve measured by the TES voltage. These measurements demonstrate that the self-heating of a detector from the TES bias circuitry plays an important role as it can cause poor thermalisation be-

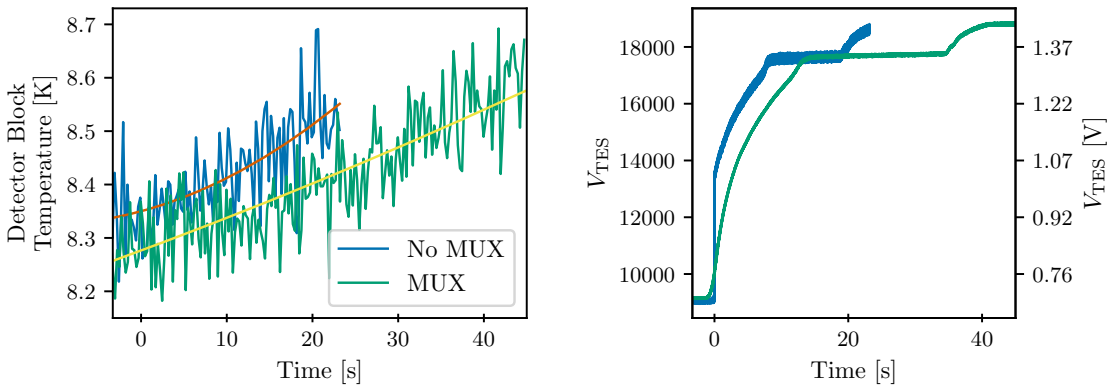


Figure 4.2: Detector block (left) and TES state (right) timelines of the central detector are shown while the cryostat was allowed to warm with detector heaters switched off. These timelines are shown for both Multiplex (MUX) and non-MUX measurement modes. Second-order polynomial fits of the temperature timelines read by the microcontroller are shown overplotted in a lighter colour for each. Timelines from each mode have been co-aligned at the steepest part of the TES transition.

tween an individual TES and the thermometer on the detector block. Though the detector block thermometer shows a similar temperature gradient during both multiplexed and unmultiplexed measurements of the TES, the TES state moves through its transition much quicker in unmultiplexed mode. When operating in multiplexed mode, the TES on a single detector is only biased when its respective row is read out in the multiplexing loop and self-heating from the TES bias circuitry is effectively reduced to a 1/7 duty cycle. This results in a better thermalisation between the TES and the detector block diode thermometer which in turn gives a more accurate measurement of the superconducting transition of a given TES. Due to the better thermalisation when operating with multiplexing, all measurements of the superconducting transition discussed here were made with multiplexing turned on unless otherwise noted.

Measurements of the superconducting transition show additional phase transitions in the upper region of the curve. These can be attributed to transitions from superconducting to normal resistances of connections and leads to the TES thermometer.

Though self-heating of the TES is reduced through multiplexing, multiplexed measurements of the TES suffer from electrical switching noise. Figure 4.3 demonstrates the effects

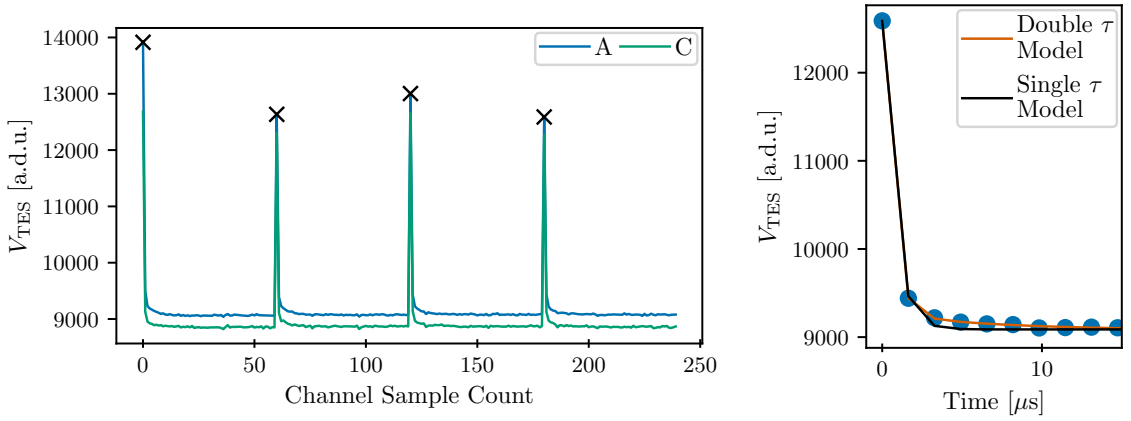


Figure 4.3: The switching noise in two channels of multiplexed measurements of the TES state with all detector heaters switched off (left). The start of each detector measurement pulse is marked by an "x". A dual decay curve model (see Equation 3.23) was fit to the switching noise profiles and compared to fits performed with a single-decay model (right). Being deemed superior, the dual decay model was fit to each instance of switching noise and the corresponding time constants are shown in Table 4.1.

of multiplexing switching noise on TES measurements. In these measurements, the detector array is operating in multiplexed mode with a pulse width of 60 loop counts (7 966 ticks, 99.58 μs) and all of the detector heaters switched off. Spikes in the detector signal can be seen at the start of each new detector measurement pulse. To determine the time constant of the signal decay from the switching noise at the start of a pulse, decay models were fit to the data. Similar to the decay model fits that are presented in §3.3.4, the sum of two decay functions (Equation 3.23) provides better fits to the decay from switching noise (as can be seen in Figure 4.3). The long time constants extracted from the switching noise decay range 6–9 μs (corresponding to $\sim$6–7 loop counts in multiplexing mode with the Analogue-to-Digital Converter (ADC) delay active, see Table 4.1). To effectively avoid switching noise in multiplexed measurements of the superconducting transition, the pulse width of detector measurements can be made large enough such that the first $\sim$10–15 loop counts ($\sim$22 μs) can be omitted. A full discussion of detector timing parameters is given in §4.1.4.

The temperature of the cryostat measured by the detector block diode during four partial warming cycles is shown in Figure 4.4. Over the temperature regime shown in each case,

Table 4.1: The short (τ_s) and long (τ_l) time constants extracted from a least-squares fit of a dual decay model (see Equation 3.23) to the switching noise in channels A and C shown in Figure 4.3.

Detector	τ_s [μs]	τ_l [μs]	Detector	τ_s [μs]	τ_l [μs]
A0	0.55 ± 0.01	6.5 ± 0.6	C0	0.54 ± 0.02	9 ± 2
A1	0.50 ± 0.02	6.6 ± 0.5	C1	0.47 ± 0.03	7 ± 1
A2	0.54 ± 0.02	6.4 ± 0.7	C2	0.53 ± 0.03	8 ± 1
A3	0.60 ± 0.02	7.0 ± 0.8	C3	0.51 ± 0.03	6 ± 1
			C4	0.53 ± 0.02	9 ± 1
			C5	0.51 ± 0.02	8 ± 1
			C6	0.53 ± 0.01	9 ± 1

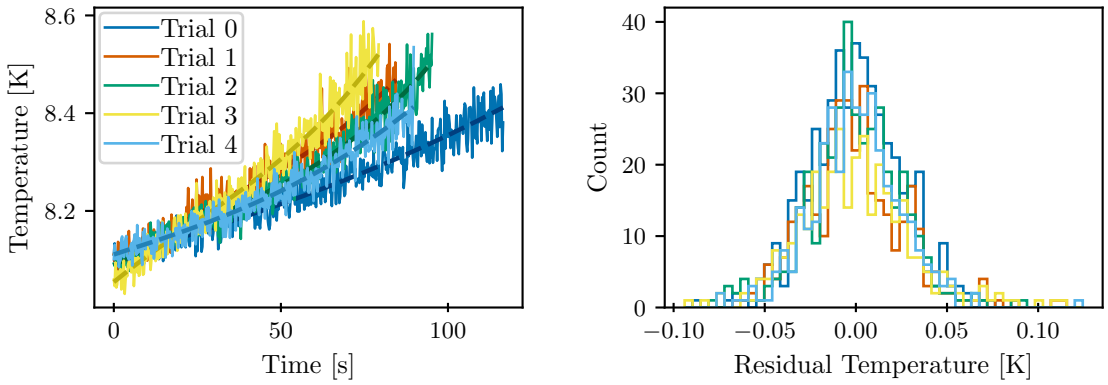


Figure 4.4: The increase in temperature during four partial warming cycles of the detector cryostat is shown in the left panel. Third-order polynomial least-squares fits to each temperature profile are shown by the dashed line in the darker colour over each. The right panel demonstrates the distribution of the residual from each fit.

the central detector has fully moved through its superconducting transition. The distribution of the residual to each polynomial fit of the temperature axis demonstrates the statistical uncertainty in temperature measurements made with the cryostat diode. The standard deviation of the residual distribution of all four trials is within 30 mK. Over the temperature range of transition measurements, the uncertainty in the absolute temperature calibration of the diode thermometer is ± 0.5 K [122].

Figure 4.5 shows multiple measurements of the superconducting transition for the TES on A0 while the detector environment has been warmed. For these measurements, a detector pulse width of 30 loop counts (4 036 ticks, 50.45 μs) was used and the TES value from

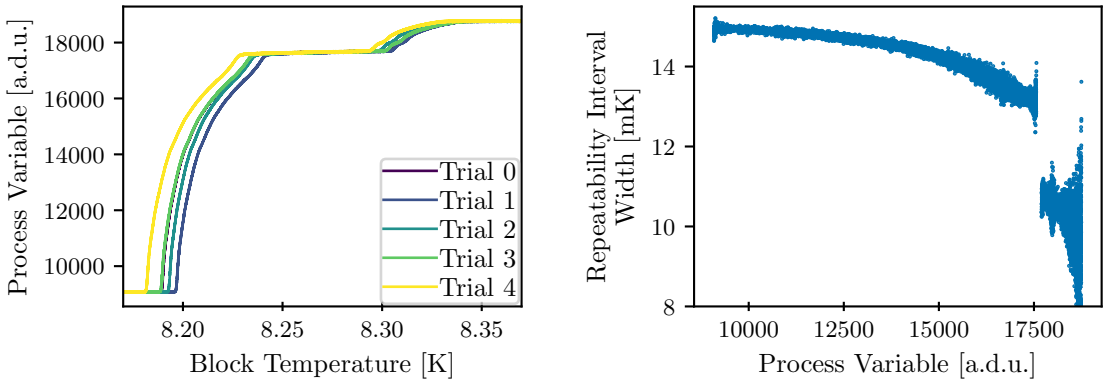


Figure 4.5: Multiple measurements of the superconducting transition of the central TES (A0) while operating in multiplexing mode are shown in the left panel while the detector environment is warmed. The repeatability interval (taken to be the difference between Trials 4 and 1) is shown in the right panel. At the start of the transition, its end, and at ∼17 500 data units, there is no temperature separation between the curves.

loop counts 15–19 (27.53–34.08 μs, inclusive) have been averaged together. These demonstrate the repeatability of measuring the superconducting transition in this fashion. While there is little discrepancy in the shape of each transition measurement (see Figure 4.7), there is a horizontal temperature offset of ∼10 mK between each measurement. I have estimated the repeatability in superconducting transition measurements to be the maximum separation in the measurements in Figure 4.5. This interval for the transition repeatability is less than half of the statistical temperature uncertainty in thermometer measurements shown in Figure 4.4. For these transition measurements, this is the difference between trials 1 and 4 which is shown in the right panel. These measurements show a critical temperature of 8.21 ± 0.02 K which agrees with values of evaporated niobium films from the literature [123, 124].

Similarly, I have the determined repeatability of transition measurements made while the cryostat environment has been cooled. These are shown in Figure 4.6. The cooling process of the cryostat is significantly faster than allowing it to warm through passive conduction to its surroundings. During the cooldown portion of a partial cryostat cycle, the TESs move through their transition ∼13 times faster than during the warming portion of

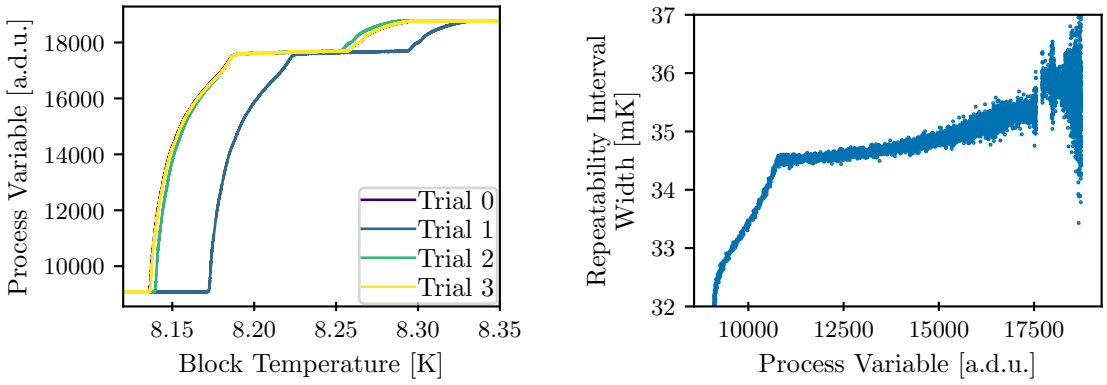


Figure 4.6: Multiple measurements of the superconducting transition of the central TES are shown in the left panel while the detector environment is allowed to cool. The width of the repeatability of the curve (taken to be the difference between Trials 0 and 1) is shown in the right panel. Note that at the start of the transition, its end and the discontinuity at ∼17 500 data units, there is no temperature separation between the curves (as in Figure 4.5).

the cycle. As a result, better thermalisation between TESs and the detector block is expected during warmup cycles. This may be evidenced by the 70 mK offset seen between transition measurements while warming up and cooling down. This offset suggests that the detector block is colder than the TES during a cooling cycle. It should be noted that this offset is only a factor of ∼2 greater than the relative uncertainty in measurements of the detector block thermometer. Additionally, there is a ∼34 mK offset between trial 1 and all other trials. This offset is substantially more than those seen during repeated measurements of the transition during a warming cycle (see Figure 4.5). The offset is comparable to the statistical uncertainty in temperature measurements made with the cryostat diode (see Figure 4.4).

As the offset between measurements of the central detector's superconducting transition are comparable to the relative uncertainty in temperature measurements made with the thermometer on the detector block, it is sensible to consider them once they have been co-aligned. Figure 4.7 shows the transition measurements from both the warming (left) and cooling (right) of the detector environment. These have been co-aligned at the start of the transition. Note that there is comparatively little deviation (to within 2 mK, see Figure 4.8)

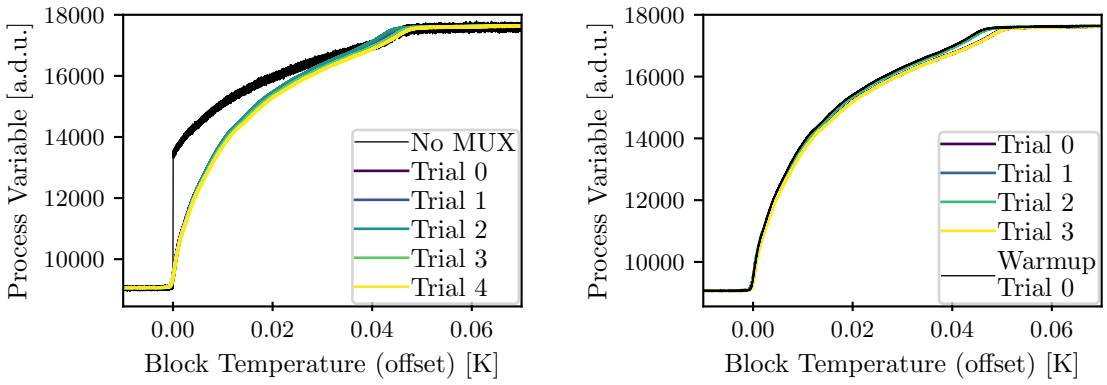


Figure 4.7: Transition measurements of the central detector while the cryostat environment was warmed (left) and cooled (right) from Figures 4.5 and 4.6 aligned to the start of their transition. An unmultiplexed measurement of the transition is shown by the narrow black curve on the left panel for comparison. Additionally, a transition measurement during a warming of the environment is shown as a narrow black curve on the right panel to improve the ease of comparison.

in the steepness and curvature of the transition across these measurements.

Measurements of the central detector's superconducting transition with different detector pulse widths while operating in multiplexed mode can be seen co-aligned in Figure 4.8. Though the detector duty cycle in each measurement remains 1/7, increasing the pulse width increases the duration of detector biasing (i.e., self-heating) and inactivity (i.e., cooling). As before, the TES measurements of loop counts 15–19 have been averaged together in each case. These variations in the absolute temperature at which the TES transitions are within the 15 mK uncertainty. Figure 4.8 shows that changing the pulse width of detector measurements does result in an increase in the steepness of the curve at longer pulse widths (suggesting greater self-heating). This results in a distribution of measurement curves that are as much as a factor of $\sim$2 larger than the nominal uncertainty in the distribution of co-aligned curves. It should be noted that this is still small compared to the uncertainty in the absolute temperature position of the superconducting curves and that the effect is substantially reduced lower on the superconducting transition. Selecting the appropriate pulse width values for measurements of a TES's superconducting transition must consider a balance between the increase in self-heating at larger pulse widths and the resultant reduction

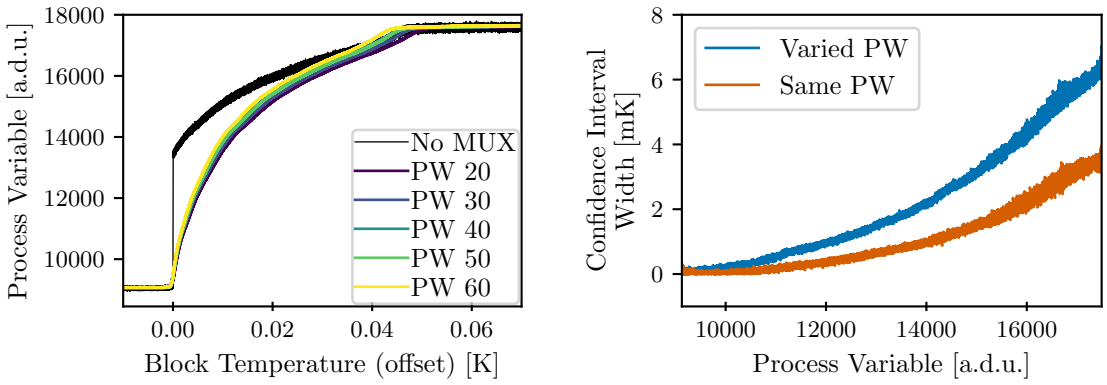


Figure 4.8: Multiplexed measurements of the central detector's superconducting transition for a variety of Pulse Widths (PWs) during a warming of the cryostat environment are shown in the left panel. These have been co-aligned to the start of their transition. As in Figure 4.7, the transition from an unmultiplexed measurement is also shown. The right panel compares the maximum width of the distribution of co-aligned curves when the pulse width is varied and when it is held constant (see the left panel of Figure 4.7).

in the frequency of switching noise.

The superconducting transitions for the entire detector array are shown in Figures 4.9 and 4.10. For these measurements, the detector array is operating in multiplexed mode with a pulse width of 40 and TES measurements from loop counts 15 to 39 have been averaged together to reduce noise. Notably, detectors B2 and B3 have significantly greater impedance throughout the temperature range shown and do not experience a transition from superconducting to normal impedance. TESs on channels C and D show much greater deviations over the transition temperatures than those on channels A and B. Additionally, the detectors on channel C show significant differences in their steepness in the upper regions of their transitions.

The sensitivity of a detector is dictated in part by the steepness of its superconducting transition (see Section 3.1). As such, detector sensitivity can be improved by selecting PID setpoints to coincide with the most sensitive region of the transition. Measurements of the TES state made by the detector system occur rapidly ($\sim$ 13 kHz sampling) and are subject to noise on the order of $\sim$25 data units in the steady state (see §4.1.4). As a consequence, determining the derivative of transition measurements which occur over $\sim$1 minute requires

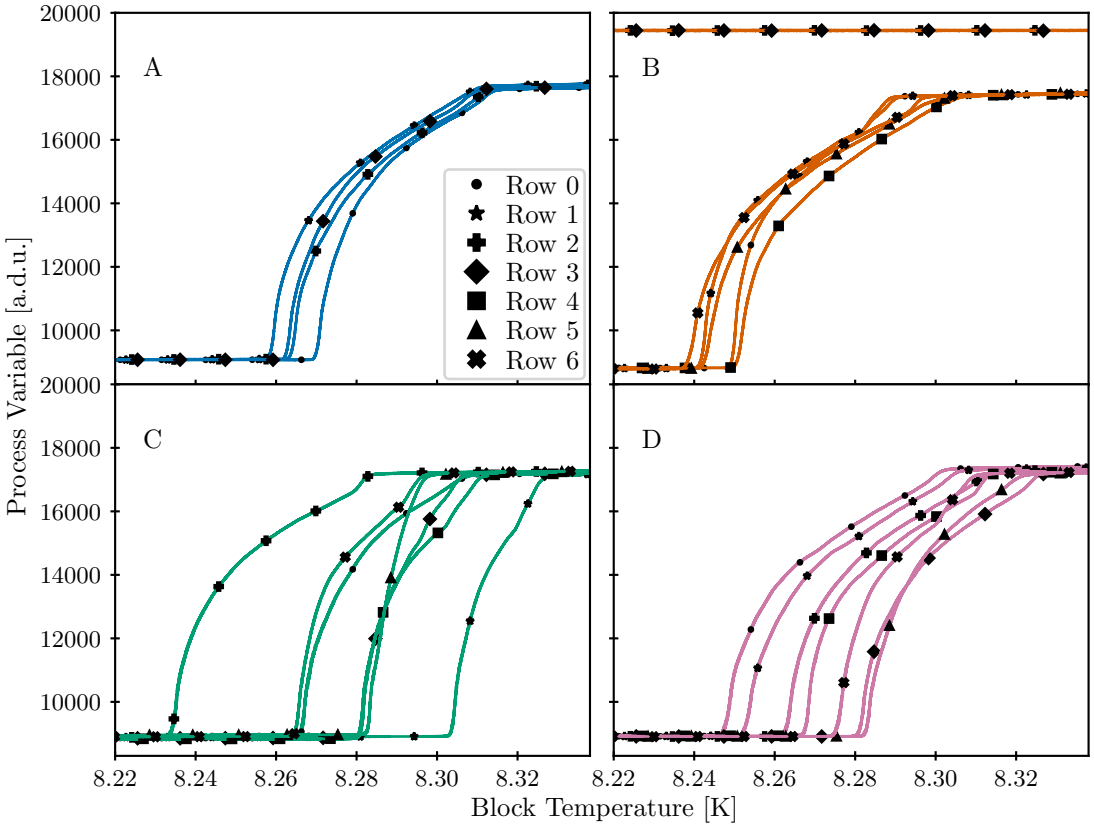


Figure 4.9: The superconducting transition for each detector in the array. Each panel represents a channel of the detector array. Detectors are marked and coloured following the convention introduced in Figure 3.8.

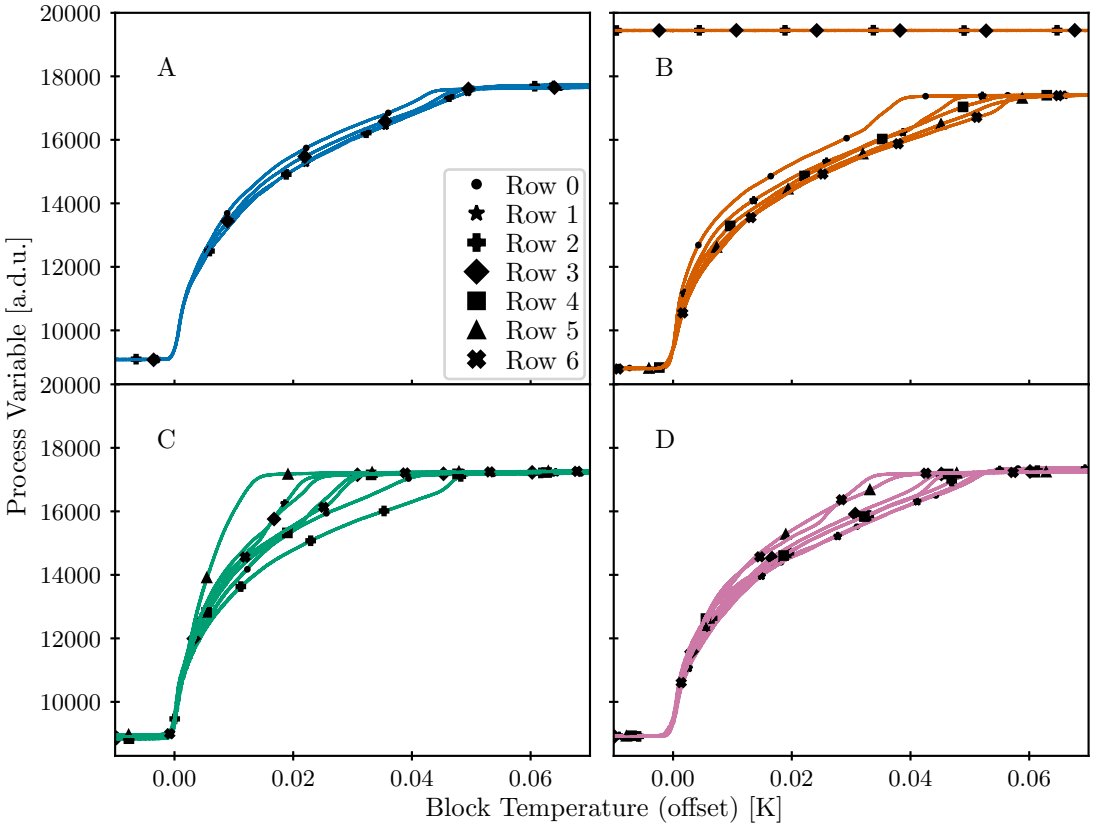


Figure 4.10: The superconducting transition for each detector in the array as in Figure 4.9 aligned at the point on the transition where the process variable is 9 415 data units. Again, the convention introduced in Figure 3.8 is employed.

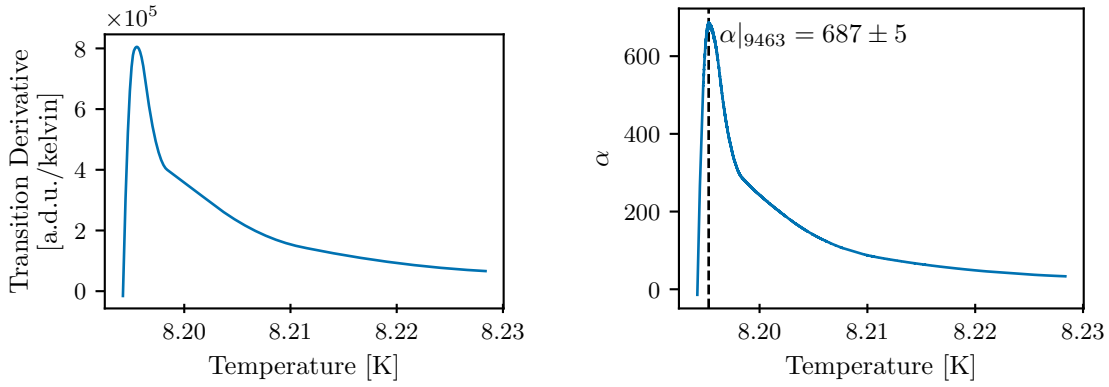


Figure 4.11: The steepness of the superconducting transition of the central detector measured in multiplexing mode. Loop counts 15–19 in the measurement pulse have been averaged together. The left panel shows the derivative of the transition determined from a smoothed cubic spline fit. The right panel shows the corresponding unitless steepness parameter, α (see Equation 3.9).

significant smoothing. Figure 4.11 shows the steepness of the central detector's transition measured with the detector operating in multiplexed mode with a pulse width of 20 loop counts (2 726 ticks, 34.08 μs). TES measurements from loop counts 15 to 19 have been averaged together. The slope has been determined by cubic spline fits to the data [125, 126]. The steepness parameter, α (see Equation 3.9), has also been evaluated at each sample giving the steepest and most sensitive region of the transition (805 ± 3 data units per milli-Kelvin) to occur at a TES voltage of 9 463 data units for the central detector.

To estimate different regions of sensitivity on the transition measurement corresponding to the steepness measurements shown in Figure 4.11, I determined breakpoints in the transition curve using a Python implementation of a segmentation algorithm developed by Muggeo (2003) [127, 128]. Using the smoothed second derivative of the transition, I determined there to be 6 dominant points of segmentation on the transition. I implemented the algorithm to find the unbiased location of 10 breakpoints on the transition. The converged breakpoints are shown by the vertical green bars with a confidence of 0.3 mK. The most sensitive region of the TES occurs between 9 175 and 10 291 data units where the sensitivity is 883 ± 3 data units per milli-Kelvin. This corresponds to a transition steepness of

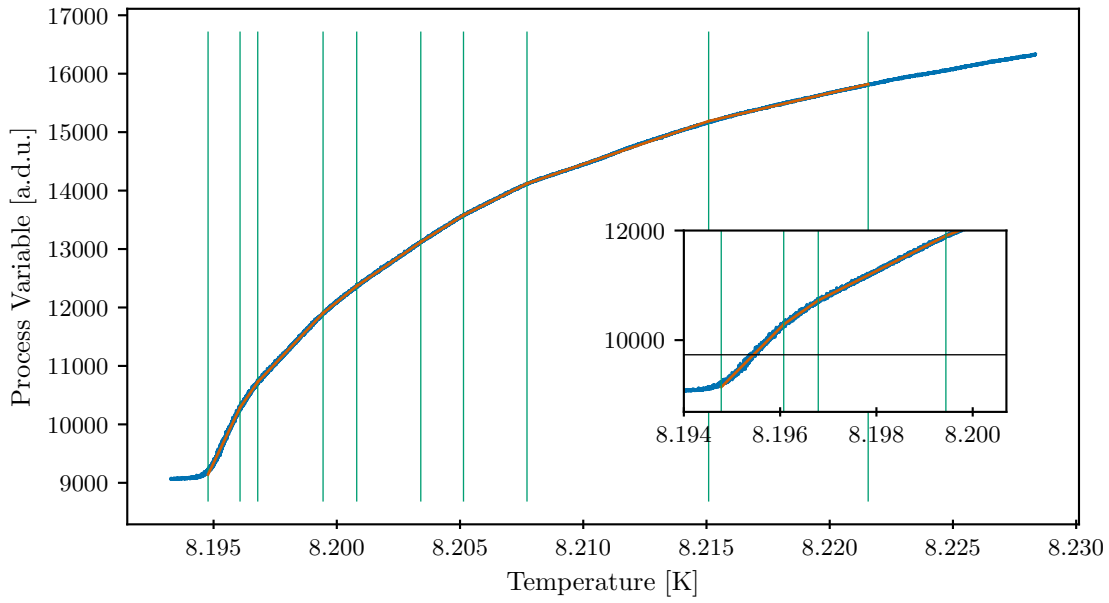


Figure 4.12: Breakpoint analysis of the superconducting transition of the central detector. Breakpoints are marked by the horizontal green lines and linear fits to each region are shown by the orange lines. The inset axes show a zoomed-in view of the most sensitive region of the transition in which the horizontal black line marks the ideal setpoint.

$\alpha = 723 \pm 2$. Through the segmentation algorithm, I have obtained similar results to the steepness of the curve determined from the cubic spline fit in Figure 4.11.

Values of α determined by the segmentation algorithm are shown in Table 4.2 to range $\sim$50–750 throughout the superconducting transition of the TES on the central detector while typical values for TES thermometers are 10–50 [102]. It should be noted, however, that the detectors under study would certainly not be considered typical TES bolometers. The TESs employed by the detectors are pure niobium with a critical temperature of $\sim$8.2 K while most TES materials are chosen such that their critical temperatures occur at a few hundred millikelvin [98, 101]. It is still possible that despite the reduction in self-heating through multiplexing, self-heating from TES bias circuitry still has a significant effect on the measurements I have made (thus causing the transitions to be measured as steeper than they actually are). The measurements I have presented and discussed could be further confirmed through measurements in which self-heating has been reduced by min-

Table 4.2: The steepness of the superconducting region of the TES on the central detector for each segment in Figure 4.12.

Segment (+8.1 K) [mK]	Segment [a.d.u]	Slope [a.d.u./mK]	α
[94.8, 96.1]	[9 175, 10 275]	882 ±3	743 ±2
[96.1, 96.8]	[10 275, 10 712]	609 ±4	475.0 ±3
[96.8, 99.4]	[10 712, 11 903]	444.9 ±0.5	322.3 ±0.3
[99.4, 100.8]	[11 903, 12 362]	339 ±1	229.2 ±0.7
[100.8, 103.4]	[12 362, 13 117]	290.0 ±0.3	186.7 ±0.2
[103.4, 105.1]	[13 117, 13 589]	265.8 ±0.5	163.3 ±0.3
[105.1, 107.7]	[13 589, 14 108]	209.7 ±0.2	124.3 ±0.1
[107.7, 115.1]	[14 108, 15 170]	144.94 ±0.06	81.32 ±0.03
[115.1, 121.6]	[15 170, 16 333]	97.68 ±0.06	51.83 ±0.03

imising the bias current to the TES through the use of a tunable potentiometer on the warm electronics board. Additionally, these measurements could be improved through the use of a better calibrated thermometer on the detector block and using a reflective plate internal to the cryostat to block the window. While the current extent of my investigation of the detector system has been to charactarise its performance without opening the cryostat or physically modifying the system, these warrant consideration for future improvements to detector calibration and performance.

4.1.2 Thermal behaviour

To determine the response of the TES itself to changing optical loads, I made use of an optically modulated coherent terahertz source. The Toptica TERASCAN 1550 continuous wave photomixer is a commercially available source that can provide coherent radiation from ∼50 to 3 300 GHz that can be intensity modulated through the bias current applied to the antenna [129, 130, 131, 132, 133]. The photomixer was positioned in front of the detectors to maximise the throughput to the central detector, A0. Multiplexing was turned off and the detector's heater bias was set to a constant value such that the TES was heated to pass through its transition slowly. This effectively allows for a slow increase in the bias temperature of the TES on its transition over time. With a quasi square-wave optical

signal modulated at 20 Hz from the photomixer, a qualitative measurement of the response of the TES thermometer to changes in optical load at different bias temperatures on the superconducting transition can be made.

The results of this experiment are shown in Figure 4.13. These demonstrate a clear separation in the response of the TES in the lower more sensitive region of its superconducting transition (i.e., with a TES voltage below 10 000 data units which is marked in orange in Figure 4.13) and the response that can be obtained operating in the upper region of its superconducting transition (i.e., with a TES voltage above 11 500 data units which is marked in green in Figure 4.13). A time constant corresponding to the TES response was extracted from a decay model that was fit to each region and is shown in the lower panel of Figure 4.13. These measurements suggest that operating with the TES setpoint in the lower region of the TES transition has the potential to improve upon detector speed by a factor of $\sim$100 depending on the chosen detector timing parameters and PID tuning (§4.3).

The dynamic thermal conductance of a TES, $G = dP/dT$, is commonly measured by measuring the power needed to bias the TES at various bath temperatures [102, 134]. This could also be achieved in practice through the use of a heating element on the absorber of each TES to obtain different static temperature conditions as in Karwan et al. [135]. Due to the biasing arrangement of the TES thermometers in our system, the bias circuity to the TES is a significant source of self-heating and they require PID control to prevent thermal runaway. This makes measurements after this fashion impractical. Instead, I have employed a technique similar to the second method performed by Karwan et al. [135] in which a small change in heater power and the corresponding change in TES temperature is monitored. In this way, G is measured directly as $G = \Delta P_{\text{heat}}/\Delta T$. The change in detector temperature is controlled by changing the setpoint of the PID and as in normal operation, the heater power required to maintain the setpoint is monitored.

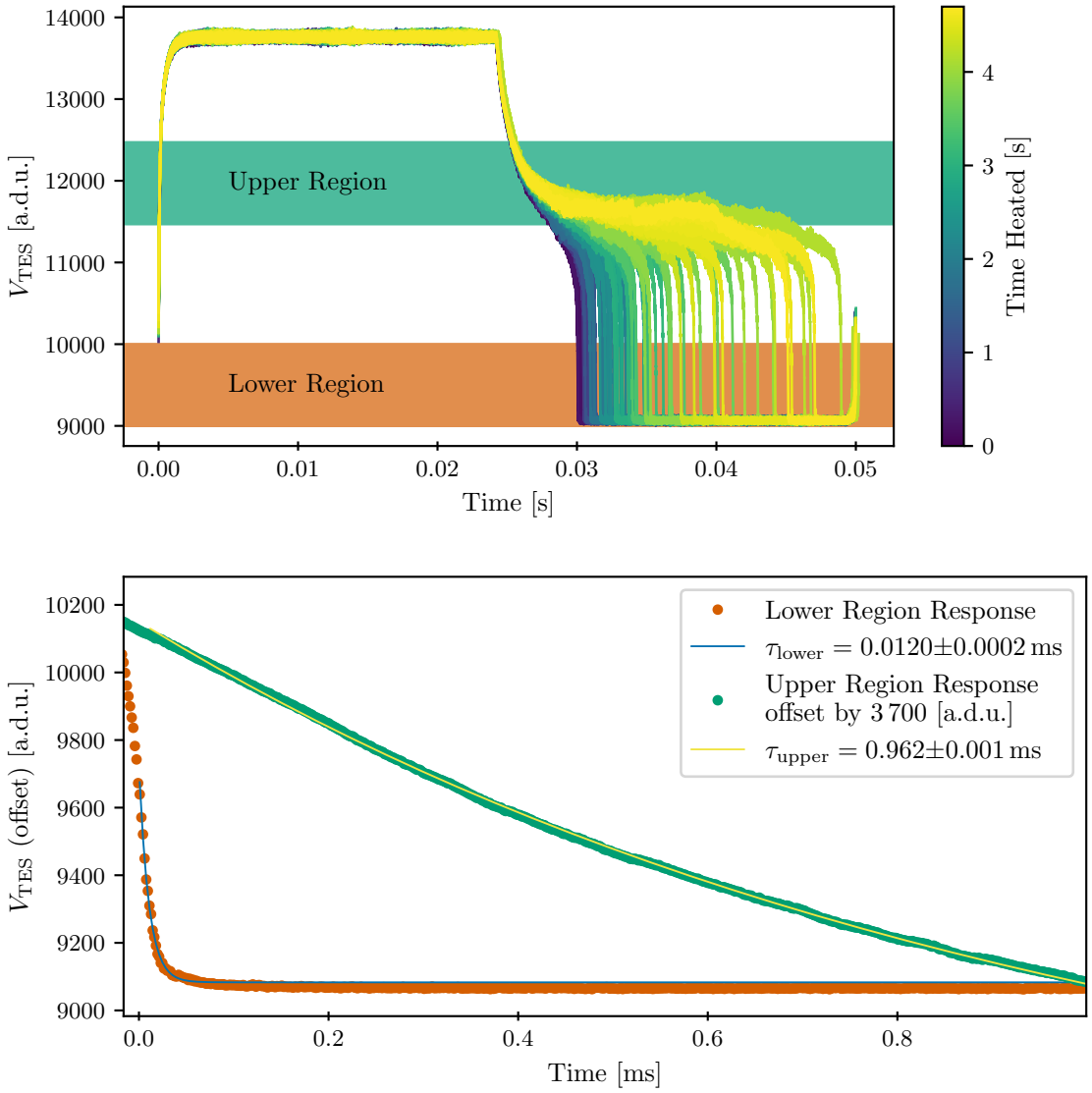


Figure 4.13: The response of the TES to optical modulation as it is heated through its superconducting transition. The response of the TES to the modulated optical load in the lower region of its superconducting transition ($V_{\mathrm{TES}} \leq 10\,000$ data units, orange) is compared to that in the upper region ($V_{\mathrm{TES}} \geq 11\,500$ data units, green, vertically offset by 3 700 data units) in the bottom panel (See Figure 4.12). A decay model has been fit to the response in each region.

For the detector to maintain a set temperature in the steady state, it is required that

$$\frac{1}{T}\int_{t_0}^{t} P_{\text{bath}}\,dt = \frac{1}{T}\int_{t_0}^{t} P_{\text{heat}}\,dt + \frac{1}{T}\int_{t_0}^{t} P_{\text{opt}}\,dt + \frac{1}{T}\int_{t_0}^{t} P_{\text{elec}}\,dt \quad [\text{W}]. \tag{4.1}$$

Provided that the time average of optical loading and electrical bias is constant, the change in the power loading of the detector is given by, $\Delta P = \Delta P_{\text{heat,avg}}$. Since the heater is only active for the specified duty cycle while conduction occurs continuously, $G = 0.4\Delta P_{\text{heat}}/\Delta T$ for a detector operating with a pulse width of 10, a blanking time of 4, and without multiplexing.

Figure 4.14 shows thermal conduction measurements for the central detector. During this measurement, the heaters corresponding to each of the other detectors have been manually switched off and the detectors are not multiplexed. The uncertainty of the process variable is taken to be the standard deviation of process variable values while at the chosen setpoint. To determine both the heater power and detector temperature in physical units, both temperature calibration of the TES and conversion from the heater Digital-to-Analogue Converter (DAC) voltage is required. The temperature calibration of the TES thermometer corresponds to the superconducting transition shown in Figure 4.12 and the uncertainty is the corresponding uncertainty in the repeatability of measurements with the same pulse width after temperature offsets have been removed. The power dissipated by the heating element is determined following the conversion detailed in §3.3.3. The repeatability of the superconducting transition is the dominant source of uncertainty in conduction measurements. In the more sensitive lower region of the transition, the dynamic thermal conduction of the central detector remains at a constant value of $0.22 \pm 0.01\,\mu$W/K.

To determine thermal conductance from the detector time constant, electrothermal feedback must be considered (see §3.1). Since the impedance of the TES is relatively high (see §3.2.1) and the values I have measured for α are large, electrothermal feedback is expected to play a significant role in detector response. Accounting for this effect requires knowledge of the bias current through the TES thermometer. As of the time of writing, we are awaiting

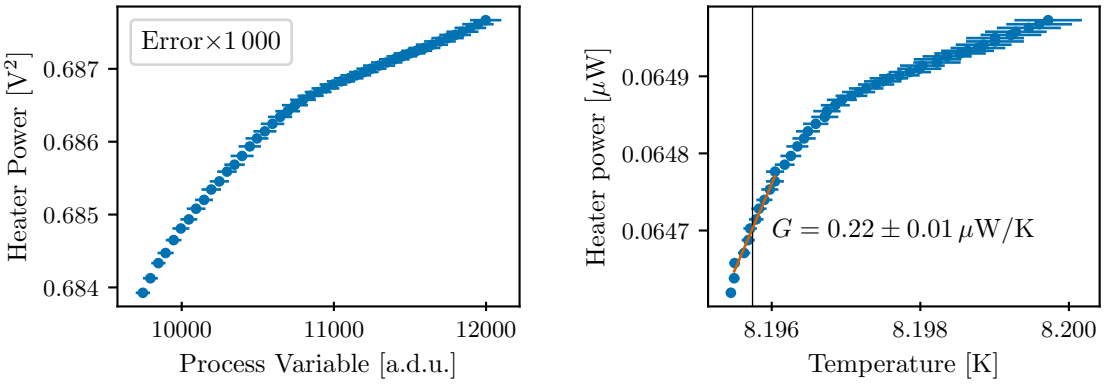


Figure 4.14: Measurements of the dynamic thermal conduction of the central detector in internal data units (left) and calibrated into physical units (right). In the left panel, error bars have been increased by a factor of 1 000 to increase visibility. In the sensitive region of the TES thermometer's operation, the thermal conduction has been determined by a linear fit shown by the orange line. The thin vertical line marks the default setpoint of the PID feedback.

confirmation from the manufacturer concerning the bias circuitry to the TES thermometers.

4.1.3 Output variable bit structure

To better understand the data output and the bit-level resolution of the detector system, I obtained a bit-level histogram of the output variable reported from the detector array for each detector. The bit-level histogram shows how often each of the 32 bits in the output variable is set to a value of one throughout the time-ordered data from the detectors. Figure 4.15 shows a bit-level histogram from 10 packets of a detector observation while a mirror was placed at the cryostat window to maintain a flat optical field (such that the detectors see themselves in the cryogenic environment at ∼8 K). Bits in positions 6–12 (marking position from the least significant bit at position 0) are set near 50% of the time showing the variation expected from detectors experiencing random fluctuations. Higher bits demonstrate the static detector signal corresponding to the constant optical load. The two highest bits are never set showing that the ADCs are not saturated. The lowest 6-bits (0–5) are unused as the PID calculation objects coded in LabVIEW calculate the output variable (heater power) as a single precision floating point number and thus do not take

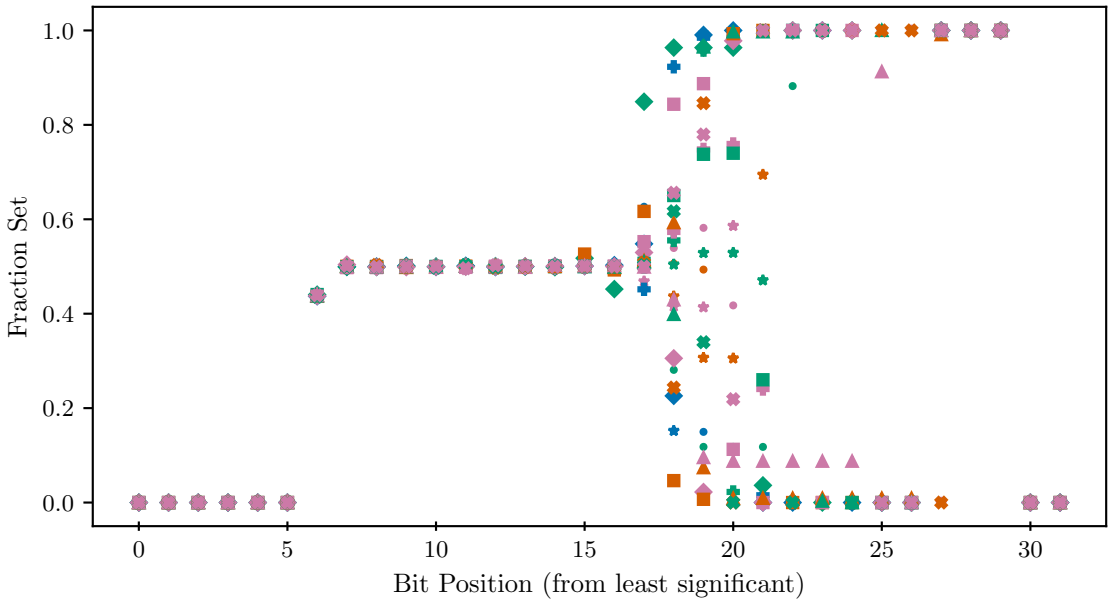


Figure 4.15: A bit-level histogram for a detector observation with a flat mirror at the entry window to the cryostat. Detector markers and colours follow the convention introduced in Figure 3.8.

advantage of the full 32-bits that can be sent to the heater DAC (see Appendix D).

Figure 4.16 shows the distributions of the output variable values corresponding to Figure 4.15. The standard deviation of each distribution is $\lesssim 2^{19}$ data units. If the noise in the detector signal can be considered to be white (i.e., spectrally flat), 4^N samples are required to increase the effective number of bits by N [136]. As such, 4^{12} samples of data are required to reduce the detector signal error level to the digitization limit of the output variable (2^6) through averaging. This corresponds to $\sim$22 minutes of detector data collection.

The output variable signals from detectors B4 and C3 show substructures within the distribution. The peaks of these have been marked in the right panel of Figure 4.16. These are equally spaced by $\sim$10 bins (5 900 data units) in each distribution corresponding to $\sim 2^{12}$ data units. The bit-level histograms for these two detectors are shown in Figure 4.17. No anomalous behaviour is seen suggesting that the multimodal distributions are indicative of the noise profile of these detectors.

It should be noted that detectors B4 and C3 have a higher integral gain term than the

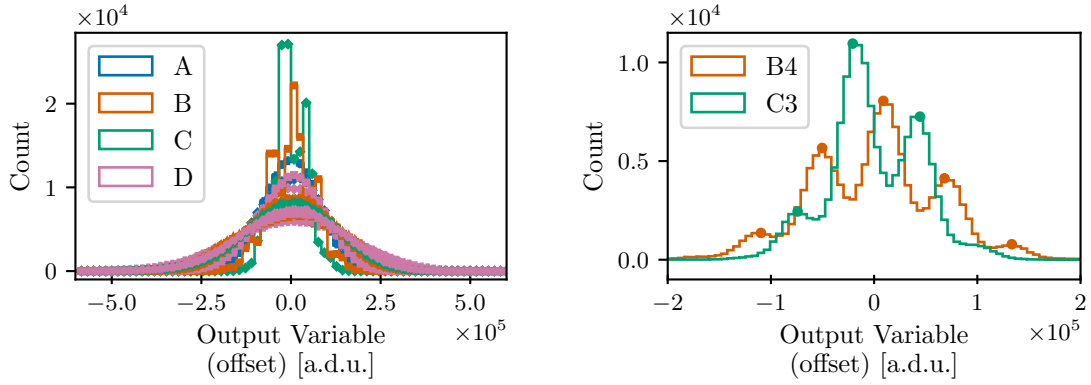


Figure 4.16: The distribution of output variable values is shown for each detector corresponding to the data from Figure 3.8 (left). Two detectors show distinct substructure in their distributions which are shown separately (right). The peak of each substructure is marked by a dot. Each histogram has been offset to account for difference in the steady state signal of each detector.

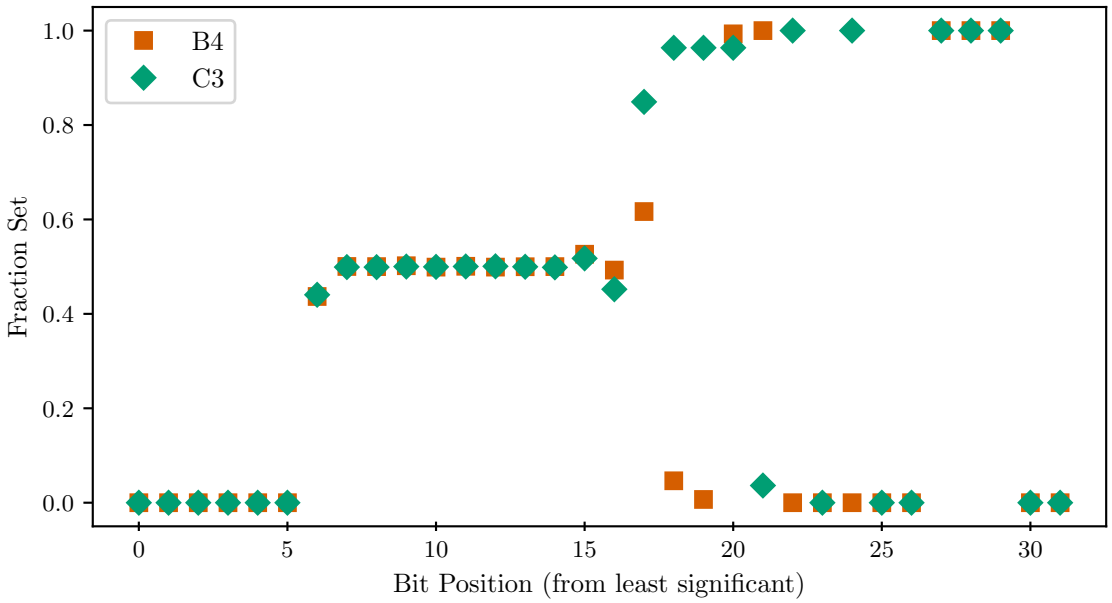


Figure 4.17: The bit-level histograms of the anomalous B4 and C3 detectors corresponding to the signal distributions shown in the right panel of Figure 4.16.

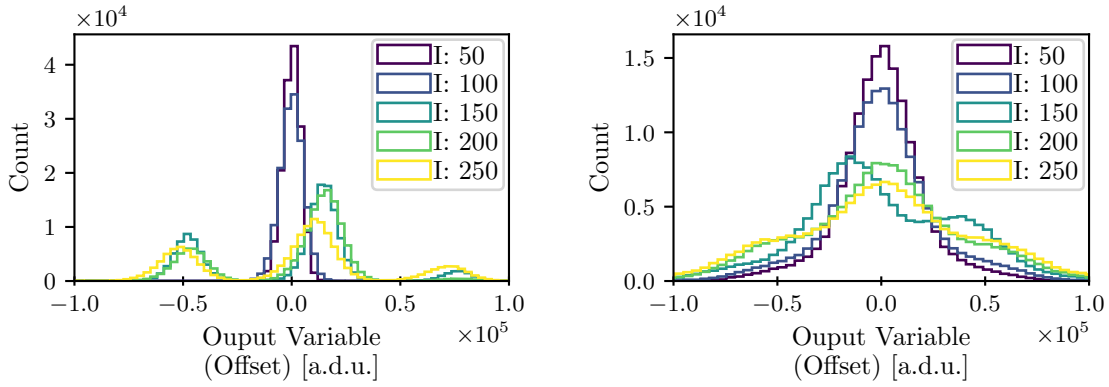


Figure 4.18: Output variable distributions for detectors B4 (left) and C3 (right) under a variety of integral-term PID weights (I) while viewing a mirror.

default settings for other detectors (having I-gains of 700 and 550 data units for B4 and C3, respectively). Figure 4.18 shows the distribution of 10 data packets of the output signal from these detectors (corresponding to ∼12 s) while viewing a static optical load provided by the mirror. These are shown for a range of integral-term PID gains similar to the default settings of other detectors. From these measurements, we see that for integral-term gains higher than 100, both detectors exhibit this multimodal behaviour. This unusual behaviour is not seen in other detectors when operating with high integral-term weighting (see §4.1.6). Additionally, when operating with integral-term gains less than 100, the distributions of the output signal from these detectors are narrow by a factor of ∼10 when compared to the output from other detectors. Reduction in the noise of detector A0 has also revealed multimoded detector behaviour. This behaviour is further discussed and characterised in §6.2.2.

4.1.4 Measurement timing

Within a single measurement pulse, the TES thermometer can transition throughout its superconducting transition depending on the time that the heater remains active and how much time is allowed to elapse before a measurement of the TES state is used in the PID loop. Through measurements of the TES voltage when in full TES profiling mode,

the fundamental behaviour of a detector can be examined while the parameters that affect measurement timing are adjusted [121]. When operating in this mode, the ADC time delay software feature must be activated. In this mode, the quantity of reported data from a single detector increases by a factor approximately equal to the chosen measurement pulse width. To focus on the characterisation of a single detector while reducing the volume of data recorded in my investigation of detector measurement timing, many of the experiments in this section were performed without multiplexing the detector system.

Operating with the ADC delay in TES profiling mode results in fundamental changes to detector timing and duty cycle (see §3.3.1). Without the ADC delay, a single detector is active for 885 ticks of the 80 MHz clock ($\sim$11 μs) and inactive for 5 310 ticks (64.13 μs) when the detector array operates with a default pulse width of 10 and in multiplexing mode. This corresponds to a frame rate of 12.91 kHz. Introducing the ADC delay to measure TES state on each loop count of a measurement pulse causes a detector measurement to increase to 1 101 ticks ($\sim$14 μs), decreasing the frame rate to 10.38 kHz. As a result, the heater on a single detector is active and inactive for longer time periods in the multiplexing loop. Additionally, modifications to the reported data structure from the detectors can result in subtle changes to the timing of a detector measurement loop. Figure 4.19 demonstrates the timing of a measurement pulse from an early version (June 2022) of the TES profiling readout mode detailed in §3.3.2 and Appendix D while the detectors are viewing a static optical load provided by a mirror at the cryostat window. In this early version, each loop count of a measurement pulse reports six 32-bit integers to maintain the cadence of nominal operation but increases the amount of data transmitted by a factor equal to the pulse width. In this older TES profiling mode, the process variable for each channel was converted to a 32-bit integer and reported along with the frame counter and metadata integer at each loop count of a detector measurement pulse with standard output-variable measurements reported at the end of the measurement pulse. As a result, the time between loop counts in the detector measurement pulse in this older TES profiling mode is 147 clock ticks ($\sim$1.84 μs) while the

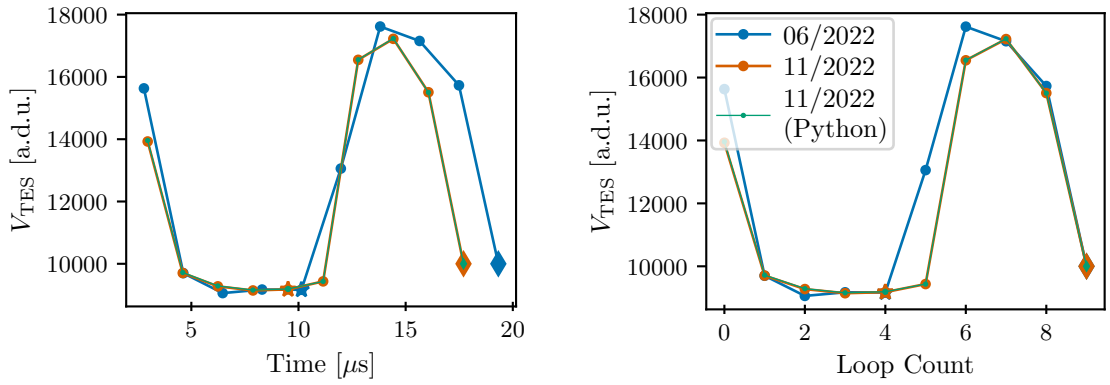


Figure 4.19: Central detector measurement pulses with different readout structures corresponding to different versions of the TES profiling readout mode (see §3.3.2). Additionally, a measurement pulse from the detectors using the Python control software outlined in §3.3.2 is shown. The measurement pulses are shown in relation to time (left) and the loop counter (right). The loop count corresponding to the heater switch-off is marked with a star (as in Figure 3.9). In each case, a single TES measurement is used in PID calculation which is marked by a diamond.

time between loop counts is 131 clock ticks ($\sim$1.64 μs) with the current implementation of the TES profiling readout mode.

Figure 4.19 also demonstrates that, as expected, operating the detector array with the Python control software described in Appendix D rather than the QMC-designed LabVIEW software does not change the timing of a measurement pulse. The output variable signals corresponding to the measurement pulses shown in Figure 4.19 are shown in Figure 4.20. This further demonstrates that there are no significant differences introduced by operating the detector array with the Python control software. The reduced time between pulses from the current control software requires less heater power resulting in a significant offset. The current implementation of control software results in a 32% narrower distribution of detector signal when operating with the current readout structure. This suggests a significant reduction in noise due to the faster timing (and reduction in heater power required to maintain the set point).

The duty cycle over which a single detector remains active when operating in multiplexing mode is 1/7 ($\sim$14.29%). Note that the duty cycle of the heater, which is determined

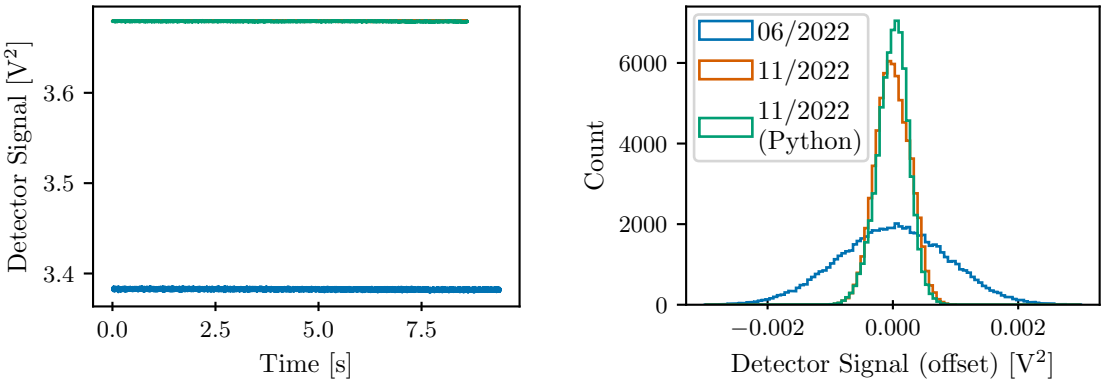


Figure 4.20: Central detector output variable signals with different readout structures corresponding to the measurement pulses and software versions outlined in Figure 4.19. The output variable signals are shown (left) as are their distributions with the offsets removed (right). Both datasets (green and orange curves) from November 2022 agree within noise and overlap in the left panel.

by the chosen blanking time, is less (see §3.3.1). When operating without multiplexing, the pulse width of the detector measurement can increased to achieve a similar detector activity duty cycle as when operating in a standard mode (defined as the time over which the TES is not in a superconducting state compared to a full detector measurement). While one might intuitively believe that increasing the pulse width by a factor of 7 should be sufficient, timing measurements in Table 4.3 demonstrate that this is not the case. Additionally, the duty cycle of the heater on a detector is the dominant factor in the thermal behaviour of a detector. Also, channel A has 3/7 measurement pulses in the multiplexing loop that do not contribute TES bias heating as a consequence of the empty detector sites.

The measurements shown in Table 4.3 are determined from the average timing values from ∼30 000 detector measurement pulses while under a static optical load provided by a mirror at the input window of the cryostat. For all pulse width values shown, the heater remained active for 749 clock ticks (∼9.36 μs) and the TES state measurement used in the PID loop occurred after 1 404 ticks (∼17.55 μs from the start of the pulse). A pulse width of 89 loop counts is required to achieve a similar detector activity duty cycle to a multiplexed detector measurement. For multiplexed and unmultiplexed operating modes to be thermally

Table 4.3: The detector activity and full-frame heater duty cycle (D.C.) when operating in TES profiling mode without multiplexing at different pulse widths (P.W.). The pulse widths discussed in Figure 4.21 are marked in their corresponding colour. Of particular note, a pulse width of 74 achieves the most similar full-frame heater D.C. to multiplexed operation while a pulse width of 89 results in a similar detector activity D.C.. The nominal timing of multiplexed operation (MUX) with the ADC delay active is also shown.

P.W.	Detector Activity Time [ticks/μs]	Total Pulse Time [ticks/μs]	Detector Activity D.C. [$\pm$0.02%]	Heater D.C. [$\pm$0.02%]
60	1 659/20.74	7 966/ 99.58	20.83	11.25
69	1 659/20.74	9 145/114.31	18.14	8.19
70	1 659/20.74	9 276/115.95	17.89	8.07
71	1 659/20.74	9 407/117.59	17.65	7.97
72	1 659/20.74	9 538/119.23	17.40	7.85
73	1 673/20.91	9 669/120.86	17.30	7.75
74	1 672/20.90	9 800/122.50	17.07	**7.64**
75	1 673/20.91	9 931/124.14	16.85	7.54
80	1 674/20.93	10 586/132.33	15.81	7.08
85	1 673/20.91	11 241/140.51	14.89	6.66
87	1 674/20.93	11 503/143.79	14.55	6.51
88	1 674/20.93	11 634/145.43	14.39	6.44
89	1 674/20.93	11 765/147.07	**14.20**	6.37
90	1 674/20.93	11 896/148.70	14.07	6.30
94	1 674/20.93	12 420/155.25	13.48	6.03
99	1 675/20.94	13 075/163.44	12.81	5.73
10 (MUX)	1 416/17.70	9 912/123.90	14.29	7.68

equivalent, matching the heater duty cycle throughout a full frame of the detector array is required. Under multiplexed operation with the TES measurement ADC delay active, the full-frame heater duty cycle for a single detector is 7.68% which is best matched by an unmultiplexed pulse width of 74.

Figure 4.21 compares the detector measurement process for multiplexed and unmultiplexed modes with different pulse widths for the central detector while viewing the static optical load provided by the mirror. Multiplexed measurements experience switching noise which can be seen in the first loop count of the measurement pulse. Otherwise, the average process variable profile and distribution of process variable values at the read index show little difference between multiplexed measurements and unmultiplexed measurements at a

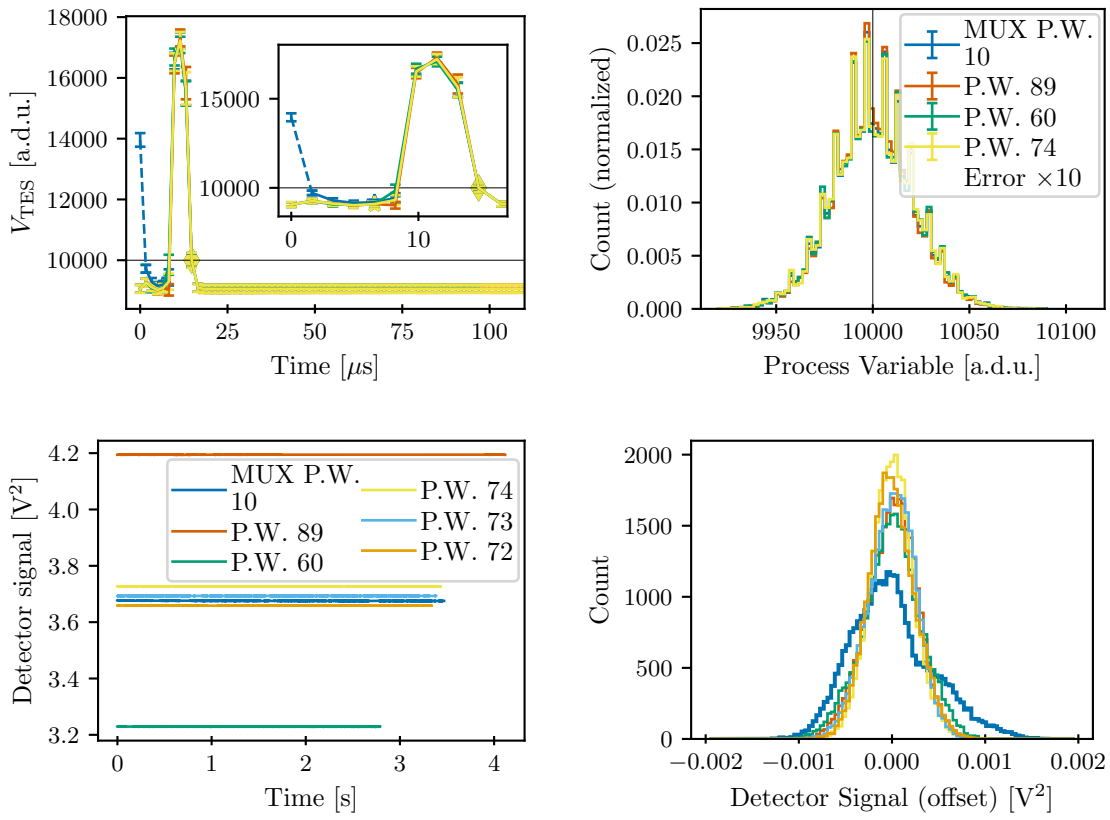


Figure 4.21: The top panels show the average process variable signal throughout a single measurement of the central detector in nominal MUX operation in TES profiling mode and unmultiplexed operation with pulse widths of 89, 60, and 74 loop counts (left) and the corresponding distribution of process variable values at the read index (right). The setpoint is marked in each by the thin black line and the heater switch-off and TES read index are marked as in Figure 4.19. The first two V_{TES} measurements (left) in the multiplexed signal are connected by a dashed line to emphasize that the higher signal level for the first measurement is a result of switching noise due to multiplexed operation. The bottom panels show the corresponding time streams of the detector output variable signal (left) for the same pulse widths and pulse widths 72 and 73. The corresponding output variable distributions with the offsets removed are also shown (right).

variety of pulse widths.

The output signal from the detector experiences significant offsets from multiplexed operation depending on the measurement pulse width. Though an unmultiplexed pulse width of 89 loop counts results in the closest detector activity duty cycle to multiplexed operation, the offset in the output signal from the detector is the largest of the examples shown. This demonstrates that matching the thermal behaviour of the detectors is the dominant factor in matching multiplexed and unmultiplexed modes. In spite of this, the best-matched heater duty cycle between both modes (to within 0.6% at an unmultiplexed pulse width of 74) does not result in the best agreement in detector signal offsets. Rather, the multiplexed detector signal's steady state corresponds to an unmultiplexed pulse width between 72 and 73. This result indicates a difference in the self-heating of the detector from the bias circuitry to the TES when operating in multiplexed and unmultiplexed modes. As the TES thermometer is not electrically biased while switching through the other 7 rows in the multiplexing, a shorter than predicted heater duty cycle when operating without multiplexing is required, if similar signal amplitudes is the goal, since the TES bias circuitry is active throughout an entire frame of detector measurements.

The differences in the distributions of output detector signal for unmultiplexed measurements show little variation over pulse width. Deviations within the width of each distribution are within 10% while the width of the distribution of multiplexed output values is 60% wider than the mean width of unmultiplexed measurements. The increased width of the multiplexed deviation can be attributed to the increased electrical pickup noise from the switching within the multiplexing loop.

The loop counter within the metadata integer is only assigned 6 bits and pulse widths larger than 63 will result in an overflow. For practicality, further studies of modifications to the timing parameter of detector measurement pulses will make use of an unmultiplexed pulse width of 60. This results in a significant offset in the steady state detector signal from nominal operation but any increase in detector noise over more multiplexing-equivalent

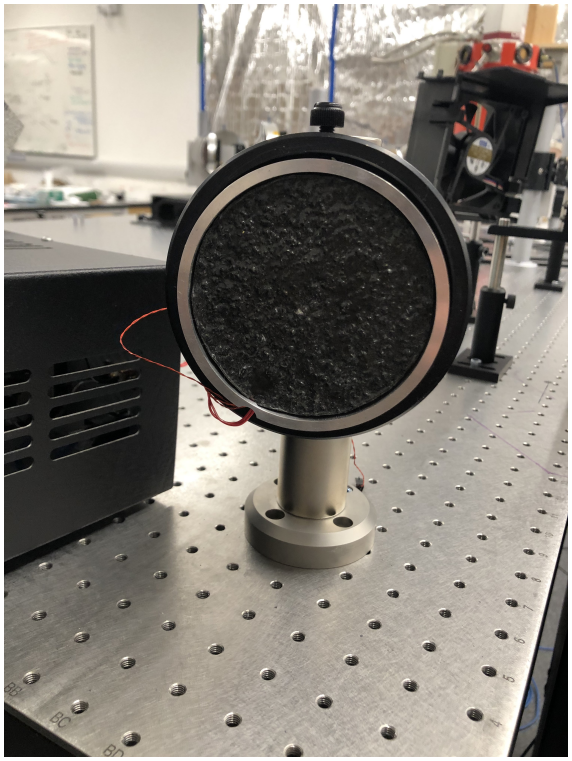


Figure 4.22: The calibrated blackbody source used in detector to provide optical loads for the detector array while studying detector timing parameters.

pulse widths is small compared to the increased deviation due to multiplexing.

To study the effects of modifying detector timing parameters while viewing a modulated optical load, a calibrated blackbody source (see Figure 4.22) and a physical chopper wheel were positioned in front of the window to the detector cryostat.

The effect of holding a fixed TES read delay while varying the time the heater is active (blanking time) is shown in Figure 4.23 for the central detector with multiplexing turned off. For blanking times that are significantly less than the read index (31), the TES is quickly heated such that the TES rapidly rises through its transition into its normal conducting state and then decays back through the transition. At the specified read index, a measurement of the TES state is made. The PID feedback loop determines the heater power necessary to heat the TES in this way such that the TES state measurement on the falling edge of the TES's profile occurs at the desired setpoint. The multimoded distribution of process variable values emphasises the error signal of the PID as the detector transitions

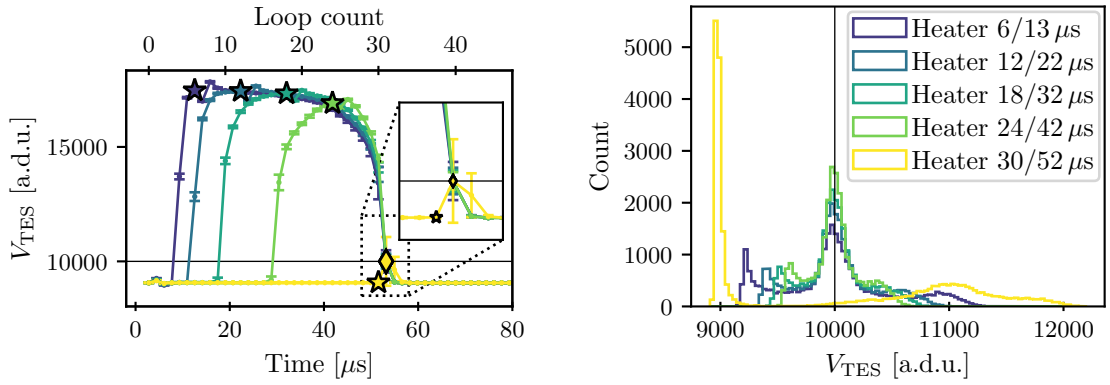


Figure 4.23: The average process variable profile for measurements of a 343 K black body source modulated at 40 Hz by a chopper (left) and the distribution of process variable values at the read index (right) for a variety of blanking times with a fixed read index. The heater switch-off and read index are marked similarly to Figure 4.19 and the setpoint is marked in each panel by the thin black line. Blanking times are given in both units of loop counts and time.

from illumination from the blackbody source to the room-temperature chopper blade. As the blanking time is increased to approach the read delay, the TES spends more time below the superconducting threshold where the process variable remains at a value of ∼9 070 data units corresponding to 0 V (∼0.7 V including line impedance). Despite this, all TES state profiles decay to nearly the same state (i.e., the requested setpoint) at the TES read index. This is particularly evident for blanking times greater than 18 loop counts (e.g., the green curves in Figure 4.23). Additionally, Elecromagnetic Interference (EMI) induced by the heater switching off occurs on the loop counts immediately following the loop count on which the heater is switched off (this is best seen in the central panel of Figure 4.26).

If the time delay between the heater switch-off and TES read index is too short (i.e., the yellow curve in Figure 4.23) the PID loop is not effective at maintaining the chosen setpoint. When operating in this way, the TES is either not heated above its superconducting transition or heated above the setpoint without sufficient time for the TES state to be measured while the thermometer cools. This can be seen in the distribution of the TES state at the read index for a blanking time of 30 loop counts in Figure 4.23.

The effects of maintaining a constant heater blanking time while the read index is varied

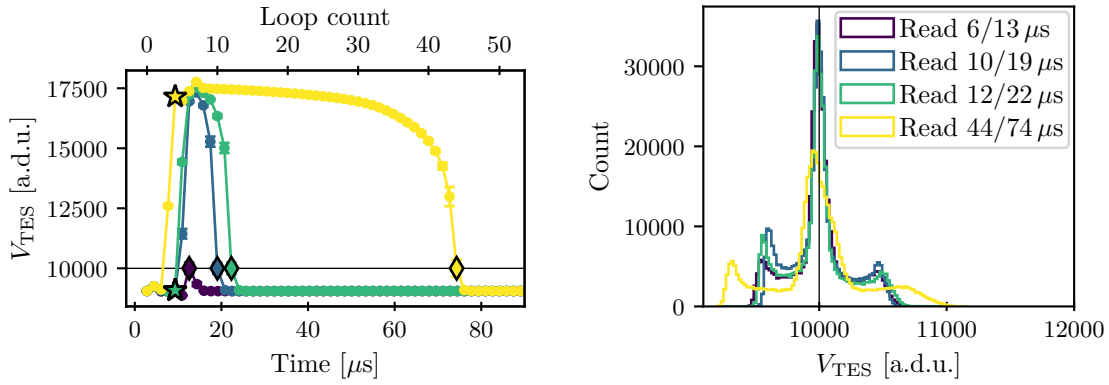


Figure 4.24: The average process variable profile for measurements of a chopped blackbody source and the distribution of process variable values at the read index as in Figure 4.23. In this instance, the blanking time is held at a constant 4 loop counts ($\sim$9.31μs) and the read index is varied. Specific loop counts and the setpoint are noted as in Figure 4.23. The read delays are given in both units of loop counts and time.

are shown in Figure 4.24. As before, I have made these measurements without multiplexing the detector array. In all cases the PID loop effectively maintains the setpoint. As in Figure 4.23, the multimoded distributions of process variable values are a result of the detector's response to the chopper. When the read delay occurs two loop counts after the heater switch-off (i.e., purple in Figure 4.24), a case similar to the 30 loop count blanking time situation shown in Figure 4.23 (yellow) in which the TES state barely rises to the setpoint at the read index rather than rising above it before decaying back down is seen. When operating in this way in Figure 4.24, the detector does succeed at maintaining the setpoint since it does not spend as long within its superconducting regime and the read index occurs 2 loop counts after the heater switch-off.

While Figures 4.23 and 4.24 are effective for profiling the effects of heater duty cycle and the delay before the TES state is used in PID calculation, the effect of the timing between these two parameters must also be studied in the context of detector signal and noise. An optimal pairing of both the blanking time and the read index will result in a narrower distribution of detector signals. The detector signal distribution is shown for three timing cases in Figure 4.25 for a variety of heater blanking times with multiplexing turned

off. From these results, we see the following changes in detector behaviour based on its timing parameters:

- If the blanking time is less than 2 loop counts (i.e., purple curves in Figure 4.25) the detector signal is unstable and the PID feedback fails to maintain the setpoint in most cases. If there is a sufficient delay after the heater switches off (i.e., 40 loop counts as in the purple curve in the bottom panel), a measurement pulse with a blanking time of 2 can be stabilised though it does result in poorer performance.

- With the exception of a blanking time of 2 loop counts, the blanking time has little effect on detector signal distributions when the time delay between the heater switch-off and TES read index is constant.

- When the delay between the heater switch-off and TES read index is 2 loop counts, the TES is not heated through its full superconducting transition and in many cases is not significantly heated to a state beyond the setpoint. In this, there is a particular exception when the delay and blanking time is 2 loop counts (shown by the purple curve in the top left panel) as the TES state rises through the transition and the setpoint is over-shot after the TES measurement.

- A time delay between the heater switch-off and TES read index that is too short or too long degrades detector performance. A time delay of 6 loop counts improves on a delay of 40 loop counts by a factor of 3.2 and on a delay of 2 loop counts by a factor of 1.7.

- A narrower distribution in the detector signal is obtained by choosing appropriate timing parameters. In particular, measuring the TES on the falling edge of the TES state transition is observed to provide a narrow detector signal distribution (shown by the top two histograms in Figure 4.25).

Measurement pulse curves corresponding to a time delay of 40 loop counts between the heater switch-off and the TES read index (bottom left panel of Figure 4.25) are shown in

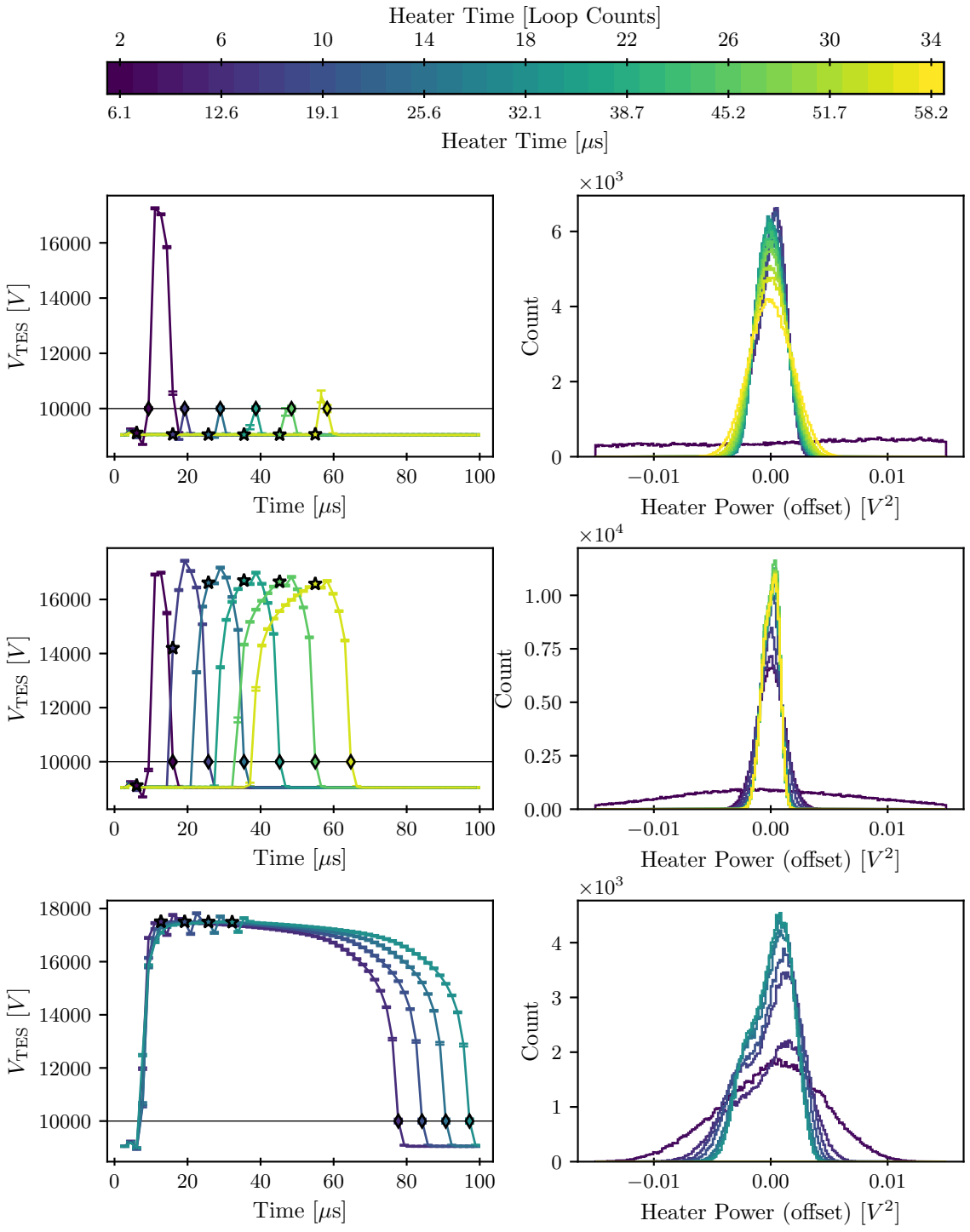


Figure 4.25: Average process variable measurement curves (left column) and the associated distributions of output variable values (right column) while viewing a static optical load provided by a room temperature mirror. These are shown for read delays that are 2 (top), 6 (middle), and 40 (bottom) loop counts after the heater switches off for a variety of heater blanking times. The heater switch-off and TES read index are marked as in Figure 4.19 for each measurement curve.

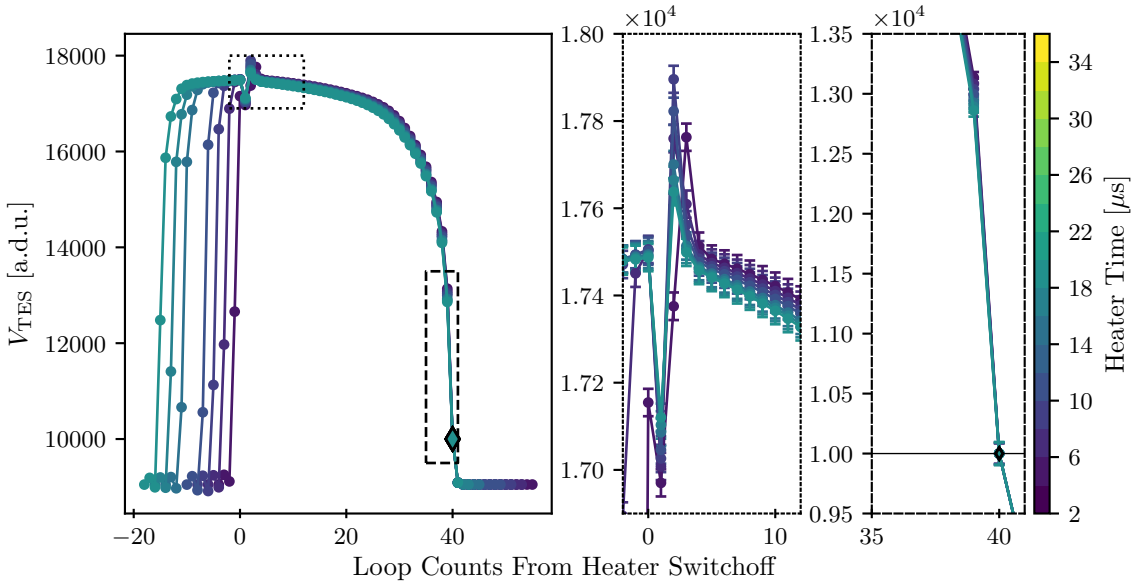


Figure 4.26: The average TES state profile during a detector measurement for a variety of heater times (left), with the TES read index spaced 40 loop counts from the heater switch-off. These are the same measurement profiles from the bottom left panel of Figure 4.25 and have been coaligned with respect to the loop count at which the heater switches off. The central panel, corresponding to the region marked by the dotted black line, emphasises the EMI from the heater switching off. The rightmost panel, corresponding to the region marked by the dashed black line, demonstrates that all curves generally agree at the TES read index.

Figure 4.26 to demonstrate the consistency in the cooling decay through a TES superconducting transition. These curves have been co-aligned with their heater switch-off and all curves agree to within $1.3\times10^{-4}\%$ at the read index. Figure 4.26 also provides a zoom-in on the EMI noise from the heater switching off. This noise appears to affect the 2–3 loop counts directly following the heater switch-off and can be avoided through an appropriate selection of the TES read index.

The effect of the heater duty cycle and TES read index timing is further explored in Figure 4.27. The width of each detector signal distribution is determined from a Gaussian fit to histograms of the data with the error bars providing a measure as to how well the data follow a Gaussian distribution. In all delay cases shown, a blanking time of 2 loop counts is particularly poor in its performance. Additionally, blanking time is shown to have little effect on the distribution of detector values for blanking times greater than six loop

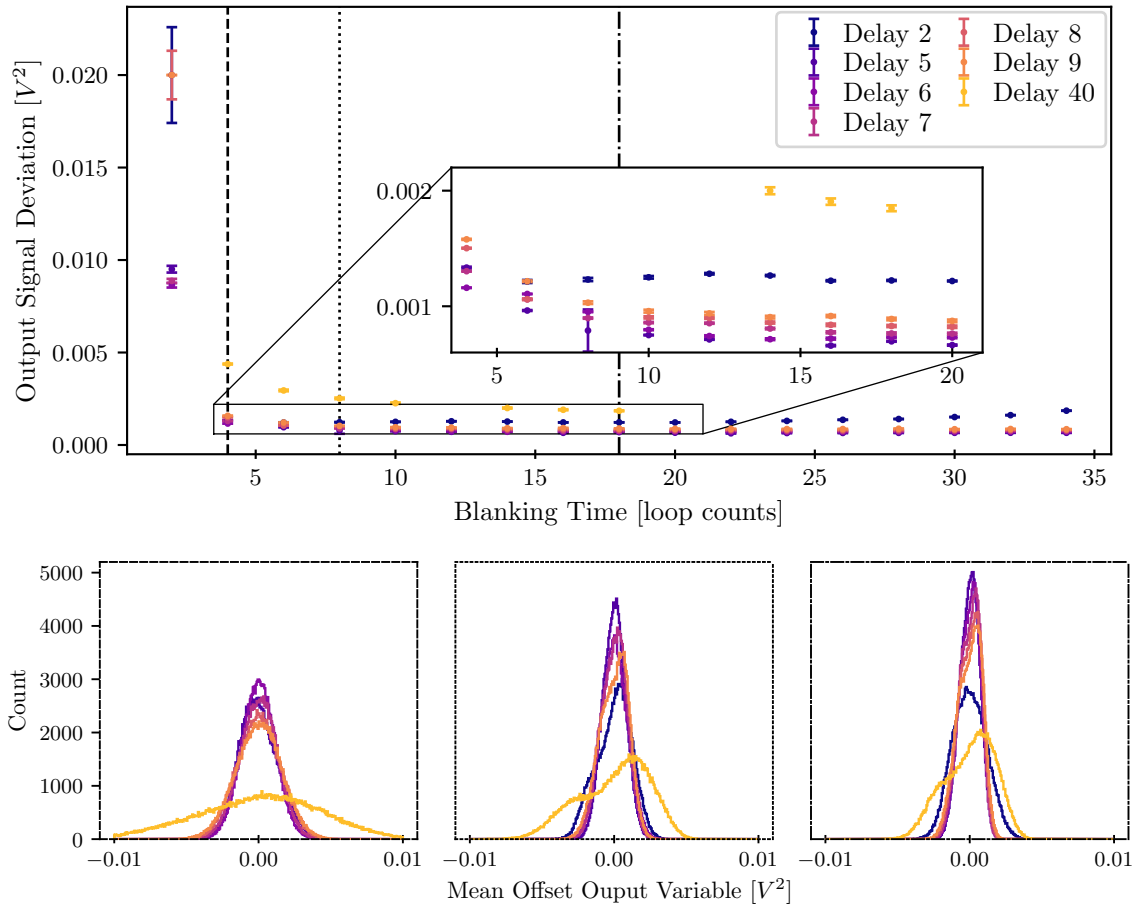


Figure 4.27: The detector signal distribution widths for various blanking times and delays (in loop counts) between the heater switch-off and the TES read index are shown in the top panel. Detector signal distributions at three selected blanking times (denoted by vertical lines at blanking times of 4, 8, and 18 in the upper panel) are also shown in the bottom panels.

counts. Likewise, a TES read state delay of 40 loop counts after the heater switches off has markedly worse performance than shorter delays. Optimal detector performance to minimise the width of the distribution of detector signal (for the parameter space explored) is achieved with a blanking time greater than 10 loop counts and a delay of 5 loop counts between the heater switch-off and the read index. Operating with these timing parameters results in a factor of $\sim$1.7 improvement in the distribution width over default timing parameters. These measurements were made without multiplexing the detector system.

4.1.5 Measured noise performance

The Signal-to-Noise Ratio (SNR) ratio of a detector can be written in terms of its Noise Equivalent Power (NEP) as

$$\mathrm{SNR} = \frac{P_{\mathrm{sig}}}{\mathrm{NEP}\sqrt{\Delta f}}, \tag{4.2}$$

where P_{sig} [W] is the signal power measured by the detector and Δf [Hz] is the electrical frequency bandwidth of the detector [137, 138]. Under nominal operation, the frequency bandwidth can be taken to be half the frame rate of the detector [86]. For the experiments presented here to measure the noise performance of the detector system, the detectors are operating in multiplexed mode with a frame rate of 12.91 kHz. Equation 4.2 can be re-arranged to determine the NEP of a detector by measuring calibrated optical loads (P_{sig}). When measuring in this way, there can be some subtlety in how detector signal and noise are respectively defined. When measuring static optical loads from a calibrated blackbody source (see Figure 4.22), the signal can be considered as the static offset in detector signal when measuring these two loads, $\overline{V}_{T1}(t) - \overline{V}_{T2}(t)$, while detector noise can be estimated as the quadrature sum of the standard deviation of each detector signal, σ_T. In such an experiment,

$$\mathrm{NEP} = \frac{\displaystyle\int_{\nu_{min}}^{\nu_{max}} B(\nu, T_1) A\Omega(\nu)\, d\nu - \int_{\nu_{min}}^{\nu_{max}} B(\nu, T_2) A\Omega(\nu)\, d\nu}{\left(\dfrac{\overline{V}_{T1}(t) - \overline{V}_{T2}(t)}{\left(\sigma_{T_1}^2 + \sigma_{T_2}^2\right)^{1/2}}\right) \sqrt{\frac{1}{2} f_{\mathrm{frames}}}} \quad [\mathrm{W}/\sqrt{\mathrm{Hz}}], \tag{4.3}$$

where A is the detector area and $\Omega(\nu)$ is the solid angle of the detector beam. In Equation 4.3, ν_{min} and ν_{max} determine the *optical* bandwidth of the detector defined by the filtering of the detector system (due to transmission filters, the feedhorn and waveguide assembly, and the detector absorber; see the left panel of Figure 4.28) while $B(\nu, T)$ is the blackbody spectral radiance (see Equation3.15). In the case of diffraction-limited single-mode coupling, $A\Omega(\nu) = \lambda^2$, where λ is the wavelength of absorbed radiation [38, 98, 139, 140]. The feedhorns coupled to the detector array are multimodal and terminate in a square

waveguide that accepts 1–118 modes over a band of 200–2 200 GHz prior to the detector [141, 142]. As a result, representing the frequency-dependant beam as $A\Omega = \lambda^2$ is a poor assumption [21, 141, 140]. The left panel of Figure 4.28 shows the $A\Omega$ product for a model in which all accepted modes of the waveguide are assumed to propagate through to the detector without attenuation such that $A\Omega(\nu) = N\lambda^2$ where N is the number of active modes at a given frequency [98]. Active modes at each frequency have been estimated using the method employed by Nikiten et al. (2011) [141] in which the number of active modes in a square wave guide are successfully estimated by the equation,

$$N \approx 1.5711 \left(\frac{\nu}{\nu_0}\right)^2 \tag{4.4}$$

In Equation 4.4, $\nu_0 = c/(2a)$ is the lowest cutoff frequency mode which is $\sim$200 GHz in the terminal waveguide of the feedhorns. As the transition over which a waveguide mode becomes active is not an immediate discontinuity, the beam model has been smoothed by a 68 GHz wide Hanning filter [143, 144]. In reality, each waveguide mode is not expected to couple to the detectors with full efficiency and the increased optical throughput from NEP calculations using the theoretical beam model will over-estimate the actual optical NEP of the detector [142]. Conversely, the lower optical throughput from a beam representative of single-mode coupling underestimates the optical NEP. To fully determine the optical NEP of the detector system, full beam mapping measurements are required [21, 140].

NEP measurements that make use of a static optical load to define detector SNR suffer from significant drifts in detector signal due to low-frequency noise (as in the right panel of Figure 4.28). Additionally, the PID controller that is used to maintain the temperature of the blackbody source may result in some slowly varying changes in the optical load. I obtained NEP measurements using static optical loads with the calibrated blackbody source positioned near the cryostat window such that the beam of the central detector was fully filled. Measurements at blackbody temperatures at 100, 70, and 40°C are shown in Figure 4.29. Measurements using both an $A\Omega$ product corresponding to single-mode coupling (left) and

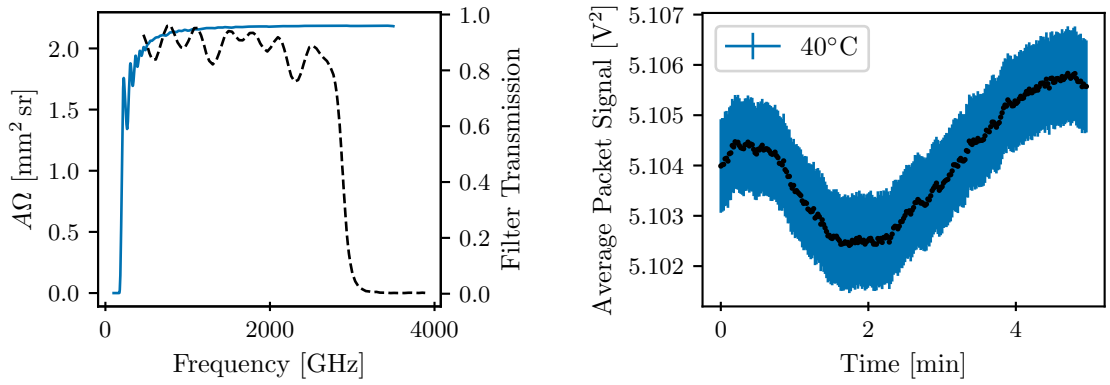


Figure 4.28: The $A\Omega$ product is shown for a multimoded beam model (ranging from 1 to 118 modes, shown by the blue line) with the detector filter transmission (dashed black line) in the left panel. The detector signal variation while measuring a static 40°C blackbody source is shown in the right panel. In this panel, the black line shows the average detector signal for each data packet and the respective standard deviations are represented by the error bars.

the multimoded beam model (right) are shown. In both curves shown in each panel, the detector signal from the blackbody at 40°C was taken to be the baseline signal (T_2) such that the known optical power is determined as

$$\Delta P_{\text{opt}} = \int_{\nu_{min}}^{\nu_{max}} B(\nu,T) A\Omega(\nu)\eta(\nu)\,d\nu - \int_{\nu_{min}}^{\nu_{max}} B(\nu,40^{\circ}\text{C}) A\Omega(\nu)\eta(\nu)\,d\nu(\nu) \quad [\text{W}], \quad (4.5)$$

where $\eta(\nu)$ is the filter profile, and the detector signal is determined to be,

$$\Delta P_{\text{det}} = |\overline{V}_{T1}(t) - \overline{V}_{40^{\circ}\text{C}}(t)| \quad [\text{V}^2]. \quad (4.6)$$

Note that the absolute value compensates for a higher optical power being represented by a lower detector heater power.

To measure the NEP without the effects of low-frequency drift in the detector signal, I made use of an optical chopper between the blackbody source and the cryostat window. In this arrangement, the optical loading on the detectors alternates between that of the blackbody source, $P_{\text{opt,T}_{\text{source}}}$ and the loading from the reflective surface of the chopper

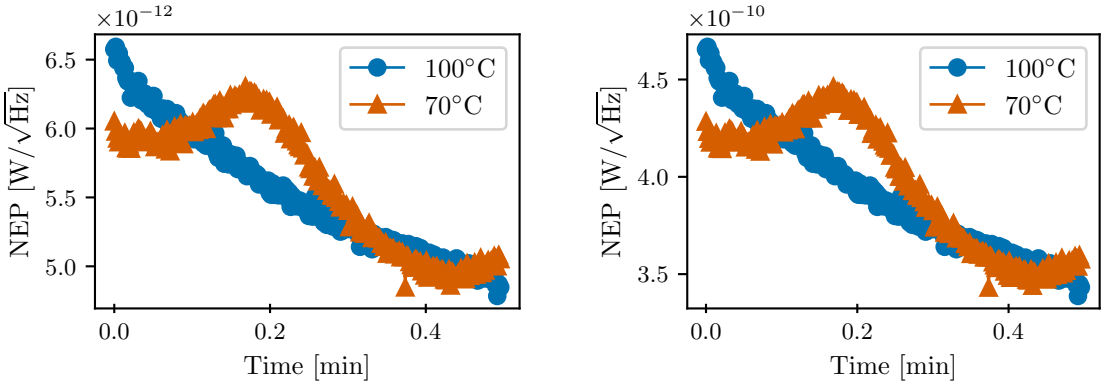


Figure 4.29: NEP measurements of the central detector using a static optical load from a blackbody source at differing temperatures. The left panel shows the result using an $A\Omega$ product representative of single-mode coupling while the right panel shows the result obtained with the multimoded beam model in Figure 4.28. Detector measurements made with static optical loads are subject to drifts in detector signal over large time scales resulting in poor NEP measurements.

blade which is comprised of contributions from the reflection of the cryostat environment and some emission at room temperature $P_{\mathrm{opt,T_{off}}} = RP_{\mathrm{opt},-267^{\circ}\mathrm{C}} + \varepsilon P_{\mathrm{opt},22^{\circ}\mathrm{C}}$, where R and ε are the reflective and emmissive coefficients of the chopper, respectively. The resulting detector signal will have an amplitude $\Delta P_{\mathrm{det},T} = |P_{\mathrm{det},T_{\mathrm{source}}} - P_{\mathrm{det,off}}|$. Since the optical properties of the chopper are unknown, making chopped measurements of the blackbody at two different temperatures allows the measured detector signal to be defined as,

$$P_{\mathrm{det,sig}} = \Delta P_{\mathrm{det},T_1} - \Delta P_{\mathrm{det},T_2} = P_{\mathrm{det},T_1} - P_{\mathrm{det},T_2} \quad [\mathrm{V}^2] \tag{4.7}$$

with the corresponding optical signal,

$$P_{\mathrm{opt,sig}} = P_{\mathrm{opt},T_1} - P_{\mathrm{opt},T_2} \quad [\mathrm{W}] \tag{4.8}$$

provided the laboratory environment is sufficiently stable between subsequent detector measurements.

To extract the SNR of the modulated detector signal I processed the data in the Fourier

domain comparing the spectral peak corresponding to the modulation frequency of the chopper to local noise. I determined the power spectrum of the modulated detector signal using the Fast Fourier Transform (FFT) algorithm implemented in the Python package `numpy` and fit the spectral peak of the modulated optical signal (see Figure 4.30) [145, 125]. To improve the convergence of the least-squares fit, I have zero-padded the power spectrum to $4\times$ the resolution given by the detector time series such that frequency sampling is 0.215 Hz. I extract the detector signal amplitude for a given measurement, $\Delta P_{\mathrm{det},T}$, as the integral of the fitted spectral peak across a band of ± 70 Hz on either side of the spectral peak. The measured detector signal is then given by

$$\Delta P_{\mathrm{det},T} = \frac{1}{140}\int_{f_{\mathrm{peak}}-70}^{f_{\mathrm{peak}}+70} P_{\mathrm{fitted}}(f,T)\,df \quad [\mathrm{V}^2], \tag{4.9}$$

where $P_{\mathrm{fitted}}(f,T)$ is the fitted power spectrum of the modulated detector signal corresponding to a chopped blackbody source with a temperature T. The noise of a single detector amplitude measurement is similarly defined as the square root of the integral of the squared residual from the fitted spectrum over the same band,

$$\Delta N_{\mathrm{det},T} = \left(\frac{1}{140}\int_{f_{\mathrm{peak}}-70}^{f_{\mathrm{peak}}+70} [P_{\mathrm{measured}}(f,T) - P_{\mathrm{fitted}}(f,T)]^2\,df\right)^{1/2} \quad [\mathrm{V}^2]. \tag{4.10}$$

Note that since the noise and fitted peak signal are integrated over the same frequency band, the bandwidth weighting of $1/(140\,[\mathrm{Hz}])$ is superfluous. I then determine the detector NEP as

$$\mathrm{NEP} = \frac{\int_{\nu_{min}}^{\nu_{max}} B(\nu,T_1)A\Omega(\nu)\eta(\nu)\,d\nu - \int_{\nu_{min}}^{\nu_{max}} B(\nu,T_2)A\Omega(\nu)\eta(\nu)\,d\nu}{\left(\frac{\Delta P_{\mathrm{det},T_1}-\Delta P_{\mathrm{det},T_2}}{(\Delta N^2_{\mathrm{det},T_1}+\Delta N^2_{\mathrm{det},T_2})^{1/2}}\right)\sqrt{\frac{1}{2}f_{\mathrm{frames}}}} \quad [\mathrm{W}/\sqrt{\mathrm{Hz}}]. \tag{4.11}$$

Figure 4.31 shows the NEP of the entire detector array using chopped optical loads as described in Equation 4.11. The two associated blackbody temperatures are 100°C and

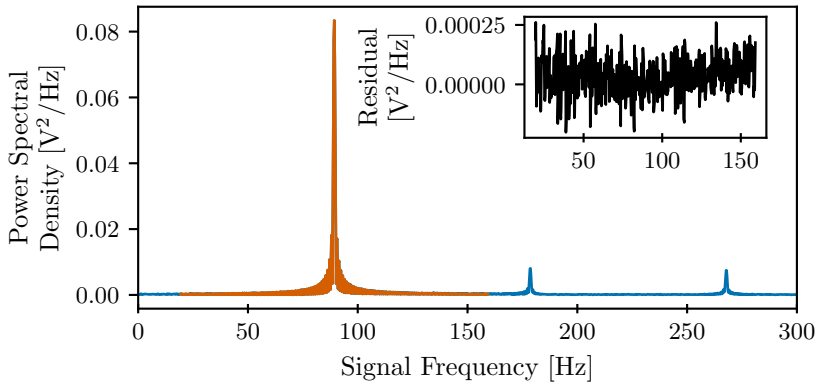


Figure 4.30: An example of a measured (blue) and fitted power spectral peak (orange) from the central detector signal while viewing a 50°C blackbody source chopped at ∼90 Hz. The residual from the fit is shown in the inset panel. Additional spectral peaks are a result of the higher-order harmonics from the quasi-square wave modulation function of the physical chopper. Note that the spectral peak corresponding to the optical modulation has a significantly higher signal amplitude than the $1/f$ noise.

50°C with optical modulation provided by the physical chopper at 90 Hz. As in Figure 4.29 the left panel shows the result assuming an $A\Omega$ product corresponding to diffraction-limited single-mode coupling in the left panel while the NEP measurements that make use of the beam model in Figure 4.28 are shown in the right panel. The manufacturer reports an NEP value of $\sim$2.8 pW/$\sqrt{\text{Hz}}$ is expected for the detectors at 200 Hz, assuming an optical throughput consistent with single-mode coupling (Table 6-2 QMC Instruments Bolometer System Manual). This is consistent with my measurements of the NEP of the detector array shown in Figure 4.31.

4.1.6 PID tuning

The effect of adjusting PID parameters on the detector output signal with a heater time of 4 loop counts and TES read delay of 10 loops is shown in Fig. 4.32, with corresponding V_{TES} histograms shown in Fig. 4.33. These show the central detector signal from a blackbody source chopped at 30 Hz averaged over several thousand periods of the chopped source. It is evident that over this parameter range, increasing the P-term has a slight effect on the amplitude decreasing by 5.8% at the highest P-gain of 3 000. Additionally, it is clear

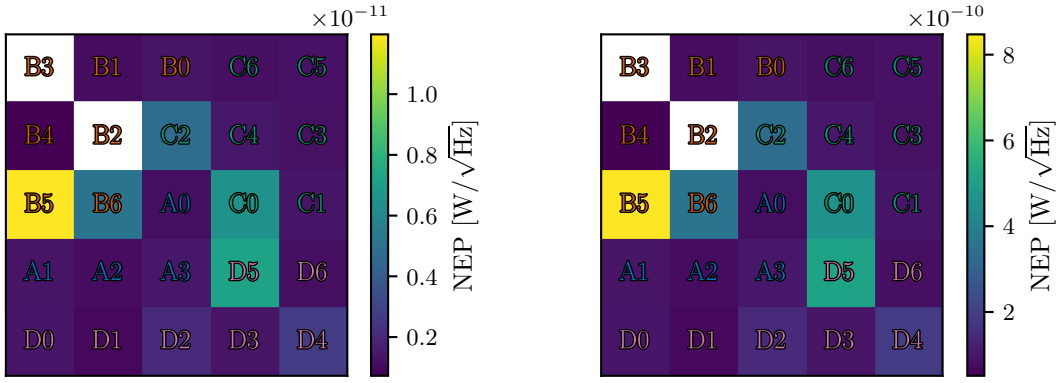


Figure 4.31: The NEP of the entire detector array measured using chopped optical loads and an $A\Omega$ product consistent with single-mode coupling (left) and multimode coupling (right). Again, note that detectors B2 and B3 are unstable.

that the I-gain has a dramatic effect on the ability of the detector to respond to optical modulation with a gain of 100 being near the limit of sufficient response at 30 Hz. Varying the derivative gain appears to have little effect on the output signal in the observed cases.

I have determined the effects of PID tuning on the width of the noise distribution of the central signal in a variety of PID conditions while viewing a static optical load provided by a mirror. Figure 4.34 demonstrates that for a variety of proportional and integral gains, the derivative term increases the noise of the system in general. These measurements, coupled with those of a modulated optical load signal shown in Figure 4.34, suggest that the derivative term of the PID loop degrades detector performance.

Figure 4.35 shows a coarse exploration of the PID parameter space of the central detector while viewing the static optical load provided by the mirror. These results demonstrate that the static noise of the system increases with both of the gains associated with the proportional and integral terms of the PID controller. Though the noise is significantly reduced with relatively passive PID control, the response of the detector to a modulated optical load shown in Figure 4.32 demonstrates that these PID conditions are not suitable for measuring a changing optical signal (e.g. the output from the DFI testbed).

To estimate the SNR performance of the detector, I observed the effects of proportional

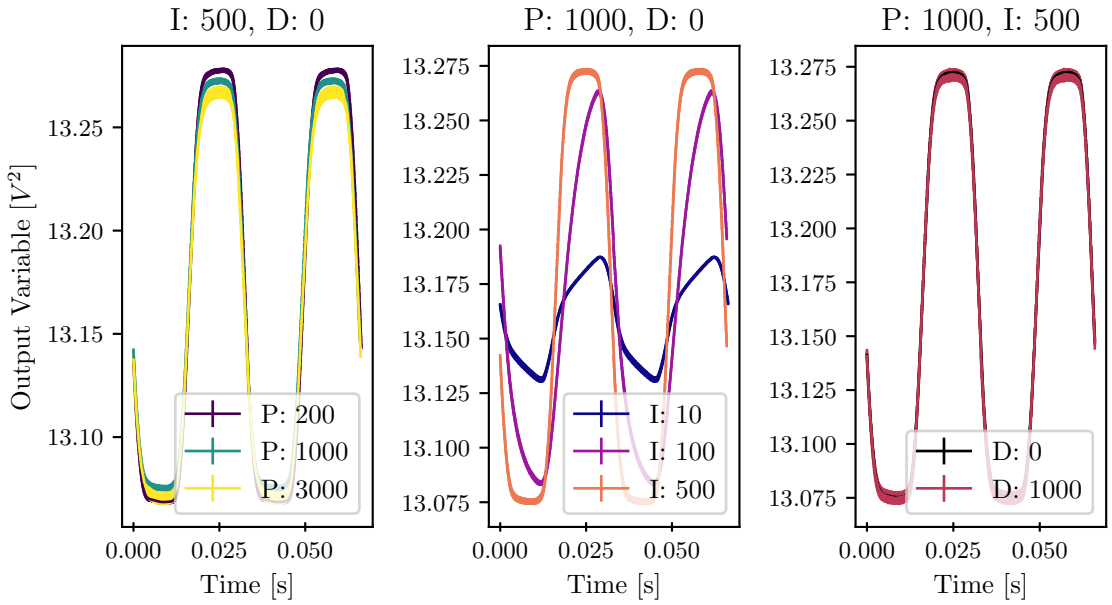


Figure 4.32: The average central detector output signal while viewing a chopped blackbody source under a variety of PID conditions.

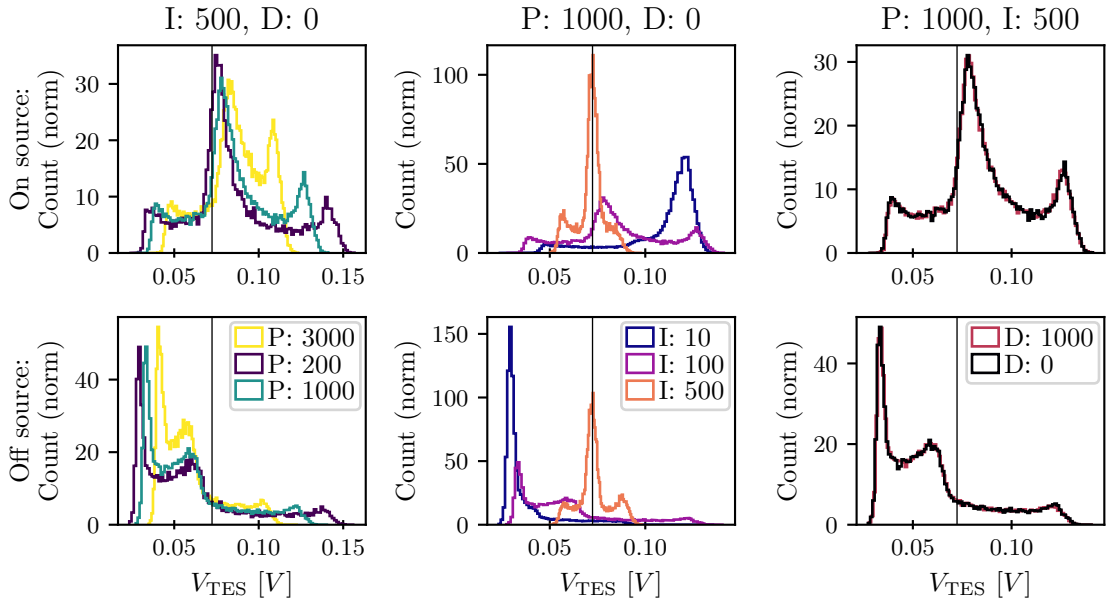


Figure 4.33: The distribution of the central detector's TES voltage at the read index corresponding to the output signals in Figure 4.32. The top row of histograms corresponds to values when the chopper is cutting on the optical loading while the bottom row corresponds to the chopper cutting off the optical loading. The setpoint is marked by the vertical black line in each panel.

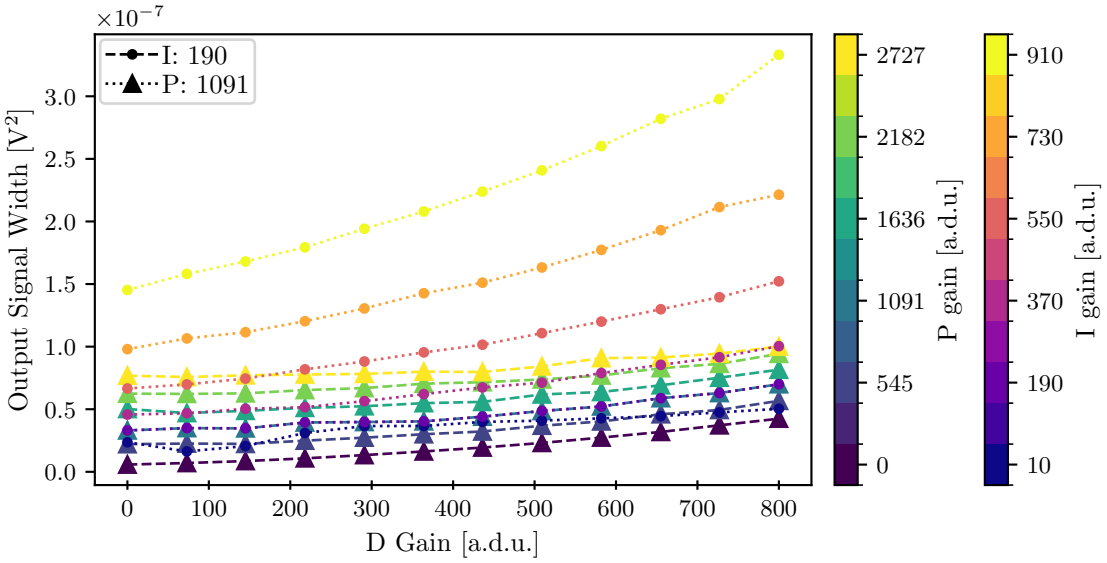


Figure 4.34: The effect of increased derivative-term weighting in the PID loop on the central detector while viewing a static optical load. Results are shown for a variety of proportional and integral term weights. Dashed lines show curves with various proportional term gains while the integral term is held at a constant weighting of 190 data units. Similarly, dotted lines mark curves with various integral term weights while the proportional term is held at a constant gain of 1 091 data units.

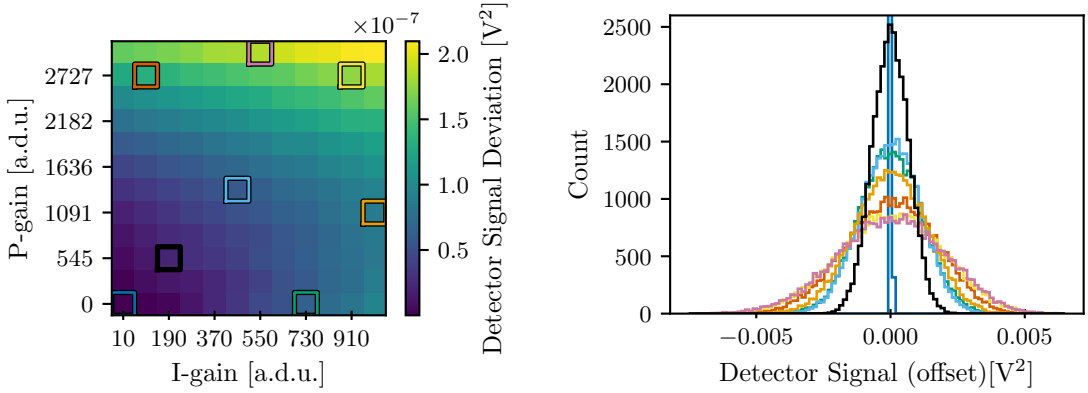


Figure 4.35: The standard deviation of the output signal from the central detector while viewing a static optical load throughout the PID parameter space is shown in the left panel. Note that the derivative term was not used in these measurements (i.e., D-gain is zero). The right panel demonstrates the distribution of the detector output signal for selected PID conditions outlined in their respective colours in the left panel.

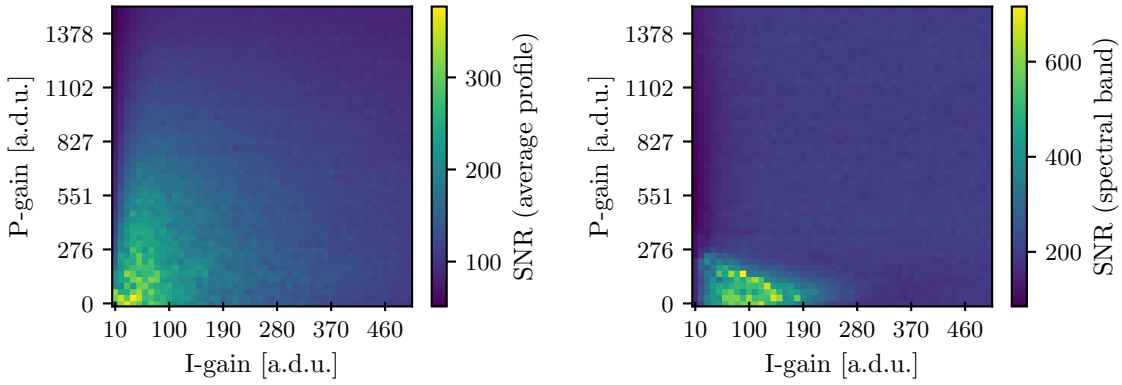


Figure 4.36: The effects varying proportional and integral-term gains on the SNR of central detector measurements of a 90°C blackbody source chopped at 40 Hz. The left panel shows SNR measurements that compare the amplitude of the average chopped signal profile to noise measured in the full detector frequency band (average profile SNR). The right panel demonstrates similar measurements in which SNR has been estimated comparing the spectral peak corresponding to the modulated optical load to noise within the same frequency band (spectral band SNR).

(P) and integral (I) term weighting the PID feedback of the central detector while viewing a 90°C blackbody modulated by a chopper at 40 Hz. Figure 4.36 demonstrates these results for a range of P and I values that reside in the lower noise regime of Figure 4.35. The SNR of the detector with respect to broadband detector noise has been estimated by comparing the amplitude of the average chopped profile from several hundred periods of the chopper to the residual of the average profile on a per-chopper period basis. Detector SNR from this metric is shown in the left panel of Figure 4.36. The SNR measurements by this metric coupled with the noise measurements examined in Figure 4.35 suggest that broadband noise is reduced at low P- and I-term gains as the detector is less responsive to high-frequency noise (see §4.3). This represents a factor of $\sim$3 improvement in broadband SNR over the default PID parameters.

To estimate the SNR of the central detector in a frequency band local to the chopped signal from the blackbody, I considered the power spectral density of the detector timeline. I took the detector signal integrated over a 20 Hz bandwidth centred on the frequency of the spectral peak corresponding to the signal from the chopped blackbody. I have estimated

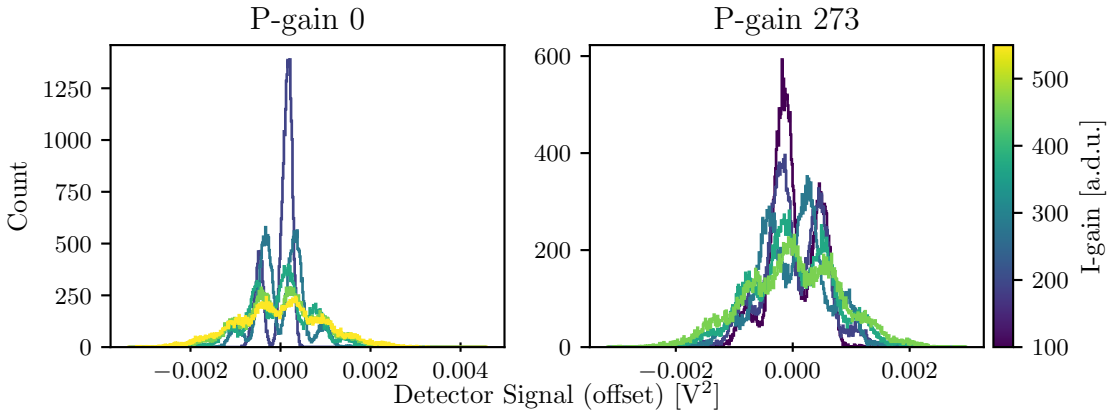


Figure 4.37: Distributions of the output signal from detector A0 while viewing a static optical load. Over the range of P-term and I-term gains shown, these distributions show multimodal behaviour.

noise as the signal from the power spectrum of the detector while viewing a static optical field provided by a mirror (under the same PID conditions) integrated over the same frequency band. These measurements are shown in the right panel of Figure 4.36. These results suggest that there is a localised range of P- and I-term gains for which the SNR in a frequency regime local to the signal from the chopped blackbody is improved by a factor of $\sim$2.6 over default parameters.

In addition to slower detector response and seemingly improved performance, the distributions of the detector signal from A0 show multimoded behaviour with low proportional and integral weighting in the PID control. Figure 4.37 demonstrates the detector distributions corresponding to P-term gains of 0 and 273 data units coupled with I-term gains ranging 100–550 data units. Note that these distributions are of a width closer to the black distribution in Figure 4.35.

Figure 4.38 demonstrates the measurement timeline from the central detector while viewing a static optical load and operating with PID parameters for which a multimodal signal distribution is seen. The multimoded detector signal distributions are a result of changes in the steady state of the detector signal that occur over $\sim$60 detector samples. Figure 4.38 also shows that these relatively rapid changes in the detector's steady state

output do not correspond to any significant changes in the TES state at the read index. In §6.2.2, I provide further discussion and characterisation of this behaviour.

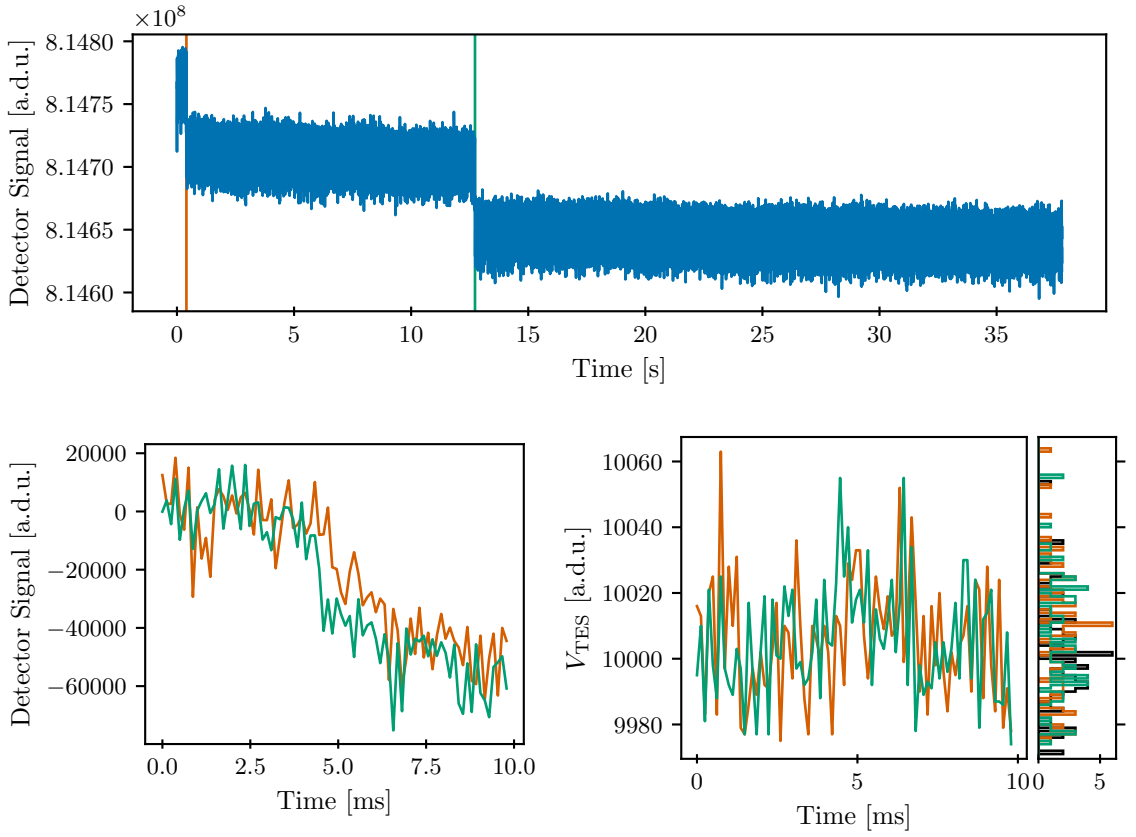


Figure 4.38: The output signal from the central detector while viewing a static optical load and operating with PID parameters for which the signal is found to be multimoded (top). Two rapid changes to the detector's steady state are experienced marked by the vertical lines. These are shown isolated in the bottom left panel. The lower right panel shows TES state measurements used in PID calculation corresponding to regions in which the steady state changes. Histograms showing their distribution are also shown. The nominal steady-state distribution of the TES state measurements used in PID calculation is shown by the black curve to provide a reference.

To identify regions of the PID parameter space where the multimoded detector signal is apparent, I have measured the number of peaks in each histogram of the detector signal with a peak-finding algorithm. In addition, the value of χ^2_{red} from a Gaussian-profile least-squares fit to the signal distribution provides an additional metric for how well the distribution follows that of a single-peaked Gaussian. These two metrics are shown in Figure 4.39 for the PID parameter space explored in Figure 4.36. These suggest that two

regions exist in which rapid changes to the steady state of the detector's output are not apparent, very low P- and I-term gains and P-gains greater than 500 data units. The examples of detector signal distributions shown in Figure 4.39 demonstrate that very low P- and I-term weights result in much narrower detector signal distributions (as suggested by Figures 4.36 and 4.35). As these discrete changes to the steady state of the detector output can be comparable to the noise inherent in the detector signal and do not occur at regular intervals (see §6.2.2), it is difficult to determine if this multimoded behaviour is present in the wider signal distributions corresponding to P-term gains greater than 500 data units.

Much of the high SNR region presented in Figure 4.36 corresponds to regions in which the rapid changes to the steady state of the detector's output are observed. Figure 4.40 shows the SNR performance by both broadband and local noise metrics focusing on P-term gains greater than 500 data units (see Figure 4.36). Again it should be noted that though low P- and I- term gains result in the narrowest distribution of detector signal, detector response speeds are severely limited in the regime (see Figure 4.32). As such, these have also been excluded from Figure 4.40. It is evident that when operating with P-term gains greater than 500 data units, the P-term has little effect on the SNR near the chopper frequency of 40 Hz and shows a similar trend to Figure 4.36 with respect to broadband SNR determined by the average chopped signal profile.

In general, detector noise performance is improved through low P-term gains paired with low I-term gains. When responding to an optical signal modulated at 90 Hz, there is a localized region centred about an I-gain of 100 data units coupled with a P-term gain of less than 200 data units for which the detector SNR is optimised. However, multimoded detector noise behaviour is apparent for P-term gains less than 500 data units. I have not conclusively determined whether this behaviour is present in the signal from PID settings that result in wider noise distributions (see §6.2.2). The optimal PID tuning of the detector system for use with an optical instrument requires additional considerations with respect to the response of the detectors to optical modulation. This will be discussed throughout the

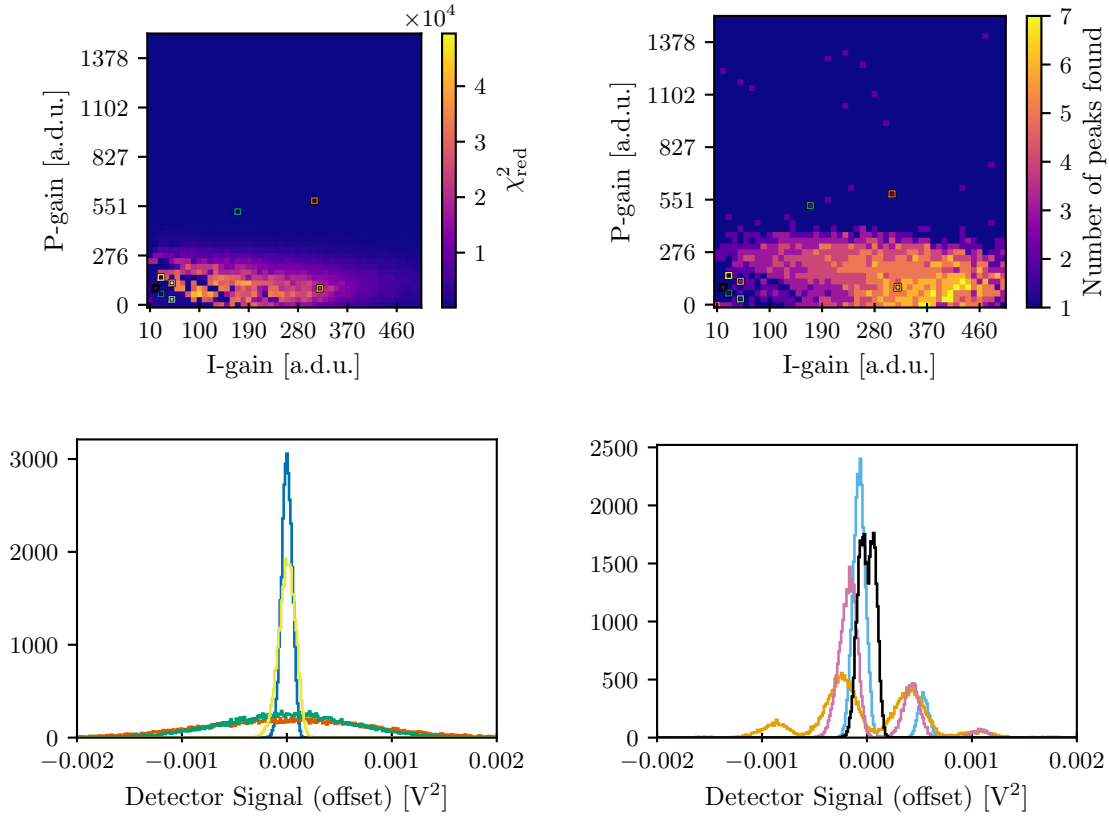


Figure 4.39: The top panels demonstrate the χ^2_{red} value obtained from single-Gaussian least-squares fits to signal distributions from the central detector (left) and the number of peaks found in each distribution (right) in the PID parameter space shown in Figure 4.36. The bottom panels show example histograms where the detector signal distributions appear to be single-moded (left) and multimoded (right).

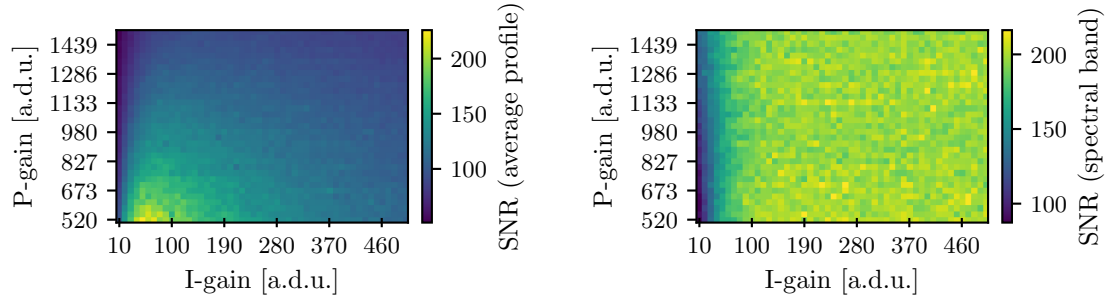


Figure 4.40: The effects varying proportional and integral-term gains on the SNR of central detector measurements of a 90°C blackbody source chopped at 40 Hz as in Figure 4.36. In this Figure, regions of the PID parameter space in which rapid changes to the steady state of the detector's output signal are seen have been excluded.

remainder of this chapter and in Chapter 5.

4.2 Considerations of low-frequency detector noise

Equation 2.51 demonstrates that a DFI instrument aims to obtain a set of spectral scans in time (interferograms) at multiple baselines (see also §5.1.1). As such, the frequency of optical modulation incident on a detector during a spectral scan of a DFI follows that of an Fourier Transform Spectrometer (FTS). For a given spectral frequency of light, the modulation frequency, f is given by,

$$f = m v_{\text{mech}} \sigma \quad [\text{Hz}], \tag{4.12}$$

where v_{mech} is the speed of the spectral scanning stage, σ is the frequency of light observed (in wavenumbers, $\nu = c\sigma$), and m is the folding factor of the interferometer. For the Mach-Zehnder design employed by the Lethbridge DFI, $m = 4$ (see Figure 2.7). Since I am afforded some choice as to the optical modulation frequency band, I can choose to occupy a regime in which the detector system experiences less noise.

Figure 4.41 shows noise spectra from the central detector and an off-axis detector measured while a mirror was placed at the input to the cryostat to reduce optical loading and ensure a static optical field. The data shown correspond to $\sim$1 minute of detector measurements. In each panel, the spectra smoothed by a 200-point Hann filter are shown by the darker curves. At frequencies lower than 5 Hz, the noise spectrum is dominated by low-frequency noise which I have determined to fall as $f^{-\alpha}$ where $\alpha = 0.45 \pm 0.01$ through a least-squares fit. After the $1/f$-dominant portion, the noise spectra flatten before encountering a roll-off with a -3 dB knee frequency at ~ 500 Hz. It should be noted that the biasing and multiplexing circuitry to the detectors are separated by two warm electronics boards. One board contains the circuitry for channels A and B and the other holds the same for channels C and D. We have seen that in §4.1.5 the expected cut at the low-frequency end of

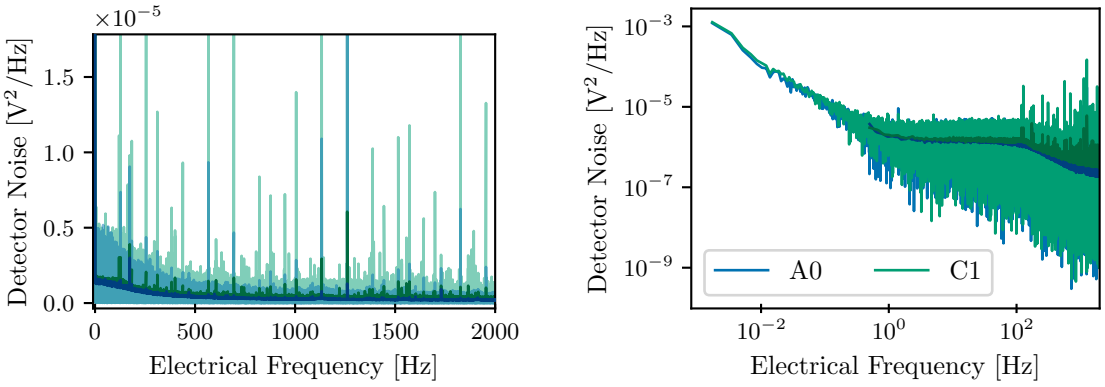


Figure 4.41: Detector noise spectra corresponding to a central and an off-axis detector are shown over linear (left) and logarithmic (right) axes. In both panels, the darker curves show the spectra smoothed by a Hann filter.

the interferometer band is assumed to be $\nu_{min} = 200\,\text{GHz}$ (as defined by the waveguide at the termination of the feedhorns). This assumption is further discussed in Chapter 5. From Equation 4.12, the minimum spectral stage scanning speed to avoid the $1/f$-noise dominant frequency band of detector noise and twice-Nyquist sample fringes from 200 GHz radiation is $v_{\text{mech}} \sim 0.75\,\text{mm/s}$ (in optical path steps, $v_{\text{opd}} \sim 3\,\text{mm/s}$).

4.3 Effective detector time constants

From Equation 4.12, it becomes apparent that an appropriately designed DFI instrument must balance the speed at which the spectral stage is scanned and the speed at which optical modulation can be measured by the detector array (while accounting for the spectral bandpass of the interferometer). This balance requires that (1) the detectors have effective time constants that are sufficiently fast to fully sample modulation from the DFI at the maximum spectral frequency of the band, σ_{max} (for a given stage velocity) and (2) the spectral stage velocity is sufficient to avoid optical modulation falling within the $1/f$-noise dominated region of the detector's noise spectrum at the lowest spectral frequency of the interferometer, σ_{min}. Through both PID tuning and modifications to the timing of a detector measurement pulse, the response of the detectors to optical modulation can be modified.

Proper optimisation of the detector system for use in the Lethbridge DFI testbed requires a balance between the noise optimisation explored in Chapter 4 and tuning the detector speed to optimally measure the optical modulation from the interferometer. Since the detector system will be operated with multiplexing when in its intended use with the DFI testbed, the measurements of the effective detector time constants I have presented in this section have been made with the detector system operating in multiplexed mode.

4.3.1 Measurement techniques

Equation 3.9 suggests a method for determining the effective time constant of a detector through its response to optical modulation as a function of frequency. It is common to measure the effective time constant of a bolometer by measuring the peak-to-peak signal amplitude while viewing a chopped optical source while the chopper frequency is increased [146]. Experiments after this fashion introduce a few challenges. Optical modulation that results from a physical chopper results in higher-order harmonics to be measured by the detector as a consequence of the quasi-square wave modulation function of the chopper [147]. Additionally, the physical size of the broadband optical sources I have available to characterise the detector array are of sizes that exceed what can be practically chopped to frequencies greater than 400 Hz by readily available mechanical choppers. These challenges led me to employ a few attempted solutions to properly determine detector time constants using both a broadband black body source and a Toptica TERASCAN photomixer source obtained later in my studies [129, 130, 131, 132, 133]. Early attempts to measure the detector response that were of a poorer quality are detailed in Appendix E. One such measurement technique demonstrated that the intensity output from photomixer source has an internal response to its modulation bias frequency.

After I had aligned the DFI in its single FTS configuration, the interferometer itself provided a natural way to obtain sinusoidal optical modulation on the detector array. Since the photomixer provides a spectrally narrow source into the FTS, the measured interfero-

gram while scanning the spectral stage is a simple cosine wave and will not suffer from the higher-order harmonics of a square wave modulation to the same degree (see Equation 2.12). With the photomixer set to an optical frequency of 800 GHz, the spectral stage was scanned at various speeds such that optical modulation up to ∼600 Hz was obtained (see Equation 4.12). Figure 4.42 shows measurements of the central detector's frequency response using the FTS in this way for two different PID gain conditions. The signal amplitude has been determined as the amplitude of a least-squares fit of a sinc function to the peak of the detector timeline power spectrum corresponding to the modulation frequency (see §2.1.3). The signal amplitude is then converted to a decibel scale as

$$\Delta V^2(\nu)\,[\mathrm{db}] = 10\log\left(\frac{\Delta V^2(\nu)\,[\mathrm{V}^2]}{\Delta V_0^2\,[\mathrm{V}^2]}\right) \quad [\mathrm{dB}] \tag{4.13}$$

where V^2 is the integrated signal amplitude from the detector power spectrum at a given modulation frequency and V_0^2 is the initial value of the response signal prior to the roll-off. These results show detector behaviour similar to the response of a bolometer detector that does not employ PID feedback with an effective time constant on the order of 0.1 ms (shown by the dashed black line, see §3.1). Additionally, these measurements demonstrate that PID tuning can be used to dramatically change detector response speed (see §4.3.4).

Though the detector signal is the heater power calculated by the PID feedback in response to a changing TES voltage (see Chapter 3), the frequency response curve of the central detector under default settings can be successfully fit by a function of similar form to the magnitude of the TES bolometer response in Equation 3.9,

$$|S_{\mathrm{det},V}|^2 \propto \frac{1}{1+(2\pi f)^2\tau_e^2} \quad [\mathrm{V}^2/\mathrm{W}]. \tag{4.14}$$

A measurement of the central detector's response made with the FTS gives the effective time constant of the central detector when under default operation as 0.96 ± 0.06 ms which corresponds to a cutoff frequency of ~ 166 Hz (see Figure 4.43). This measurement shows

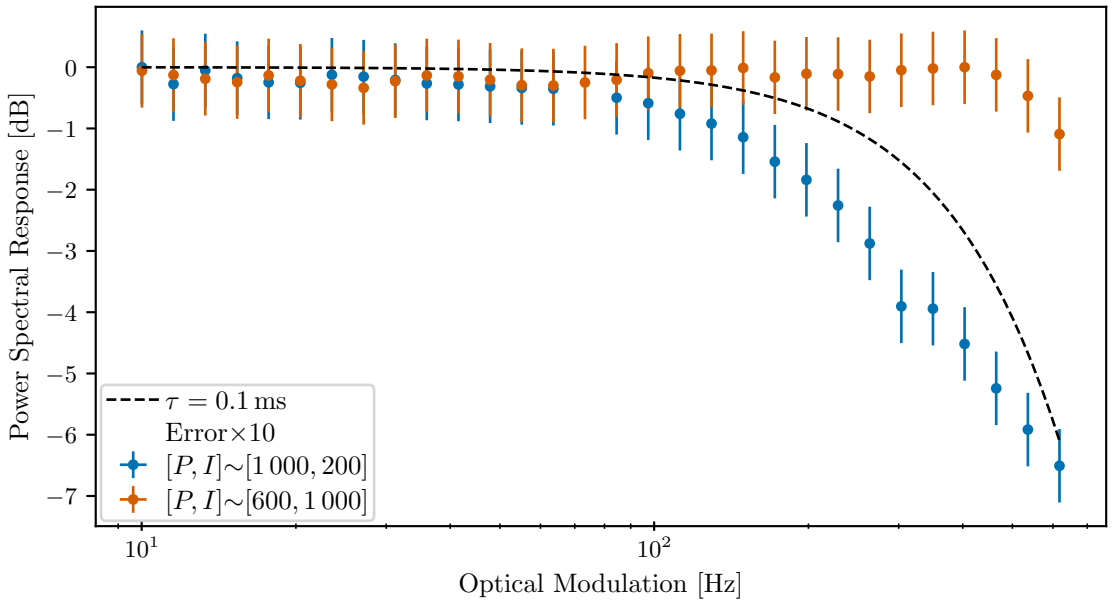


Figure 4.42: The central detector's frequency response measured using optical modulation from the FTS and a coherent source for two PID gain conditions. A nominal bolometer response model is shown as a dashed black line.

the detector response in its default configuration to be significantly less than the ∼1 500 Hz reported by the manufacturer (Table 6-2 QMC Instruments Bolometer System Manual). However, it should be noted that measurements of the TES response to the chopped optical signal of the photomixer (see Figure 4.13) show the TES thermometer itself to have a cutoff frequency of at least 13 000 Hz. The extremely fast response of the TES suggests that much faster detector speeds can be obtained through PID tuning and modifications to the timing of a detector measurement pulse.

While effective and elegant, measurements of the detector frequency response using the FTS do not hold the simplicity inherent in measurements of a source with a chopper wheel. Additionally, the photomixer power falls at a rate of ∼0.02 dB/GHz [129]. This limits optical modulation with sufficient SNR on the detectors to ∼600 Hz since the modulation frequency of light from the FTS depends on both the speed of the scanning mirror and the optical frequency of the source (see Equation 4.12). The photomixer source provides a sufficiently small beam to be chopped by a 6-hole chopper wheel allowing measurements

over frequencies of ∼8–800 Hz. The right panel of Figure 4.43 shows frequency response measurements of the central detector made with the chopped photomixer source compared to measurements with the FTS. Measurements of the chopped photomixer suffer from significant noise that can be attributed to the poor chopping of the photomixer beam by the six-hole chopper wheel (see Figure 4.44). Despite these discrepancies, measurements of this type are successful at approximating the cutoff frequency of the detector and can be used to efficiently determine the effects of different detector conditions and settings on its frequency response (see §3.3.1).

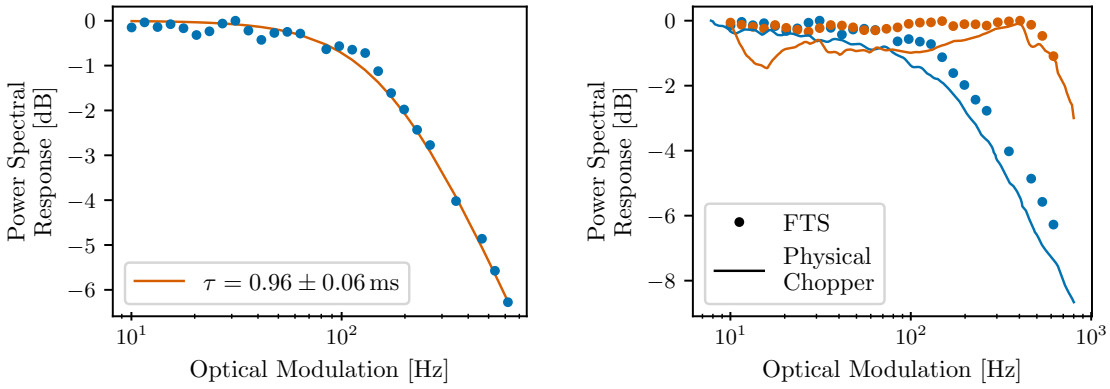


Figure 4.43: A detector response model fit to the frequency response of the central detector with default operational parameters measured with modulation from the FTS is shown in the left panel. The right panel shows measurements of the central detector's response made with the FTS and with the chopped photomixer source for both PID conditions shown in Figure 4.42.

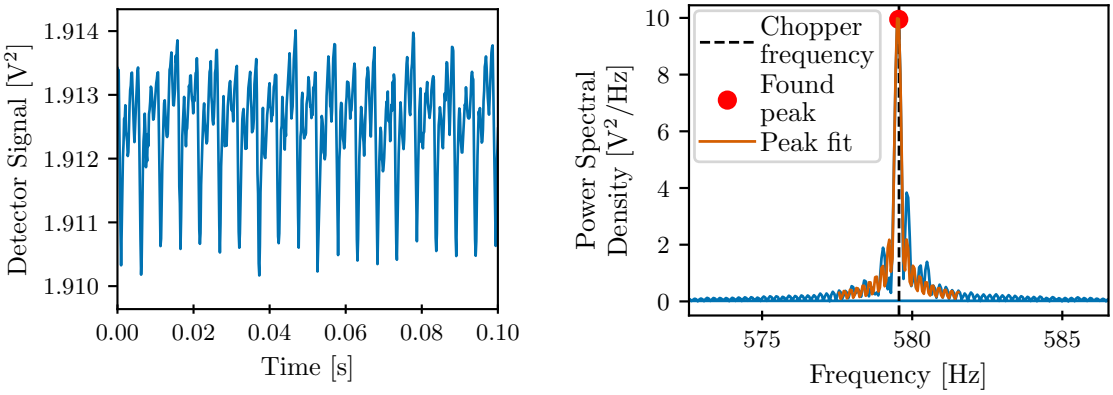


Figure 4.44: The central detector signal while viewing a photomixer source and a physical chopper (left) and the corresponding peak in its power spectrum (right).

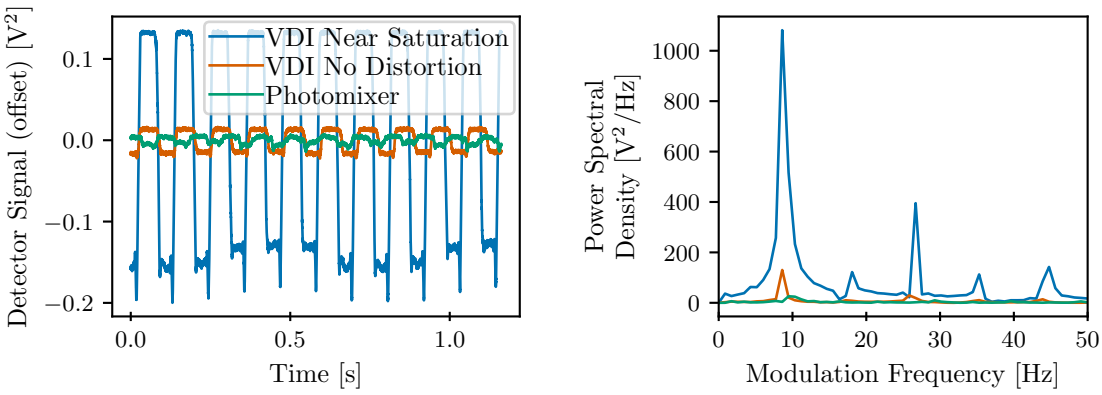


Figure 4.45: The central detector's signal while viewing a high-power VDI source as it nears detector saturation and the photomixer source are shown in the left panel. These have been modulated with a mechanical chopper. The spectral peak corresponding to the modulation frequency is shown for each case in the right panel.

4.3.2 Near-saturation response

To test the response of the detector under substantial optical loading, I have made use of a Virginia Diodes (VDI) Tx-163 custom frequency multiplier diode source with an internal attenuator that limits its output power (provided by Blue Sky Spectroscopy Inc., Lethbridge, Canada). The frequency response of the central detector was measured when the attenuator on the VDI source was tuned such that the detector signal was just below saturation ($\sim$17.8 mW source output at 320 GHz) and to a level at which distortion in the expected waveform was no longer seen when mechanically chopped at 20 Hz ($\sim$17 mW at 320 GHz). Figure 4.45 shows the chopped signal of the VDI source at both power settings compared to the signal obtained with the Toptica photomixer source and a mechanical chopper.

The results of response measurements approaching detector saturation are shown in Figure 4.46 where they are compared to the nominal response measured using optical modulation from the FTS. Measurements at high chopper frequencies showed significant deviations from the expected profile of the power spectral peak resulting in poor fits to the data (see the right panel of Figure 4.46). To compensate for poor fits of the spectral peak, the detector signal has been determined as the raw measured power spectral intensity integrated

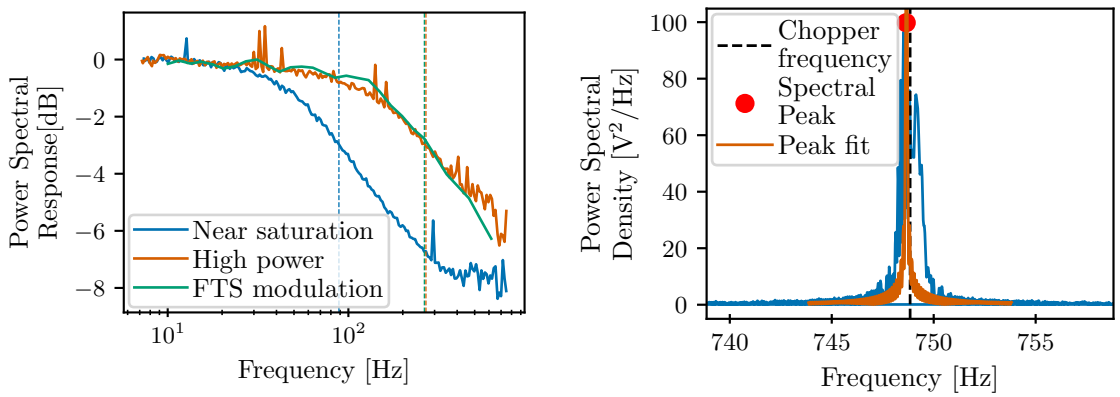


Figure 4.46: The response of the central detector to a high-power source and an optical chopper is shown in the left panel with the detector nearing saturation. These results are compared to nominal optical modulation from the FTS. The -3 dB cutoff frequency from each response measurement is marked by a dashed vertical line. The right panel shows the power spectral peak associated with the response measurement at 748 Hz at which the fit to the spectral peak is poor.

over a 10 Hz bandwidth centred on the chopper frequency. The -3 dB cutoff frequency when measuring the VDI source at a high power (but not approaching saturation) agrees with the -3 dB frequency under nominal optical loading within error (269 ± 3 Hz). Under an optical load that nears saturation, the detector remains linear in its response over a smaller bandwidth experiencing a -3 dB cutoff at 89 ± 3 Hz. Note that the -3 dB cutoff from the detector power spectral response (V^2), $f_{-3\,\mathrm{dB}}$ is not necessarily an equivalent measurement to the bolometer cutoff frequency, $f_{co} = 1/(2\pi\tau_e)$, determined by the fitted time constant in Equation 4.14.

The near-saturation behaviour of the TES bolometers under study differs from the typical behaviour of other bolometers and photodetectors. As a simple example, FTS measurements in which the modulation from the instrument exceeds the dynamic range of the detector results in a "clipping" of the interferogram (see Fulton et al. 2016 [83]). This effect is simulated on an interferogram measured by the Lethbridge DFI testbed (see Chapter 5) in Figure 4.47 and shows not only a loss of information but deleterious effects in the spectral domain (seen as the spectrum does not reduce to zero at the edges of the band nor in bands with significant atmospheric absorption). In addition, bolometers often experience

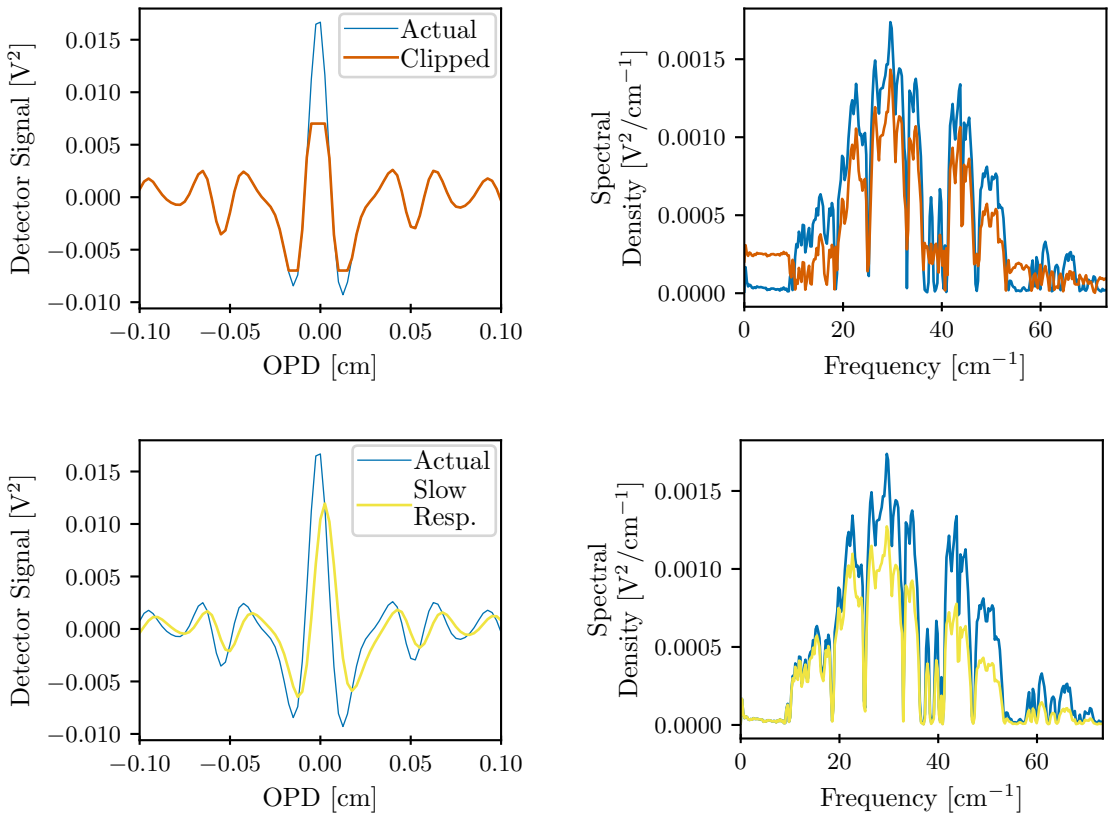


Figure 4.47: The top panels show the simulated effect of "clipping" an interferogram measured with the DFI as would be experienced by a typical photodetector reaching the limits of its dynamic range. This is shown in both the signal (left) and spectral (right) domains. The filtering effect of a feedback-controlled TES bolometer due to a slowing in its response as it approaches its dynamic range limits is shown in the bottom panels.

nonlinearity effects as they approach saturation (see Bendo et al., 2013 [148], Swinyard, et al., 2014 [149], and Fulton et al. 2016 [83]). On the other hand, the feedback-controlled TES detector array maintains linearity but experiences a slower response as optical loading nears saturation. As a result, the detector response behaves as a low-pass filter on the measured optical modulation from the FTS resulting in a loss of spectral information at higher spectral frequencies. This is shown in the bottom panels of Figure 4.47. This slowing of the detectors is significantly more subtle and must be considered when the detectors approach optical modulation equivalent to $\sim$0.3 V^2 (peak-to-peak).

4.3.3 Detector timing

In Section 4.1, I have explored the effects of the adjustable detector timing parameters on detector noise (taken to be the width of the distribution of the output signal). As detector speed plays an integral role in the efficacy of the detector array for a DFI instrument, I have conducted a similar characterisation of the detector timing parameter space with respect to detector frequency response.

The most significant timing parameter to affect detector response is the chosen pulse width as this parameter has the greatest effect in defining the time required for a single PID detector measurement to be made. Figure 4.48 shows the response of the central detector to optical modulation provided by the photomixer source and an optical chopper (as in Figure 4.44) at different pulse widths. Here, the detector signal at the respective chopper frequency is taken to be the integrated signal from a fit to the power spectral peak at the chopper frequency over a 4 Hz bandwidth. Noise in the signal is similarly defined as the integrated spectral density over the same frequency band once the fitted peak has been subtracted. Figure 4.48 demonstrates that the frequency of the -3 dB frequency knee (marked by the vertical dashed lines) decreases significantly with pulse width and suggests that pulse widths greater than 30 experience their cutoff at frequencies less than 10 Hz. A linear fit to the response curves from pulse widths of 30 and 40 loop counts (28.38 and 37.38 μs, respectively) give the power law roll-off as $f^{-\beta}$ where $\beta = 0.768 \pm 0.009$.

Section 4.1 also demonstrates that detector noise properties depend on the chosen pulse width. Figure 4.48 shows the SNR profile of the central detector as its pulse width is changed. A consistent profile (within noise) across the pulse widths examined is seen. Additionally, we see the decrease in SNR at frequencies less than 20 Hz which can be attributed in part to the $1/f$-noise dominant band of the detector (see Figure 4.41).

Measurements of the lower cutoff frequencies associated with pulse widths 30 and 40 required the use of modulation from the FTS as the chopper wheel does not reliably rotate at such low frequencies. For these measurements, the photomixer source was used at an op-

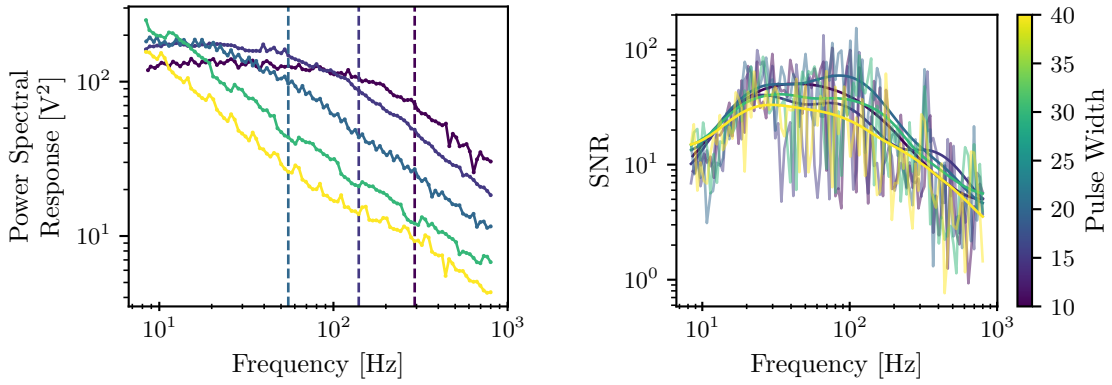


Figure 4.48: The signal (left) and SNR (right) response of the central detector to optical modulation at pulse widths of 10, 15, 20, 30, and 40 loop counts (i.e., increasing the time required for detector measurements). In the left panel, the -3 dB cutoff frequencies are marked by the vertical dashed line and in the right panel the darker curves show a 40-point Hann-smoothing of the data.

tical frequency of 400 GHz while the spectral stage moved at speeds ranging from 30 μm/s to 5.925 mm/s. It should be noted that the motion of the translation stage has not been well characterised at speeds lower than 300 μm/s [150]. Figure 4.49 shows frequency response measurements of the central detector at these lower frequencies. The cutoff frequencies at the measured pulse widths are summarised in Table 4.4. Detector pulse widths greater than 20 are not suitable for use with the DFI testbed as they do not provide sufficient detector speed to avoid noisy detector bands.

Table 4.4: The -3 dB cutoff frequency of the response curves at different detector pulse widths as shown in Figure 4.48.

Pulse Width [loop counts]	10	15	20	30	40
Pulse Width [μs]	11.06	14.88	19.38	28.38	37.38
$f_{-3\,\mathrm{dB}}$ [Hz]	290 ± 10	140 ± 5	55 ± 2	10 ± 3	6 ± 3

To preserve consistent detector response across a wide band of optical modulation frequencies, detector pulse widths should not exceed 15 loop counts. A collection of response curves corresponding to the central detector with different timing parameter settings (see §4.1.4) is shown in Figure 4.50. These curves correspond to the optimal set of timing parameters based upon output signal noise demonstrated in Figure 4.27. The vertical offset of

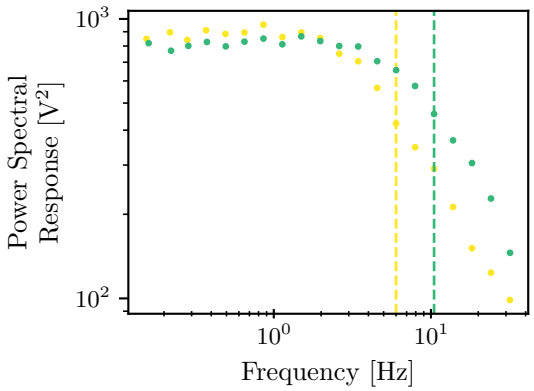


Figure 4.49: The response of the central detector to low-frequency optical modulation from the FTS with a pulse width of 30 (green) and 40 (yellow). As in Figure 4.48, the −3 dB cutoff of each response measurement is shown by the vertical line in the respective colour.

Table 4.5: The −3 dB cutoff corresponding to each frequency response measurement in Figure 4.50.

Pulse Width	Blanking Time	Read Index	$f_{-3\,\mathrm{dB}}$ [Hz]
10	4	9	266 ± 9
12	4	11	133 ± 5
14	4	13	101 ± 3
12	6	11	306 ± 11
14	6	13	145 ± 5
16	6	15	132 ± 8
14	8	13	253 ± 9
16	8	15	145 ± 5
18	8	17	110 ± 4

each curve corresponds to the time the heater remains active with lower blanking times experiencing a greater vertical offset. This matches the results in §4.1.4 as with a lower heater duty cycle, more heater power is required to maintain the detector's setpoint. In all cases, a spacing of 5 loop counts between the heater switch-off and read index results in a higher −3 dB cutoff frequency. The highest −3 dB cutoff frequency, ∼310 Hz, corresponds to a pulse width of 12 with a blanking time of 6 and a read index of 11. The −3 dB cutoff for each curve is summarised in Table 4.5. With the increased peak amplitude at the chopper frequency at shorter blanking times, a significant improvement in SNR is also seen.

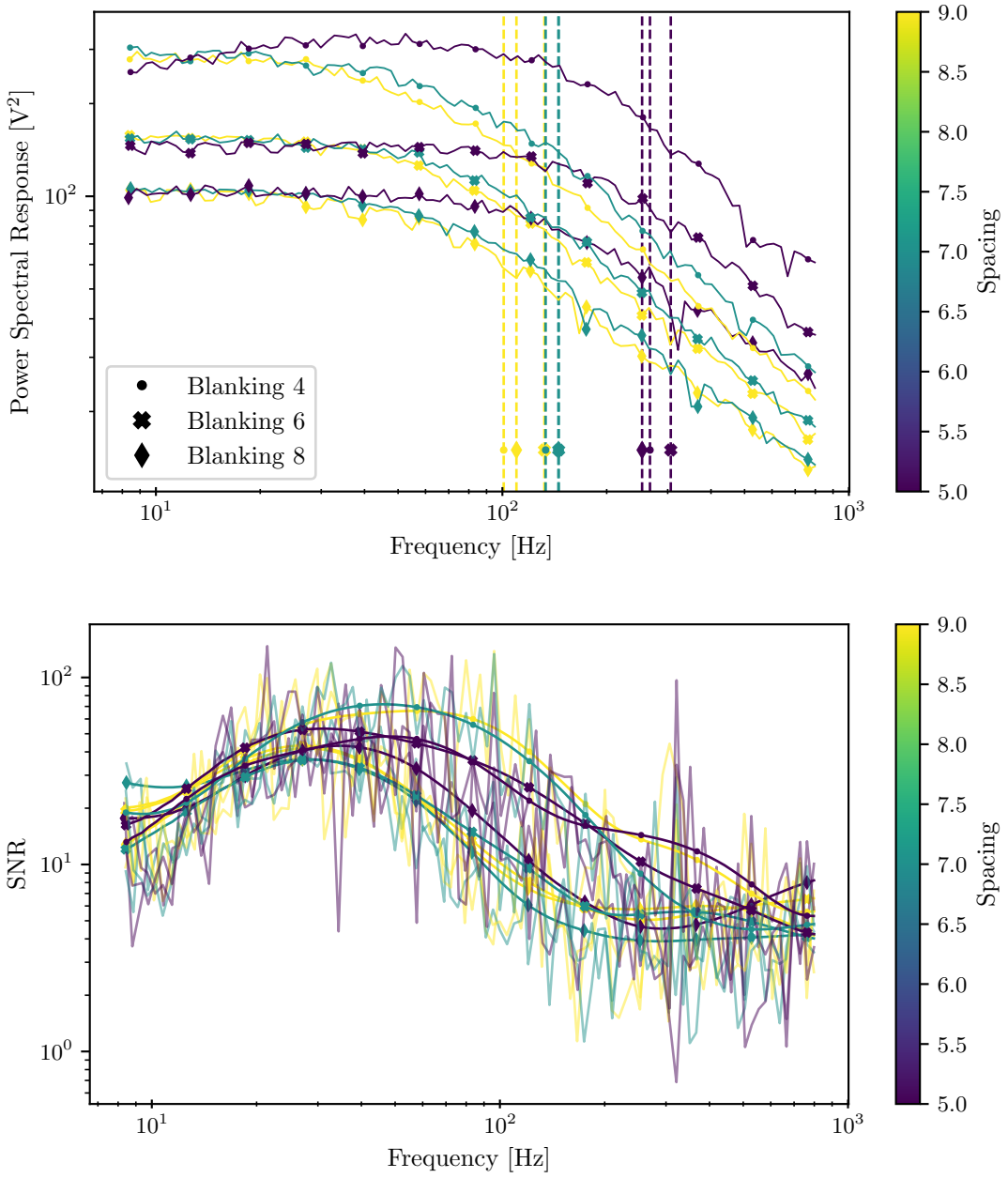


Figure 4.50: The frequency response of the central detector operating with a variety of detector timing parameters (top) and the associated SNR (bottom). As in Figure 4.48, the dashed vertical lines indicate the -3 dB frequency cutoff and darker curves indicate a 40-point Hann smoothing of a curve. Each curve is coloured by the number of loop counts between the heater switch-off and the read index while different markers indicate the blanking time. Each measurement was made with a pulse width one greater than the read index such that the read index is the last loop count of a measurement pulse. See §4.1.4 for additional details.

4.3.4 PID effects

Figures 4.32 and 4.42 have demonstrated that PID tuning can have a dramatic effect on the response of a detector and that the weight of the integral (I) term plays a dominant role in this. To study the effects of PID tuning on detector response, I have measured the central detector response under a variety of PID conditions using the photomixer and a physical chopper (see §4.3.1). Figure 4.51 shows a coarse exploration of the parameter space. The gain of the derivative (D) term is seen to have very little effect on the response of the detector while the gains of the proportional (P) term and the integral term can significantly alter the response of the detector. Of particular note, are two PID conditions in which the detector response deviates from linearity at lower frequencies (P:1 500, I:10, D:0, shown in the pink curve in the bottom panel of Figure 4.51) and prior to the high-frequency roll-off (P:0, I:500, D:0, shown by the yellow curve in the upper left panel of Figure 4.51). Additionally, increasing the weight of the integral term can increase the detector's -3 dB cutoff frequency to the limits of what can be effectively measured with current test equipment.

Figure 4.52 shows a summary of P-term and I-term tuning on the effective time constant of the central detector. I have obtained these through a least-squares fit of Equation 4.14 to the detector's response while viewing the photomixer source with a chopper. These demonstrate (as with Figure 4.51) that the I-gain has dominant control of detector response speed and that detector response speed is improved by a high weighting of the I term coupled with a low weighting of the P term. In all cases, an I-term gain of 10 data units results in a high uncertainty in the fitted detector time constant. This is a result of significant deviations from the expected response profile under these PID conditions. Figure 4.53 demonstrates the value of χ^2_{red} as a goodness of fit parameter throughout the explored parameter space which demonstrates poor fitting of the response profiles with an I-gain of 10 data units. For these cases, the -3 dB cutoff frequency (also shown in Figure 4.53) provides a better estimate of detector response speeds as it is less sensitive to abnormal response profiles.

In the images summarising the parameter space in Figures 4.52 and 4.53, particular con-

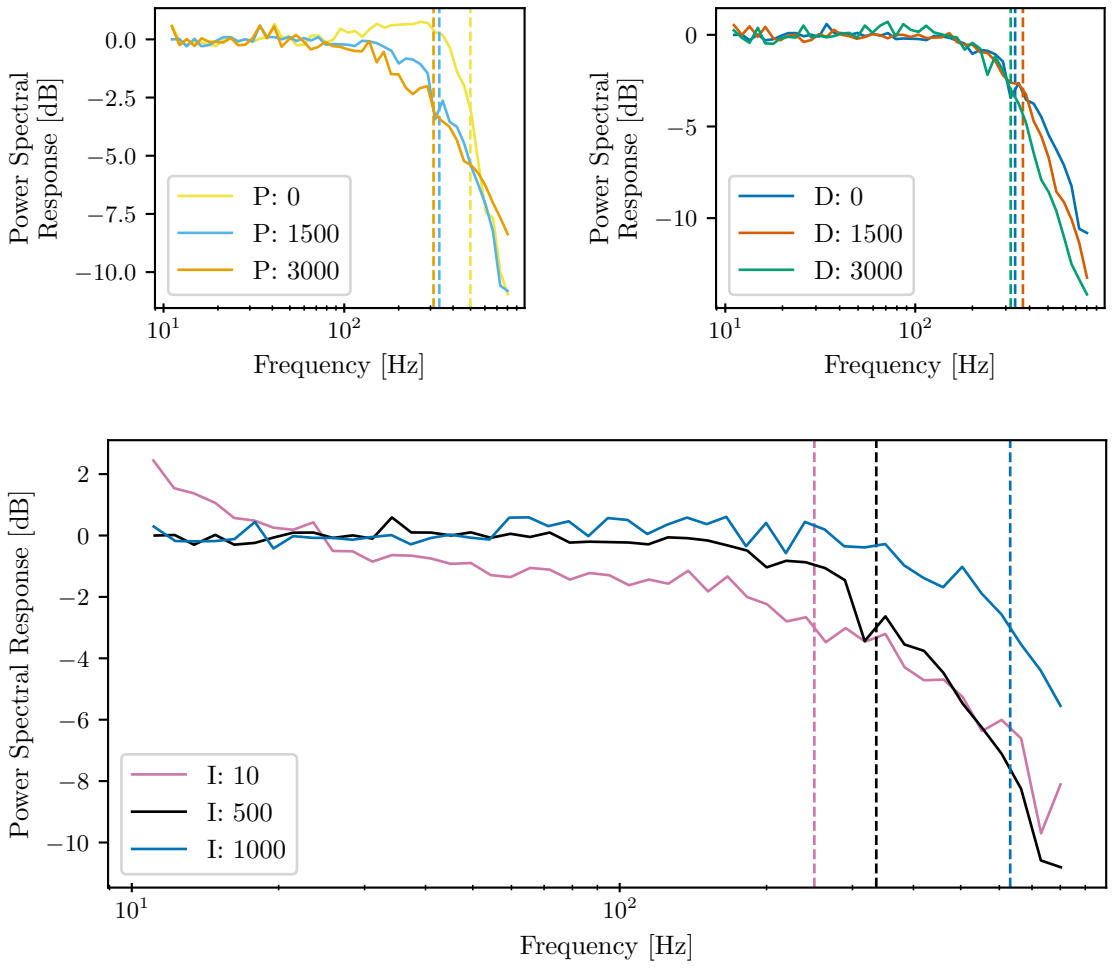


Figure 4.51: The response of the central detector to optical modulation from the chopped photomixer source in a variety of PID conditions. The top left panel shows the effects of changing proportional-term gain (P), and the top right panel demonstrates the same for derivative-term gains (D) as does the lower panel for integral-term gains (I). In each panel, the -3 dB cutoff frequency of each curve is shown by a dashed vertical line.

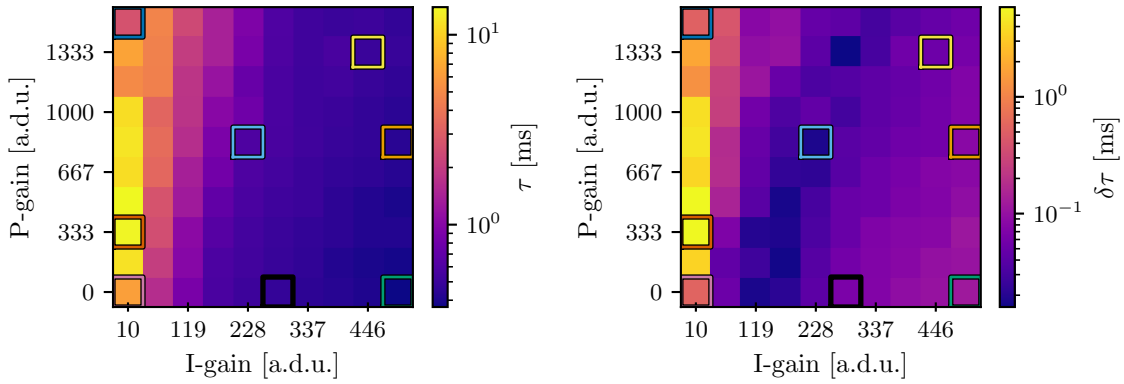


Figure 4.52: The effective time constant (left) and associated uncertainty (right) of the central detector under different P and I term weighting in its PID control. Each time constant value is determined from a least-squares fit to the response of the detector to a photomixer source that has been modulated with a chopper wheel. Cases of particular interest are outlined by a coloured square and their response profiles are shown in Figure 4.54.

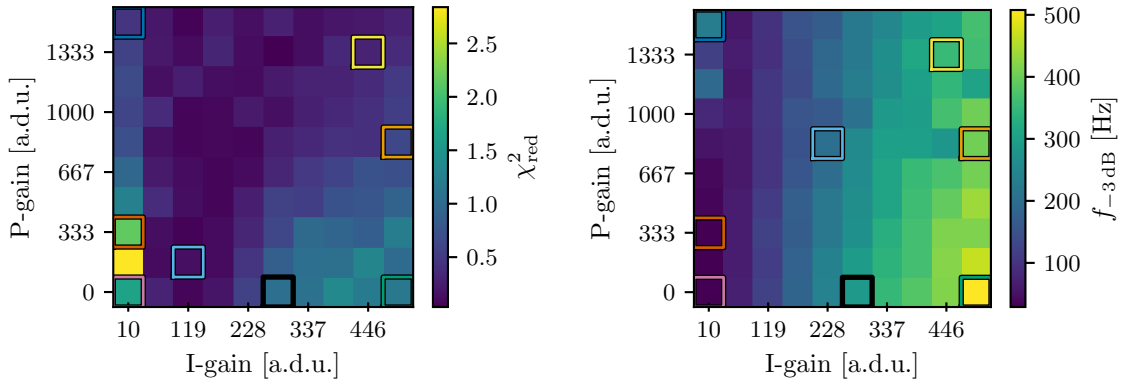


Figure 4.53: The value of χ^2_{red} as a goodness of fit metric for the time constant measurements of the central detector in Figure 4.52 is shown in the left panel. The right panel shows the -3 dB cutoff frequency associated with the response profile in each P and I gain condition. As in Figure 4.52, cases of interest have been emphasised and are shown in more detail in Figure 4.54.

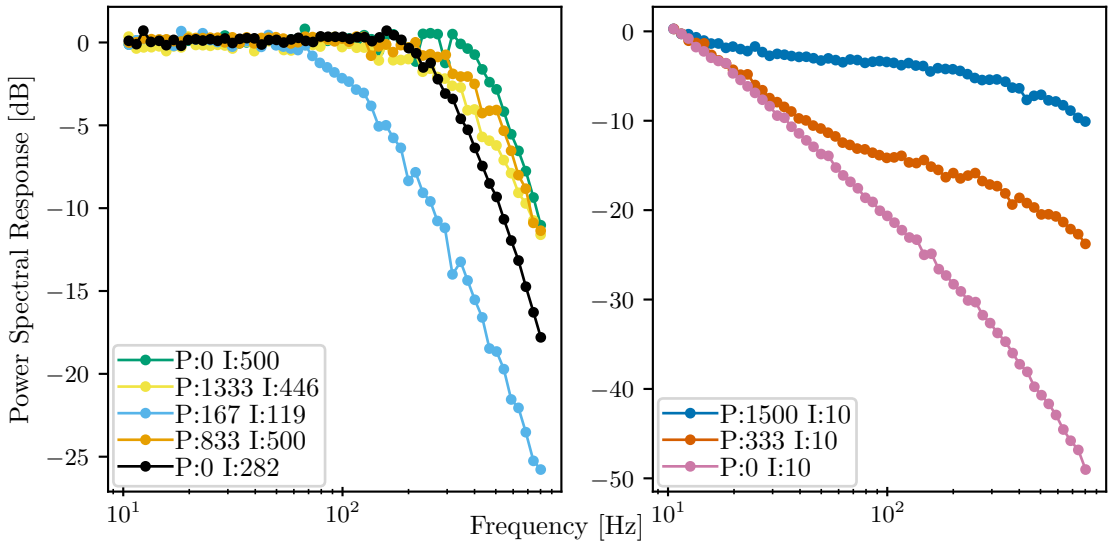


Figure 4.54: The response of the central detector corresponding to particular P and I gain conditions of interest denoted in Figures 4.52 and 4.53. Response measurements with an I gain of 10 show significant non-linearities prior to the high-frequency cutoff. These are shown in the right panel while more typical responses are shown in the left.

ditions of interest have been emphasised. The corresponding profiles to these are shown in Figure 4.54. I-term gains of 10 data units are shown to experience significant non-linearities at low frequencies suggesting that perhaps there is another -3 dB knee at lower frequencies than can be measured with the chopper. Such a low I-term weight is not suitable for effective detector operation. Additionally, response curves corresponding to no proportional control in the PID are shown to be effective. However, it should be noted that these profiles show a slight rise in their response as they approach the high-frequency cutoff.

I have shown in §4.1.6 that detector noise is also coupled with PID tuning. Figure 4.55 shows the SNR of the P and I gain parameter space explored throughout this section at the -3 dB cutoff frequency. This has been determined in a similar manner to §4.1.5 in which the spectral peak corresponding to the modulated optical load has been compared to noise in a similar frequency band. These results, in addition to §4.1.6 show that though the central detector sees faster response with a high weighting of the I term and a low weighting of the P term, this comes at a cost of poorer SNR.

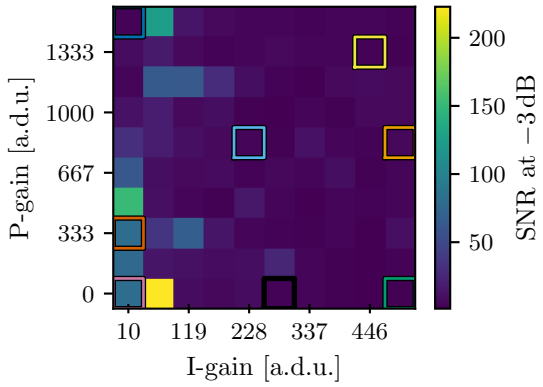


Figure 4.55: The SNR of the central detector signal while responding to the modulated optical load provided by the photomixer and chopper at the -3 dB cutoff frequency. These measurements are shown for the same parameter space explored in Figures 4.52–4.54. The measurements corresponding to each of the profiles in Figure 4.54 are marked in a similar fashion to the corresponding figures.

4.4 Conclusions

Throughout this chapter, I have detailed the general characterisation measurements of the detector array which have determined pathways for improved performance. I have measured the superconducting transition of the detector array and determined that it is most sensitive operating about $\sim$9 500 data units. Additionally, I have measured the dynamic thermal conductance of the central detector to be $0.22 \pm 0.01\,\mu$W/K. I have also presented measurements of the NEP of the detector array when operating under default parameters.

Both PID and detector timing parameters can be adjusted to change the noise performance and response speed of the detector array. I have found that operating the central detector with heater active for 6 loop counts (12.71 μs) or greater coupled with reading the TES state 5 loop counts (8.13 μs) after the heater switches off results in the best noise performance for the parameter space explored (resulting in improvement over the default parameters by a factor of $\sim$1.7). Additionally, I have found that operating the central detector with a pulse width of 12 loop counts (12.86 μs), a blanking time of 6 loop counts (3.73% multiplexed duty cycle), and a 5 loop count delay (8.13 μs) between the heater switch-off and TES state reading results in the fastest detector response for the parameter space I have

explored ($f_{-3\text{db}} = 306 \pm 11$ Hz).

The PID tuning of the detector array has been shown to be most sensitive to the integral term gain. Through PID tuning, I have modified the time constant of the central detector through 0.4 ± 0.1–14 ± 6 ms. Though improved noise performance is achieved with relatively passive PID control (up to a factor of $\sim$3 improvement over default parameters), fast detector response speed requires a high weighting of the integral term. Additionally, I have shown that under a significant optical load that nears the saturation point of the central detector, linear response is preserved (albeit over a much smaller electrical frequency band).

Optimisation of the detector array for a particular use case requires a balance of speed and sensitivity. The PID optimisation of the detector array for use in the DFI testbed requires the detector response to be tuned such that optical modulation from DFI occurs outside low-frequency dominated regions of the detectors' electrical frequency band while maintaining adequate sampling rates to measure optical modulation from the testbed. In Chapter 5, I determine an optimal set of detector parameters to improve the performance of the central detector as an integrated component of the DFI testbed.

Chapter 5

Performance of the Double Fourier Interferometer and Detector Assembly

> We have peered into a new world and have seen that it is more mysterious and more complex than we had imagined. Still more mysteries of the universe remain hidden. Their discovery awaits the adventurous scientists of the future. I like it this way.
>
> –Vera Rubin (1928–2016) [151]

The spectral and temporal capabilities of the feedback-controlled Transition Edge Sensor (TES) bolometer array require careful consideration to effectively incorporate the system as the detector array of the Lethbridge Double Fourier Interferometery (DFI) testbed. Through this chapter, I examine spectral measurements of the testbed beamsplitters and the detector system as an integrated part of the assembly. I have used these measurements to determine that the spectral performance of the interferometer would be improved with a change to the angle of incidence of the beamsplitters in the optical path of the testbed. Using a calibrated blackbody source, I have determined a calibration Relative Spectral Response Function (RSRF) that spectrally profiles the central detector of the array as an integrated part of the interferometer. As in Chapter 4, much of my investigations throughout this chapter focus on the performance of the central detector. Extending this analysis to optimise the performance of the other detectors in the array is discussed in §6.2.1. Though the central detector is the primary focus, the measurements in this chapter were made with the detector system operating in its multiplex mode as this is the intended operational mode of the detector system as an integrated component of the DFI assembly. Informed by my inves-

tigation of the detector system in Chapter 4 I have determined a set of optimised detector parameters which I have shown to reduce spectral noise in measurements made with the DFI testbed by as much as 79% (i.e., reducing spectral Noise Equivalent Power (NEP) by a factor of 4.8 or to 21% the value of its noise while operating with default parameters) for the central detector. I have also provided a discussion of spectral measurement techniques of the testbed and phase correction.

5.1 The DFI testbed as a spectrum analyser

To further optimise and test the performance of the detector array as an integrated component of the DFI testbed, I have made use of the testbed operating as a nominal single-Fourier Transform Spectrometer (FTS) to spectrally characterise the full assembly. These measurements have provided important insights into the optimal detector time constants to effectively sample DFI interferograms and determine the calibration of the detector array necessary to relate detector signals to optical units. I will refer to the DFI testbed operating as a single-FTS as "the FTS".

As many of the optical measurements within this chapter I discuss in this section are spectral, it becomes important to note a distinct difference between *signal* frequency bands and *spectral* frequency bands. As I have discussed in Chapter 2, spectral measurements made with an FTS are the result of a Fourier transform of detector measurements sampled in Optical Path Difference (OPD) giving a spectrum in *optical* frequency space. Also, these are determined from detector measurements that are sampled in time and can also be thought of with respect to an *electrical* power spectral density which is the Fourier transform of detector measurements which have been sampled in time. This relationship is shown explicitly in Equation 4.12. I refer to the frequency axis of measurements in the context of *optical* frequency as *spectral/optical* frequencies and the frequency axis of measurements in the context of the temporal sampling of the detector system as *signal/temporal* frequencies. It is also worth reiterating here that wavenumbers [cm^{-1}] provide a natural op-

tical frequency unit for FTS measurements.

As a broadband blackbody source for the FTS, I have made use of a calibrated Pegasus RS422 Pyrometer calibration unit that is capable of reaching temperatures up to 1 200°C (see Figure 5.1). This source has an exit aperture with a diameter of $\sim$20 mm and can be used to obtain spectral measurements with the FTS that have a high Signal-to-Noise Ratio (SNR). Though the source is effective, operating it at its maximum temperature for long time periods ($>$10 hours) without the secondary ceramic piece has resulted in multiple failures in the heating element coiled around the cavity. Due to these failures, we replaced the heating element late into my studies and the calibration of the blackbody has not been fully verified since the replacement. All measurements made with this blackbody source in this chapter occurred prior to the repairs unless otherwise specified.

5.1.1 FTS modes of measurement

Interferograms from an FTS can be measured using one of two techniques: Step-and-Integrate (S&I), and Rapid Scan (RS). In the S&I method, precise amounts of OPD are stepped through (i.e., the spectral arm is stepped some set distance) waiting for a prescribed integration time at each step. To increase the SNR of the measurement, longer periods of time are waited at each step. S&I measurements are susceptible to low-frequency noise and it is common to use a mechanical optical chopper coupled with a lock-in amplifier to remove the majority of the noise from the measured signal [81, 152]. RS FTS measurements consist of scanning the desired OPD range at a constant velocity. Through multiple RSs, several interferograms are obtained that can be averaged together either in the interferogram domain or spectral domain to increase SNR. With this method, optical modulation from the FTS can be naturally chosen to occur outside of the low signal frequency bands which are often noise-dominated.

In §4.2, I have shown that detector system is dominated by $1/f$-noise at signal frequencies less than 5 Hz. This makes them unsuited for S&I FTS measurements without an

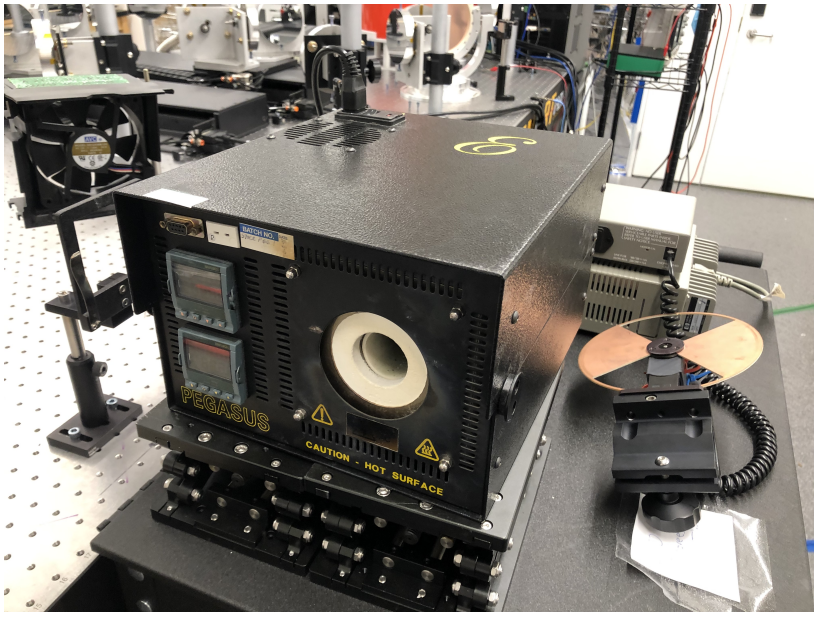


Figure 5.1: The high-temperature blackbody used as a broadband source for the FTS. A secondary ceramic piece can be inserted into the front of the cavity reducing the exit aperture from 40 mm to 20 mm and improving thermalisation. FTS measurements and calibration of the blackbody were performed with this secondary ceramic piece in place.

arrangement similar to a lock-in amplifier. Figure 5.2 shows three example interferogram measurements from the FTS using the S&I technique without any external modulation from a mechanical chopper. These measurements were obtained from ∼1 600 steps of stage motion (a total of ∼4 cm of OPD) each with 7 300 (0.56 seconds), 7 600 (0.59 seconds), and 9 400 (0.72 seconds) detector samples of integration while viewing a blackbody source at a temperature of 1 200°C. The central burst of the interferogram is apparent in each case; however, low-frequency noise has caused drifts in the detector signal that are a factor of ∼4 lower amplitude than the central burst. These drifts are measured as low-frequency (signal) modulation in the interferogram. Both the 0.56 s/step and 0.72 s/step interferograms shown in Figure 5.2 show modulation with a period of ∼150 seconds which may indicate that the Proportional-Integral-Derivative (PID) controller used to maintain the blackbody source temperature may in part contribute to these low-frequency drifts.

Low-frequency (signal) drifts in the interferogram can be associated with the portion of the interferogram that has spectral frequency components lower than 150 GHz. Since

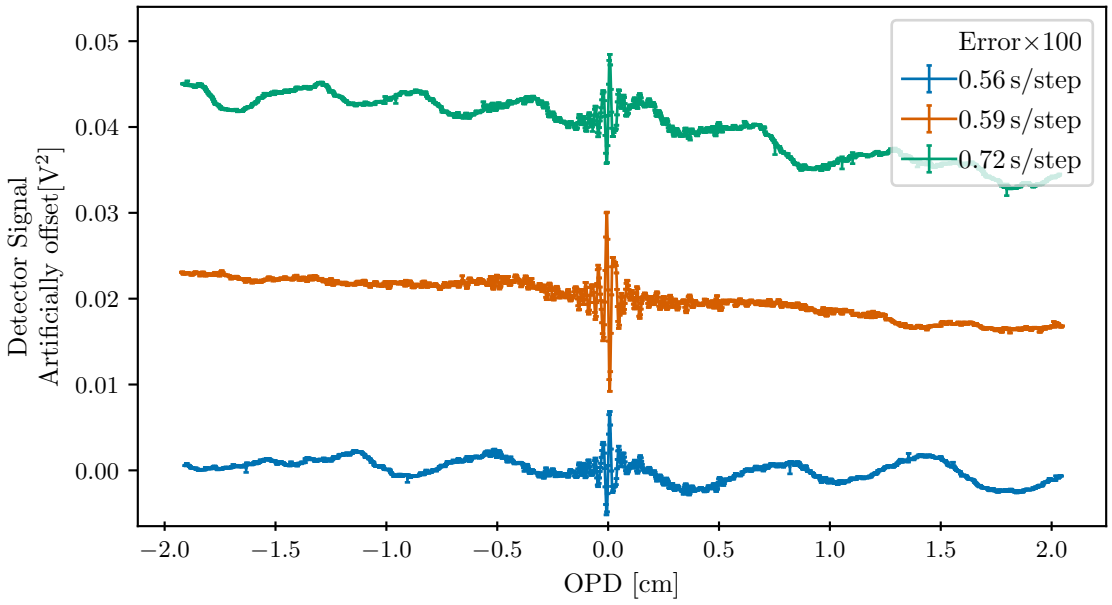


Figure 5.2: Three interferograms corresponding to a blackbody at 1 200°C measured from the FTS using the central detector and the S&I technique. Each interferogram has been artificially offset for visual clarity. Error bars (which have been exaggerated by a factor of 100) show the standard deviation of the detector signal while integrating at each step.

the low-frequency limit of the spectral bandpass to the detector is 250 GHz (see §5.3), all signals with spectral frequency components less than 150 GHz can be assumed to contain no spectral content from the source. A boxcar filter with this frequency cutoff allows for the separation and removal of these unwanted components. These contributions, $V^2_{\text{low}}(z)$, are determined as,

$$V^2_{\text{low}}(z) = \mathcal{F}^{-1}\{\mathcal{F}[V^2(z)_{\text{measured}}]^{\nu=150}_{\nu=0}\} \quad [\text{V}^2], \tag{5.1}$$

where $\mathcal{F}$ is the Fourier transform operator (see Chapter 2) and $V^2_{\text{meas}}(z)$ is the S&I interferogram measurement. Removal of these unwanted low frequency signal drifts is simply performed,

$$V^2_{\text{corrected}}(z) = V^2_{\text{meas}}(z) - V^2_{\text{low}}(z) \quad [\text{V}^2]. \tag{5.2}$$

Note that this correction for low-frequency drifts in the interferogram modulation signal is

similar to the baseline correction used for processing RS interferograms measured with the Spectral and Photometric Imaging Receiver (SPIRE) FTS (see Fulton et al., 2016 [83]).

Figure 5.3 shows the successful low-frequency correction of the S&I interferogram in Figure 5.2 (blue). The spectrum from the corrected S&I measurement is compared against an RS measurement with equivalent bandwidth, spectral resolution, and integration time ($\sim$800 scans at a speed of 10 mm/s, see §5.1.2 and §5.3). Though I have successfully removed low-frequency modulation from the S&I interferogram, there is still significantly more noise at the low-frequency end of the FTS spectral band (optical). Additional differences in the spectra are a consequence of filtering from the detector time constant (see §5.3), changes in the atmospheric environment of the laboratory between the times of observation, and deleterious effects from the low frequency removal at the edges of the interferogram (see the top panel of Figure 5.3).

Without the use of external optical modulation, S&I spectral measurements with the DFI testbed operating as an FTS are successful. This said, due to increased noise at the low-frequency end of the spectral band that cannot be easily removed, the testbed is better suited for RS spectral measurements (as anticipated from noise measurements of the detector array), experiencing 85% less root-mean-square spectral noise at the low-frequency edge of the spectral bandpass. The possible utility of S&I measurements with the DFI testbed are further considered in §6.2.6.

5.1.2 Processing rapid-scan interferograms

To obtain a suitable SNR, RS measurements made with the DFI can often exceed more than 1 000 scans of the spectral arm of the interferometer making it impractical to perform the analysis of an entire hours-long time stream of detector data using a computer with 16–32 GB of Random Access Memory (RAM). Here I will discuss how RS measurements from the FTS are processed and averaged.

The motion of the Aerotech stage can be accurately determined from its internal Pulse

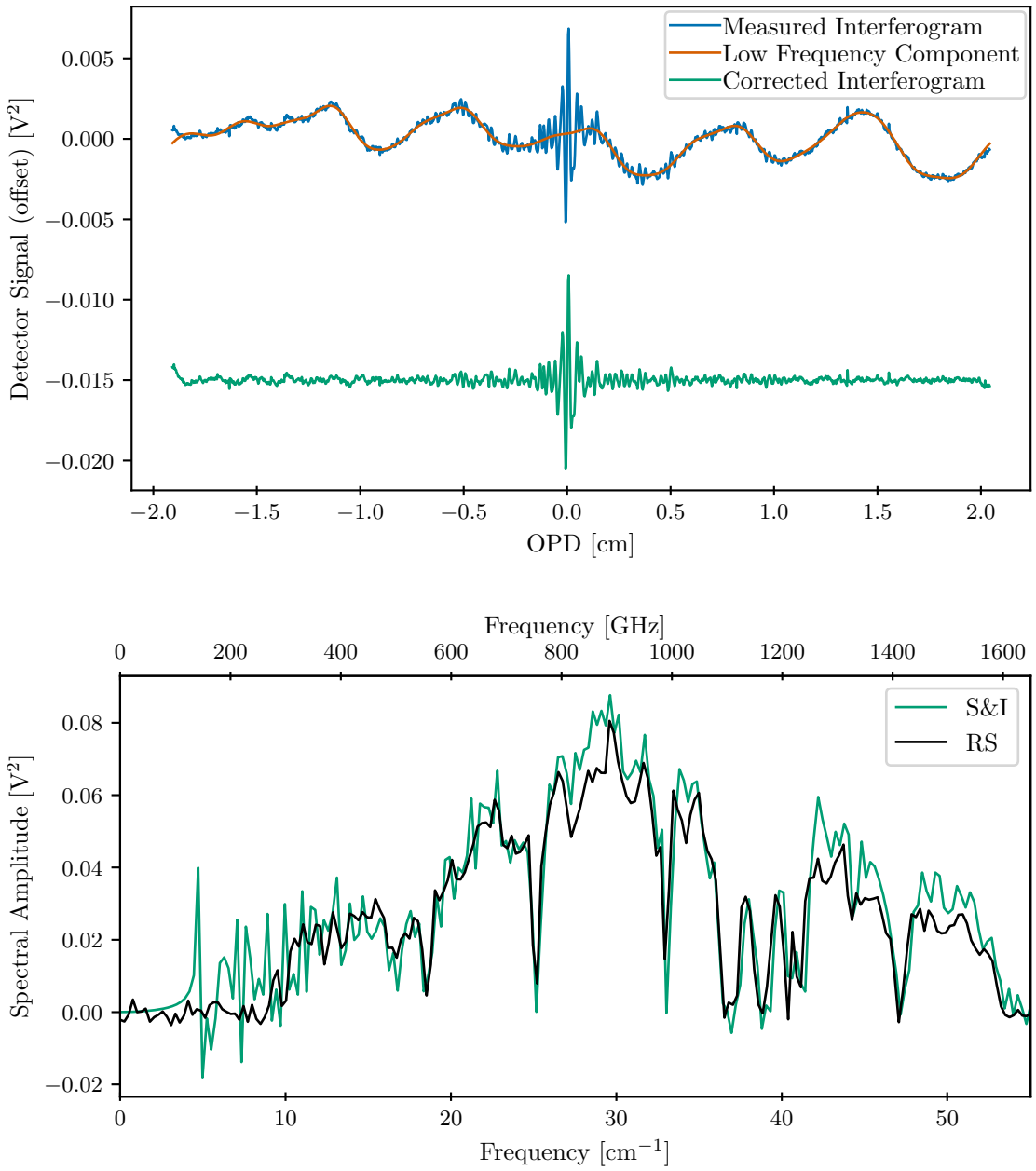


Figure 5.3: The low-frequency correction of an S&I interferogram presented in Figure 5.2 (blue) and the corresponding spectrum. The S&I measured spectrum is compared to a spectrum obtained through an RS measurement with equivalent integration time. Both spectra have been phase corrected (see Chapter 2 and §5.2.2). Note the significant atmospheric absorption features at 554, 755, 989, 1 106, 1 166, 1 228, and 1 414 GHz (see §5.3).

Synchronized Output (PSO), which is used to send triggering pulses to the detector array. These are recorded in the trigger state metadata bit of detector time streams [150]. For each scan, the start position of the stage is queried and recorded before the motion begins as is the end position. Nominally the PSO signal is set to pulse every 6.25 μm of stage travel (25 μm OPD). Once the detector timeline has been separated into scans of the spectral stage (based upon the PSO triggering pulses), each scan's detector timeline is truncated, removing 1 120 PSO pulses-worth of detector samples from either end of the scan (corresponding to 7 mm) to account for the acceleration of the stage at the start and end of a scan (see Weiler, 2016 [150]).

A common stage position vector, $\overline{z}_{\text{mech}}$, is established as linearly spaced values between the average scan start and end positions with the 7 mm acceleration windows subtracted. The number of positional samples is then determined as

$$\overline{n}_{z_{\text{mech}}} = \frac{\overline{L} - 2w}{\Delta z_{\text{PSO}}}, \tag{5.3}$$

where $\overline{L}$ is the average scan length, w is the 7 mm acceleration window, and Δz_{PSO} is the PSO pulse distance. The motion of the stage for the majority of the scan (i.e., between the acceleration windows) is assumed to be linear [150] and the positional vector corresponding to the detector timeline for an individual scan, $z_{\text{det},n}$, is determined as a linear sampling of the interval $[Z_{\text{start},n} + w, Z_{\text{end},n} - w]$, where $Z_{\text{start},n}$ and $Z_{\text{end},n}$ are the recorded start and end positions of that scan, respectively. Note that for reverse scans, w is negative and the ordering of both $z_{\text{det},n}$ and the detector timeline is reversed. As the steady-state offset of the interferogram does not contain any spectral information, it is taken to be the median value of the interferogram and subtracted. As full measurement pulses to obtain output from the detector system sample at 12.91 kHz (under default operational conditions, see Chapter 4) and the effective time constant of the central detector is 0.96 ms (corresponding to 12 detector samples), the interferogram from a single scan is first smoothed by a corresponding low-pass filter. This filtered interferogram signal is matched to the common positional vec-

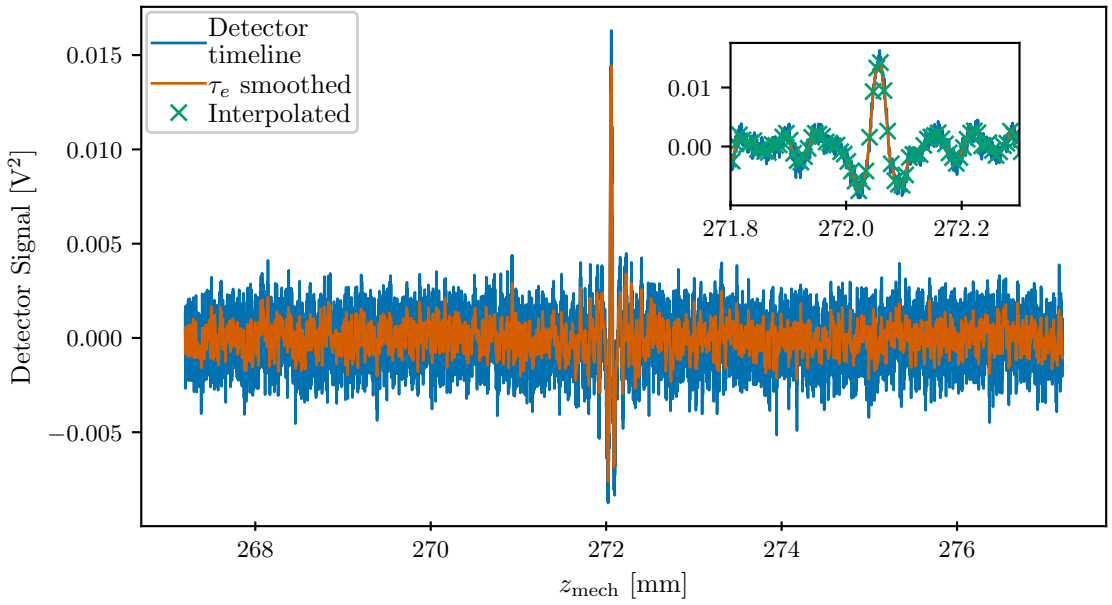


Figure 5.4: The interpolation of a single interferogram measured by the central detector for RS averaging.

tor $\bar{z}_{\mathrm{mech}}$ through a cubic spline interpolation. The interpolated detector timelines for each scan are averaged with all other scans having the same direction of stage travel to obtain an average forward interferogram and an average reverse interferogram. It should be noted that this sampling of the detector timeline limits the spectral Nyquist frequency of FTS observations to 6 THz (optical frequency). The interpolation process of an interferogram from a single scan is shown in Figure 5.4.

Figure 5.5 shows the distribution of the central Zero Path Difference (ZPD) fringe locations of interferograms measured by the central detector from 3 000 scans of the spectral stage (1 500 forward, 1 500 reverse) while viewing a blackbody source at 1 200°C. The fringe locations are given as positional values from the spectral stage prior to and after the interferograms have been interpolated onto a common positional vector. While scanning at 7 mm/s, detectors are read out every 0.54 μm corresponding to the binwidth of the first histogram. The bin size of the second histogram matches the sampling of the common positional axis determined from the PSO setting of 6.25 μm. The distribution of central fringe positions is within the positional accuracy of the stage at these speeds ($\sim$10 μm) [150]. Ad-

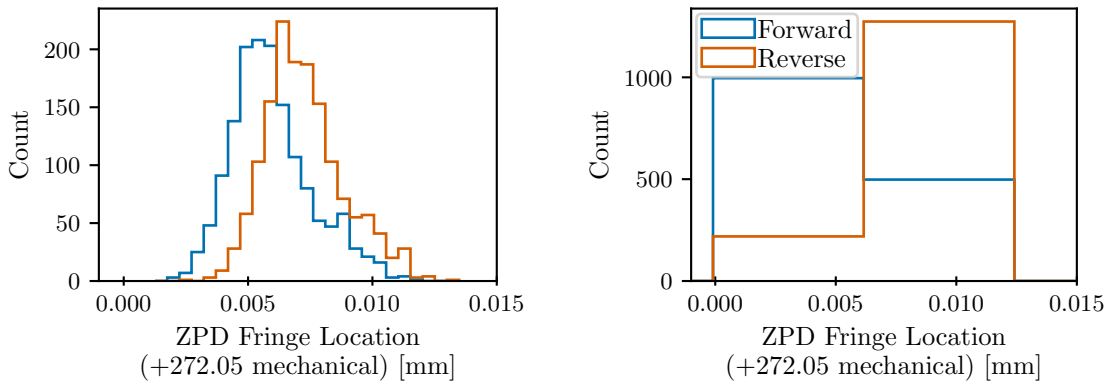


Figure 5.5: The location of the ZPD fringe throughout 3 000 bidirectional scans of the FTS before (left) and after (right) the positional axis of each scan has been interpolated to a common positional vector. Positions are given as the mechanical position on the translation stage.

ditionally, interferograms are repeatable across scans to within rounding error of the PSO defined positional axis and can be effectively averaged together to improve SNR.

To further improve averaging performance by compensating for sampling differences between scans, each scan can be corrected for the resultant linear phase term before interpolation and averaging (see §2.1.4). The correction is applied by estimating the closest sample to ZPD and taking a symmetric Fourier transform about that point (taken to be the maximum value for symmetric interferograms, or the middle sample between the positive and negative peaks for antisymmetric interferograms, see §5.2.2). A linear fit to the phase is obtained within the FTS frequency band (weighted by the spectral intensity; see Figure 5.6) and then the phase term is transformed back to the OPD domain to obtain a linear phase correction function. This function is then convolved with the interferogram [71, 83, 153]. After the linear phase correction, the interferogram is averaged in the usual way.

An example interferogram and spectrum measured by the central detector during a RS observation of a 950°C blackbody with the FTS are shown in Figure 5.7. Here, a single scan of the FTS is compared to the average of 1 500 forward scans of the FTS. As the beamsplitters employed by the FTS have significant phase effects, I will provide a full discussion of phase correcting the data in §5.2.2. Reverse scans of the FTS are discussed

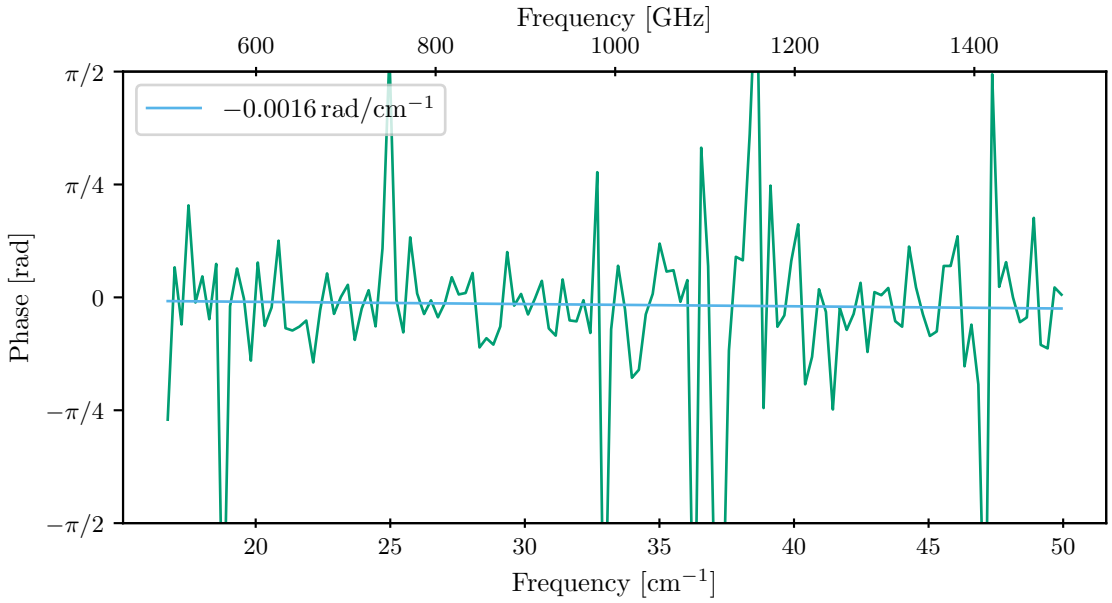


Figure 5.6: A linear fit to the phase measured with a single scan of the FTS.

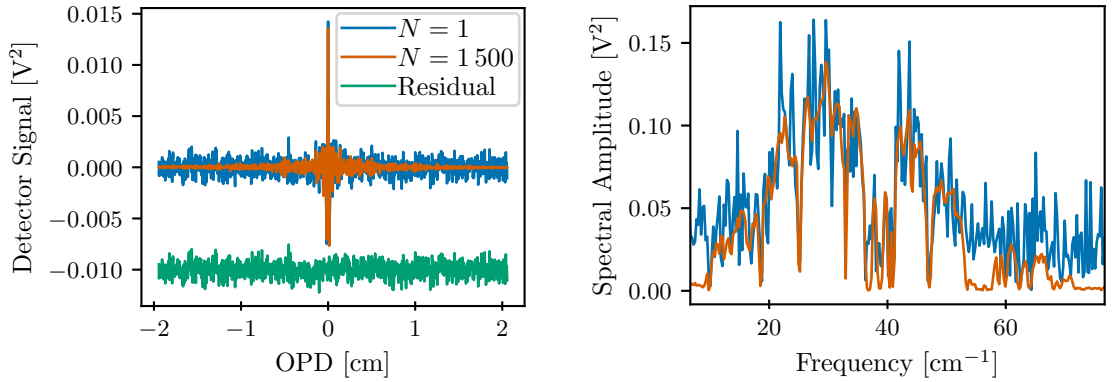


Figure 5.7: An interferogram from a single scan of the FTS and the average interferogram from 1 500 scans while viewing a 950°C blackbody source are shown in the left panel. The right panel shows the corresponding spectra. As in Figure 5.3, there is significant spectral attenuation from the atmospheric environment of the laboratory.

in §6.2.5.

5.2 Beamsplitter performance

The nominal beamsplitters employed in the interferometer are inductive-capacitive metal-mesh non-polarising intensity beam dividers designed by QMC Instruments that are similar to those employed by the *Herschel* SPIRE FTS [76, 146, 154]. To spectrally characterise the detector array as an integrated part of the DFI testbed, the spectral filtering from the beamsplitters must be determined.

5.2.1 Spectral bandpass

To measure bandpass and efficiency of the beamsplitters, I made use of a commercial Toptica TERASCAN continuous wave photomixer source with its accompanying receiver (see Figure 5.8) [129, 130, 131, 132, 133]. Through the permutations of 3 wavelength-tunable $\sim$1 550 nm Infrared (IR) laser sources incident on the photomixer antenna, transmission spectroscopy from 50 to 3 300 GHz over three bands is possible. The photomixer receiver measures the photocurrent induced by the incident electric field from the terahertz radiation which gives the terahertz spectrum as the envelope of the photocurrent beat frequency as the difference frequency between the two input lasers is scanned. It should be noted that the photomixer power falls at a rate of $\sim$0.02 dB/GHz [129].

To measure the transmission of the beamsplitter, first I obtained a spectrum of the background laboratory environment without a beamsplitter in the optical path which I then compared to a spectrum taken with the beamsplitter inserted. The beamsplitter transmission spectrum is then determined,

$$S_{\mathrm{BS,trans}}(\nu) = \frac{S_{\mathrm{BS,background}}(\nu)}{S_{\mathrm{background}}(\nu)}. \tag{5.4}$$

As the photocurrent is a measure of the electric field, the frequency-dependant transmission

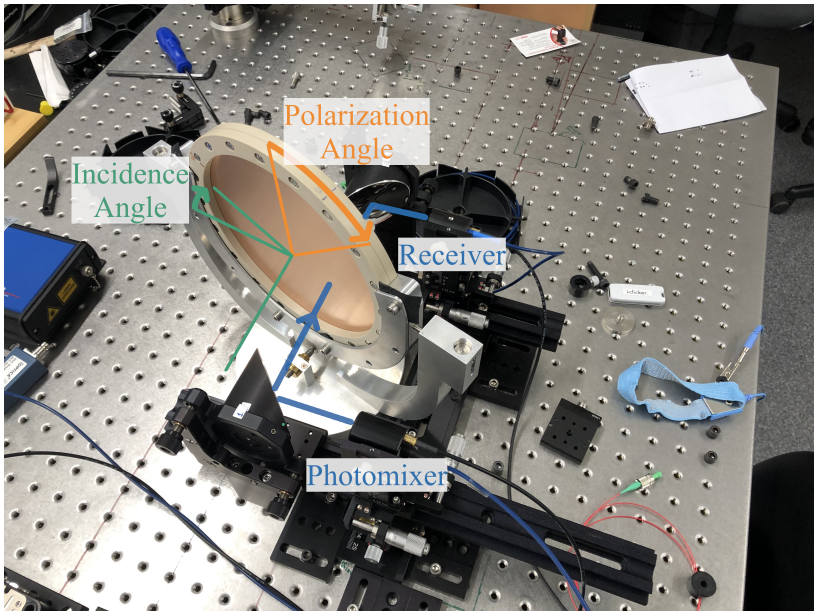


Figure 5.8: The arrangement of the Toptica photomixer and receiver for measuring beamsplitter transmission spectra. The angle of the beamsplitter with respect to the polarisation of the source is determined by the rotation about the optical axis while the angle of incidence is given by the rotation of the beamsplitter surface about the vertical axis.

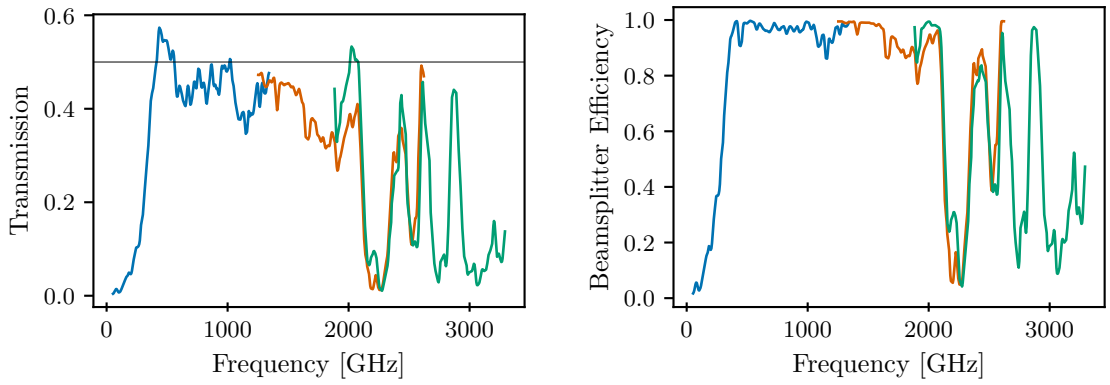


Figure 5.9: The transmission (left) and efficiency (right, see Equation 5.5) spectra of the beamsplitter at 45° of incidence over all three photomixer bands. Each band is separated by colour.

coefficient is determined as,

$$T(\nu) = S^2_{\mathrm{BS,trans}}(\nu) \tag{5.5}$$

This experimental arrangement is shown in Figure 5.8. The transmission spectrum and associated efficiency of the beamsplitter at an angle of 45° to incidence is shown in Figure 5.9. The photomixer-receiver combination only measures the transmission spectrum of the beamsplitter in this arrangement and since beamsplitter absorption is expected to be small, beamsplitter efficiency is approximated as,

$$\eta_{\mathrm{BS}}(\nu) = 4T(\nu)[1 - T(\nu)]. \tag{5.6}$$

Note that for an ideal beamsplitter $T(\nu) = 0.5$ and Equation 5.6 would give a value of one. The beamsplitter experiences a sharp cut-on at 380 GHz and a cut-off at 2 100 GHz. At higher frequencies than the cut-off, transmission does not fully reach zero, but is significantly attenuated. Additionally, there are some narrow features in which near-full beamsplitter efficiency is recovered. Also of particular note are the losses of efficiency at 1 150 GHz and 1 850 GHz.

I further studied the effectiveness of the beamsplitters at different angles of incidence and different angles with respect to the source polarisation with this arrangement. The DFI testbed makes use of the beamsplitters in the optical path at a 45° incidence angle. However, the beamsplitters (being similar to those employed by the SPIRE FTS) are designed for optimal performance at an incidence angle of 22° [155, 156, 157]. The photomixer source is linearly polarised along the vertical axis of Figure 5.8 allowing for transmission measurements with the beamsplitters at perpendicular polarisation orientations. I measured the transmission of a terahertz beamsplitter with the outer layer of the beamsplitter appearing to run parallel to the polarisation of the photomixer and after I had rotated the beamsplitter 90° from its initial orientation with respect to the source polarisation. I refer to these two polarisation orientations as parallel and perpendicular, respectively. The performance of

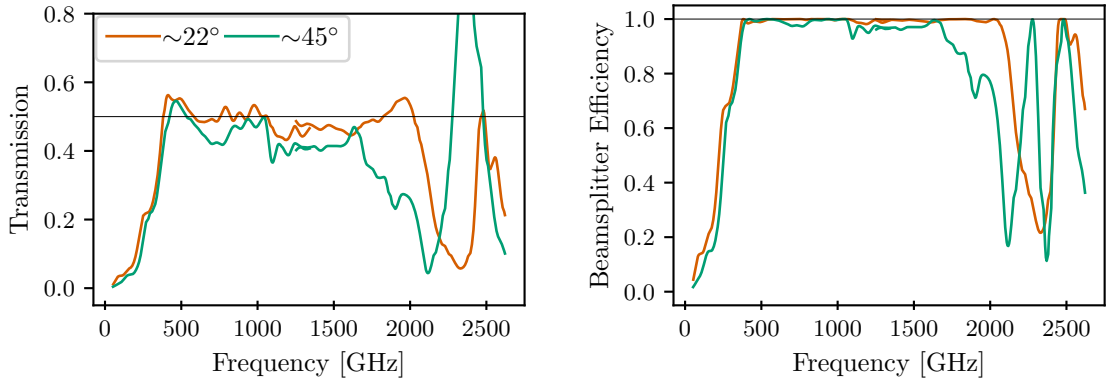


Figure 5.10: The transmission (left) and efficiency (right) spectra of the beamsplitter over two photomixer bands at 22° and 45° angles of incidence. These measurements correspond to the parallel polarisation orientation of the beamsplitter.

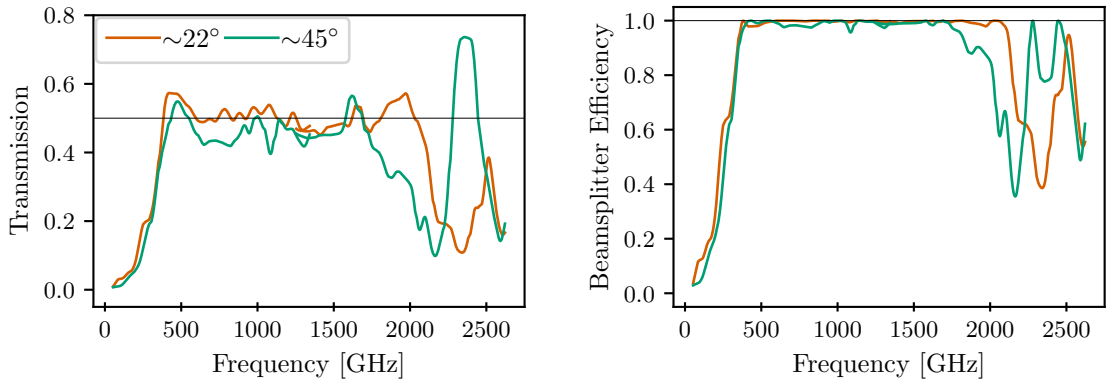


Figure 5.11: The transmission (left) and efficiency (right) spectra similar to those in Figure 5.10 with the beamsplitter in the perpendicular polarisation orientation.

the beamsplitter in the high-frequency band is irregular and not suitable for science use in the DFI testbed. Additionally, the testbed is not sensitive to frequencies above 2.2 THz (see §5.3). As such, I have used only the low- and middle-frequency bands of the photomixer in these measurements.

Figure 5.10 shows transmission spectra measurements I have made with the beamsplitter in the parallel polarisation orientation. Figure 5.11 demonstrates similar measurements with the beamsplitter rotated 90° about the optical axis (i.e., in the perpendicular polarisation configuration). From these measurements, it is evident that beamsplitter performance is improved at 22° of incidence as the beamsplitter efficiency remains flat before sharply cutting off at 2 130 GHz. This corresponds to a $\sim$7% increase in bandwidth over operating at 45° incidence. Additionally, operating with a 45° angle of incidence results in a significant loss in efficiency near 1 900 GHz and increased transmission in the narrow features beyond the nominal frequency cut-off.

The bandpass of the beamsplitter for each polarisation angle is shown in Figure 5.12 at 22° and 45° incidence angles. At 45° incidence, the parallel polarisation beamsplitter efficiency begins to cut off an additional 100(5) GHz ($\sim$7%) lower than the perpendicular polarisation efficiency. Both cutoffs at 45° occur at a lower frequency than when operated at 22° where no such separation in cutoff frequency between orthogonal polarisation states occurs (as seen in Figures 5.10 and 5.11).

From phase measurements of the beamsplitter I obtained with the FTS (see §5.2.2), it was apparent that the beamsplitters have different optical properties depending on which side is first in the optical path. I repeated these measurements of the beamsplitter efficiency while changing the incidence angle after I had flipped the beamsplitter such that the first face in the optical path was reversed (i.e., the face on the transmitted side was now on the reflected side).

Figure 5.13 compares the bandpass of the beamsplitters when opposite sides occur first in the optical path (again at incidence angles of 22° and 45°). At both angles of incidence,

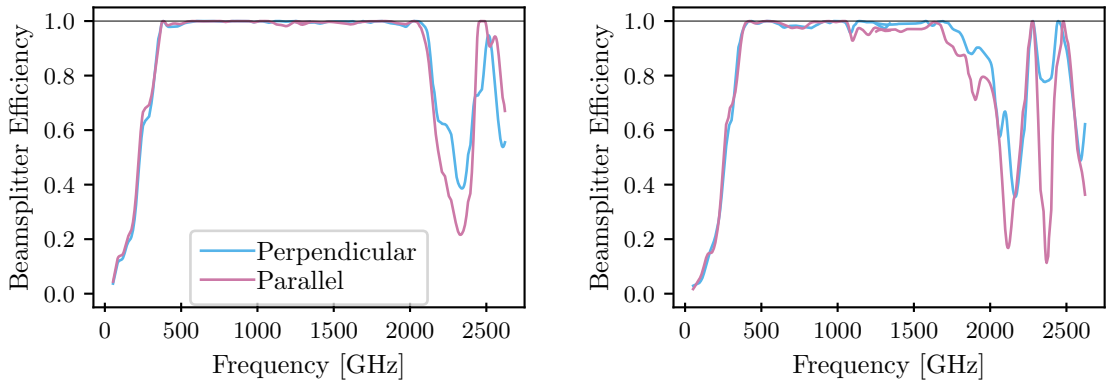


Figure 5.12: The beamsplitter efficiency at an incidence angle of 22° (left) and 45° (right) at orthogonal polarisation angles. These measurements correspond with the orange and green curves in Figures 5.10 and 5.11.

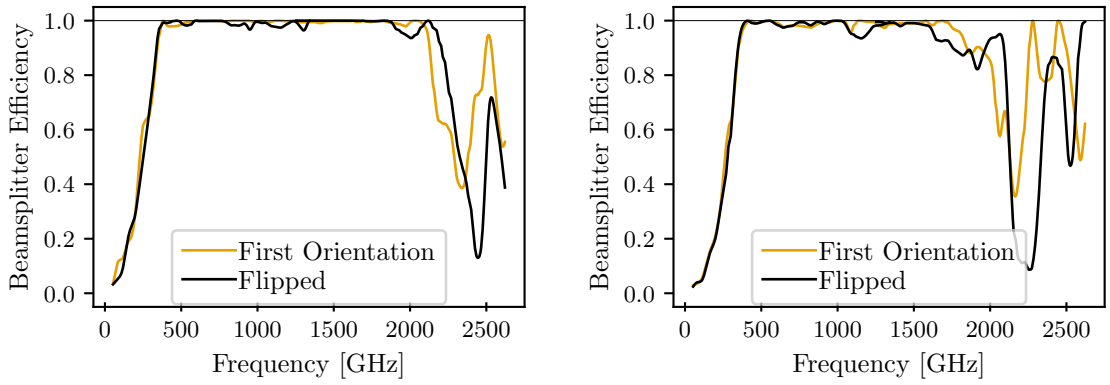


Figure 5.13: Beamsplitter efficiency is shown for when opposing sides are first in the optical path at incidence angles of 22° (right) and 45° (right).

there is a separation at the start of the high-frequency cutoff of $\sim$4% of the bandwidth at 22° incidence and $\sim$12% at 45° depending on which side is first in the optical path.

Operating the beamsplitters at an incidence angle of $\sim$22° results in a significantly greater bandwidth extending the start of the high-frequency cutoff from 1 780 GHz to 2 100 GHz. Additionally, it maintains a consistent frequency band between polarisation states, and reduces the separation at the high-frequency bandpass cutoff resulting from different sides of the beamsplitter being first in the optical path. It should be noted that the measurements I have presented in this section demonstrate the most rigorous beamsplitter bandpass measurements that I have made and that these features have also been seen in early measurements that I have made in a similar arrangement [158]. As a result of the advantages seen, significant improvement in the bandpass of the interferometer could be seen by reconfiguring the optical layout such that light is incident on the beamsplitters at 22°.

5.2.2 Phase effects and phase correction

Determining the phase from the Fourier transform of the double-sided interferogram requires some additional processing considerations. First, I have taken the sample closest to ZPD as the maximum peak sample in the interferogram if it is symmetric (as in Figure 5.7). If the interferogram is antisymmetric (as in Figure 5.3), the closest sample to ZPD is taken to be the sample between the minimum and maximum peaks. The interferogram is then truncated on one side, if needed, so as to be symmetrically sampled about the estimated ZPD and subsequently Fourier-transformed. The measured phase is then determined as the argument of the complex-valued spectrum. It must be noted that correct computation of the phase requires the use of the `arctan2` function [159], which has been implemented in Python [145], to compute $\phi \in [-\pi, \pi]$. Additionally, the computation of the phase results in the wrapping of any values outside of the function's boundary.

The interferogram and measured phase from a single scan of the FTS while viewing

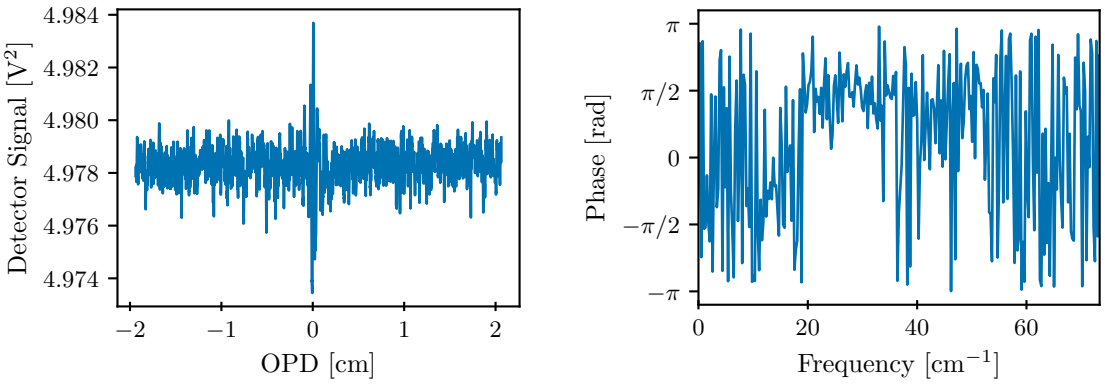


Figure 5.14: An example interferogram (left) and phase spectrum (right) measured by the central detector of the FTS while viewing 1 200°C blackbody source from a single spectral scan.

a 1 200°C blackbody source with the central detector is shown in Figure 5.14. The SNR of the phase spectrum from a single FTS scan is poor making unwrapping phase rollovers at $\pm\pi$ difficult and engendering a poor confidence in phase correction on a scan-by-scan basis. As a result, it is particularly useful to develop standard phase products for the DFI from calibration observations of the FTS that have attained a high SNR through averaging.

Figure 5.16 shows the phase measured by the central detector from an FTS observation of a 1 200°C blackbody source in three different configurations. Each observation is determined from the average of 1 500 forward scans of the FTS. Here, I have defined the symmetric input configuration of the FTS as corresponding to a source positioned at the input such that one path through the interferometer is reflected by both beamsplitters and the other path transmits through both beamsplitters (see Figure 5.15). The antisymmetric input corresponds to the opposite case in which the source is positioned such that each interferometer path experiences both a beamsplitter reflection and transmission. Additionally, the third case (which I have referred to as the opposing beamsplitter configuration) is the result of flipping one of the beamsplitters in its mount such that the flipped beamsplitter now has its opposite side first in the optical path.

The phase measurements in Figure 5.16 demonstrate that there is a significant phase

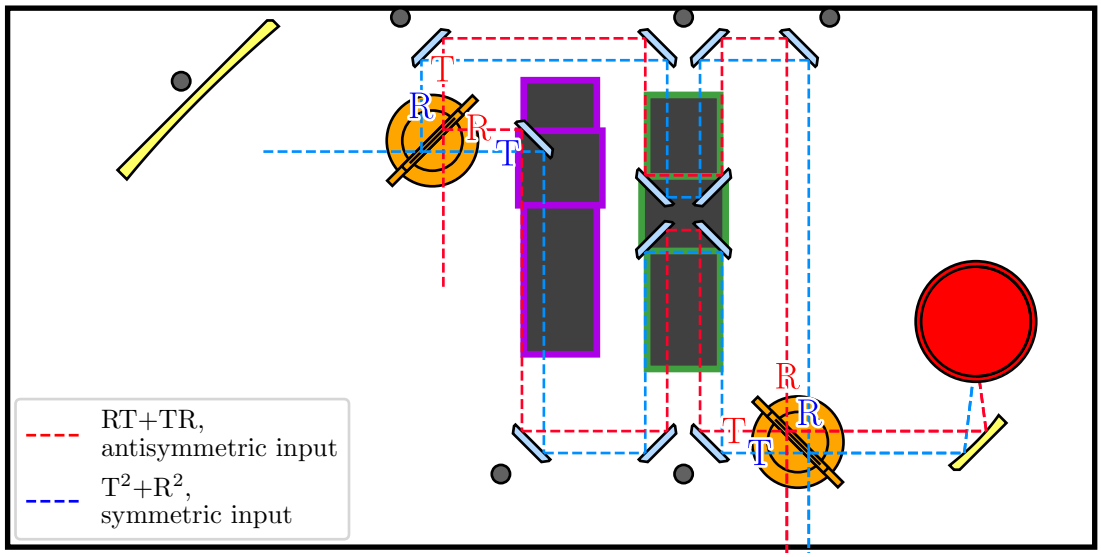


Figure 5.15: The symmetric (blue) and antisymmetric (red) inputs of the FTS.

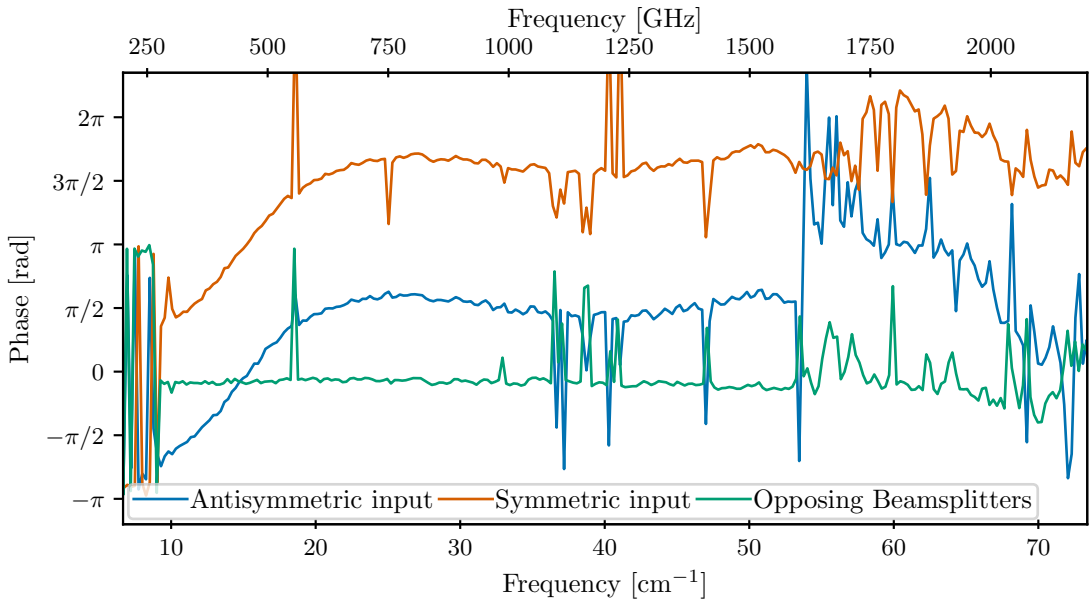


Figure 5.16: The measured phase from an FTS measurement of a 1 200°C blackbody in three FTS configurations.

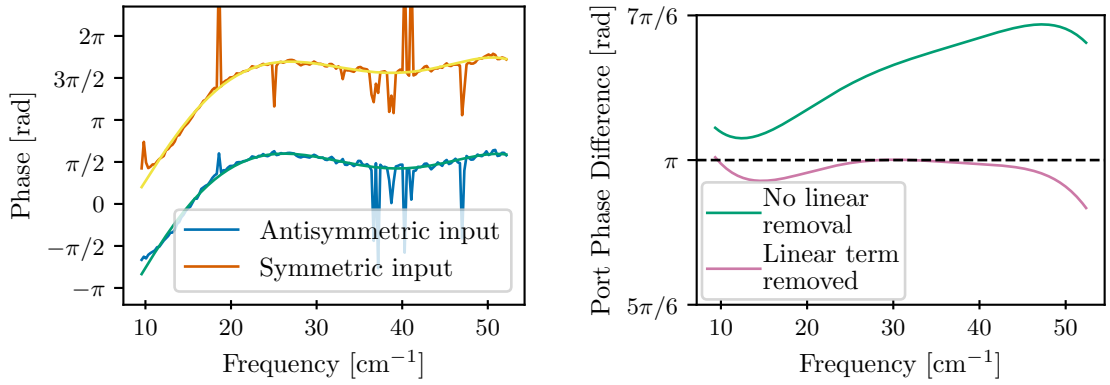


Figure 5.17: The fitted phase in the region of the spectrum that has high amplitude corresponding to corresponding to a source at each input of the FTS is shown in the left panel (see Figure 5.16). Polynomial fits to each curve in the left panel are also shown. The phase difference between each port is shown in the right panel. The expected phase difference between each port, π, is shown by the dashed black line in the right panel.

contribution from the beamsplitters and that they have a sidedness (i.e., phase effects depend on which side of the beamsplitter is first in the optical path). In the opposing beamsplitter configuration, the phase contributions from the beamsplitter have been reduced as the phase contributions "cancel out" to a significant degree while in a non-opposing arrangement, these effects are effectively doubled.

In the absence of beamsplitter emission/absorption effects, the phase difference between each symmetric and antisymmetric input is π [71, 160]. Figure 5.17 shows the difference in the measured phase at each input. As the spectral amplitude at frequencies $\notin [280, 1570]$ GHz is low and phase noise is high, there is significantly lower confidence in phase measurements in these regions. A 5th-order polynomial has been fit to these regions and the difference between each fit is shown to give a phase difference greater than π. As it is possible that the sampling in each arrangement has led to slight differences in the linear phase term (see Chapter 2), the difference in the phase measurement at each port has also been computed after the slope of a linear fit to each region has first been removed. This linear phase compensation brings the phase difference between each port much closer to the expected value of π.

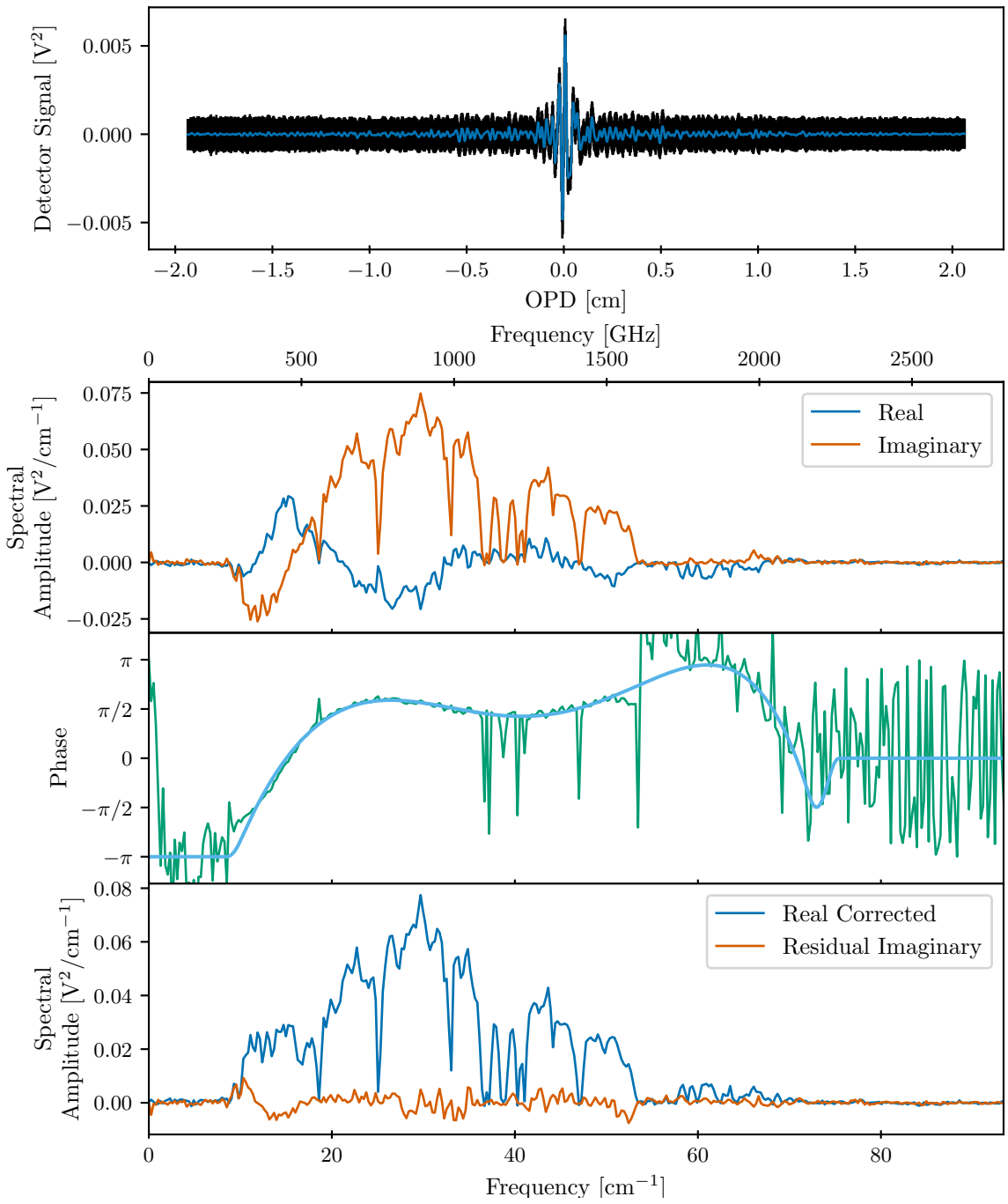


Figure 5.18: The phase correction of a spectral measurement of a 1 200°C blackbody source from the central detector corresponding to 1 800 scans of the FTS. The FTS beamsplitters are not in their opposing configuration (see Figure 5.16). The top panel shows the average interferogram. Black errorbars show the standard deviation across all scans. Note that the uncertainty in the average interferogram is the standard deviation scaled by $1/\sqrt{N}$ (where N is the number of scans). The upper middle panel shows the complex-valued uncorrected spectrum. The phase spectrum is shown in the lower middle panel with a fit to the measured phase shown in light blue. The bottom panel shows the real corrected spectrum and residual imaginary components.

Figure 5.18 shows the interferogram and complex spectrum of a 1 200°C blackbody spectrum measured by the central detector of the FTS. I have determined the interferogram from 1 800 forward scans of the FTS. The blackbody has been positioned at the antisymmetric input of the FTS and the beamsplitters in their non-opposing configuration (i.e., corresponding to the blue curve of Figure 5.16). The phase spectrum and corrected FTS spectrum are shown in Figure 5.18. The phase spectrum has been fit by a 5th-order polynomial and forced to smoothly decay to $-\pi$ and 0 at the end of the spectral bandpass. In spite of the non-linear phase effects from the beamsplitter, the spectrum can be recovered through phase correction. Using the fitted phase spectrum outlined in Figure 5.18, the imaginary portion of the spectrum due to phase errors is reduced by 95% across the spectral band through phase correction (see §2.1.4).

While operating with beamsplitters in the opposing configuration significantly reduces non-linear phase effects in the FTS, there are some additional considerations when phase correcting spectra in this configuration. Figure 5.19 shows an interferogram and the corresponding complex spectrum (prior to phase correction) from an FTS measurement of a 1 200°C blackbody measured with the FTS in this configuration. The interferogram was measured by the central detector and was generated from the average of 1 500 forward scans of the FTS (see §6.2.5). The increased signal over the measurements with the beamsplitters in their opposing configuration (see Figure 5.18) is a result of better positioning of the blackbody in the input of the FTS. Of particular note is that the real spectrum is negative-valued prior to the cut-on band of the FTS. It must be noted that these interferograms do not employ a baseline subtraction of signals that correspond to frequencies less than the spectral band of the FTS that was discussed in §5.1.1. In addition to the negatively valued spectrum at lower frequencies, there is a small amount of radiation measured (SNR$\sim$4) between 2 500 and 2 600 GHz that is not seen in the previous spectral measurements in Figure 5.18. Note that this frequency band appears to be above the regime that the detector system is sensitive to and corresponds to a drop to 40% beamsplitter efficiency

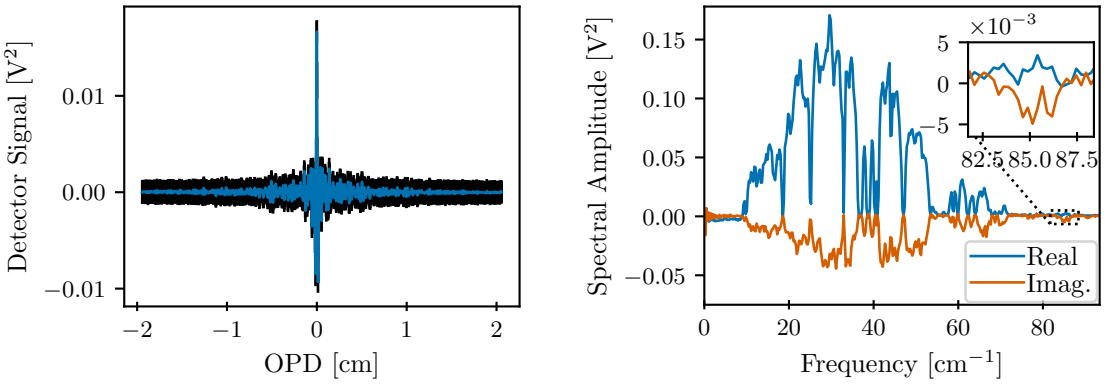


Figure 5.19: A measured interferogram from the central detector while viewing a blackbody source at 1 200°C is shown in the left panel with the beamsplitters arranged in their opposing configuration in the FTS. As in Figure 5.18, black error bars show the standard deviation of all 1 500 scans at each point. The corresponding complex-valued spectrum prior to phase correction is shown in the right panel. The inset in this plot shows a small degree of measured radiation in a high frequency band.

between the first and second transmission features after the beamsplitter's high-frequency cut-off (see Figure 5.9). Both of these anomalies have been observed in multiple spectral measurements in this FTS configuration.

Figure 5.20 shows the phase spectrum and the phase-corrected FTS spectrum corresponding to the measurements in Figure 5.19. Though spectral amplitude is low prior to 300 GHz, a phase of $\sim \pi$ is clearly seen. When corrected, this results in a positive real-valued spectrum in this regime. Additionally, there is a significant discontinuity from π to the region in which the spectral amplitude has a high SNR (300–2.2 GHz). The fit to the phase spectrum (shown as the yellow curve in the left panel) has been forced to decay rapidly to the value of the high SNR regime within the low spectral amplitude regime as confidence in the phase in this regime is low. The phase spectrum has been fit with a 5th-order polynomial and a least-squares fitting algorithm [125] between 300 and 2 160 GHz and has been forced to decay to π and 0 at the low and high-frequency edges of the band, respectively.

The high-band radiation seen in Figure 5.19 has been marked in the phase spectrum in Figure 5.20 in orange. This observed feature occurs after the fit to the phase would have

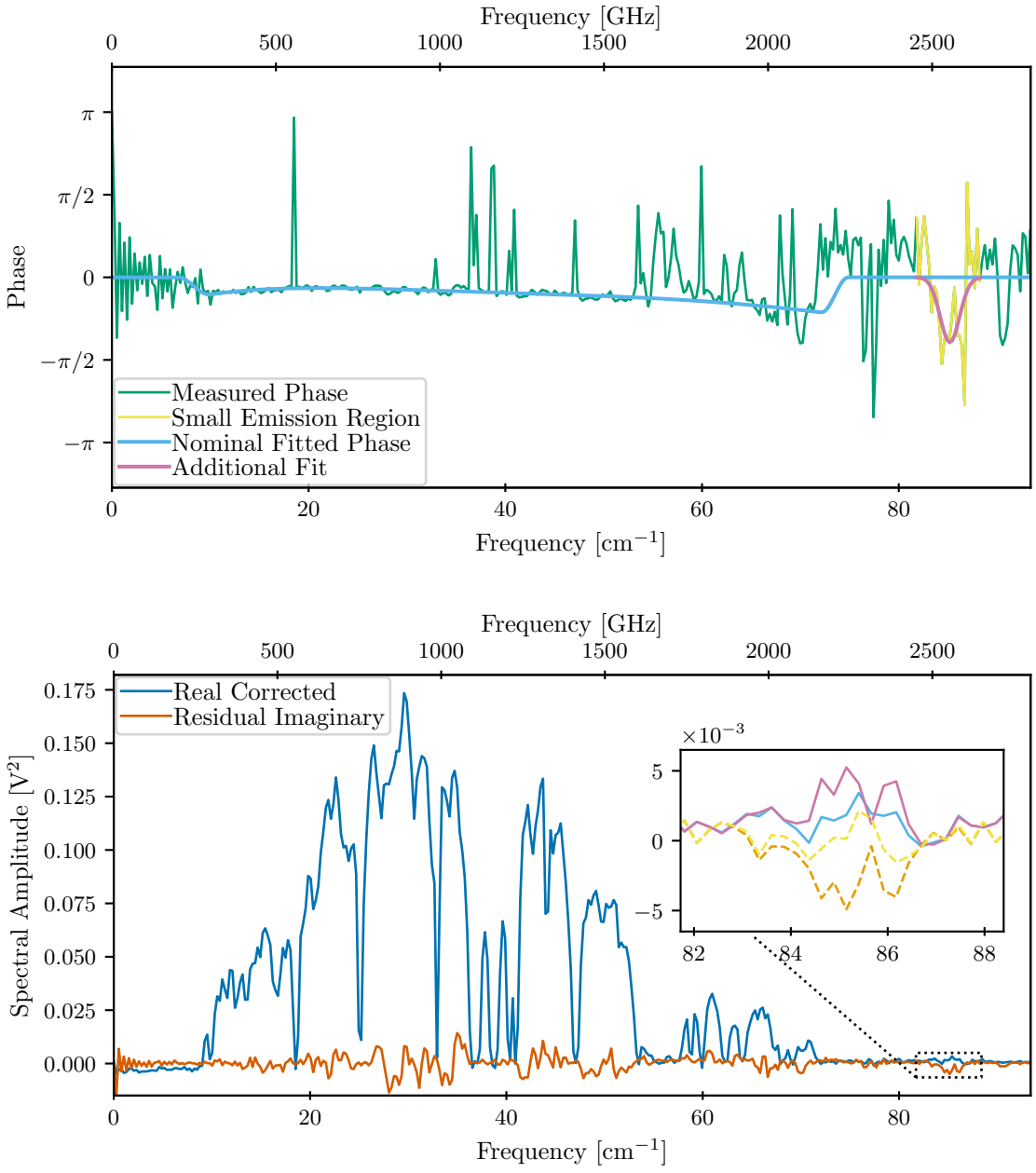


Figure 5.20: The measured phase spectrum from the FTS measurement of a 1 200°C shown in Figure 5.19 (top) and phase-corrected spectrum (bottom) with the FTS beamsplitters in their opposing configuration. In the top panel, a fit to the measured phase is shown in yellow and an additional fit to the small emission region between 2 500 and 2 600 GHz (shown in yellow) is also shown by the light blue feature. The corrected spectrum using the nominal fit to the measured phase is shown in the bottom panel. In the inset, the light blue (real) and dashed light orange (imaginary) curves show the corrected spectrum in the small emission region where the phase has been taken to be 0 (as in the main panel), the pink (real) and dashed yellow (imaginary) curves show the corrected spectrum if the Gaussian fit to the phase (shown in the panel above) is included in the phase correction.

normally been forced to 0 due to the low spectral amplitude between it and the high SNR band of the FTS. A Gaussian fit to the region has been included in the phase spectrum fit (shown in green) in an attempt to provide some phase correction in this region. The bottom panel of Figure 5.20 shows the results of a phase correction including this additional fit to the region (green) and without it (yellow).

5.3 Relative Spectral Response of the DFI

The spectrum measured by a single detector in the interferometer experiences filtering by the various optical components of the assembly, the atmospheric environment of the lab, and the spectral responsivity of the detectors themselves. The spectrum observed by a single detector $S_{n,m}(\nu)$ located at channel n, row m with a blackbody source placed at one of the inputs of the interferometer can be written [139],

$$S_{n,m}(\nu) = R_{n,m}(\nu)\iota(\nu)\eta\varepsilon^2(\nu)e^{-\tau}B(\nu,T)A\Omega(\nu) \quad [\mathrm{W/Hz}]. \tag{5.7}$$

In Equation 5.7, $R_{n,m}(\nu)$ is the RSRF of the interferometer for the detector (n,m), η is the mirror efficiency of the interferometer, $\varepsilon(\nu)$ is the efficiency of the beamsplitters (which has been assumed to be the same for both), $\iota(\nu)$ is the transmission of the optical lowpass filter employed by the detector assembly, $e^{-\tau}$ is the atmospheric absorption from the laboratory environment, $B(\nu,T)$ is the blackbody spectrum at the input at temperature T, A is the absorbing area of the detector, and $\Omega(\nu)$ is the detector solid angle. The FTS employs 14 mirrors (including an input collimator and output focusing mirror) that have been assumed to have a reflectivity of $\sim$0.97 giving, $\eta = 0.65$. In principle, all of the factors in Equation 5.7 that attenuate the measured spectrum may also depend on the pixel coordinates n and m depending on changes in the optical path to the given detector.

The RSRF function provides an empirical calibration function by which the detector signal can be related to the optical power measured by the detector. Some known contribu-

tions to the spectral response function are the spectral response of the detector array itself, internal cryostat thermal filters, and emission from the beamsplitters.

Figure 5.21 shows a measured blackbody spectrum from the FTS with all known sources of optical filtering. It can be seen that the low-frequency end of the spectrum is defined (in part) by the terahertz beamsplitter efficiency rather than the cut-off frequency of the waveguide's lowest mode (see §4.1.5). The high-frequency edge of the band occurs at the high-frequency cut-off of the beamsplitter but the spectrum already experiences substantial attenuation at frequencies greater than 1 750 GHz that cannot be fully accounted for by atmospheric absorption and the decrease in beamsplitter efficiency at these frequencies. Additionally, the cutoff frequency of the optical low-pass filter employed by QMC Instruments in the construction of the detector system occurs at $\sim$3 THz and the beamsplitter experiences several narrow-band regions of increased efficiency beyond its cut-off yet the detector does not receive significant throughput at frequencies greater than 2.2 THz. It should also be noted that the manufacturer has not been able to fully confirm that the 100 cm^{-1} filter is indeed the filter in use with the detector array as of the time of writing.

At the time that I made the spectral measurements with the FTS necessary to determine the RSRF of the assembly, my measurements of the central detector's time constant were not completed. As such, the detector time constant was assumed to be on the order of the value reported by the manufacturer ($\sim$0.1 ms) for which the chosen 7 mm/s scanning speed of the spectral stage was more than sufficient to avoid any filtering from the response of the detector. As I have measured the central detector's time constant to be nearly an order of magnitude slower (see §4.3), there is significant filtering from the detector response which must be considered with Equation 5.7. This filtering from the detector is shown in Figure 5.21 and has been considered in determining the RSRF. Note that this filtering due to the time constant of the detector is seen in the comparison between S&I and RS measurements in Figure 5.3.

The atmospheric absorption model is determined from the atmospheric modelling soft-

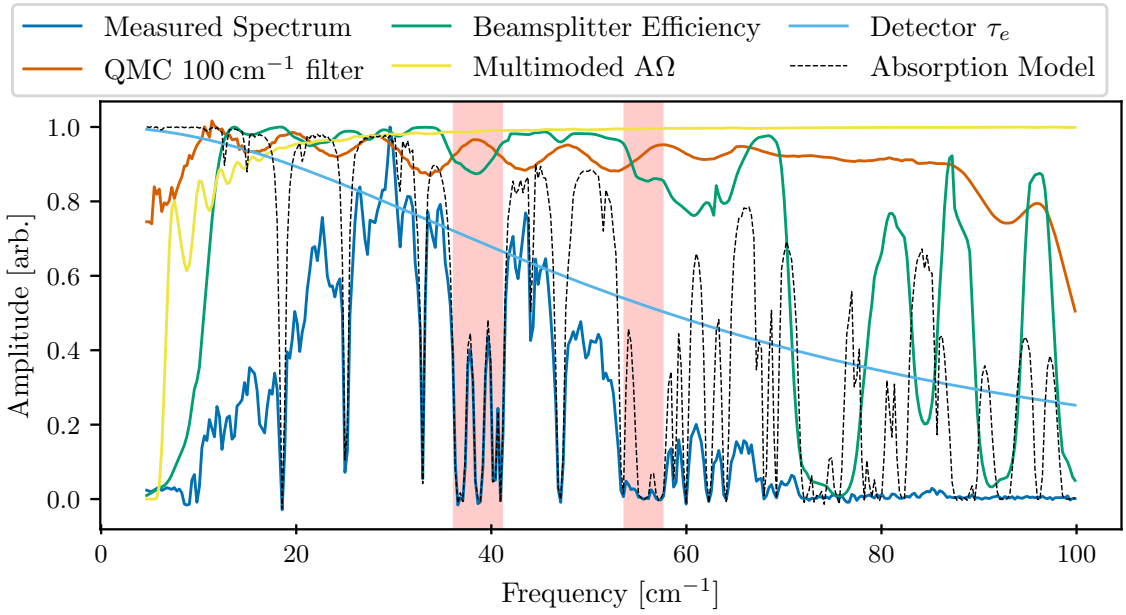


Figure 5.21: The profiles of known sources of optical filtering in the FTS and detector assembly compared to a measured blackbody spectrum from the FTS. Regions that are dominated by strong atmospheric absorption features have been marked in red.

ware, `am` [161]. The model corresponds to a composite gas cell representation of the laboratory environment with water absorption and a terrestrial dry air model. The path length of the gas cell is taken to be equal to the optical path of the FTS. To effectively match the line widths of the atmospheric model to the features measured by the FTS, the sinc Instrument Line Shape (ILS) of the spectra (see §2.1.3) was convolved with the atmospheric model and an optimisation routine was used to minimise the residual between measured spectrum and model in the regions of strong absorption features [125]. To account for the response function in the measured spectrum, a linear function determined by a fit to 3 points on either side of the measured line has been removed and the feature has been scaled to match the expected relative amplitudes of the model spectrum. After each line has been matched to the model in this way, the residual in the vicinity of each line is calculated. The generated atmospheric models were allowed to vary in temperature, humidity, pressure, and path length to within the uncertainty in these measurements of the laboratory environment. The atmospheric model determined by the convergence of the optimisation routine is summarised in

Table 5.1: The atmospheric model for the laboratory environment calculated with `am` [161].

	Converged Model	Laboratory Weather Station
Humidity [%]	15.05±0.08	18 ± 3
Temperature [°C]	18.02 ± 0.01	21 ± 3
Pressure [atm]	0.878 ± 0.001	0.90 ± 0.02
Path Length [m]	6.852 ± 0.001	6.94 ± 0.10

Table 5.1.

Equation 5.7 can be modified with the introduction of a parameter, $k(\nu)$, to represent the spectra of extraneous sources to the interferometer. As the blackbody source is placed at one input to the interferometer, the second input is occupied by the room temperature environment of the laboratory which provides a differential signal in the interferometer. This is often assumed to be the dominant contribution to $k(\nu)$ [139]. With the introduction of $k(\nu)$, Equation 5.7 is written,

$$S_{n,m}(\nu) = R_{n,m}(\nu)\iota(\nu)\eta\varepsilon^2(\nu)e^{-\tau}[B(\nu,T)A\Omega(\nu) - k(\nu)] \quad [\mathrm{W/Hz}]. \tag{5.8}$$

The extraneous spectral features can be decoupled from measurements of the RSRF by measuring a calibrated blackbody source at different temperatures,

$$R_{n,m}(\nu) = \frac{S_{n,m}(\nu,T_2) - S_{n,m}(\nu,T_1)}{\iota(\nu)\eta\varepsilon^2(\nu)e^{-\tau}A\Omega(\nu)[B(\nu,T_2) - B(\nu,T_1)]} \quad [\mathrm{V^2/W}]. \tag{5.9}$$

Once the RSRF is measured in this way, $k(\nu)$ can be determined through re-arranging Equation 5.8.

I have measured the central detector's RSRF from FTS measurements of the calibrated Pegasus blackbody source at a temperature of 950°C and 1 200°C. The measured spectra are obtained from 1 500 rapid scans of the FTS in the forward direction travelling at a speed of 7 mm/s and have been processed as described in §5.1.2. Additionally, the beamsplitters were positioned in the opposing configuration to minimise their phase effects and the spectra were phase corrected as described in §5.2.2. Figure 5.22 shows the spectral response of

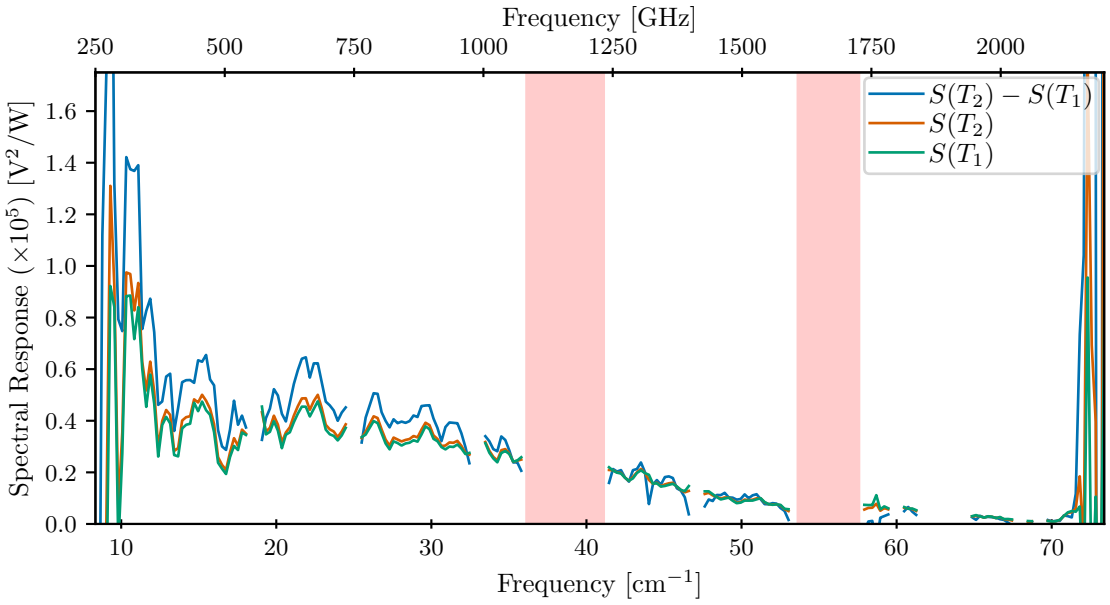


Figure 5.22: The RSRF of the FTS and detector assembly determined from spectral measurements of a blackbody source at a temperature of 950°C (T_1) and 1 200°C (T_2). These are determined from Equation 5.7 (for individual temperatures) and Equation 5.9 (for the differential blackbody temperature measurement). Frequency bands that are dominated by atmospheric absorption are marked in red.

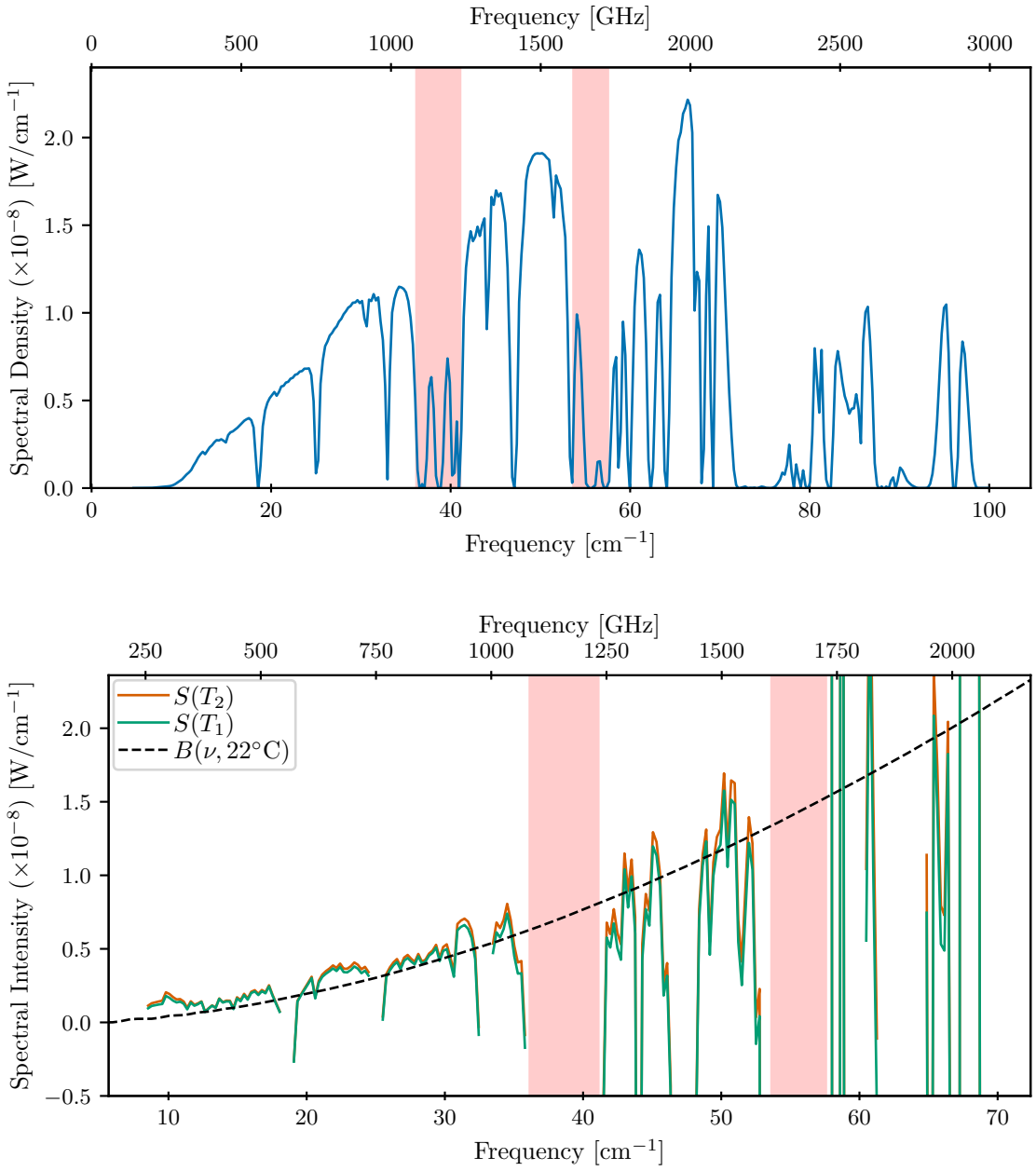


Figure 5.23: A theoretical 950°C blackbody spectrum as it would be measured by the FTS if it had an RSRF of unity (see Equation 5.7). The spectrum has been filtered by atmospheric absorption, the efficiency of the FTS beamsplitters, a multi-moded beam model, the detector response, and a 100 cm^{-1} low-pass optical filter. The bottom panel shows the extraneous spectral features in FTS measurements of the blackbody at 950°C (T_1) and 1 200°C (T_2). A room-temperature blackbody model corresponding to the second input of the FTS coupled through the multi-moded beam model is shown by the dashed black line. As in Figures 5.21 and 5.22, regions dominated by atmospheric absorption have been marked in red.

the FTS and detector system assembly. Both theoretical and measured spectra have low values in frequency regimes that are dominated by atmospheric absorption. As a consequence, there is low confidence in measurements of the RSRF in these regions and they have been masked. The RSRF of the assembly experiences a sharper cut-on at 250 GHz than can be accounted for by the efficiency profile of the beamsplitters and the beam model. The response is relatively level from 500 to 800 GHz after which it gradually decreases. The spectral bandpass of the interferometer over which high SNR spectral information can be obtained is 200–2 200, GHz. The theoretical 950°C blackbody spectrum with all the known sources of filtering presented in Figure 5.21 is shown in the top panel of Figure 5.23.

The extraneous spectral features in FTS measurements are shown in the bottom panel of Figure 5.23. The measurements are severely affected by strong atmospheric absorption in the spectrum as both the model and measured spectrum vanish at these features. In spite of this, these measurements show good agreement with the expected profile of a room-temperature blackbody coupled to the FTS through its second input. Deviations from the expected profile are indicative (in part) of how well the detector beam is approximated by the multimoded beam model.

5.3.1 Maximum spectral stage scanning speed

From Equation 4.12, we see that the maximum speed of the spectral scanning stage in the interferometer requires that the detectors are sufficiently fast to measure the optical modulation in the interferogram from the highest frequency component of the FTS's spectral bandpass. When operating in their default mode, the fitted detector time constant is 0.96 ± 0.06 ms. To fully Nyquist sample the highest frequency of radiation from the FTS (defined by its bandpass) with this time constant, spectral scanning speeds must not exceed 2.77 ± 0.02 mm/s.

Chapter 4 has shown that through the tuning of both PID parameters and the timing of the detector measurement, the time constants and noise properties of the detectors can be

Table 5.2: The detector parameters required to fully sample the spectral bandpass of the DFI at the minimum and maximum scanning speed of the spectral stage.

Detector parameter	At minimum speed (0.75 mm/s)
Pulse width [loop counts]	$\leq$20
Integral gain [a.d.u.]	$\geq$64
Integral gain (with P-gain $>$ 500) [a.d.u.]	$\geq$120
Detector time constant [ms]	$\leq$3.6

tuned for a specific use case. To avoid low-frequency dominated signal bands of the central detector, I have determined that a DFI spectral scanning speed greater than 0.75 mm/s (mechanical) is needed. At this speed, detector time constants that are as fast as 3.6 ms ($f_{\text{co}} = 44\,Hz$) are required to fully Nyquist sample the spectral bandpass of the interferometer (taken to be 200–2 200 GHz). Table 5.2 summarises the limiting PID gains and suitable detector timing parameters to fully sample the FTS bandpass for the minimum spectral scanning speeds of the DFI. Recall that detector time constants are primarily limited by the integral-term gain of the PID loop and the pulse width of detector measurements (see §4.3).

5.4 Spectral noise characterisation

Considering the detector time constant needs of the detector array as an integrated component of the DFI testbed, I have determined a set of detector parameters to improve the central detector's performance. These are summarised in Table 5.3.

Using the FTS, the spectral nature of noise sources in the full assembly can be measured [71]. It is instructive to consider not only noise within the spectral bandpass of the interferometer, but also noise outside of this spectral band that is isolated from photon noise (see 3.1.2). The spectral region below the passband of the FTS provides an indication of total noise that is significantly affected by $1/f$-noise (see §4.2) while the region above the passband provides an estimate of noise that is well isolated from $1/f$-noise [71].

Table 5.3: Detector parameters that I have selected to provide a better optimised detector central detector for the DFI testbed are shown with the default parameters. Selected detector performance metrics are also shown.

Detector Parameter	Default	Optimised
Pulse width [loop counts]	10	12
Blanking time [loop counts]	4	6
Read index [loop counts]	9	11
Setpoint [a.d.u.]	10 000	9 500
P-gain [a.d.u.]	1 000	600
I-gain [a.d.u.]	200	150
D-Gain [a.d.u.]	0	0
Detector time constant [ms]	0.96 ± 0.06	1.65 ± 0.01
Detector array framerate [kHz]	12.913	11.106
Time per sample [μs] / [ticks]	11.063 / 885	10.863 / 1 029

In Fourier transform spectroscopy, the spectral NEP can be expressed as,

$$\mathrm{NEP}_{\mathrm{FTS}} = \varsigma \sqrt{\frac{\Delta\sigma}{2\nu_{\mathrm{stage}}}} \quad [\mathrm{W}/\sqrt{\mathrm{Hz}}], \tag{5.10}$$

where $\varsigma\,[\mathrm{W/cm^{-1}}]$ represents spectral noise, $\nu_{\mathrm{stage}}\,[\mathrm{cm_{OPD}/s}]$ is the scanning speed of the FTS's spectral stage, and $\Delta\sigma\,[\mathrm{cm^{-1}}]$ is the spectral resolution (see §A.5 for additional details) [71, 162]. To determine spectral noise, I have considered 200 forward scans of the FTS and subtracted the average spectrum from each single-scan spectrum. Assuming that the noise amplitudes of each scan are statistically independent, the total spectral noise is determined from the quadrature sum of the noise from each scan ($\varsigma^2 = 1/N^2 \sum_i^N \varsigma_i^2$). Figure 5.24 compares spectral noise in the central detector obtained from spectral measurements (in units of raw detector signal) of a blackbody source at 1 100°C using the default parameters set by QMC Instruments and measurements using the optimised parameters. Figure 5.25 shows the corresponding $\mathrm{NEP}_{\mathrm{FTS}}$ from each spectral noise measurement. Calibration of the spectral noise has made use of the RSRF of the FTS assembly discussed in §5.3. Note that this limits the spectral NEP band to 250–2 200 GHz. The optimised detector parameters result in a 37–79% reduction in noise throughout the spectral band (i.e., improving spectral

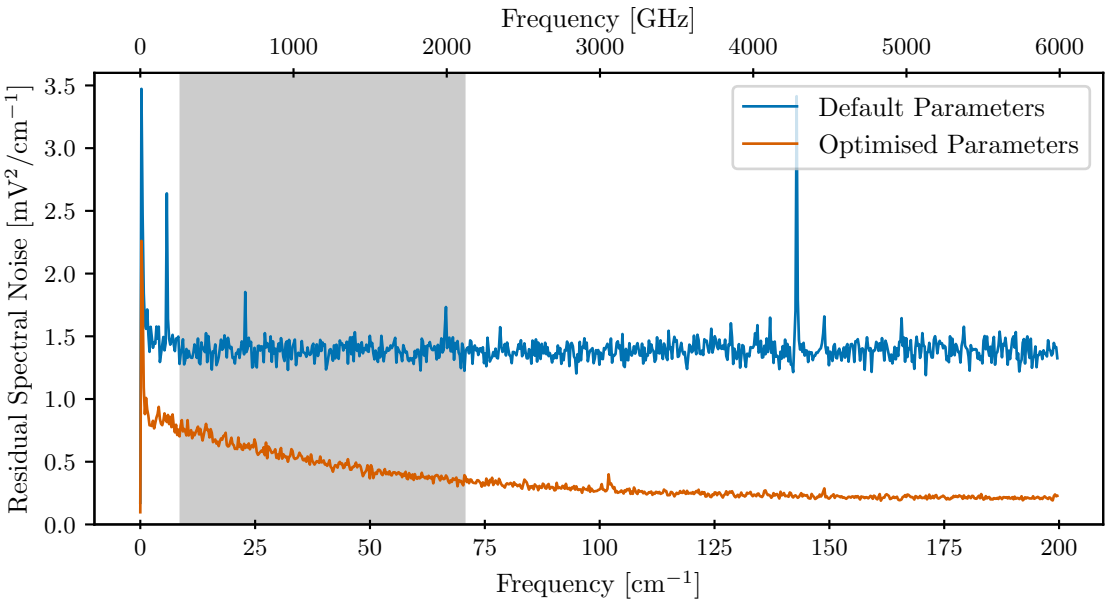


Figure 5.24: The spectral noise measured by the FTS while viewing a blackbody source with the default parameters set by QMC Instruments (see §3.3.1) and with the optimised parameters I have determined. The region shaded in grey marks the spectral bandpass of the FTS.

noise by a factor of 1.6–4.8). Both of these measurements were made after the Pegasus blackbody source had been repaired and the absolute calibration of the calculated NEP is less certain.

5.5 Conclusions

Throughout this section, I have discussed the results from experiments to characterise the TES detector array as an integrated component of the DFI assembly. I have shown that the low-frequency noise experienced by the detectors is such that S&I measurements of the FTS have poor performance without the use of external modulation.

Using a commercial Toptica photomixer and receiver unit, I have measured the spectral performance of the metal-mesh beamsplitters employed by the FTS. Through these, I have demonstrated that reconfiguring the optical system of the DFI such that light is incident on the beamsplitters at 22° will improve the high SNR bandpass of the FTS by ∼7% and reduce

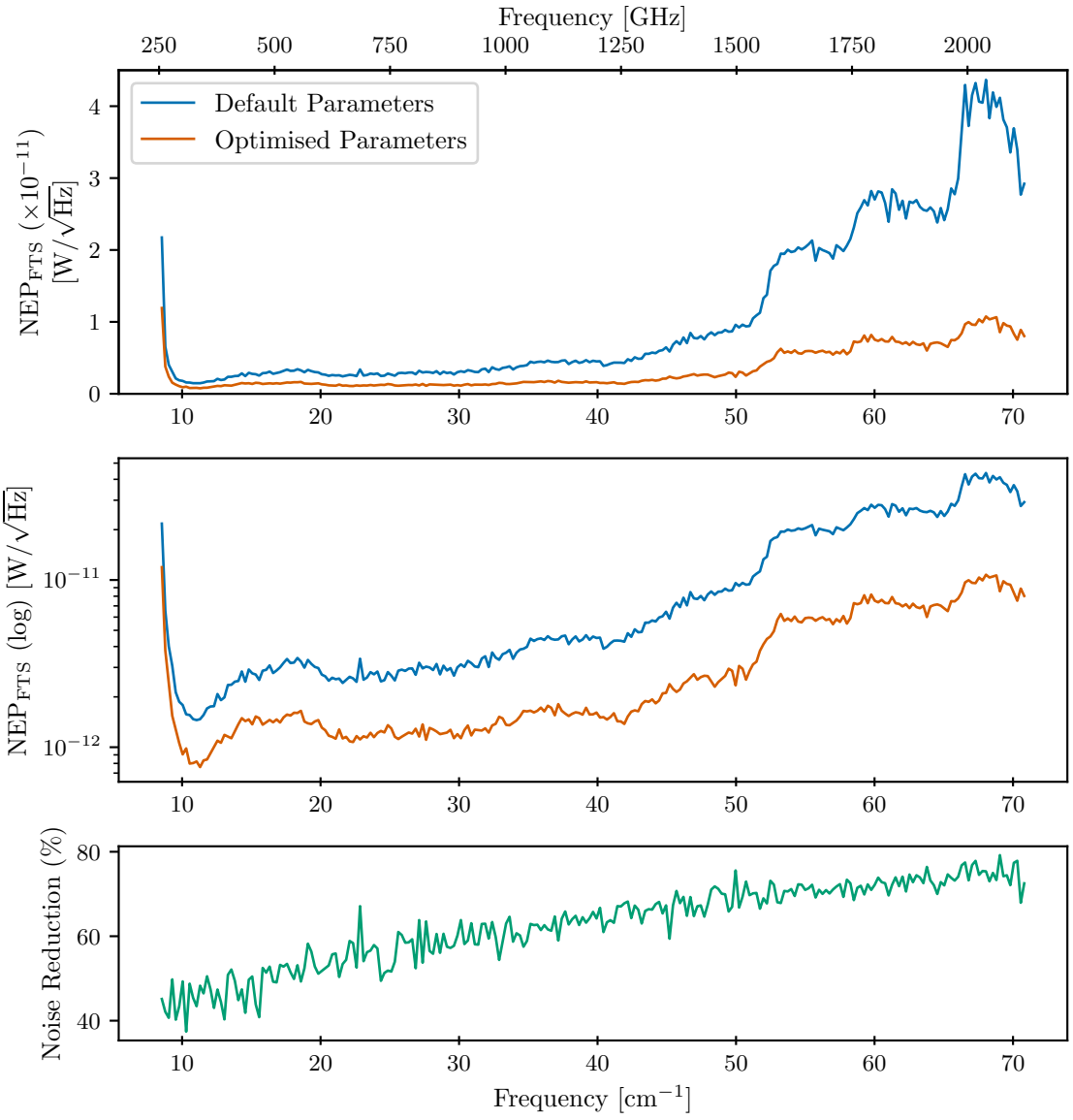


Figure 5.25: The spectral NEP of the central detector in the DFI testbed using default and optimised detector parameters. These measurements correspond to the spectral noise shown in Figure 5.24 and have used the calibration RSRF in Figure 5.22.

other undesirable effects. I have demonstrated that the beamsplitters have a sidedness that is of particular importance for their non-linear phase effects.

From RS observations with the FTS, I have determined the high SNR spectral bandpass of the interferometer to be 250–2 200 GHz and measured the RSRF of the central detector as an integrated part of the DFI assembly. This bandpass requires detector time constants that are faster than 3.6 ms to fully Nyquist sample the optical modulation from the DFI testbed. The known optical filtering of the detector system cannot account for the reduction in the optical throughput at the high spectral frequency band of the FTS. Some ambiguities as to the actual optical filters employed by the detector system await further communication from the manufacturer. Additionally, I have shown that the optimised suite of detector parameters discussed in Chapter 4 reduce the spectral $\mathrm{NEP}_{\mathrm{FTS}}$ of the assembly by 37–79% throughout the spectral band.

Chapter 6

Future Characterisation and Conclusions

> What counts is not what sounds plausible, not what we'd like to believe, not what one or two witnesses claim, but only what is supported by hard evidence, rigorously and skeptically examined.
>
> –Carl Sagan (1934–1996) [163]

Throughout this work, I have presented and discussed the results of experiments I have conducted to characterise a unique array of feedback-controlled Transition Edge Sensor (TES) bolometers and optimise it to serve as a detector system for a far-Infrared (IR) Double Fourier Interferometery (DFI) testbed instrument. In this chapter, I provide a summary of the content of this thesis. Additionally, my investigations have uncovered several avenues to further characterise the detector system which may lead to further improvements in its performance. I present and discuss the results of my initial investigations into these in this chapter as well. I have also included a brief discussion of Kinetic Inductance Detectors (KIDs) as a developing detector technology for the far-IR.

6.1 Conclusions

Through these experiments, I have measured the superconducting transitions of the detector array and determined the most sensitive region on the transition of the central detector. Through this thermal characterisation, I have also determined the dynamic thermal conductance of the central detector. I have characterised the effect of both Proportional-Integral-Derivative (PID) tuning and modifications to the timing of detector measurements

on the noise characteristics and response of the central detector. Additionally, I have measured the optical Noise Equivalent Power (NEP) of the detector array. Using the DFI testbed, I have spectrally characterised the central detector and the beamsplitters employed in the assembly. Through this work, I have determined a set of optimal detector parameters and demonstrated that they reduce the spectral noise of the DFI testbed by $\sim$70%. These results are summarised in §6.1.4 and Table 6.1. Included with these measurements, I have provided the necessary discussion of theoretical concepts needed to provide important context for this work.

6.1.1 Double Fourier Interferometry

Through DFI, transformative progress in the spatial resolution of astronomical observation in the far-IR can be achieved. Modern far-IR observing platforms have yet to achieve the finer than sub-arcsecond spatial resolution readily available from facilities operating at both shorter and longer wavelengths. As such, there has been significant interest in instruments of this type. This has led to substantial investigation by the United States, European, and Japanese astronomy communities. To further study this technique and improve its technology readiness, we have constructed a laboratory-based DFI testbed instrument.

In spite of the promising capabilities of DFI instruments, understanding the spatial and spectral interferometric measurements made with DFI instruments is non-trivial. As such, I have discussed the Michelson stellar interferometer, Fourier Transform Spectrometers (FTSs), and how these instruments are related to DFI. In particular, I have discussed the practical considerations and consequences of spectroscopic measurements made with a physical FTS. These are of particular importance for the characterisation and optimisation of the detector array as an integrated part of the DFI assembly. Coupled with this, I have discussed my role in the construction of the Lethbridge DFI testbed, presented its optical configurations, and outlined the alignment strategy that I employed. This instrument stands unique among DFI testbeds as it operates as an imaging FTS in the far-IR employing an

array of feedback-controlled TES bolometers.

6.1.2 Feedback-controlled TES bolometers

The array of TES bolometers that have been developed by QMC Instruments is a bespoke system that can be configured for several use cases as a far-IR detector system. Characterising the array's performance and optimising it for use in the DFI testbed has been a substantial undertaking and I have presented and discussed the results of my experiments to characterise the noise performance, responsivity, and thermal behaviour of the detector array.

Through these experiments, I have determined the most sensitive region of the central detector's superconducting transition and determined its dynamic thermal conductance. I have demonstrated that substantial changes to the detector measurement process and performance can be achieved through the adjustable timing of detector measurements and the tuning of the PID feedback control. Additionally, I have shown that the response speed and noise performance of the detector must be balanced depending on the intended application. The results of these characterisation experiments are further summarized in §6.1.4.

6.1.3 Integration of the detector array in the DFI testbed

To spectrally characterise the detector array as an integrated part of the DFI assembly, I have conducted experiments to measure the spectral performance of the interferometer. I have presented measurements of the spectral bandpass of the metal-mesh beamsplitters employed by the testbed. Through these, I have shown that a 7% improvement in the spectral bandwidth of the interferometer would be achieved by an optical redesign such that the angle of incident light on the beamsplitters is $\sim 22^{\circ}$. Using the DFI instrument as an FTS and spectrum analyser, I have measured the phase effects of the beamsplitters and shown that through a change in orientation, the non-linear phase effects from these can be minimized. With these characterisation experiments, I have determined a calibration Relative Spectral Response Function (RSRF) of the detector array and interferometer assembly and shown

Table 6.1: A summary of the central detector characterisation determined in this work.

Detector Performance Parameter	Default Settings	Optimised Settings
T_c [K]	8.2 ± 0.5	N/A
α	743 ± 2	N/A
Dynamic thermal conductance [μW/K]	0.22 ± 0.01	N/A
Saturation power at 320 GHz [nW]	$\sim$0.5	N/A
$\mathrm{NEP}_{\mathrm{optical}}$ at 90 Hz modulation [W/$\sqrt{\mathrm{Hz}}$]	9.4×10^{-10}	N/A
$\overline{\mathrm{NEP}}_{\mathrm{optical,FTS}}\big\vert_{250\,\mathrm{GHz}}^{2\,200\,\mathrm{GHz}}$ [W/$\sqrt{\mathrm{Hz}}$]	11.2×10^{-12}	3.4×10^{-12}
Effective time constant [ms]	0.96 ± 0.06	1.65 ± 0.01

that the interferometer has a spectral bandpass of 250–2 200 GHz. Through the appropriate selection of PID parameters, detector time constants can be adjusted such that the full spectral band of the FTS can be adequately sampled and low-frequency dominated signal bands of the detectors can be avoided.

Informed by my investigation in Chapter 4, I have determined a set of detector parameters that have reduced the spectral noise of the DFI testbed by $\sim$70%.

6.1.4 Detector performance summary

Through the experiments discussed in the work, I have measured several parameters of the array's central detector that describe the behaviour and performance of a feedback-controlled TES bolometer as a far-IR detector. These results are summarized in Table 6.1. Note that despite the slower response of the detector when operating with these parameters, they result in a substantial improvement in noise performance.

6.2 Future Characterisation

The efforts that I have presented and discussed in this work have provided an overall characterisation of the detector array as an integrated part of the DFI testbed. My studies can be applied to the entire detector array and have uncovered behaviours of the detector system that warrant further investigation. Here I discuss these topics and the results of

experiments that I have conducted to demonstrate avenues for further characterisation of the detector system.

6.2.1 Extending optimisation to the full array

This work has discussed tuning the operational parameters of the detector array to improve the system's performance and has in many cases been limited to an examination of the central detector of the array. In §4.1.1, I have shown that detector behaviour varies across the array and each detector may need dedicated PID tuning. To fully optimise the performance of the system, much of the analysis presented in this work can be extended to the other detectors of the array.

While this process is time-consuming, many of the measurements that are required are already in hand. Figure 6.1 shows that experiments employing the photomixer source have been measured by the full detector array. Measurements to determine the optimal parameters of the central detector to reduce noise while maintaining a sufficient time constant also contain the information necessary to optimise other detectors in the array (Chapter 4).

The high-temperature Pegasus blackbody source used to spectrally characterise the central detector (Chapter 5) only serves as a large enough source to characterise a few detectors at a time with a sufficient Signal-to-Noise Ratio (SNR). Figure 6.2 shows the output from the entire detector array during a FTS measurement of the blackbody source. As such, experiments using this source will require more iterations to characterise the entire detector array.

6.2.2 Multimoded detector behaviour

In §4.1.6, I have noted that with a subset of PID gains, multimoded behaviour in the central detector's signal when viewing a static optical load can be seen. These are the result of rapid changes to the steady state of the detector signal. To determine if these are a consequence of changes to the TES state, I conducted a series of measurements with the detectors operating in their TES profiling readout mode. Note that in doing so, the timing

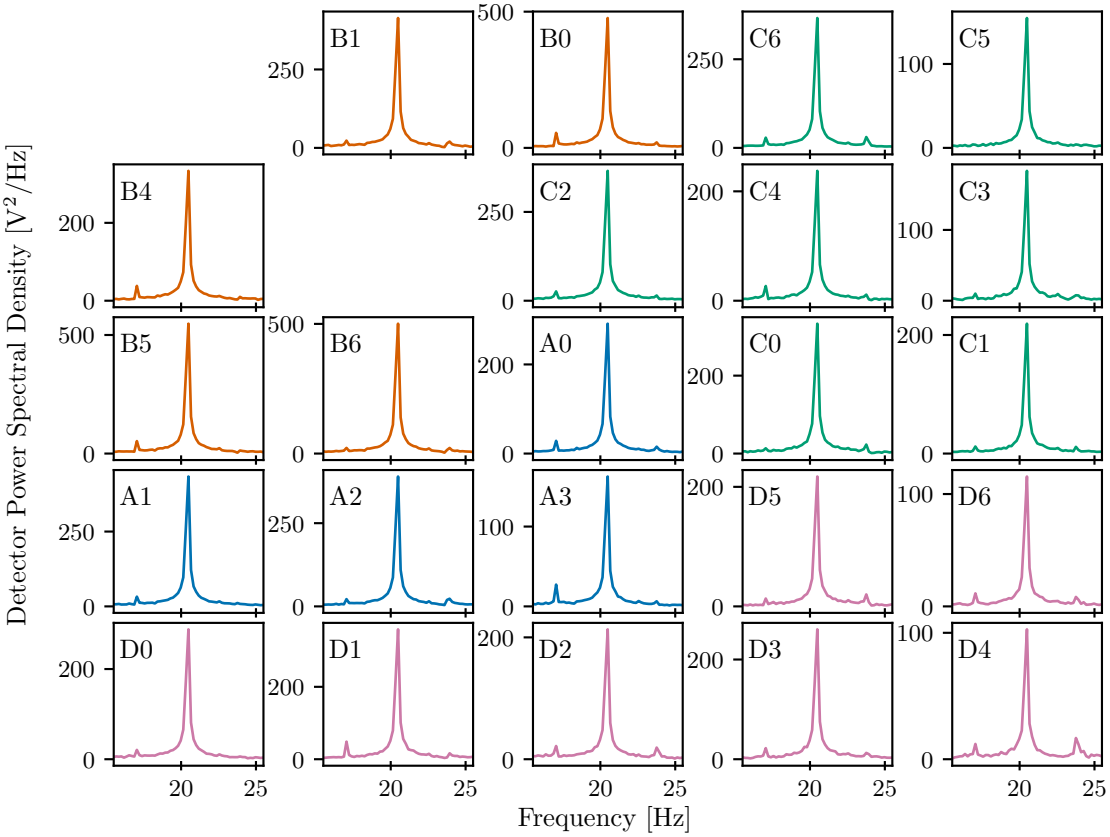


Figure 6.1: The spectral peak of detector signals while the full detector array views a photomixer source modulated by a physical chopper at ∼20 Hz. The layout of panels in the figure matches the convention of Figure 3.8. It should be noted that there are significant differences in detector calibration across the array.

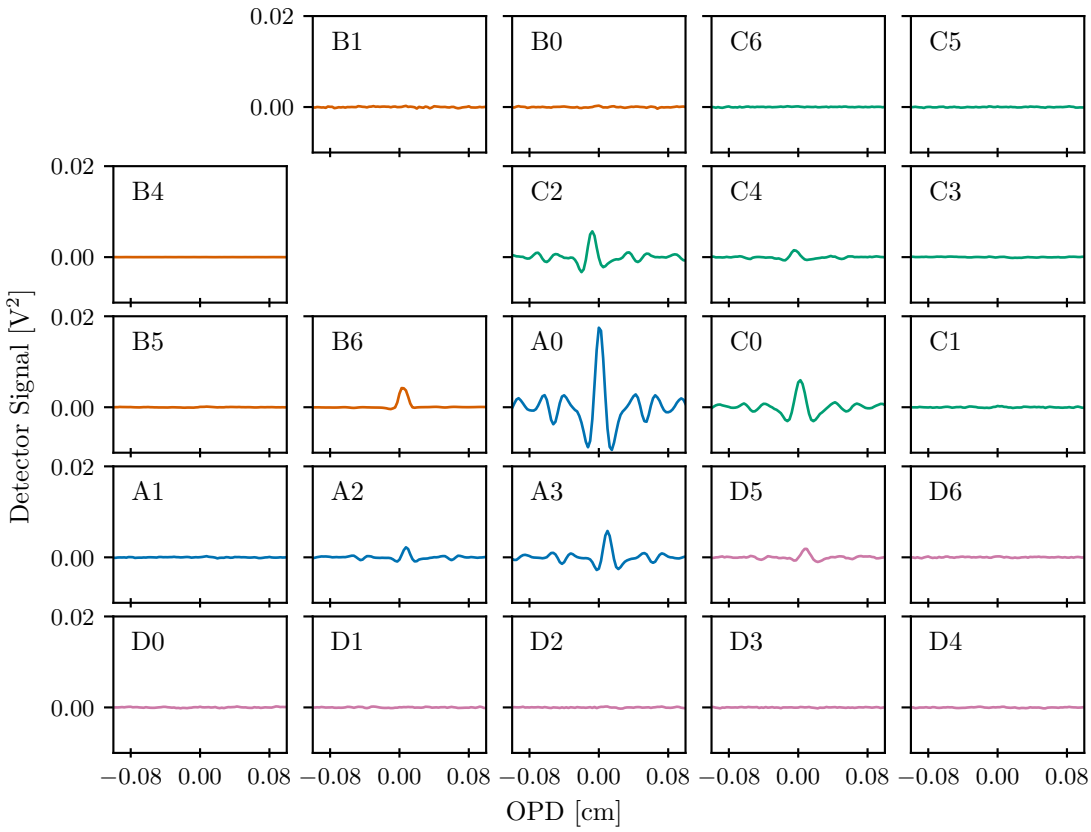


Figure 6.2: The interferograms viewed by each detector of the array corresponding to 100 spectral scans of the FTS while viewing the Pegasus blackbody source at 1 200°C.

of detector measurement pulses is fundamentally changed (see §4.1.4). Figure 6.3 demonstrates a measurement time stream from the central detector operating with proportional- and integral-term gains of 520 and 120, respectively, for which the multimodal detector behaviour can be seen. Two changes to the detector's steady state that occur over $\sim$50 detector samples are seen (marked in orange and green). Measurements of the TES profile near these transitions and the distribution of TES measurements that are used in the PID calculation show that these sharp changes do not coincide with differences from the nominal behaviour of the TES (marked in yellow). Additionally, there is no significant change to the distribution of TES at the read index.

Figure 6.4 shows the distribution of the TES state at each loop count within the measurement pulse for all three different regions. No significant changes to the distributions are seen across all three of these regions and the mean values corresponding to each agree to within ± 2 data units. This further suggests that these different steady states of the detector signal do not correspond to changes in the behaviour of the TES thermometer.

Figure 6.5 demonstrates a time-stream of data from the central detector that experiences a significant number of abrupt changes to its steady state. The distribution of the detector signal shows four modes of the detector's steady-state response. The amplitude of steady-state transitions corresponding to 10 minutes of detector data is also shown in Figure 6.5. The two largest groupings of transition amplitudes are clustered about a value of $\pm 650\,\mathrm{mV}^2$ which is near to (but not exactly) a flip of the 16th bit of the PID output variable. Additionally, there are clusters about $\pm 1\,300\,\mathrm{mV}^2$. As a point of clarity, it must be noted that these steady-state changes occur over 30–70 samples of the detector and are significantly larger than digitization effects from the 6 unused bits of the detector signal (see §4.1.3).

To determine if PID tuning has an effect on the distribution of the detector's multimoded profile, I determined the amplitude of the abrupt steady-state changes under a variety of PID conditions. These distributions are shown in Figure 6.6. Despite the changes in the detector's PID conditions, the amplitudes of these transitions remain grouped about $\pm 650\,\mathrm{mV}^2$

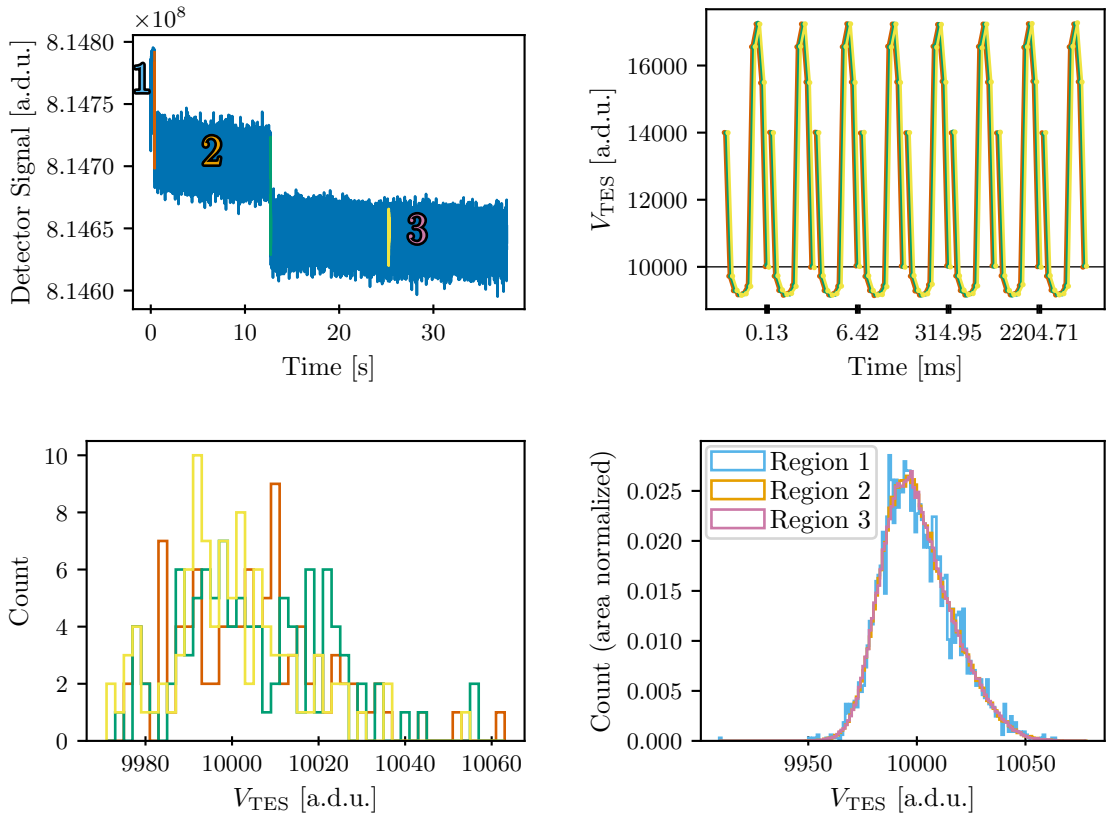


Figure 6.3: Measurements made with the central detector while viewing a static optical load and operating under PID conditions that result in a multimodal signal distribution are shown in the upper left panel. Regions where the signal experiences a sharp change in its steady state are coloured in orange and green, while a steady-state region of the signal is coloured in yellow. Three steady-state regions are also labelled. The upper right panel shows the TES behaviour during four full detector measurement pulses during the change in detector signal and in a steady-state region. The bottom left panel compares the distribution of the 50 TES state measurements at the read index for both transition regions and in the steady-state region. The bottom right panel demonstrates the distribution of TES state measurements at the read index in all three steady-state regions.

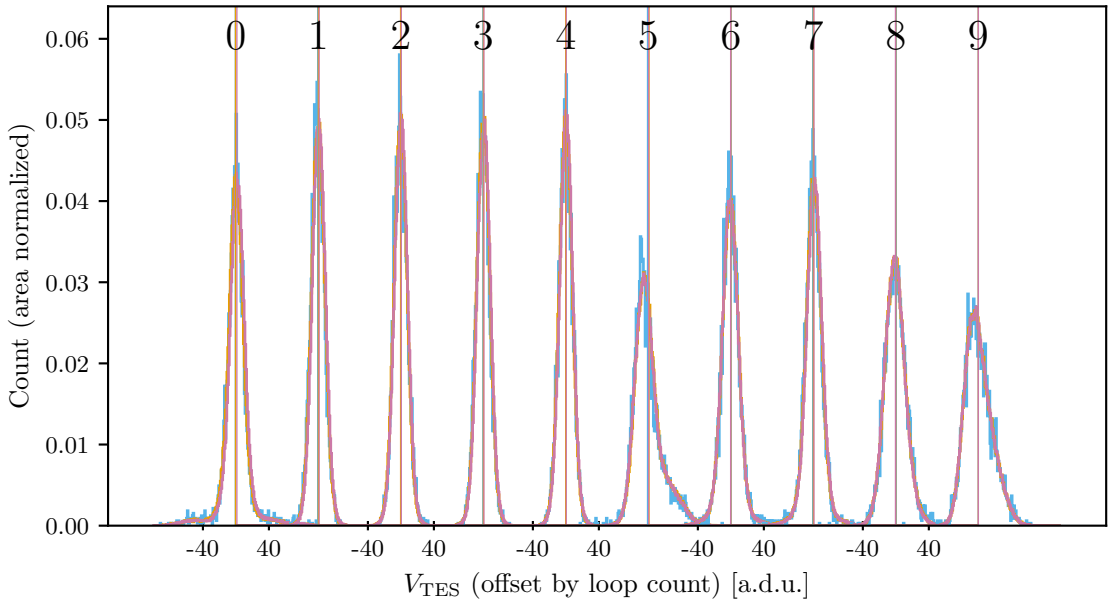


Figure 6.4: The distribution of the the TES thermometer state at each loop count of a measurement pulse for the three steady state regions identified in Figure 6.3. Each distribution has been grouped by the mean value at each loop count across all three distributions and offset for visual clarity. The vertical line marks the mean value of the distribution for each region.

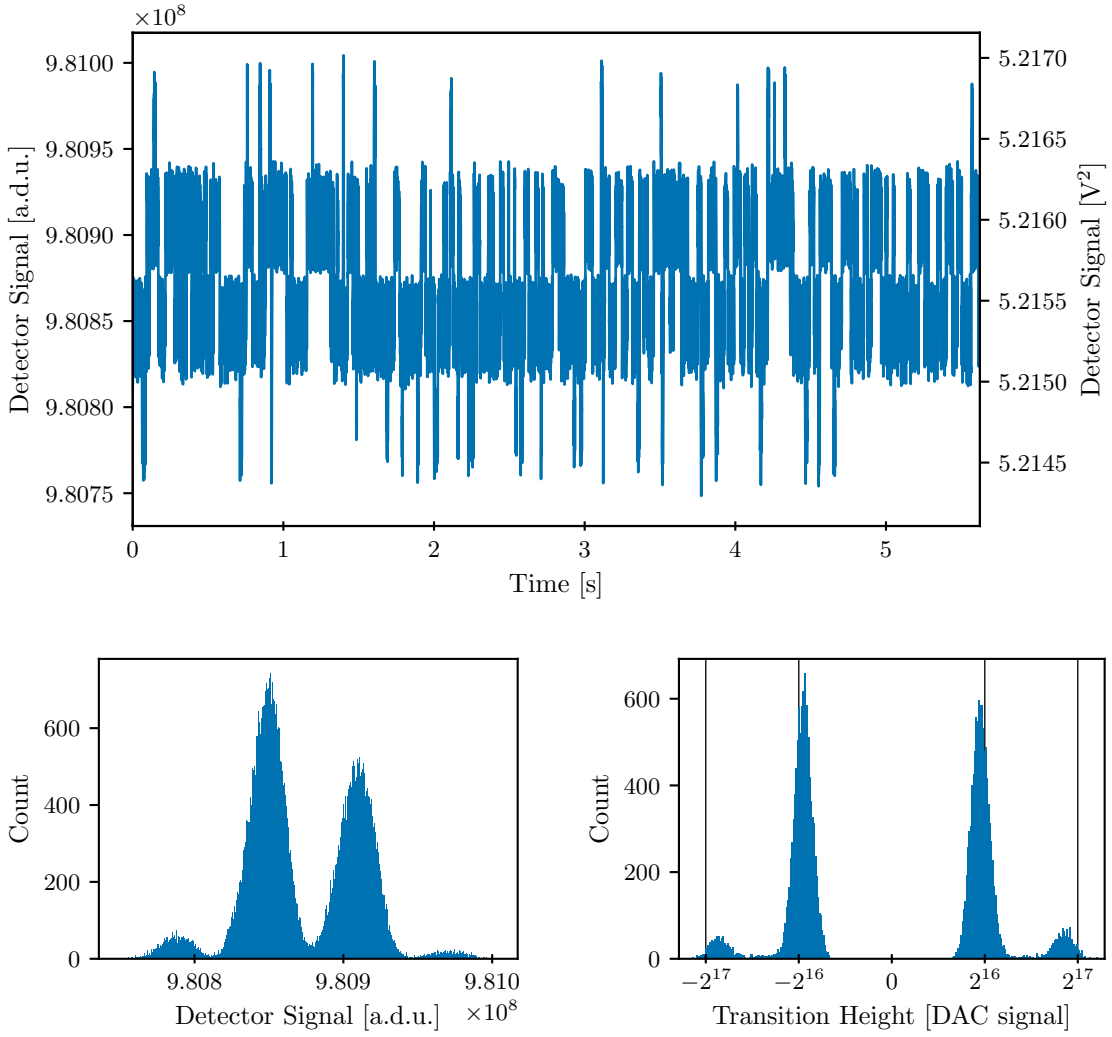


Figure 6.5: A time stream of data from the central detector that experiences several abrupt changes to its steady state while under a static optical load. The steady-state modes are shown in the detector signal distribution in the lower left panel. The lower right panel shows the distribution of the amplitude of transitions between modes from 10 minutes of detector data. Note that the detector signal corresponds to the 32-bit number sent to the heater Digital-to-Analogue Converter (DAC). The integer values corresponding to the 16th and 17th bits (counting from the least significant bit as bit 0) are marked by the vertical black lines.

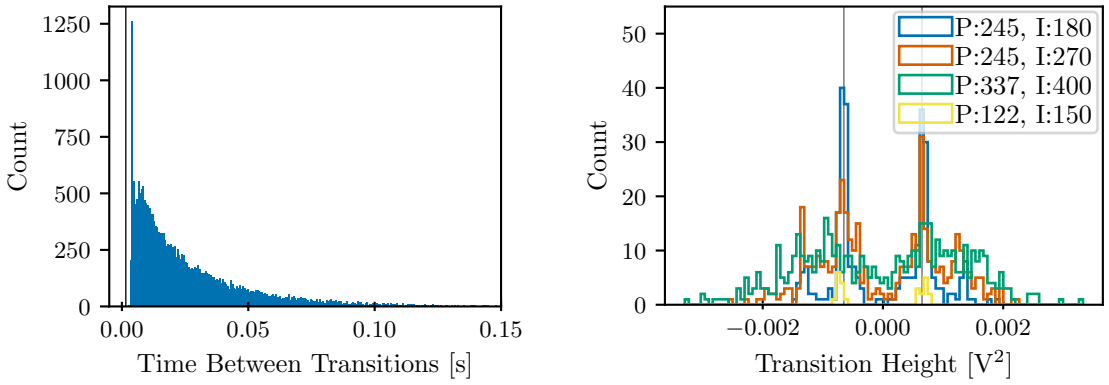


Figure 6.6: The time between transitions in the central detector's steady state (corresponding to the 10 minutes of detector measurements in Figure 6.5) is shown in the left panel. The vertical black line shows the smallest time interval between transitions that can be detected by the transition finding algorithm. The distribution of the amplitudes of steady-state changes in the central detector signal under a variety of PID conditions is shown in the right panel.

(shown by the vertical grey lines) and $\pm 1\,300\,\mathrm{mV}^2$. Increasing the integral-term gain of the PID loop is shown to increase the number of these transitions.

As these changes in the steady state do not increase in amplitude with changes to the proportional and integral terms of the PID loop, it becomes difficult to determine if they are present in signals with noise of a comparable amplitude (see §4.1.6). Additionally, Figure 6.6 demonstrates that transitions do not occur at regular intervals. This further increases the difficulty of isolating these effects from noisy signals through time averaging. It should be noted that to avoid false detections, the algorithm I have implemented to detect abrupt changes in the detector's steady-state signal is limited such that it will not report transitions within 20 detector samples of each other (corresponding to 1.55 ms). If this multimodal behaviour is a result of PID conditions and is not an underlying behaviour of the system, the optimzied parameters discussed in §5.4 have been chosen to have a proportional term gain higher than 500 data units. When coupled with the reduction in noise due to the selection of optimized detector measurement timing parameters, multimodal behaviour is observed with these optimised PID settings. This further suggests that this behaviour may not be a result of PID tuning and instead is present in all detector measurements and may be nominally

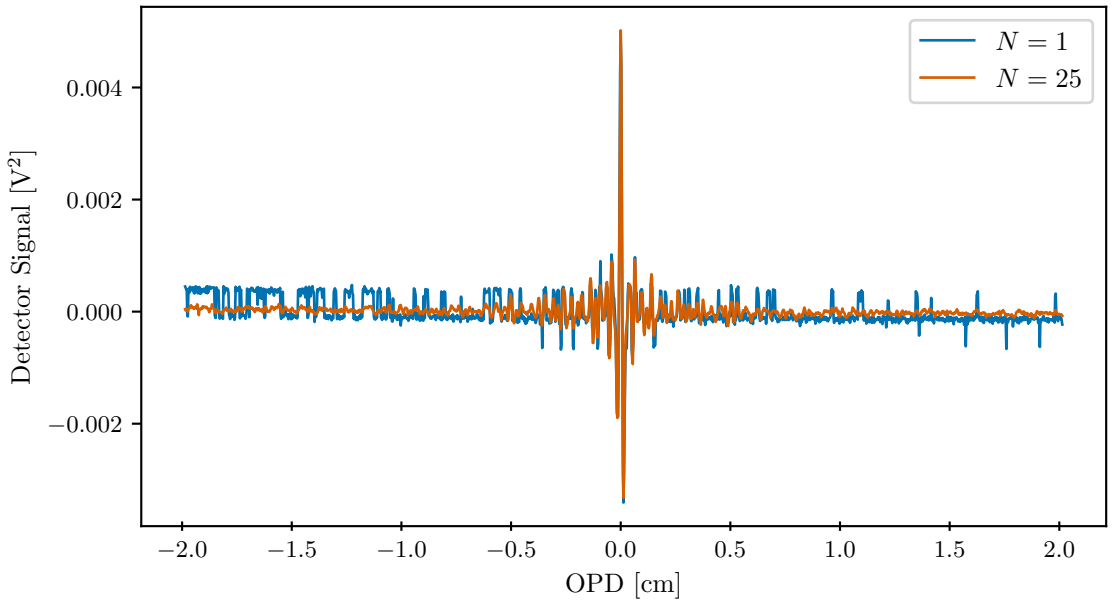


Figure 6.7: An interferogram measured by the central detector of the DFI testbed from a single spectral scan is compared against the average of 25 forward scans. The PID gain conditions of the detector are such that rapid changes to the detector's steady state signal can be seen.

hidden within the noise.

Through this elementary characterisation of these rapid changes to the detector's steady state, it is apparent that they can be mitigated to a significant degree through time averaging. Figure 6.7 shows a comparison between an interferogram obtained from a single spectral scan of the DFI testbed to the average of 25 forward scans. For these measurements, the central detector's PID gains were tuned such that rapid changes to the central detector's steady state are apparent.

While the effects of rapid changes to the detector's steady state can be treated through averaging, understanding the fundamental cause of these and if they are present in all detector measurements may provide further insight into detector performance and provide avenues for further optimisation.

6.2.3 Detector system beam-mapping

Both the detector NEP measurements discussed in Chapter 4 and measurements of the RSRF of the central detector and FTS assembly discussed in Chapter 5 depend on the frequency-dependant beam profile of the detector array. These measurements have employed a beam model in which all modes of the waveguide at the termination of the feed-horn are considered to propagate without attenuation. Though measurements of extraneous spectral features observed in the interferometer suggest that the multimoded beam model does provide a good approximation (see §5.3), these measurements do show some deviation from the expected profile and suffer from a high degree of atmospheric absorption.

Using the DFI testbed as an FTS with a broadband point source placed at one of its inputs, the (optical) frequency-dependent beam profile of each detector in the array can be determined. By taking spectral measurements of the FTS as the source is scanned through a raster pattern, the beam can be determined by a comparison of the spectral intensity at each position and frequency [21, 140].

6.2.4 Detector cross-talk

In Chapter 3, I discussed the coupling between the thermal and electrical behaviour of a TES bolometer. As such, detectors within the array experience both thermal and electrical coupling to each other. To study both thermal and electrical cross-talk, I manually cycled the heater of the central detector between a state of inactivity and near its maximum heating output and measured the response of other detectors within the array.

Figure 6.8 shows the average response of each detector in row 0 (other than A0) to the heating element on the central detector switching from an unpowered state to near its maximum heating power. For these measurements, the detector array is operating without multiplexing and the heater on the central detector has been cycled 100 times. Two prominent features can be seen: a dramatic drop in signal that occurs over less than 0.4 ms, and a decay feature with a longer time constant. While detector C0 is physically the closest to the

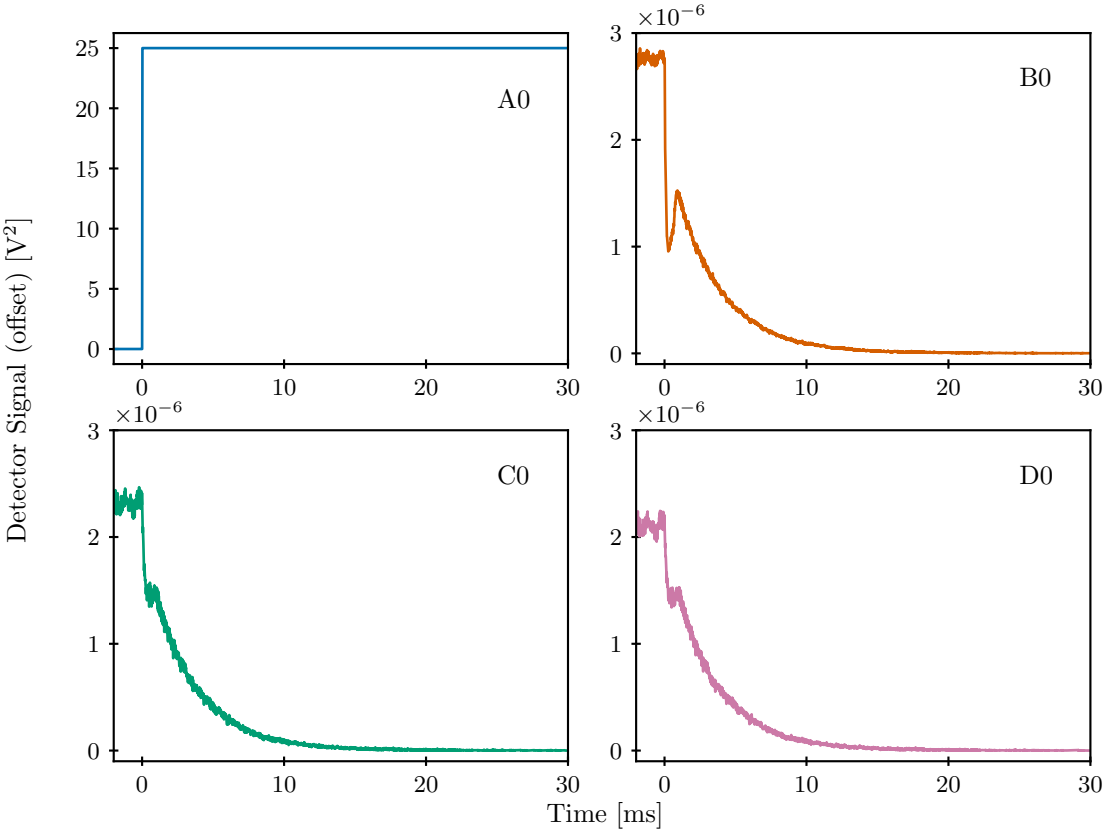


Figure 6.8: The response of detectors B0, C0, and D0 to a significant change in the power dissipated in the heater on detector A0.

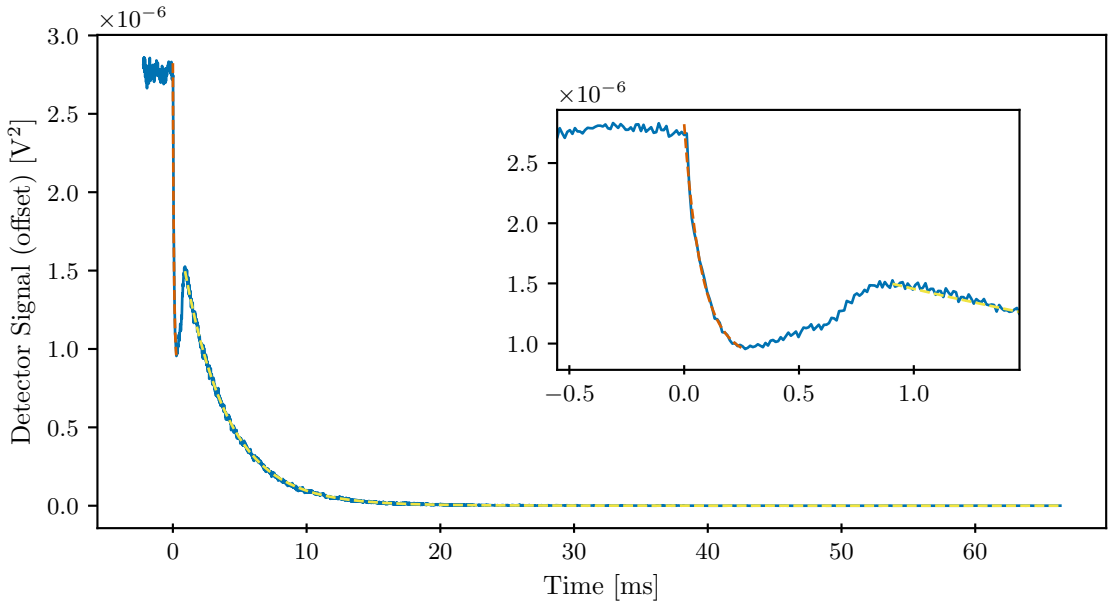


Figure 6.9: The response of detector B0 to a significant change in the power dissipated in the heater on detector A0 (as shown in Figure 6.8). Each feature of the detector's response was fit with a decay model. These are shown by the lightly coloured dashed lines. The inset shows a zoom-in on the first feature which has a rapid response.

central detector and greater thermal coupling is expected (see Figure 3.8), B0 experiences the most significant change to its equilibrium state.

A decay model was fit to both features of the response to a change in the heater state on A0. These are shown for detector B0 in Figure 6.9 and the parameters from each least-squares fit are summarized for all three responding detectors in Table 6.2. The feature with the slower response shows similar properties across all three detectors while the feature with the rapid time constant is much stronger in detector B0. It should be noted that channels A and B share a warm electronics board suggesting that the feature with a rapid time constant is a consequence of electrical cross-talk while the feature with a slower time constant is likely to be a result of thermal cross-talk.

When the detector system is employed by the DFI, the central burst of an interferogram corresponds to a change in heater power of $\sim$0.006 V^2, which is significantly smaller than the 25 V^2 change in heater power that I have used in this experiment. Despite this, the cross-

Table 6.2: Parameters extracted from a least-squares fit of the rapid and slow response features to a large change in the heater state on the central detector. See Figures 6.8 and 6.9.

Fitted Parameter	B0	CO	D0
Amplitude (rapid)	0.568	0.140	0.090 8
[mV^2]	$\pm$ 0.002	$\pm$ 0.001	$\pm$ 0.000 5
Amplitude (slow)	1.938 515	1.921 796	1.935 356
[mV^2]	$\pm$ 0.000 002	$\pm$ 0.000 005	$\pm$ 0.000 004
Time constant	0.096	0.18	0.16
(rapid) [ms]	$\pm$ 0.005	$\pm$ 0.03	$\pm$ 0.03
Time constant	6.463	6.30	6.32
(slow) [ms]	$\pm$ 0.009	$\pm$ 0.01	$\pm$ 0.01

talk features from this extreme example are small in relation to other detector noise features that have been discussed throughout Chapter 4 and §6.2.2 (by $\sim$3 orders of magnitude). The cross-talk effects that I have discussed may be affected by the chosen detector parameters. This dependence should be investigated promptly.

6.2.5 Forward and reverse scanning of the spectral stage

The majority of spectral measurements made with the DFI presented in this work correspond to a single direction of travel for the scanning spectral stage. Studying the asymmetries between scanning directions of an FTS can provide a useful method to decouple temporal sampling effects and optical features [139]. Figure 6.10 shows the average of 1 500 forward and reverse scans of the DFI in its FTS configuration. The residual shows a difference in the measurements from each scanning direction of the FTS which may indicate sampling differences between each direction. Should this be the case, the development of phase correction products from multiple scans of the FTS should consider each scan direction independently [83].

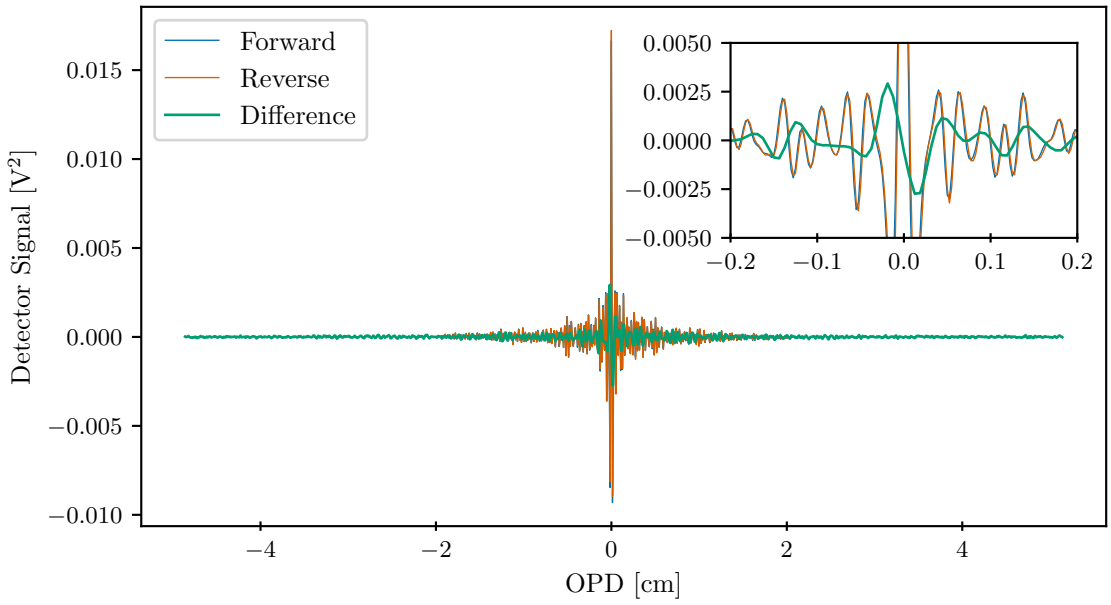


Figure 6.10: Average interferograms determined from 1 500 forward and reverse scans of the DFI testbed operating as an FTS and viewing a 1 200°C blackbody source.

6.2.6 Performance at multiple baselines

Much of the optimisation of the array I have discussed throughout this work has focused on the performance of the detector array with the DFI testbed operating as a nominal FTS. While the DFI instrument is used to measure interferograms in a similar fashion to an FTS, there are some important distinctions between both modes of operation. The spectra measured by the DFI testbed occur at different baseline separations and are attenuated by the complex visibility of the source (see Chapter 2). In general, spectra measured by the DFI testbed will have much lower amplitude than those measured in FTS mode. I have shown in Chapter 4 that detector noise is significantly reduced when operating with a relatively slow and passive PID control. If Step-and-Integrate (S&I) measurements made with the DFI testbed had an arrangement similar to a lock-in amplifier where external modulation is used to reject the low-frequency noise of the detectors, detector response speed need only be fast enough to sample the external modulation. In the DFI testbed's current rapid scan measurement strategy, detector time constants must be sufficiently fast to measure

the optical modulation from the highest optical frequency of its spectral bandpass while the spectral stage scans fast enough to avoid low-frequency dominated detector bands (see §5.3.1). It should be noted that should S&I measurements be made with the testbed, a full characterisation of the digital processing of observations of this type would be required.

In addition to lower amplitude spectra, the testbed only makes use of a single beamsplitter when operating in its full DFI configuration. As a result, the reduction in beamsplitter phase effects by changing their orientation in the optical path explored in Chapter 5 cannot be accomplished. Also, the beamsplitter phase effect characterisation that I have discussed cannot decouple the effects from a single beamsplitter. Using the DFI testbed and a third metal-mesh beamsplitter would allow the further investigation of beamsplitter performance that is required to fully characterise beamsplitter phase effects in the testbed operating in its spatial-spectral configuration.

6.3 Advancing far-IR interferometry in the next decade

The decision not to pursue a space-based far-IR interferometry mission proposal for NASA's forthcoming 4th quarter 2023 far-Infrared (IR)/X-ray probe-class mission opportunity prompts us, as members of the far-IR community, to consider how to advance DFI in the next decade in an effort to attain observations with sub-arcsecond angular resolution [12, 44, 50]. In their review, Farrah et al. (2018) note that detailed simulation, laboratory validation, and balloon-borne pathfinder missions are important steps towards future space-based far-IR interferometers [6]. Due to the limited capabilities of balloon-borne far-IR interferometers to achieve science goals beyond engineering demonstrations, there is an added onus on laboratory-based far-IR interferometry instruments as technology development platforms.

The DFI testbed instrument at the University of Lethbridge, to my knowledge, currently serves as the only operating far-IR DFI with a multipixel array of homodyne far-IR detectors. Building upon the technology and algorithm developments of the U.K. [55, 56, 57],

U.S.A. [53, 54], and Japanese [58] DFI testbed instruments, the Lethbridge DFI represents another significant step towards a laboratory-based analogue of a potential space-based DFI instrument particularly with respect to its wide-field imaging capabilities. With a well-calibrated and optimised detector system, coupled with the decades of FTS expertise within the University of Lethbridge Astronomical Instrumentation Group, the DFI we have constructed is well-positioned to continue technology development for DFI instruments throughout the next decade. This future work will further investigate how DFI instruments address the long-term goals of the international astronomical community and will prepare for future community reviews (e.g., the U.S. astronomy community decadal review process, the Canadian Astronomical Society Long Range Planning, and the European Space Agency Voyage 2050).

6.4 KIDS and the forward path for FIR detectors

As I have discussed in Chapter 3, the development of detector arrays with higher pixel counts and improved sensitivities has played a significant role in the progress of far-IR astronomy. Recently, astronomy at far-IR (and similar) wavelengths have turned to a superconducting detector technology other than TES bolometers, KIDs [164, 165, 166]. These detectors consist of a superconducting resonator that changes its resonant frequency and quality factor when incident light is absorbed. The absorbed light breaks Cooper pairs in the superconducting material and thus changes its kinetic inductance [102, 167]. KIDs are currently the simplest approach to high-multiplex-factor frequency-domain multiplexing and are significantly easier to fabricate than TES bolometers [6, 102]. As a consequence, they hold significant promise for large-format far-IR detector arrays [6, 102, 164].

KIDs have recently seen adoption by a number of far-IR and Sub-Millimetre (sub-mm) observatories including the Next-Generation Balloon-borne Large-Aperture Submillimeter Telescope (BLAST-TNG) [168] and The Mexico UK Sub-mm Camera for Astronomy (MUSCAT) [169]. With the NEP of the current generation of low-noise KIDs reach-

ing NEPs of $\sim 10^{-19}$ [W/$\sqrt{\text{H}}$], they have also seen particular attention for application in future space-based far-IR observatories including the Probe far-Infrared Mission for Astrophysics (PRIMA) [170, 171]. KIDs are a well-positioned technology to see further use and incorporation in the coming generation of far-IR observatories.

6.5 Final thoughts

This work ultimately represents a significant effort to understand and improve the performance of a complex system and is the result of several years of carefully designed experiments and data analysis. This has been a process of learning, iterating, and improving as I have navigated the unique position of fundamentally characterising a detector system without unfettered access to its fundamental components.

At the conclusion of my thesis, I find myself recalling two particular conversations that stand firmly in my mind. The first of these was a short discussion during an annual conference with a colleague who was also engaged in studying and developing astronomical instrumentation. Throughout the conversation, we discussed the importance of a rigorous examination of the instrumentation involved in any experiment, and through it, we arrived at the conclusion that truly understanding an instrument in all its aspects can only be described as beautiful.

The second conversation was a product of a meeting of the instrument performance modelling working group for the Space Interferometer for Cosmic Evolution (SPICE) [50] (in which it has been a privilege to participate). In this meeting, Dr. Leisawitz, who has a substantial career studying far-IR space observatories and interferometry from a space-based platform, made the well-justified statement that instruments of this type are an inevitability.

As we, as a community, endeavour to make substantial strides in the capabilities of far-IR instruments, progress through a rigorous examination of experiments conducted with laboratory-based instruments is crucial. A technical understanding of these instruments

and their systems is vital. Characterising this unique array of detectors stands as a foundational part of building the Lethbridge DFI that will continue to build towards a greater understanding of DFI in the far-IR.

Bibliography

[1] Bang Wong. Points of view: Color blindness. *Nature Methods*, 8(6), 2011.

[2] Charles Babbage. *Reflections on the Decline of Science in England, and on Some of Its Causes*. B. Fellowes, Ludgate Street; and J. Booth, Duke Street, Portland Place., 1830.

[3] Norwood Russell Hanson. *Patterns of Discovery: An Inquiry into the Conceptual Foundations of Science*. Cambridge University Press., revised edition edition, 1958.

[4] Ryley Hill, Kiyoshi W. Masui, and Douglas Scott. The Spectrum of the Universe. *Applied Spectroscopy*, 72(5):663–688, May 2018.

[5] Frank P. Helmich and R. J. Ivison. FIRI—A far-infrared interferometer. *Experimental Astronomy*, 23(1):245–276, March 2009.

[6] Duncan Farrah, Kimberly Ennico Smith, David Ardila, Charles M. Bradford, Michael Dipirro, Carl Ferkinhoff, Jason Glenn, Paul Goldsmith, David Leisawitz, Thomas Nikola, Naseem Rangwala, Stephen A. Rinehart, Johannes Staguhn, Michael Zemcov, Jonas Zmuidzinas, James Bartlett, Sean Carey, William J. Fischer, Julia Kamenetzky, Jeyhan Kartaltepe, Mark Lacy, Dariusz C. Lis, Lisa Locke, Enrique Lopez-Rodriguez, Meredith MacGregor, Elisabeth Mills, Samuel H. Moseley, Eric J. Murphy, Alan Rhodes, Matt Richter, Dimitra Rigopoulou, David Sanders, Ravi Sankrit, Giorgio Savini, John-David Smith, and Sabrina Stierwalt. Review: far-infrared instrumentation and technological development for the next decade. *Journal of Astronomical Telescopes, Instruments, and Systems*, 5:020901, April 2019.

[7] Giovanni Bignami and European Space Agency. *Cosmic vision: Space science for Europe 2015–2025*. ESA Publications Division, 2005.

[8] P.R. Roelfsema and the SPICA constortium. SPICA:Unveiling the obscure Universe. Technical report, SRON Netherlands Institute for Space Research, October 2016.

[9] National Academies of Sciences, Engineering, and Medicine. *Pathways to Discovery in Astronomy and Astrophysics for the 2020s*. National Academies Press, Washington DC, 2021.

[10] David Leisawitz, Charles Baker, Amy Barger, Dominic Benford, Andrew Blain, Rob Boyle, Richard Broderick, Jason Budinoff, John Carpenter, Richard Caverly, Phil Chen, Steve Cooley, Christine Cottingham, Julie Crooke, Dave DiPietro, Mike DiPirro, Michael Femiano, Art Ferrer, Jacqueline Fischer, Jonathan P. Gardner, Lou Hallock, Kenny Harris, Kate Hartman, Martin Harwit, Lynne Hillenbrand, Tupper

Hyde, Drew Jones, Jim Kellogg, Alan Kogut, Marc Kuchner, Bill Lawson, Javier Lecha, Maria Lecha, Amy Mainzer, Jim Mannion, Anthony Martino, Paul Mason, John Mather, Gibran McDonald, Rick Mills, Lee Mundy, Stan Ollendorf, Joe Pellicciotti, Dave Quinn, Kirk Rhee, Stephen Rinehart, Tim Sauerwine, Robert Silverberg, Terry Smith, Gordon Stacey, H. Philip Stahl, Johannes Staguhn, Steve Tompkins, June Tveekrem, Sheila Wall, and Mark Wilson. The space infrared interferometric telescope (SPIRIT): High-resolution imaging and spectroscopy in the far-infrared. *Advances in Space Research*, 40(5):689–703, January 2007.

[11] Thomas G. Phillips and Jocelyn Keene. Submillimeter astronomy. *IEEE Proceedings*, 80(11):1662–1678, November 1992.

[12] Hendrik Linz, Henrik Beuther, Maryvonne Gerin, Javier R. Goicoechea, Frank Helmich, Oliver Krause, Yao Liu, Sergio Molinari, Volker Ossenkopf-Okada, Jorge Pineda, Marc Sauvage, Eva Schinnerer, Floris van der Tak, and Martina Wiedner. Bringing high spatial resolution to the Far-infrared – A giant leap for astrophysics. *arXiv e-prints*, page arXiv:2002.06693, February 2020.

[13] B. Gundlach and J. Blum. The Stickiness of Micrometer-sized Water-ice Particles. *Astrophysical Journal*, 798(1):34, January 2015.

[14] D. E. Backman, A. Dasgupta, and R. E. Stencel. Model of a Kuiper Belt Small Grain Population and Resulting Far-Infrared Emission. *Astrophysical Journal*, 450:L35, September 1995.

[15] P. Santos-Sanz, E. Lellouch, S. Fornasier, C. Kiss, A. Pal, T. G. Müller, E. Vilenius, J. Stansberry, M. Mommert, A. Delsanti, M. Mueller, N. Peixinho, F. Henry, J. L. Ortiz, A. Thirouin, S. Protopapa, R. Duffard, N. Szalai, T. Lim, C. Ejeta, P. Hartogh, A. W. Harris, and M. Rengel. "TNOs are Cool": A survey of the trans-Neptunian region. IV. Size/albedo characterization of 15 scattered disk and detached objects observed with Herschel-PACS. *Astronomy and Astrophysics*, 541:A92, May 2012.

[16] J. E. Dyson and D. A. Williams. *Physics of the interstellar medium*. 1980.

[17] A. G. G. M. Tielens. *The Physics and Chemistry of the Interstellar Medium*. 2005.

[18] Dan M. Watson, Nuria P. Calvet, William J. Fischer, W. J. Forrest, P. Manoj, S. Thomas Megeath, Gary J. Melnick, Joan Najita, David A. Neufeld, Patrick D. Sheehan, Amelia M. Stutz, and John J. Tobin. Evolution of Mass Outflow in Protostars. *Astrophysical Journal*, 828(1):52, September 2016.

[19] P. Manoj, D. M. Watson, D. A. Neufeld, S. T. Megeath, R. Vavrek, Vincent Yu, R. Visser, E. A. Bergin, W. J. Fischer, J. J. Tobin, A. M. Stutz, B. Ali, T. L. Wilson, J. Di Francesco, M. Osorio, S. Maret, and C. A. Poteet. Herschel/PACS Spectroscopic Survey of Protostars in Orion: The Origin of Far-infrared CO Emission. *Astrophysical Journal*, 763(2):83, February 2013.

[2020] The Vaccines. Come of Age.

[20] E. Furlan, W. J. Fischer, B. Ali, A. M. Stutz, T. Stanke, J. J. Tobin, S. T. Megeath, M. Osorio, L. Hartmann, N. Calvet, C. A. Poteet, J. Booker, P. Manoj, D. M. Watson, and L. Allen. The Herschel Orion Protostar Survey: Spectral Energy Distributions and Fits Using a Grid of Protostellar Models. *Astrophysical Journal Supplement Series*, 224(1):5, May 2016.

[21] Gibion Makiwa. *A study of the physics of the interstellar medium using the Herschel-SPRE instrument*. PhD thesis, University of Lethbridge, 2014.

[22] P. Panuzzo, N. Rangwala, A. Rykala, K. G. Isaak, J. Glenn, C. D. Wilson, R. Auld, M. Baes, M. J. Barlow, G. J. Bendo, J. J. Bock, A. Boselli, M. Bradford, V. Buat, N. Castro-Rodríguez, P. Chanial, S. Charlot, L. Ciesla, D. L. Clements, A. Cooray, D. Cormier, L. Cortese, J. I. Davies, E. Dwek, S. A. Eales, D. Elbaz, T. Fulton, M. Galametz, F. Galliano, W. K. Gear, H. L. Gomez, M. Griffin, S. Hony, L. R. Levenson, N. Lu, S. Madden, B. O'Halloran, K. Okumura, S. Oliver, M. J. Page, A. Papageorgiou, T. J. Parkin, I. Pérez-Fournon, M. Pohlen, E. T. Polehampton, E. E. Rigby, H. Roussel, N. Sacchi, M. Sauvage, B. Schulz, M. R. P. Schirm, M. W. L. Smith, L. Spinoglio, J. A. Stevens, S. Srinivasan, M. Symeonidis, B. Swinyard, M. Trichas, M. Vaccari, L. Vigroux, H. Wozniak, G. S. Wright, and W. W. Zeilinger. Probing the molecular interstellar medium of M82 with Herschel-SPIRE spectroscopy. *Astronomy and Astrophysics*, 518:L37, July 2010.

[23] Michael G Hauser and Eli Dwek. The cosmic infrared background: measurements and implications. *Annual Review of Astronomy and Astrophysics*, 39(1):249–307, 2001.

[24] Andrew W. Blain, Ian Smail, R. J. Ivison, J. P. Kneib, and David T. Frayer. Submillimeter galaxies. *Physics Reports*, 369(2):111–176, October 2002.

[25] Piero Madau and Mark Dickinson. Cosmic star-formation history. *Annual Review of Astronomy and Astrophysics*, 52(1):415–486, 2014.

[26] J. L. Pineda, W. D. Langer, T. Velusamy, and P. F. Goldsmith. A Herschel [C ii] Galactic plane survey. I. The global distribution of ISM gas components. *Astronomy and Astrophysics*, 554:A103, June 2013.

[27] Simons Observatory Collaboration et al. The Simons Observatory: science goals and forecasts. *Journal of Cosmology and Astroparticle Physics*, 2019(2):056, February 2019.

[28] Planck Collaboration et al. Planck 2018 results - xi. polarized dust foregrounds. *A&A*, 641:A11, 2020.

[29] Frank J. Low. Low-temperature germanium bolometer. *J. Opt. Soc. Am.*, 51(11):1300–1304, Nov 1961.

[30] P. Langley. The bolometer. *Nature*, 25:14–16, 1881.

[31] K. Shivanandan, D. P. McNutt, S. Price, and T. Murdock. Far Infrared Sky Survey Experiment. In I. J. Spiro, editor, *Utilization of infrared detectors*, volume 132 of *Society of Photo-Optical Instrumentation Engineers (SPIE) Conference Series*, pages 75–80, January 1978.

[32] G. Neugebauer, H. J. Habing, R. van Duinen, H. H. Aumann, B. Baud, C. A. Beichman, D. A. Beintema, N. Boggess, P. E. Clegg, T. de Jong, J. P. Emerson, T. N. Gautier, F. C. Gillett, S. Harris, M. G. Hauser, J. R. Houck, R. E. Jennings, F. J. Low, P. L. Marsden, G. Miley, F. M. Olnon, S. R. Pottasch, E. Raimond, M. Rowan-Robinson, B. T. Soifer, R. G. Walker, P. R. Wesselius, and E. Young. The Infrared Astronomical Satellite (IRAS) mission. *Astrophysical Journal*, 278:L1–L6, March 1984.

[33] W. S. Holland, D. Bintley, E. L. Chapin, A. Chrysostomou, G. R. Davis, J. T. Dempsey, W. D. Duncan, M. Fich, P. Friberg, M. Halpern, K. D. Irwin, T. Jenness, B. D. Kelly, M. J. MacIntosh, E. I. Robson, D. Scott, P. A. R. Ade, E. Atad-Ettedgui, D. S. Berry, S. C. Craig, X. Gao, A. G. Gibb, G. C. Hilton, M. I. Hollister, J. B. Kycia, D. W. Lunney, H. McGregor, D. Montgomery, W. Parkes, R. P. J. Tilanus, J. N. Ullom, C. A. Walther, A. J. Walton, A. L. Woodcraft, M. Amiri, D. Atkinson, B. Burger, T. Chuter, I. M. Coulson, W. B. Doriese, C. Dunare, F. Economou, M. D. Niemack, H. A. L. Parsons, C. D. Reintsema, B. Sibthorpe, I. Smail, R. Sudiwala, and H. S. Thomas. SCUBA-2: the 10 000 pixel bolometer camera on the James Clerk Maxwell Telescope. *Monthly Notices of the Royal Astronomical Society*, 430(4):2513–2533, April 2013.

[34] Walter M. Elsasser. Far Infrared Absorption of Atmospheric Water Vapor. *Astrophysical Journal*, 87:497, June 1938.

[35] Ian M. Chapman, David A. Naylor, and Robin R. Phillips. Correlation of atmospheric opacity measurements by SCUBA and an infrared radiometer. *Monthly Notices of the Royal Astronomical Society*, 354(2):621–628, October 2004.

[36] Ian Myles Chapman. The atmosphere above Mauna Kea at mid-infrared wavelengths. Master's thesis, University of Lethbridge, 2002.

[37] M. J. Griffin et al. The Herschel-SPIRE instrument and its in-flight performance. *Astronomy and Astrophysics*, 518:L3, July 2010.

[38] Max Born and Emil Wolf. *Principles of optics : electromagnetic theory of propagation, interference and diffraction of light*. 1999.

[39] Eugene Hecht. *Optics*. Addison-Wesley Publishion Company, second edition, 1987.

[40] Martin Harwit, David Leisawitz, and Stephen Rinehart. A far-infrared/submillimeter kilometer-baseline interferometer in space. *New Astronomy Reviews*, 50(1):228–234, 2006. First Light and Reionization: Theoretical Study and Experimental Detection of First Luminous Sources in the Universe.

[41] National Research Council et al. *Astronomy and astrophysics in the new millennium*. National Academies Press, Washington DC, 2001.

[42] A Lyngvi, J. M. P. Armengol, A Barton, G Chirulli, D Escorial, P Fabry, S Gidlund, D Hagelschuer, P Holsters, M Khan, et al. Far infrared interferometer technology reference study. In *57th International Astronautical Congress*, pages A3–1, 2006.

[43] D Schito, S Pezzuto, and W Holland. Far Infra-red Space Intereferometer Critical Assessment:definition/update of key science questions and relevant data products. Technical report, 2014. Last Editor: L. Spinoglio.

[44] Hendrick Linz, Henrik Beuther, Maryvonne Gerin, Javier R Goicoechea, Frank Helmich, Oliver Krause, Yao Liu, Sergio Molinari, Volker Ossenkopf-Okada, Jorge Pineda, Marc Sauvage, Eva Schinnerer, Floris van der Tak, and Martina Wiedner. ESA Voyage 2050 White Paper bringing high spatial resolution to the Far-infrared–A giant leap for astrophysics. *arXiv preprint arXiv:2002.06693*, 2020.

[45] Dominic J. Beford and David T. Leisawitz. Probing the Invisible Universe: The case for far-ir / submillimeter interferometry. In *New Concepts for Far-Infrared and Submillimeter Space Astronomy*, 2004.

[46] S. A. Rinehart, G. Savini, W. Holland, O. Absil, D. Defrère, L. Spencer, D. Leisawitz, M. Rizzo, R. Juanola-Paramon, and D. Mozurkewich. The path to interferometry in space. In Fabien Malbet, Michelle J. Creech-Eakman, and Peter G. Tuthill, editors, *Optical and Infrared Interferometry and Imaging V*, volume 9907, page 99070S. International Society for Optics and Photonics, SPIE, 2016.

[47] Stephen Rinehart, J. Arenberg, E. Baines, C. H. Chen, L. Ilsedore Cleeves, M. J. Creech-Eakman, D. Dale, W. Danchi, D. Farrah, R. Juanola-Parramon, S. Kraus, J. S. Knight, S. Lipscy, D. T. Leisawitz, M. A. MacGregor, B. Mennesson, J. Monnier, D. A. Naylor, R. O'Connor, A. Roberge, G. Savini, H. Schmitt, M. Sewilo, L. D. Spencer, T. A. ten Brummelaar, G. van Belle, and H. W. Yorke. A Long-Term Vision for Space-Based Interferometry. In *Bulletin of the American Astronomical Society*, volume 51, page 222, September 2019.

[48] David Leisawitz, John C. Mather, Jr. Harvey Moseley, S., and Xiaolei Zhang. The Submillimeter Probe of the Evolution of Cosmic Structure (SPECS). *Astrophysics and Space Science*, 269:563–567, December 1999.

[49] Martin Harwit, David Leisawitz, and Stephen Rinehart. A far-infrared/submillimeter kilometer-baseline interferometer in space. *New Astronomy Reviews*, 50(1-3):228–234, March 2006.

[50] David Leisawitz, Susanne Aalto, Jennifer Bergner, Matteo Bonato, Colm bracken, Stephen Eales, Duncan Farrah, Grant Kennedy, Alan Kogut, Joshua Lovell, Luca Matra, Taro Matsuo, Brenda Matthews, Melissa McClure, Lee Mundy, Joan Najita, Nicole Pawellek, Petr Pokorny, David Sanders, Nicholas Scoville, Irene Shivaei, Locke Spencer, Kate Su, Jessica Sutter, Leon Trapman, Carole Tucker, C. Meg

Urry, Serena Viti, David Wilner, Grant Wilson, Mark Wyatt, Dave DiPietro, Michael DiPirro, Tupper Hyde, Antonios Seas, and Steven Tompkins. The Space Interferometer for Cosmic Evolution (SPICE) Far-IR Probe. In *American Astronomical Society Meeting Abstracts*, volume 55 of *American Astronomical Society Meeting Abstracts*, page 160.04, January 2023.

[51] S. A. Rinehart, M. Rizzo, D. J. Benford, D. J. Fixsen, T. J. Veach, A. Dhabal, D. T. Leisawitz, L. G. Mundy, R. F. Silverberg, R. K. Barry, J. G. Staguhn, R. Barclay, J. E. Mentzell, M. Griffin, P. A. R. Ade, E. Pascale, G. Klemencic, G. Savini, and R. Juanola-Parramon. The Balloon Experimental Twin Telescope for Infrared Interferometry (BETTII): An Experiment for High Angular Resolution in the Far-Infrared. *Publications of the Astronomical Society of the Pacific*, 126(941):660, July 2014.

[52] S. A. Rinehart, A. Dhabal, D. Fixsen, R. Juanola-Parramon, D. Leisawitz, S. Maher, J. E. Mentzell, L. Mundy, M. Rizzo, H. Sampler, E. Sharp, R. Silverberg, M. Casalprim Torres, T. Veach, J. Vila Hernández de Lorenzo, P. A. R. Ade, C. Tucker, E. Pascale, and G. Savini. The Balloon Experimental Twin Telescope for infrared interferometry (BETTII): first flight. In Heather K. Marshall and Jason Spyromilio, editors, *Ground-based and Airborne Telescopes VII*, volume 10700 of *Society of Photo-Optical Instrumentation Engineers (SPIE) Conference Series*, page 107000F, July 2018.

[53] David T. Leisawitz, Brad J. Frey, Douglas B. Leviton, Anthony J. Martino, William L. Maynard, Lee G. Mundy, Stephen A. Rinehart, Stacy H. Teng, and Xiaolei Zhang. Wide-field imaging interferometry testbed I: purpose, testbed design, data, and synthesis algorithms. In Michael Shao, editor, *Interferometry in Space*, volume 4852 of *Society of Photo-Optical Instrumentation Engineers (SPIE) Conference Series*, pages 255–267, February 2003.

[54] Roser Juanola-Parramon, David T. Leisawitz, Matthew R. Bolcar, Stephen F. Maher, Stephen A. Rinehart, Alex Iacchetta, and Giorgio Savini. The Wide-field Imaging Interferometry Testbed (WIIT): recent progress in the simulation and synthesis of WIIT data. In Fabien Malbet, Michelle J. Creech-Eakman, and Peter G. Tuthill, editors, *Optical and Infrared Interferometry and Imaging V*, volume 9907 of *Society of Photo-Optical Instrumentation Engineers (SPIE) Conference Series*, page 990740, August 2016.

[55] P Ade and E Pascale. Far Infra-red Space Intereferometer Critical Assessment:multiple beam combining spectral-spatial interferometer testbed. Technical report, 2014. Last Editor: L. Spinoglio.

[56] Locke D. Spencer, David A. Naylor, Giorgio Savini, and Peter A. R. Ade. Spatial/spectral interferometry development for far-infrared space applications. In *2014 39th International Conference on Infrared, Millimeter, and Terahertz waves (IRMMW-THz)*, pages 1–2, 2014.

[57] William F. Grainger, Roser Juanola-Parramon, Peter A. R. Ade, Matt Griffin, Flo Liggins, Enzo Pascale, Giorgio Savini, and Bruce Swinyard. Demonstration of spectral and spatial interferometry at THz frequencies. *Appl. Opt.*, 51(12):2202–2211, Apr 2012.

[58] Izumi S. Ohta, Makoto Hattori, and Hiroshi Matsuo. Development of a multi-Fourier-transform interferometer: imaging experiments in millimeter and submillimeter wave bands. *Appl. Opt.*, 46(15):2881–2892, May 2007.

[59] Locke D Spencer, Peter A R Ade, William F Grainger, Matt J Griffin, Roser Juanola-Parramon, David A Naylor, Enzo Pascale, Giorgio Savini, and Bruce M Swinyard. Development of a far-infrared double Fourier spatial/spectral interferometry laboratory testbed instrument. In *Fourier Transform Spectroscopy*, pages FT4A–6. Optica Publishing Group, 2015.

[60] Locke D Spencer, David A Naylor, Jeremy P Scott, Vince F Weiler, Roderick K MacCrimmon, Geoffrey R H Sitwell, and Peter A R Ade. A far-infrared spatial/spectral Fourier interferometry laboratory-based testbed instrument. In *Millimeter, Submillimeter, and Far-Infrared Detectors and Instrumentation for Astronomy VIII*, volume 9914, pages 430–442. SPIE, 2016.

[61] Locke D Spencer, Chris S Benson, Jeremy P Scott, Geoffrey R H Sitwell, Adam Sundberg, Vince F Weiler, and David A Naylor. Progress towards a far-infrared spatial/spectral interferometry laboratory testbed instrument. In *Fourier Transform Spectroscopy*, pages FT3B–1. Optica Publishing Group, 2018.

[62] Jeremy Scott, Chris Benson, and Locke Spencer. Design, operation, and characterization of a laboratory spatial-spectral fourier transform interferometer. *IEEE Transactions on Terahertz Science and Technology*, 13(6):636–644, 2023.

[63] A. A. Michelson and F. G. Pease. Measurement of the Diameter of α Orionis with the Interferometer. *Astrophysical Journal*, 53:249–259, May 1921.

[64] Ludwig Mach. Ueber einen interferenzrefraktor. *Zeitschrift für Instrumentenkunde*, 12(3):89, 1892.

[65] Richard Feynman. Nobel lecture. Nobel Prize Outreach, 1965.

[66] John Herivel. *Joseph Fourier: the man and the physicist*. Clarendon Press, 1975.

[67] Jean Baptiste Joseph baron Fourier. *Théorie analytique de la chaleur*. F. Didot, 1822. Title translation: The Analytical Theory of Heat.

[68] Kenneth Franklin Riley, Michael Paul Hobson, and Stephen John Bence. *Mathematical methods for physics and engineering: a comprehensive guide*. Cambridge university press, 2006.

[69] Peter Gustav Lejeune Dirichlet and Philipp Ludwig Seidel. *Die Darstellung ganz willkürlicher Functionen durch Sinus-und Cosinusreihen: von Lejeune Dirichlet (1837), und Note über eine Eigenschaft der Reihen, welche discontinuirliche Functionen darstellen, von Philipp Ludwig Seidel (1847)*, volume 116. W. Engelmann, 1900.

[70] Rao B Visvesvara et al. *Signals and systems*. PHI Learning Pvt. Ltd., 2008.

[71] Locke Dean Spencer. *Imaging Fourier transform spectroscopy from a space based platform: the Herschel/SPIRE Fourier transform spectrometer.* PhD thesis, University of Lethbridge, 2009.

[72] Sumner P Davis, Mark C Abrams, and James W Brault. *Fourier transform spectrometry*. Elsevier, 2001.

[73] Albert A Michelson and Edward W Morley. On the relative motion of the earth and of the luminiferous ether. *Sidereal Messenger, vol. 6, pp. 306-310*, 6:306–310, 1887.

[74] Alex Abramovici, William E Althouse, Ronald WP Drever, Yekta Gürsel, Seiji Kawamura, Frederick J Raab, David Shoemaker, Lisa Sievers, Robert E Spero, Kip S Thorne, et al. Ligo: The laser interferometer gravitational-wave observatory. *science*, 256(5055):325–333, 1992.

[75] F Grandmont, L Drissen, Julie Mandar, S Thibault, and Marc Baril. Final design of SITELLE: a wide-field imaging Fourier transform spectrometer for the Canada-France-Hawaii Telescope. In *Ground-Based and Airborne Instrumentation for Astronomy IV*, volume 8446, page 84460U. International Society for Optics and Photonics, 2012.

[76] Kjetil Dohlen, Alain Origne, Dominque Pouliquen, and Bruce M. Swinyard. Optical design of the SPIRE instrument for FIRST. In James B. Breckinridge and Peter Jakobsen, editors, *UV, Optical, and IR Space Telescopes and Instruments*, volume 4013 of *Society of Photo-Optical Instrumentation Engineers (SPIE) Conference Series*, pages 119–128, July 2000.

[77] Robert John Bell and R. N. Bracewell. Introductory Fourier Transform Spectroscopy. *American Journal of Physics*, 41(1):149–151, January 1973.

[78] Edward G. Codding and Gary Horlick. Apodization and Phase Information in Fourier Transform Spectroscopy. *Applied Spectroscopy*, 27(2):85–92, March 1973.

[79] David A Naylor and Margaret K Tahic. Apodizing functions for Fourier transform spectroscopy. *JOSA A*, 24(11):3644–3648, 2007.

[80] A. S. Filler. Apodization and Interpolation in Fourier-Transform Spectroscopy. *Journal of the Optical Society of America (1917-1983)*, 54(6):762, June 1964.

[81] Locke Dean Spencer. Spectral characterization of the Herschel/SPIRE photometer. Master's thesis, University of Lethbridge, 2005.

[82] Bhagwandas Pannalal Lathi and Roger A Green. *Signal processing and linear systems*, volume 2. Oxford University Press Oxford, 1998.

[83] T. Fulton, D. A. Naylor, E. T. Polehampton, I. Valtchanov, R. Hopwood, N. Lu, J.-P. Baluteau, G. Mainetti, C. Pearson, A. Papageorgiou, S. Guest, L. Zhang, P. Imhof, B. M. Swinyard, M. J. Griffin, and T. L. Lim. The data processing pipeline for the Herschel SPIRE Fourier Transform Spectrometer. *Monthly Notices of the Royal Astronomical Society*, 458(2):1977–1989, 02 2016.

[84] Janine Connes. Computing Problems in Fourier Spectroscopy. In George A. Vanasse, Jr. Stair, A. T., and Doran J. Baker, editors, *Fourier Spectroscopy*, page 83, January 1971.

[85] Harry Nyquist. Certain topics in telegraph transmission theory. *Transactions of the American Institute of Electrical Engineers*, 47(2):617–644, 1928.

[86] C.E. Shannon. Communication in the presence of noise. *Proceedings of the IRE*, 37(1):10–21, jan 1949.

[87] James W Cooley and John W Tukey. An algorithm for the machine calculation of complex Fourier series. *Mathematics of computation*, 19(90):297–301, 1965.

[88] Christiaan Huygens. *Traité de la lvmière: où sont expliquées les causes de ce qui luy arrive dans la réflexion & dans la réfraction, et particulièrement dans l'étrange réfraction dv cristal d'Islande*. Pierre van der Aa, 1967.

[89] Auguste Fresnel. Mémoire sur la diffraction de la lumière. *Oeuvres complétes*, 1:247–363, 1819.

[90] Pieter Hendrik van Cittert. Die wahrscheinliche Schwingungsverteilung in einer von einer Lichtquelle direkt oder mittels einer Linse beleuchteten Ebene. *Physica*, 1(1-6):201–210, 1934.

[91] Frederik Zernike. The concept of degree of coherence and its application to optical problems. *Physica*, 5(8):785–795, 1938.

[92] J. M. Mariotti and S. T. Ridgway. Double Fourier spatio-spectral interferometry - Combining high spectral and high spatial resolution in the near infrared. *Astronomy and Astrophysics*, 195(1-2):350–363, April 1988.

[93] Maxime J. Rizzo, Lee G. Mundy, Arnab Dhabal, Dale J. Fixsen, Stephen A. Rinehart, Dominic J. Benford, David Leisawitz, Robert Silverberg, Todd Veach, and Roser Juanola-Parramon. Far-infrared double-fourier interferometers and their spectral sensitivity. *Publications of the Astronomical Society of the Pacific*, 127(956):1045, oct 2015.

[94] D. A. Naylor and B. G. Gom. Fts-2: A submillimetre astronomical imaging fourier transform spectrometer. In *Fourier Transform Spectroscopy/ Hyperspectral Imaging and Sounding of the Environment*, page FWA1. Optica Publishing Group, 2007.

[95] Heike Kamerlingh Onnes. Nobel lecture. Nobel Prize Outreach, 1913.

[96] M F Kessler, J A Steinz, M E Anderegg, J Clavel, G Drechsel, P Estaria, J Faelker, J R Riedinger, A Robson, B G Taylor, et al. The infrared space observatory (ISO) mission. *Astronomy and Astrophysics*, 315:L27–L31, 1996.

[97] W. S. Holland, E. I. Robson, W. K. Gear, C. R. Cunningham, J. F. Lightfoot, T. Jenness, R. J. Ivison, J. A. Stevens, P. A. R. Ade, M. J. Griffin, W. D. Duncan, J. A. Murphy, and D. A. Naylor. SCUBA: a common-user submillimetre camera operating on the James Clerk Maxwell Telescope. *Monthly Notices of the Royal Astronomical Society*, 303(4):659–672, March 1999.

[98] P. L. Richards. Bolometers for infrared and millimeter waves. *Journal of Applied Physics*, 76(1):1–24, July 1994.

[99] A. Rogalski. History of infrared detectors. *Opto-Electronics Review*, 20(3):279–308, January 2012.

[100] Donald H. Andrews, Robert M. Milton, and Warren Desorbo. A fast superconducting bolometer. *Journal of the Optical Society of America (1917-1983)*, 36(9):518, September 1946.

[101] Kent D Irwin and Gene C Hilton. Transition-edge sensors. *Cryogenic particle detection*, pages 63–150, 2005.

[102] P. D. Mauskopf. Transition Edge Sensors and Kinetic Inductance Detectors in Astronomical Instruments. *PASP*, 130(990):082001, August 2018.

[103] Wayne Holland, William Duncan, and Matthew Griffin. Bolometers for Submillimeter and Millimeter Astronomy. In Snezana Stanimirovic, Daniel Altschuler, Paul Goldsmith, and Chris Salter, editors, *Single-Dish Radio Astronomy: Techniques and Applications*, volume 278 of *Astronomical Society of the Pacific Conference Series*, pages 463–491, December 2002.

[104] Anonymous. Minutes of the Philadelphia meeting December 28, 29, 30, 1926. *Phys. Rev.*, 29:350–373, Feb 1927.

[105] H. Nyquist. Thermal Agitation of Electric Charge in Conductors. *Physical Review*, 32(1):110–113, July 1928.

[106] John C. Mather. Bolometer noise: nonequilibrium thoery. *Applied Optics*, 21(6):1125–1129, March 1982.

[107] Amy N. Bender, Jean-François Cliche, Tijmen de Haan, Matt A. Dobbs, Adam J. Gilbert, Joshua Montgomery, Neil Rowlands, Graeme M. Smecher, Ken Smith, and Andrew Wilson. Digital frequency domain multiplexing readout electronics for the next generation of millimeter telescopes. In Wayne S. Holland and Jonas Zmuidzinas, editors, *Millimeter, Submillimeter, and Far-Infrared Detectors and Instrumentation for Astronomy VII*, volume 9153 of *Society of Photo-Optical Instrumentation Engineers (SPIE) Conference Series*, page 91531A, July 2014.

[108] A. N. Bender, P. A. R. Ade, Z. Ahmed, A. J. Anderson, J. S. Avva, K. Aylor, P. S. Barry, R. Basu Thakur, B. A. Benson, L. S. Bleem, S. Bocquet, K. Byrum, J. E. Carlstrom, F. W. Carter, T. W. Cecil, C. L. Chang, H. M. Cho, J. F. Cliche, T. M. Crawford, A. Cukierman, T. de Haan, E. V. Denison, J. Ding, M. A. Dobbs, S. Dodelson, D. Dutcher, W. Everett, A. Foster, J. Gallicchio, A. Gilbert, J. C. Groh, S. T. Guns, N. W. Halverson, A. H. Harke-Hosemann, N. L. Harrington, J. W. Henning, G. C. Hilton, G. P. Holder, W. L. Holzapfel, N. Huang, K. D. Irwin, O. B. Jeong, M. Jonas, A. Jones, T. S. Khaire, L. Knox, A. M. Kofman, M. Korman, D. L. Kubik, S. Kuhlmann, C. L. Kuo, A. T. Lee, E. M. Leitch, A. E. Lowitz, S. S. Meyer, D. Michalik, J. Montgomery, A. Nadolski, T. Natoli, H. Ngyuen, G. I. Noble, V. Novosad, S. Padin, Z. Pan, J. Pearson, C. M. Posada, W. Quan, S. Raghunathan, A. Rahlin, C. L. Reichardt, J. E. Ruhl, J. T. Sayre, E. Shirokoff, G. Smecher, J. A. Sobrin, A. A. Stark, K. T. Story, A. Suzuki, K. L. Thompson, C. Tucker, L. R. Vale, K. Vanderlinde, J. D. Vieira, G. Wang, N. Whitehorn, W. L. K. Wu, V. Yefremenko, K. W. Yoon, and M. R. Young. Year two instrument status of the SPT-3G cosmic microwave background receiver. In Jonas Zmuidzinas and Jian-Rong Gao, editors, *Millimeter, Submillimeter, and Far-Infrared Detectors and Instrumentation for Astronomy IX*, volume 10708 of *Society of Photo-Optical Instrumentation Engineers (SPIE) Conference Series*, page 1070803, July 2018.

[109] B. P. Crill, P. A. R. Ade, E. S. Battistelli, S. Benton, R. Bihary, J. J. Bock, J. R. Bond, J. Brevik, S. Bryan, C. R. Contaldi, O. Doré, M. Farhang, L. Fissel, S. R. Golwala, M. Halpern, G. Hilton, W. Holmes, V. V. Hristov, K. Irwin, W. C. Jones, C. L. Kuo, A. E. Lange, C. Lawrie, C. J. MacTavish, T. G. Martin, P. Mason, T. E. Montroy, C. B. Netterfield, E. Pascale, D. Riley, J. E. Ruhl, M. C. Runyan, A. Trangsrud, C. Tucker, A. Turner, M. Viero, and D. Wiebe. SPIDER: a balloon-borne large-scale CMB polarimeter. In Jr. Oschmann, Jacobus M., Mattheus W. M. de Graauw, and Howard A. MacEwen, editors, *Space Telescopes and Instrumentation 2008: Optical, Infrared, and Millimeter*, volume 7010 of *Society of Photo-Optical Instrumentation Engineers (SPIE) Conference Series*, page 70102P, July 2008.

[110] EBEX Collaboration, Maximilian Abitbol, Asad M. Aboobaker, Peter Ade, Derek Araujo, François Aubin, Carlo Baccigalupi, Chaoyun Bao, Daniel Chapman, Joy Didier, Matt Dobbs, Stephen M. Feeney, Christopher Geach, Will Grainger, Shaul Hanany, Kyle Helson, Seth Hillbrand, Gene Hilton, Johannes Hubmayr, Kent Irwin, Andrew Jaffe, Bradley Johnson, Terry Jones, Jeff Klein, Andrei Korotkov, Adrian Lee, Lorne Levinson, Michele Limon, Kevin MacDermid, Amber D. Miller, Michael Milligan, Kate Raach, Britt Reichborn-Kjennerud, Carl Reintsema, Ilan Sagiv, Graeme Smecher, Gregory S. Tucker, Benjamin Westbrook, Karl Young, and Kyle Zilic. The EBEX Balloon-borne Experiment—Detectors and Readout. *The Astrophysical Journal Supplement Series*, 239(1):8, November 2018.

[111] P.D. Mauskopf, P.A.R. Ade, J. Beyer, M.P. Bruijn, J.R. Gao, D.M. Glowacka, D.J. Goldie, D. Griffin, M. Griffin, H.F.C. Hoevers, P. Khosropanah, P. Kooijma, P.A.J. de Korte, Dmitry Morozov, J.Anthony Murphy, Créidhe O'Sullivan, Marcel Ridder, Neil Trappe, H. van Weers, J. van der Kuur, and Stafford Withington. A tes focal

plane for spica-safari. In *21st International Symposium on Space Terahertz Technology 2010, ISSTT 2010*, pages 246–255. Elsevier, 2010.

[112] M. L. Ridder, P. Khosropanah, R. A. Hijmering, T. Suzuki, M¿ P Bruijn, H. F. C Hoevers, J. R. Gao, and M. R. Zuiddam. Fabrication of low-noise TES arrays for the SAFARI instrument on SPICA. *Journal of Low Temperature Physics*, 184:60–65, 2016.

[113] P. Khosropanah, T. Suzuki, M. L. Ridder, R. A. Hijmering, H. Akamatsu, L. Gottardi, J. van der Kuur, J. R. Gao, and B. D. Jackson. Ultra-low noise TES bolometer arrays for SAFARI instrument on SPICA. In Wayne S. Holland and Jonas Zmuidzinas, editors, *Millimeter, Submillimeter, and Far-Infrared Detectors and Instrumentation for Astronomy VIII*, volume 9914, page 99140B. International Society for Optics and Photonics, SPIE, 2016.

[114] D. Leisawitz, E. Amatucci, R. Carter, M. DiPirro, A. Flores, J. Staguhn, C. Wu, L. Allen, J. Arenberg, L. Armus, C. Battersby, J. Bauer, R. Bell, P. Beltran, D. Benford, E. Bergin, C. M. Bradford, D. Bradley, D. Burgarella, S. Carey, D. Chi, A. Cooray, J. Corsetti, E. De Beck, K. Denis, L. Dewell, M. East, S. Edgington, K. Ennico, L. Fantano, G. Feller, D. Folta, J. Fortney, J. Generie, M. Gerin, Z. Granger, G. Harpole, K. Harvey, F. Helmich, L. Hilliard, J. Howard, M. Jacoby, A. Jamil, T. Kataria, S. Knight, P. Knollenberg, P. Lightsey, S. Lipscy, E. Mamajek, G. Martins, M. Meixner, G. Melnick, S. Milam, T. Mooney, S. H. Moseley, D. Narayanan, S. Neff, T. Nguyen, A. Nordt, J. Olson, D. Padgett, M. Petach, S. Petro, J. Pohner, K. Pontoppidan, A. Pope, D. Ramspacher, T. Roellig, I. Sakon, C. Sandin, K. Sandstrom, D. Scott, K. Sheth, J. Steeves, K. Stevenson, L. Stokowski, E. Stoneking, K. Su, K. Tajdaran, S. Tompkins, J. Vieira, C. Webster, M. Wiedner, E. L. Wright, and J. Zmuidzinas. The Origins Space Telescope: mission concept overview. In Makenzie Lystrup, Howard A. MacEwen, Giovanni G. Fazio, Natalie Batalha, Nicholas Siegler, and Edward C. Tong, editors, *Space Telescopes and Instrumentation 2018: Optical, Infrared, and Millimeter Wave*, volume 10698 of *Society of Photo-Optical Instrumentation Engineers (SPIE) Conference Series*, page 1069815, July 2018.

[115] Peter C. Nagler, John E. Sadleir, and Edward J. Wollack. Transition-edge sensor detectors for the Origins Space Telescope. *Journal of Astronomical Telescopes, Instruments, and Systems*, 7:011005, January 2021.

[116] W. S. Holland, D. Bintley, E. L. Chapin, A. Chrysostomou, G. R. Davis, J. T. Dempsey, W. D. Duncan, M. Fich, P. Friberg, M. Halpern, K. D. Irwin, T. Jenness, B. D. Kelly, M. J. MacIntosh, E. I. Robson, D. Scott, P. A. R. Ade, E. Atad-Ettedgui, D. S. Berry, S. C. Craig, X. Gao, A. G. Gibb, G. C. Hilton, M. I. Hollister, J. B. Kycia, D. W. Lunney, H. McGregor, D. Montgomery, W. Parkes, R. P. J. Tilanus, J. N. Ullom, C. A. Walther, A. J. Walton, A. L. Woodcraft, M. Amiri, D. Atkinson, B. Burger, T. Chuter, I. M. Coulson, W. B. Doriese, C. Dunare, F. Economou, M. D. Niemack, H. A. L. Parsons, C. D. Reintsema, B. Sibthorpe, I. Smail, R. Sudiwala, and H. S. Thomas. SCUBA-2: the 10 000 pixel bolometer camera on the James Clerk Maxwell

Telescope. *Monthly Notices of the Royal Astronomical Society*, 430(4):2513–2533, 03 2013.

[117] Nicolas Minorsky. Directional stability of automatically steered bodies. *Journal of the American Society for Naval Engineers*, 34(2):280–309, 1922.

[118] Locke D Spencer, Rashmi V Sudiwala, Chris S Benson, Jeremy P Scott, Manimeldura Dinula De Silva, Tyrone Jones, James Cox, Ken Wood, and Peter A R Ade. Optimization of a cryogenic transition-edge sensor detector array for far-infrared astrophysics. In *Space Telescopes and Instrumentation 2022: Optical, Infrared, and Millimeter Wave*, volume 12180, pages 1018–1035. SPIE, 2022.

[119] Kenneth Levenberg. A method for the solution of certain non-linear problems in least squares. *Quarterly of applied mathematics*, 2(2):164–168, 1944.

[120] Heinrich R. Hertz. Keynote address. Tribute to H. Helmholtz, Imperial Palace, Berlin, 1891.

[121] Locke D Spencer, Rashmi V Sudiwala, Chris S Benson, Jeremy P Scott, Manimeldura Dinula De Silva, Tyrone Jones, James Cox, Ken Wood, and Peter A R Ade. Optimization of a cryogenic transition-edge sensor detector array for far-infrared astrophysics. In *Space Telescopes and Instrumentation 2022: Optical, Infrared, and Millimeter Wave*, volume 12180, pages 1018–1035. SPIE, 2022.

[122] Lakeshore Cryotronics. *Model 3402 Temperature Controller User's Manual*. Lake Shore Cryotronics, Inc.

[123] D. Gerstenberg and P. M. Hall. Superconducting Thin Films of Niobium, Tantalum, Tantalum Nitride, Tantalum Carbide, and Niobium Nitride. *Journal of the Electrochemical Society*, 111(8):936, August 1964.

[124] V. Novotny and P. P. M. Meincke. Single superconducting energy gap in pure niobium. *Journal of Low Temperature Physics*, 18(1-2):147–157, January 1975.

[125] Pauli Virtanen, Ralf Gommers, Travis E. Oliphant, Matt Haberland, Tyler Reddy, David Cournapeau, Evgeni Burovski, Pearu Peterson, Warren Weckesser, Jonathan Bright, Stéfan J. van der Walt, Matthew Brett, Joshua Wilson, K. Jarrod Millman, Nikolay Mayorov, Andrew R. J. Nelson, Eric Jones, Robert Kern, Eric Larson, C J Carey, İlhan Polat, Yu Feng, Eric W. Moore, Jake VanderPlas, Denis Laxalde, Josef Perktold, Robert Cimrman, Ian Henriksen, E. A. Quintero, Charles R. Harris, Anne M. Archibald, Antônio H. Ribeiro, Fabian Pedregosa, Paul van Mulbregt, and SciPy 1.0 Contributors. SciPy 1.0: Fundamental Algorithms for Scientific Computing in Python. *Nature Methods*, 17:261–272, 2020.

[126] Paul Dierckx. An algorithm for smoothing, differentiation and integration of experimental data using spline functions. *Journal of Computational and Applied Mathematics*, 1(3):165–184, 1975.

[127] Vito MR Muggeo. Estimating regression models with unknown break-points. *Statistics in medicine*, 22(19):3055–3071, 2003.

[128] Charlie Pilgrim. Piecewise-regression (aka segmented regression) in Python. *Journal of Open Source Software*, 6(68), 2021.

[129] Anselm J. Deninger, A. Roggenbuck, S. Schindler, and S. Preu. 2.75 THz tuning with a triple-DFB laser system at 1550 nm and InGaAs photomixers. *Journal of Infrared, Millimeter, and Terahertz Waves*, 36(3):269–277, March 2015.

[130] F. Rettich, N. Vieweg, O. Cojocari, and A. Deninger. Field Intensity Detection of Individual Terahertz Pulses at 80 MHz Repetition Rate. *Journal of Infrared, Millimeter, and Terahertz Waves*, 36(7):607–612, July 2015.

[131] Dennis Stanze, Anselm Deninger, Axel Roggenbuck, Stephanie Schindler, Michael Schlak, and Bernd Sartorius. Compact cw Terahertz Spectrometer Pumped at 1.5 μm Wavelength. *Journal of Infrared, Millimeter, and Terahertz Waves*, 32(2):225–232, February 2011.

[132] N. Vieweg, F. Rettich, A. Deninger, H. Roehle, R. Dietz, T. Göbel, and M. Schell. Terahertz-time domain spectrometer with 90 dB peak dynamic range. *Journal of Infrared, Millimeter, and Terahertz Waves*, 35(10):823–832, October 2014.

[133] M. Yahyapour, N. Vieweg, A. Roggenbuck, F. Rettich, O. Cojocari, and A. Deninger. A Flexible Phase-Insensitive System for Broadband CW-Terahertz Spectroscopy and Imaging. *IEEE Transactions on Terahertz Science and Technology*, 6(5):670–673, September 2016.

[134] G. C. Jaehnig, K. Arnold, J. Austermann, D. Becker, S. Duff, N. W. Halverson, M. Hazumi, G. Hilton, J. Hubmayr, A. T. Lee, M. Link, A. Suzuki, M. Vissers, S. Walker, and B. Westbrook. Development of Space-Optimized TES Bolometer Arrays for LiteBIRD. *Journal of Low Temperature Physics*, 199(3-4):646–653, March 2020.

[135] Karwan Rostem, Dorota M. Glowacka, David J. Goldie, and Stafford Withington. Thermal conductance measurements for the development of ultra low-noise transition-edge sensors with a new method for measuring the noise equivalent power. In William D. Duncan, Wayne S. Holland, Stafford Withington, and Jonas Zmuidzinas, editors, *Millimeter and Submillimeter Detectors and Instrumentation for Astronomy IV*, volume 7020, page 70200L. International Society for Optics and Photonics, SPIE, 2008.

[136] James C Candy and Gabor C Temes. *Oversampling delta-sigma data converters: theory, design, and simulation*. John Wiley & Sons, 1991.

[137] Crèidhe O'Sullivan and J. Anthony Murphy. *Field Guide to Terahertz Sources, Detectors, and Optics*, volume FG28. SPIE Press, 2012.

[138] K. M. van Vliet. Noise limitations in solid state photodetectors. *Applied Optics*, 6(7):1145, July 1967.

[139] Locke D. Spencer, David A. Naylor, Bruce M. Swinyard, Asier A. Aramburu, Trevor R. Fulton, Tanya L. Lim, Samuel D. Ronayette, and Ian S. Schofield. A Fourier transform spectrometer for ground testing of the Herschel/SPIRE instrument. In John C. Mather, editor, *Optical, Infrared, and Millimeter Space Telescopes*, volume 5487 of *Society of Photo-Optical Instrumentation Engineers (SPIE) Conference Series*, pages 501–512, October 2004.

[140] Gibion Makiwa, David A. Naylor, Marc Ferlet, Carl Salji, Bruce Swinyard, Edward Polehampton, and Matthijs H. D. van der Wiel. Beam profile for the herschel–spire fourier transform spectrometer. *Appl. Opt.*, 52(16):3864–3875, Jun 2013.

[141] Pavel V. Nikitin, Daniel D. Stancil, and Elena A. Erosheva. Estimating the number of modes in multimode waveguide propagation environment. In *2011 IEEE International Symposium on Antennas and Propagation (APSURSI)*, pages 1662–1665, 2011.

[142] G. Gallot, S. P. Jamison, R. W. McGowan, and D. Grischkowsky. Terahertz waveguides. *Journal of the Optical Society of America B Optical Physics*, 17(5):851–863, May 2000.

[143] Bram N. R. Lap, Willem Jellema, Stafford Withington, and David A. Naylor. Modal simulation framework for the design and verification of future few-mode far-infrared spectrometers. In Jonas Zmuidzinas and Jian-Rong Gao, editors, *Millimeter, Submillimeter, and Far-Infrared Detectors and Instrumentation for Astronomy XI*, volume 12190, page 121901T. International Society for Optics and Photonics, SPIE, 2022.

[144] Julius von Hann and Robert DeCourcy Ward. *Handbook of climatology*. MacMillan, 1903.

[145] Charles R. Harris, K. Jarrod Millman, Stéfan J. van der Walt, Ralf Gommers, Pauli Virtanen, David Cournapeau, Eric Wieser, Julian Taylor, Sebastian Berg, Nathaniel J. Smith, Robert Kern, Matti Picus, Stephan Hoyer, Marten H. van Kerkwijk, Matthew Brett, Allan Haldane, Jaime Fernández del Río, Mark Wiebe, Pearu Peterson, Pierre Gérard-Marchant, Kevin Sheppard, Tyler Reddy, Warren Weckesser, Hameer Abbasi, Christoph Gohlke, and Travis E. Oliphant. Array programming with NumPy. *Nature*, 585(7825):357–362, September 2020.

[146] Bradley Gustav Gom. A cryogenic detector for submillimetre astronomy. Master's thesis, University of Lethbridge, 1999.

[147] Virgil-Florin Duma. Optical choppers with circular-shaped windows: Modulation functions. *Communications in Nonlinear Science and Numerical Simulations*, 16(5):2218–2224, May 2011.

[148] G. J. Bendo, M. J. Griffin, J. J. Bock, L. Conversi, C. D. Dowell, T. Lim, N. Lu, C. E. North, A. Papageorgiou, C. P. Pearson, M. Pohlen, E. T. Polehampton, B. Schulz, D. L. Shupe, B. Sibthorpe, L. D. Spencer, B. M. Swinyard, I. Valtchanov, and C. K. Xu. Flux calibration of the Herschel-SPIRE photometer. *Monthly Notices of the Royal Astronomical Society*, 433(4):3062–3078, August 2013.

[149] B. M. Swinyard, E. T. Polehampton, R. Hopwood, I. Valtchanov, N. Lu, T. Fulton, D. Benielli, P. Imhof, N. Marchili, J. P. Baluteau, G. J. Bendo, M. Ferlet, M. J. Griffin, T. L. Lim, G. Makiwa, D. A. Naylor, G. S. Orton, A. Papageorgiou, C. P. Pearson, B. Schulz, S. D. Sidher, L. D. Spencer, M. H. D. van der Wiel, and R. Wu. Calibration of the Herschel SPIRE Fourier Transform Spectrometer. *Monthly Notices of the Royal Astronomical Society*, 440(4):3658–3674, June 2014.

[150] Vincent Weiler. Nanosecond-level data acquisition for experimental astrophysics. Master's thesis, University of Lethbridge, 2016.

[151] Anne Cowley. Bright galaxies, dark matters. *Science*, 277(5332):1618–1619, 1997.

[152] David A. Naylor, Brad G. Gom, Margaret K. Tahic, and Gary R. Davis. Astronomical spectroscopy using an aliased step-and-integrate Fourier transform spectrometer. In C. Matt Bradford, Peter A. R. Ade, James E. Aguirre, James J. Bock, Mark Dragovan, Lionel Duband, Lieko Earle, Jason Glenn, Hideo Matsuhara, Bret J. Naylor, Hien T. Nguyen, Minhee Yun, and Jonas Zmuidzinas, editors, *Z-Spec: a broadband millimeter-wave grating spectrometer: design, construction, and first cryogenic measurements*, volume 5498 of *Society of Photo-Optical Instrumentation Engineers (SPIE) Conference Series*, pages 685–694, October 2004.

[153] Michael L. Forman, W. Howard Steel, and George A. Vanasse. Correction of Asymmetric Interferograms Obtained in Fourier Spectroscopy. *Journal of the Optical Society of America (1917-1983)*, 56(1):59, January 1966.

[154] Peter A. R. Ade, Giampaolo Pisano, Carole Tucker, and Samuel Weaver. A review of metal mesh filters. In Jonas Zmuidzinas, Wayne S. Holland, Stafford Withington, and William D. Duncan, editors, *Millimeter and Submillimeter Detectors and Instrumentation for Astronomy III*, volume 6275 of *Society of Photo-Optical Instrumentation Engineers (SPIE) Conference Series*, page 62750U, June 2006.

[155] Bruce M. Swinyard, Peter A. Ade, Matthew J. Griffin, Kjetil Dohlen, Jean-Paul Baluteau, Dominque Pouliquen, Diddier Ferand, Pascal Dargent, Guy Michel, Jerome Martignac, Louis Rodriguez, Donald E. Jennings, Martin E. Caldwell, Anthony G. Richards, Peter A. Hamilton, and David A. Naylor. FIRST-SPIRE spectrometer: a novel imaging FTS for the submillimeter. In James B. Breckinridge and Peter Jakobsen, editors, *UV, Optical, and IR Space Telescopes and Instruments*, volume 4013 of *Society of Photo-Optical Instrumentation Engineers (SPIE) Conference Series*, pages 196–207, July 2000.

[156] Matthew J. Griffin, Bruce M. Swinyard, and Laurent G. Vigroux. SPIRE instrument for FIRST. In James B. Breckinridge and Peter Jakobsen, editors, *UV, Optical,*

and IR Space Telescopes and Instruments, volume 4013 of *Society of Photo-Optical Instrumentation Engineers (SPIE) Conference Series*, pages 184–195, July 2000.

[157] Kjetil Dohlen, Alain Origne, Dominque Pouliquen, and Bruce M. Swinyard. Optical design of the SPIRE instrument for FIRST. In James B. Breckinridge and Peter Jakobsen, editors, *UV, Optical, and IR Space Telescopes and Instruments*, volume 4013 of *Society of Photo-Optical Instrumentation Engineers (SPIE) Conference Series*, pages 119–128, July 2000.

[158] Chris S. Benson, Jeremy S. Scott, and Locke D. Spencer. Characterization of a Feedback Controlled TES Array in a Double-Fourier Interferometer. Oral presentation at the annual general meeting of the Canadian Astronomical Society, 2023.

[159] E.I. Organick. *A Fortran IV Primer*. Addison-Wesley series in computer science and information processing. Addison-Wesley, 1966.

[160] David A. Naylor, Locke D. Spencer, and Peter A.R. Ade. The effects of beamsplitter emission in a balanced fourier transform spectrometer. In *2008 33rd International Conference on Infrared, Millimeter and Terahertz Waves*, pages 1–2, 2008.

[161] Scott Paine. *The am atmospheric model*. Smithsonian Astrophysical Observatory.

[162] E. Serabyn and E. W. Weisstein. Fourier Transform Spectroscopy of the Orion Molecular Cloud Core. *Astrophysical Journal*, 451:238, September 1995.

[163] Carl Sagan. Cosmos, episode 12: Encyclopaedia galactica. Public Broadcasting Service Station, KCET., 1980.

[164] Simon Doyle, Jack Naylon, Philip Mauskopf, Adrian Porch, Stafford Withington, David Goldie, Dorota M. Glowacka, Jochem J. A. Baselmans, Stephen J. C. Yates, and Henk Hoevers. Lumped element kinetic inductance detectors for far-infrared astronomy. In William D. Duncan, Wayne S. Holland, Stafford Withington, and Jonas Zmuidzinas, editors, *Millimeter and Submillimeter Detectors and Instrumentation for Astronomy IV*, volume 7020 of *Society of Photo-Optical Instrumentation Engineers (SPIE) Conference Series*, page 70200T, July 2008.

[165] M. Griffin, J. Baselmans, A. Baryshev, S. Doyle, M. Grim, P. Hargrave, T. Klapwijk, J. Martin-Pintado, A. Monfardini, A. Neto, H. Steenbeek, I. Walker, K. Wood, A. D'Addabbo, P. Barry, A. Bideaud, B. Blázquez, J. Bueno, M. Calvo, J. L. Costa-Kramer, L. Ferrari, A. Gómez-Gutiérrez, J. Goupy, N. Llombart, and S. Yates. SPACEKIDS: kinetic inductance detectors for space applications. In Wayne S. Holland and Jonas Zmuidzinas, editors, *Millimeter, Submillimeter, and Far-Infrared Detectors and Instrumentation for Astronomy VIII*, volume 9914 of *Society of Photo-Optical Instrumentation Engineers (SPIE) Conference Series*, page 991407, July 2016.

[166] Thomas L. R. Brien, Peter A. R. Ade, Peter S. Barry, Edgar Castillo-Domınguez, Daniel Ferrusca, Thomas Gascard, Victor Gómez, Peter C. Hargrave, Amber L.

Hornsby, David Hughes, Enzo Pascale, Josie D. A. Parrianen, Abel Perez, Sam Rowe, Carole Tucker, Salvador Ventura González, and Simon M. Doyle. MUSCAT: the Mexico-UK Sub-Millimetre Camera for AsTronomy. In Jonas Zmuidzinas and Jian-Rong Gao, editors, *Millimeter, Submillimeter, and Far-Infrared Detectors and Instrumentation for Astronomy IX*, volume 10708 of *Society of Photo-Optical Instrumentation Engineers (SPIE) Conference Series*, page 107080M, July 2018.

[167] S. Doyle, P. Mauskopf, J. Naylon, A. Porch, and C. Duncombe. Lumped Element Kinetic Inductance Detectors. *Journal of Low Temperature Physics*, 151(1-2):530–536, April 2008.

[168] Adrian Sinclair. *In-Flight Performance of the BLAST-TNG Balloon-Borne Far-Infrared Telescope and Development of a Reconfigurable Readout on the RFSoC Platform for Frequency Multiplexed Superconducting Detector Arrays*. PhD thesis, Arizona State University, 2021.

[169] T. L. R. Brien, S. Doyle, D. H. Hughes, P. A. R. Ade, P. S. Barry, E. Castillo-Domínguez, C. Dodd, C. Dunscombe, S. Eales, D. Ferrusca, V. Gómez-Rivera, P. Hargrave, J. L. Hernández-Rebollar, A. Hornsby, J. House, J. M. Jáuregui-Garcia, P. D. Mauskopf, D. Murias, A. Papageorgiou, E. Pascale, N. Peretto, A. Pérez-Fajardo, S. Rowe, D. Sánchez-Argüelles, M. W. L. Smith, K. Souccar, R. Sudiwala, M. Tapia, A. T. Campos, C. Tucker, M. Velázquez de la Rosa Becerra, S. Ventura-González, and I. Walker. The Mexico UK Sub-mm Camera for Astronomy (MUSCAT) on-sky commissioning: performance of the cryogenic systems. In Jonas Zmuidzinas and Jian-Rong Gao, editors, *Millimeter, Submillimeter, and Far-Infrared Detectors and Instrumentation for Astronomy XI*, volume 12190 of *Society of Photo-Optical Instrumentation Engineers (SPIE) Conference Series*, page 1219018, August 2022.

[170] Nicholas F. Cothard, Christopher Albert, Andrew D. Beyer, Charles M. Bradford, Pierre Echternach, Byeong-Ho Eom, Logan Foote, Marc Foote, Steven Hailey-Dunsheath, Reinier M. J. Janssen, Elijah Kane, Henry LeDuc, Joanna Perido, Jason Glenn, and Peter K. Day. Parallel Plate Capacitor Aluminum KIDs for Future Far-Infrared Space-Based Observatories. *arXiv e-prints*, page arXiv:2311.00773, November 2023.

[171] Logan Foote, Chris Albert, Jochem Baselmans, Andrew Beyer, Nicholas Cothard, Peter Day, Steven Hailey-Dunsheath, Pierre Echternach, Reinier Janssen, Elijah Kane, Henry Leduc, Lun-Jun Liu, Hien Nguyen, Joanna Perido, Jason Glenn, Jonas Zmuidzinas, Charles, and Bradford. High-sensitivity Kinetic Inductance Detector Arrays for the Probe Far-Infrared Mission for Astrophysics. *arXiv e-prints*, page arXiv:2311.02175, November 2023.

[172] Robert Jordan. *Shadow Rising: Book Four of "The Wheel of Time"*, volume 4. Tor Books, 1992.

[173] J. Zmuidzinas and P.L. Richards. Superconducting detectors and mixers for millimeter and submillimeter astrophysics. *Proceedings of the IEEE*, 92(10):1597–1616, 2004.

[174] Charles Hutton and Richard Pearson. *The Philosophical Transactions of the Royal Society of London, from Their Commencement, in 1665, to the Year 1800*, volume 18. C. and R. Baldwin, 1809.

[175] National Instruments. Python API for interacting with LabVIEW FPGA devices. Technical report, 2017. Maintained by Michael Strain and Mose Gumble.

[176] National Instruments. *LabVIEW Help Manual*, 2015.

Appendix A

Derivations

Humankind is made for uncertainty, struggle, choice, and change.
–*Amys*, from Robert Jordan's "Shadow Rising" (1992) [172]

A.1 Phonon noise

A.1.1 Ballistic transmittance

This treatment of phonon noise follows that of Mauskopf (2018) [102]. If all phonons are transmitted ballistically across the thermal link of a bolometer, the power conducted along the link in one direction is given by,

$$P_{\text{link}} = \sum_i \int_{\nu_i}^{\infty} \frac{h\nu}{\exp\left(\frac{h\nu}{k_B T}\right) - 1} d\nu, \quad [\text{W}] \tag{A.1}$$

where T is the temperature of the of the phonons emitted at one end of the line. In Equation A.1, the sum is over all photon modes that can propagate down the link with each mode, i, having a corresponding cutoff frequency, ν_i. The number of modes that can propagate for a particular phonon energy $E = h\nu$ can be represented by the function $N_{\text{modes}}(\nu)$ and the sum can be incorporated into the integral,

$$P_{\text{link}} = \int_0^{\infty} N_{\text{modes}}(\nu) \frac{h\nu}{\exp\left(\frac{h\nu}{k_B T}\right) - 1} d\nu, \quad [\text{W}]. \tag{A.2}$$

Considering the transfer of photons emitted from either end of the link (at temperatures T_a and T_b) the total power transmitted becomes,

$$P = \int_0^{\infty} N_{\text{modes}}(\nu)\, h\nu \left[\frac{1}{\exp\left(\frac{h\nu}{k_B T_a}\right) - 1} - \frac{1}{\exp\left(\frac{h\nu}{k_B T_b}\right) - 1} \right] d\nu, \quad [\text{W}]. \tag{A.3}$$

It is common to take the transmitted power on bath temperature as following a power-law form,

$$P = B(T_a^n - T_b^n) \quad [\text{W}], \tag{A.4}$$

where the parameters n and B can be determined by fits to experimental data [102].

We can consider the phonon noise as comprised of contributions from the statistical variation in the arrival time of particles ($\mathrm{NEP}_{\mathrm{shot}}$) and the fluctuation in wave intensity for bosonic fields due to the beating between different frequency modes ($\mathrm{NEP}_{\mathrm{wave}}$) [102, 173],

$$\mathrm{NEP}^2_{\mathrm{phonon}} = \mathrm{NEP}^2_{\mathrm{shot}} + \mathrm{NEP}^2_{\mathrm{wave}} \quad [\mathrm{W}^2/\mathrm{Hz}]. \tag{A.5}$$

For ballistic phonon transport across a link with mode structure of dimensionality, d, the number of modes can be written $N_{\mathrm{modes}}\,d\nu = A\nu^{d-1}\,d\nu = A\nu^{n-2}\,d\nu$. The shot noise power contribution from one side of the link with is given by,

$$\begin{aligned}
\mathrm{NEP}^2_{\mathrm{shot}}(T) &= 2\int_0^\infty h\nu\frac{dP}{d\nu}\,d\nu \\
&= 2\int_0^\infty N_{\mathrm{modes}}(\nu)\frac{(h\nu)^2\,d\nu}{\exp\left(\frac{h\nu}{k_BT_b}\right)-1} \\
&= 2\int_0^\infty A\nu^{n-2}\frac{(h\nu)^2\,d\nu}{\exp\left(\frac{h\nu}{k_BT_b}\right)-1} \\
&= 2A\frac{k_B^{n+1}}{h^{n-1}}T^{n+1}\int_0^\infty \frac{x^n\,dx}{e^x-1} \quad [\mathrm{W}^2/\mathrm{Hz}].
\end{aligned} \tag{A.6}$$

Note the substitution $x = h\nu/(k_BT)$. With a further substitution of $B = A\frac{k_B^n}{h^{n-1}}\xi(n-1)$, where $\xi(n) = \int_0^\infty \frac{x^n\,dx}{e^x-1}$ the shot noise term can be written,

$$\mathrm{NEP}^2_{\mathrm{shot}}(T) = 2k_BTBT^n\frac{\xi(n)}{\xi(n-1)} \quad [\mathrm{W}^2/\mathrm{Hz}]. \tag{A.7}$$

With the transmitted power through the thermal link from this end represented by $P = BT^n$ and with $G = dP/dT$, Equation A.7 becomes

$$\mathrm{NEP}^2_{\mathrm{shot}}(T) = 2k_BT^2G(T)\frac{\xi(n)}{n\xi(n-1)} \quad [\mathrm{W}^2/\mathrm{Hz}]. \tag{A.8}$$

The wave noise term can be written, [102]

$$\begin{aligned}
\mathrm{NEP}^2_{\mathrm{wave}}(T) &= 2\int_0^\infty A\nu^{n-2}\frac{(h\nu)^2\,d\nu}{\left[\exp\left(\frac{h\nu}{k_BT_b}\right)-1\right]^2} \\
&= 2A\frac{k^{n+1}}{h^{n-1}}T^{n+1}\int_0^\infty \frac{x^n}{(e^x-1)^2} \quad [\mathrm{W}^2/\mathrm{Hz}].
\end{aligned} \tag{A.9}$$

With the previous substitution, $B = A\frac{k_B^n}{h^{n-1}}\xi(n-1)$, this becomes

$$\mathrm{NEP}^2_{\mathrm{wave}}(T) = 2k_BTBT^n\frac{\phi(n)}{\xi(n-1)} \tag{A.10}$$

$$= 2k_BT^2G(T)\frac{\phi(n)}{n\xi(n-1)} \quad [\mathrm{W}^2/\mathrm{Hz}]. \tag{A.11}$$

where $\phi(n) = \int_0^\infty \frac{x^n\,dx}{(e^x-1)^2}$. With both the shot and wave noise contributions considered, the total phonon noise can be written

$$\mathrm{NEP}^2_{\mathrm{phonon}}(T) = 2k_BT^2G(T)\frac{\phi(n)+\xi(n)}{n\xi(n-1)} \quad [\mathrm{W}^2/\mathrm{Hz}]. \tag{A.12}$$

The sum

$$\begin{aligned}\phi(n)+\xi(n) &= \int_0^\infty \frac{x^n\,dx}{e^x-1} + \frac{x^n\,dx}{(e^x-1)^2} \\ &= \int_0^\infty \frac{x^n e^x\,dx}{(e^x-1)^2}\end{aligned} \tag{A.13}$$

can be integrated by parts with $v = x^n$ and $du = e^x\,dx/(e^x-1)^2$ such that

$$\begin{aligned}\phi(n)+\xi(n) &= -\frac{x^n}{e^x-1}\bigg|_0^\infty - \left(-n\int_0^\infty \frac{x^{n-1}\,dx}{e^x-1}\right) \\ &= (0) + n\int_0^\infty \frac{x^{n-1}\,dx}{e^x-1} \\ &= n\xi(n-1).\end{aligned} \tag{A.14}$$

This result gives

$$\mathrm{NEP}^2_{\mathrm{phonon}}(T) = 2k_BT^2G(T) \quad [\mathrm{W}^2/\mathrm{Hz}]. \tag{A.15}$$

with the total phonon noise contribution from both sides of the thermal link as

$$\mathrm{NEP}^2_{\mathrm{phonon}} = 2k_BT^2G(T_a) + 2k_BT^2G(T_b) \quad [\mathrm{W}^2/\mathrm{Hz}]. \tag{A.16}$$

This expression is Equation 3.12 in Chapter 3.

A.1.2 The scattering, absorption, and/or emission limit

A different expression for phonon noise can be obtained with the opposing limit to the previous ballistic transmission. I.e., when phonon transmission along the thermal link is dominated by scattering and emission/absorption processes. This treatment follows that of

Mather [106]. Phonon noise contributions can be expressed as

$$\mathrm{NEP}^2_{\mathrm{phonon}} = 4k_B \frac{\int_{T_b}^{T_a} T^2 G^2(T)\, dT}{\int_{T_b}^{T_a} G(T)\, dT} \quad [\mathrm{W}^2/\mathrm{Hz}], \tag{A.17}$$

where $G(t)$ represents the varying thermal conductivity along the thermal link. With $G(t) = G(T_a)(t/T_a)^d$ where d is the effective number of phonon propagation modes,

$$\begin{aligned}
\mathrm{NEP}^2_{\mathrm{phonon}} &= 4k_B G(T_a) \frac{T_a^d}{T_a^{2d}} \frac{\int_{T_b}^{T_a} t^{2d+2}\, dt}{\int_{T_b}^{T_a} t^d\, dt} \\
&= 4k_B \frac{G(T_a)}{T_a^d} \frac{d+1}{2d+3} \frac{T_a^{2d+3} - T_b^{2d+3}}{T_a^{d+1} - T_b^{d+1}} \\
&= 4k_B T_a^2 G(T_a) \frac{n}{2n+1} \frac{T_a^{2n+1} - T_b^{2n+1}}{T_a^{n+1}\left(T_a^n - T_b^n\right)} \quad [\mathrm{W}^2/\mathrm{Hz}],
\end{aligned} \tag{A.18}$$

where $n = d+1$. This expression is Equation 3.13 in Chapter 3 and matches the expression in Mauskopf (2018) [102].

A.2 Photon noise, Eq. 3.16

Photon noise is caused by random fluctuations in the rate of a detector's radiation absorption. This derivation fololows treatments by Mather (1982) [106] and Spencer (2009) [71]. The spectral density of fluctuations in absorbed power, χ, is given by [138]

$$\chi = 2 \int Q_\nu h\nu [1 + \kappa(\nu)]\, d\nu \quad [\mathrm{W}^2/\mathrm{Hz}], \tag{A.19}$$

where Q_ν is the radiant power absorbed per unit optical bandwidth, and $\kappa(\nu)$ is the effective photon mode occupation number [106]. The effective photon mode occupation number is given by

$$\kappa(\nu) = \frac{\eta \varepsilon t}{\exp\left(\frac{h\nu}{k_b T_s}\right) - 1}, \tag{A.20}$$

where t is the transmissivity of the optical system, η is the detector absorptivity, and ε and T_S are the emmissivity and temperature of the source, respectively. In Equation A.19, Q_ν is given by

$$Q_\nu = 2\eta\varepsilon t A\Omega(\nu) \frac{h\nu^3}{c^2} \frac{1}{\exp\left(\frac{h\nu}{k_b T_s}\right) - 1} \quad [\mathrm{W}^2/\mathrm{Hz}], \tag{A.21}$$

where A is the detector area and $\Omega(\nu)$ is the solid angle of the beam seen by the detector. The square of the photon NEP is the fluctuations in radiation absorption rate,

$$\begin{aligned}(\mathrm{NEP}_i)^2 &= \chi \\ &= 2\int Q_\nu h\nu[1+\kappa(\nu)]\,d\nu \\ &= 2\int 2(\eta\varepsilon t)A\Omega(\nu)\frac{h\nu^3}{c^2}\frac{1}{\exp\left(\frac{h\nu}{k_bT_s}\right)-1}h\nu[1+\kappa(\nu)]\,d\nu \\ &= 4\int \frac{h^2\nu^4}{c^2}\frac{\eta\varepsilon tA\Omega(\nu)}{\exp\left(\frac{h\nu}{k_bT_s}\right)-1}\left[1+\frac{\eta\varepsilon t}{\exp\left(\frac{h\nu}{k_bT_s}\right)-1}\right]d\nu \\ &= \frac{4h^2}{c^2}\int \frac{\eta\varepsilon tA\Omega(\nu)\nu^4}{\exp\left(\frac{h\nu}{k_bT_s}\right)-1}\left[1+\frac{\eta\varepsilon t}{\exp\left(\frac{h\nu}{k_bT_s}\right)-1}\right]d\nu \quad [\mathrm{W}^2/\mathrm{Hz}] \end{aligned} \tag{A.22}$$

This expression is equivalent to Equation 3.16 in Chapter 3.

A.3 Spectral representation of the mutual coherence function

A.3.1 A note on Fourier analysis

The choice in the usage of the (forward) Fourier transform,

$$f(t) = \int_{-\infty}^{\infty} F(\nu)e^{-2\pi i\nu t}\,dt \tag{A.23}$$

and the inverse (reverse) Fourier transform,

$$F(\nu) = \int_{-\infty}^{\infty} f(t)e^{2\pi i\nu t}\,dt \tag{A.24}$$

is fairly arbitrary as the difference (with the exception of the normalisation that may be employed by the digital Fast Fourier Transform (FFT) software [145]) is merely a matter of phase (see §2.1.4). In this thesis, the optical frequency spectrum of a function measured in time or Optical Path Difference (OPD) is determined by the inverse Fourier transform (see Chapter 2).

A.3.2 Equation 2.37

To arrive at a spectral representation of the mutual coherence function, we follow a treatment similar to Born and Wolf (1999) beginning with Equation 2.36 [38],

$$\Gamma_{1,2}(\tau) = \lim_{T\to\infty}\frac{1}{2T}\int_{-\infty}^{\infty}\Psi(P_1,t+\tau)\Psi^*(P_2,t)\,dt \quad [\mathrm{W/m}^2]. \tag{A.25}$$

We replace $\Psi(P_1, t+\tau)$ with it's spectral representation and reorder the integration

$$\begin{aligned}\Gamma_{1,2}(\tau) &= \lim_{T\to\infty}\frac{1}{2T}\int_{-\infty}^{\infty}\left[\int_{-\infty}^{\infty}\psi(P_1,\nu)e^{-2\pi i\nu(t+\tau)}\,d\nu\right]\Psi^*(P_2,t)\,dt \quad [\mathrm{W/m^2}]\\ &= \lim_{T\to\infty}\frac{1}{2T}\int_{-\infty}^{\infty}\left[\int_{-\infty}^{\infty}\Psi^*(P_2,t)dt\right]\psi(P_1,\nu)e^{-2\pi i\nu(t+\tau)}\,d\nu. \end{aligned} \tag{A.26}$$

Splitting the exponent, we arrive at

$$\begin{aligned}\Gamma_{1,2}(\tau) &= \lim_{T\to\infty}\frac{1}{2T}\int_{-\infty}^{\infty}\left[\int_{-\infty}^{\infty}\Psi^*(P_2,t)e^{-2\pi it}dt\right]\psi(P_1,\nu)e^{-2\pi i\nu\tau}\,d\nu.\\ &= \lim_{T\to\infty}\frac{1}{2T}\int_{-\infty}^{\infty}\psi(P_1,\nu)\psi^*(P_2,\nu)e^{-2\pi i\nu\tau}\,d\nu, \end{aligned} \tag{A.27}$$

which is Equation 2.37.

A.4 Normalisation of the mutual coherence function

A.4.1 Normalisation

It should be noted that the complex degree of coherence is normalised such that $|\gamma_{1,2}(\tau)| \leq 1$ (see §2.3) [38]. If we consider some non-infinite disturbance,

$$\Re[V_T(P,t)] = \begin{cases}\Re[V(P,t)] & |t| \leq T,\\ 0 & |t| \geq T\end{cases} \tag{A.28}$$

and

$$V_T(t) = \Re[V_T(t)] + i\Im[V_T(t)] = 2\int_0^{\infty} v_T(\nu)e^{-2\pi i\nu t}\,d\nu. \tag{A.29}$$

By the Schwartz inequality (i.e., $|\langle\vec{u},\vec{v}\rangle|^2 \leq \langle\vec{u},\vec{u}\rangle\cdot\langle\vec{v},\vec{v}\rangle$),

$$\left|\int_{-\infty}^{\infty}V_T(P_1,t+\tau)V_T^*(P_2,t)\,dt\right|^2 \leq \int_{-\infty}^{\infty}V_T(P_1,t+\tau)V_T^*(P_1,t+\tau)\,dt\int_{-\infty}^{\infty}V_T(P_2,t)V_T^*(P_2,t)\,dt. \tag{A.30}$$

In this first integral on the right hand side we may replace $t+\tau$ by t. Dividing both sides by $4T^2$ and taking the limit $T\to\infty$,

$$\begin{aligned}&\lim_{T\to\infty}\frac{1}{4T^2}\left|\int_{-\infty}^{\infty}V_T(P_1,t+\tau)V_T^*(P_2,t)\,dt\right|^2\\ &\qquad\leq \lim_{T\to\infty}\frac{1}{4T^2}\int_{-\infty}^{\infty}V_T(P_1,t)V_T^*(P_1,t)\,dt\int_{-\infty}^{\infty}V_T(P_2,t)V_T^*(P_2,t)\,dt\\ &|\Gamma_{1,2}(\tau)|^2 \leq \Gamma_{1,1}(0)\Gamma_{2,2}(0)\\ &|\gamma_{1,2}(\tau)| \leq 1. \end{aligned} \tag{A.31}$$

A.5 FTS NEP

The noise present in an FTS spectrum is given by $\varsigma\,[\mathrm{W/cm^{-1}}]$ and thus the noise power is written,

$$\varsigma_{\mathrm{power}} = \varsigma\Delta\sigma \quad [\mathrm{W}], \tag{A.32}$$

where $\Delta\sigma$ is the spectral resolution of the observation. NEP is determined by multiplying the signal noise [W] by the square root of the observation time required to obtain the measurement [$\sqrt{\mathrm{s}} = 1/\sqrt{\mathrm{Hz}}$]. In an FTS, this is defined by the scanning motion of the spectral arm. Spectral resolution and the scanned OPD are related by,

$$L = \frac{1}{2\Delta\sigma} \quad [\mathrm{cm\ OPD}]. \tag{A.33}$$

The time to record the FTS scan is then,

$$t_{\mathrm{scan}} = \left(\frac{1}{2\Delta\sigma}\right)(v_{\mathrm{stage}})^{-1} \quad [\mathrm{s}], \tag{A.34}$$

where v_{stage} [cm OPD/s] is the scanning speed of the spectral arm. The measured NEP in an FTS is then given as

$$\begin{aligned}
\mathrm{NEP_{FTS}} &= \varsigma\Delta\sigma\sqrt{\frac{\frac{1}{2\Delta\sigma}}{v_{\mathrm{Stage}}}} \\
&= \varsigma\Delta\sigma\sqrt{\frac{1}{2\Delta\sigma v_{\mathrm{stage}}}} \\
&= \varsigma\sqrt{\frac{\Delta\sigma^2}{2\Delta\sigma v_{\mathrm{stage}}}} \\
&= \varsigma\sqrt{\frac{\Delta\sigma}{2v_{\mathrm{stage}}}} \quad [\mathrm{W}/\sqrt{\mathrm{Hz}}].
\end{aligned} \tag{A.35}$$

This is the expression presented in §5.4.

Appendix B

Alignment of the Lethbridge Double-Fourier Interferometer

We need not hesitate to admit that the Sun is richly stored with inhabitants.
–William Herschel (1738–1822) [174]

The single Fourier Transform Spectrometer (FTS) configuration of the Double Fourier Interferometery (DFI) testbed consists of 2 off-axis parabolic mirrors, 12 optical flats, 2 beamsplitters, and 2 translation stages. All mirrors, with the exception of the large primary collimator, are mounted with manual tip and tilt adjustment provided by three set-screw actuators. Beamsplitters are also mounted such that they can achieve similar adjustments through pairs of manual set-screw actuators. I conducted the alignment of the DFI by eye using an optical Helium-Neon (HeNe) laser.

Figure B.1 demonstrates the guiding principle of the optical alignment. Using the two beamsplitters, two resonant optical cavities are constructed, one on the input side of the interferometer and the other on the detector side. In this way, the majority of interferometer optical components can have their alignment verified over a significant optical path. Since each cavity experiences multiple passes of the alignment beam, these will interfere when a cavity is well aligned and if the alignment source has a sufficiently long coherence length. The beam height on the optics table is defined by the centre of the optical flats mounted to the translation stages as their current mounting does not allow for their height to be adjusted.

I aligned the DFI on two occasions, the first alignment being September 2022 from which the first spectral fringes of the interferometer were measured and the second being December 2022. The need for a second alignment was the unfortunate consequence of the removal of several mirrors from the assembly by another student in haste to obtain measurements for an impending conference presentation. The first aligned optical design differed slightly from the final design presented in Chapter 2 and is shown in its alignment configuration in Figure B.2. After the misalignment, the DFI was redesigned to follow its current configuration. On both occasions, I employed the same general alignment procedure and I will only fully discuss the alignment of the second design in this work.

B.1 Motivations for the second design

After the significant misalignment, the DFI underwent small design adjustments. The first optical design of the DFI though functional, required the focal length of the primary

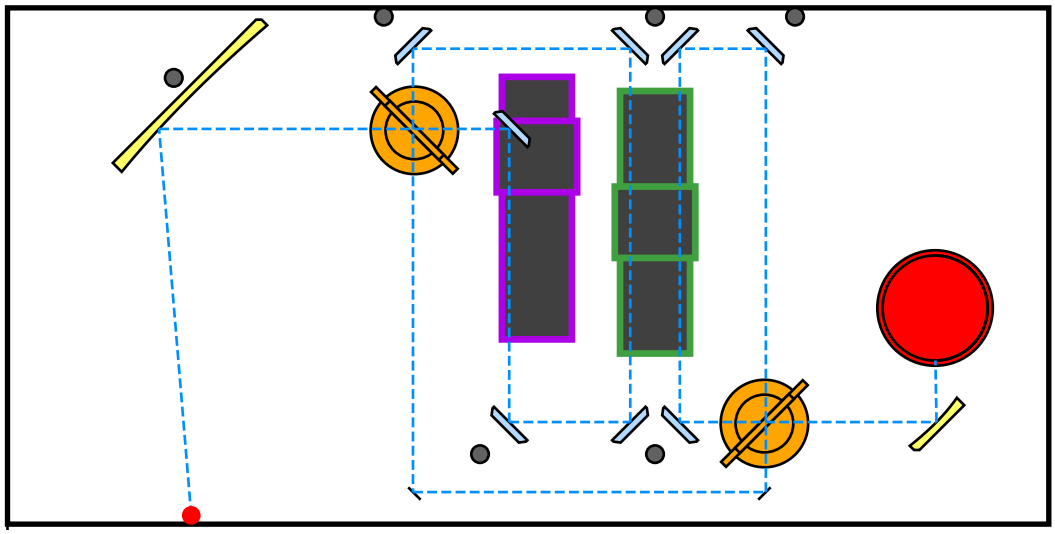


Figure B.1: The DFI testbed in its alignment configuration. This image matches Figure 2.9.

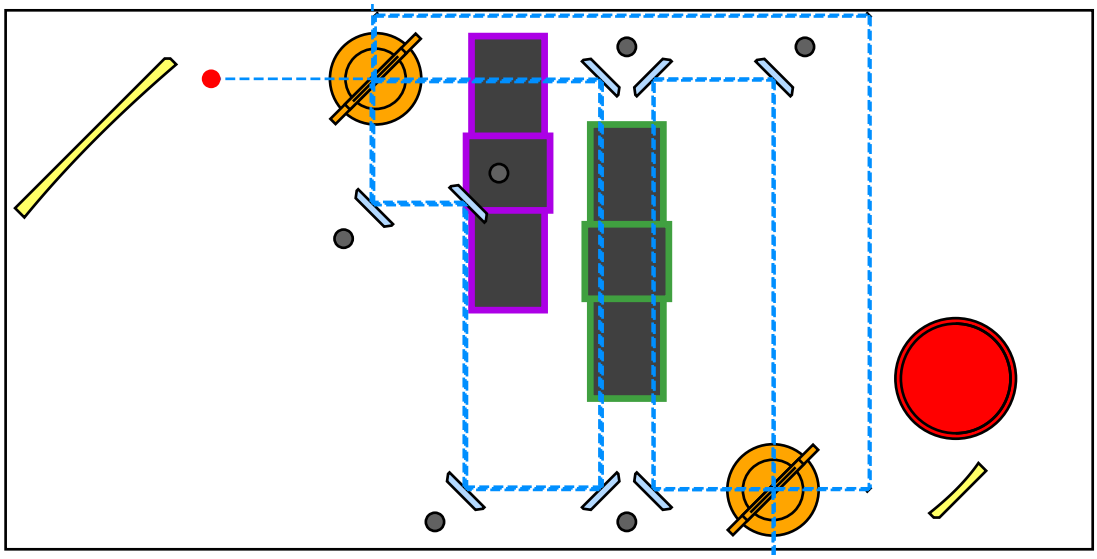


Figure B.2: The first DFI optical design while in its alignment configuration. In this design there is one less folding mirror, however the focal point of the primary collimator is not on the optics bench.

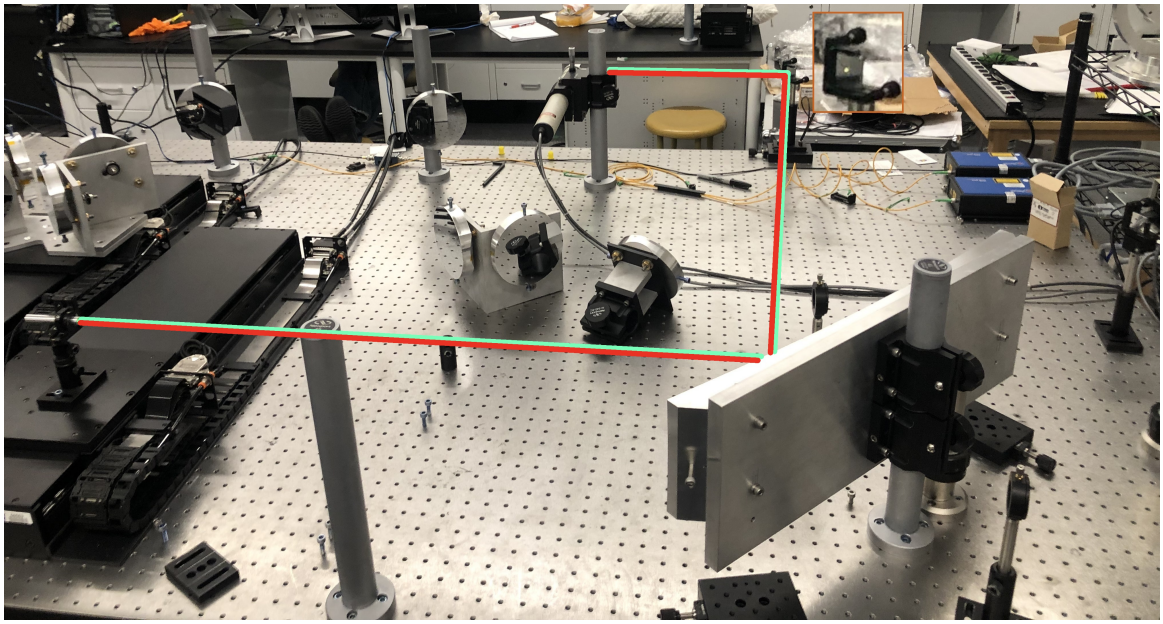


Figure B.3: The incorporation of the primary mirror in the alignment of the interferometer using two alignment lasers.

collimating mirror to reside off of the optics table. This design consequence was a result of passing the beam to the second cavity through relay optics on the same side of the interferometer as the primary mirror. For a source to reside on the table at the focal length of the primary mirror, a folding mirror placed between the source and the primary collimator was required.

B.1.1 Beamsplitters

For the alignment of the first configuration, I employed broadband beamsplitter cubes purchased from ThorLabs. During the alignment of the second design, I discovered that these beamsplitter introduced a significant vertical tilt to the transmitted beam and I constructed other broadband beamsplitters from Mylar to replace these in the alignment process. The design and construction of these beamsplitters are detailed in Appendix C.

B.2 Incorporating the primary mirror

Due to the size and weight of the primary mirror, the tip and tilt actuators employed by other components in the optical assembly could not be incorporated into the mounting of the primary mirror. As a result, a reflection from the optical axis of the primary mirror defines a plane that may not be well aligned with the plane defined by the translation stages and the optics table. Since the translation stages could be securely mounted to the surface of the optics table, the entire interferometer was aligned to the coordinate axes defined by these. This was done such that the grid of the optics table's breadboard defined the coordinate system of the horizontal plane. Efforts were made to minimise the primary mirror's misalignment with these coordinate axes through coarse adjustments using a level and additional supports before securing the primary mirror in its mount.

In an attempt to include the primary mirror in the optical alignment, the optical alignment beam was input to the interferometer through the focal point of the primary mirror. To ensure that the output reflection from the primary mirror was well-aligned with the optics table, an adjustable mirror was mounted to a third translation stage that was positioned at the focal point of the primary mirror. With this in place, the combination of the adjustable laser mount and focal point mirror could be positioned and misaligned with the grid of the optics table such that the reflected beam from the primary mirror was well-aligned with the coordinate axes of the optics table.

The incorporation of the primary mirror employed a second alignment laser mounted to the spatial translation stage at the correct beam height and adjusted in tip and tilt such that it was well aligned to the coordinate axes of the table. The position of this second laser could then be moved with the translation stage to aid in locating the focal point of the primary mirror (see Figure B.3). The incoming beam alignment was set using the adjustable laser mount, the tip and tilt of the focal point mirror, and the position of the focal point mirror such that the beams from the second alignment laser (green) and HeNe (red) were co-aligned.

Through this process, I was able to determine a more optimal coupling of the primary mirror's focal point to the interferometer prior to fixing the mirror in its mount.

B.3 Aligning the first cavity flats

After the primary mirror was incorporated into the alignment, I added the optical flats necessary to create the first resonant cavity. Here I will introduce the general procedure I employed to ensure the alignment beam was well-aligned with the coordinate axes defined by the table after a reflection.

1. A pinhole at the appropriate beam height (defined by the flats on the translation stages) is brought as close to the mirror as possible (care must be taken to avoid damaging any optical surfaces) and positioned at the desired beam location referencing the breadboard grid of the table.

2. The mirror's position is adjusted using all three actuators such that the reflected beam passes through the pinhole.

3. The pinhole is then positioned at the desired beam axes as far from the reflector as possible while resting on the table, again referencing the table's breadboard. The tip and tilt of the reflecting mirror are then adjusted such that the beam passes through the pinhole. Optical flats are placed sequentially when possible such that longer optical paths for positioning the pinhole are possible. When only a short optical path is available for alignment, another movable reflector that has its tilt in the vertical plane aligned with the table axes is used to send the reflected beam to somewhere on the table where a larger optical path can be achieved. Note that this moving mirror cannot be used to improve the alignment of the beam in the horizontal plane.

4. The pinhole is again brought close to the mirror and the process is repeated until sufficient alignment is achieved.

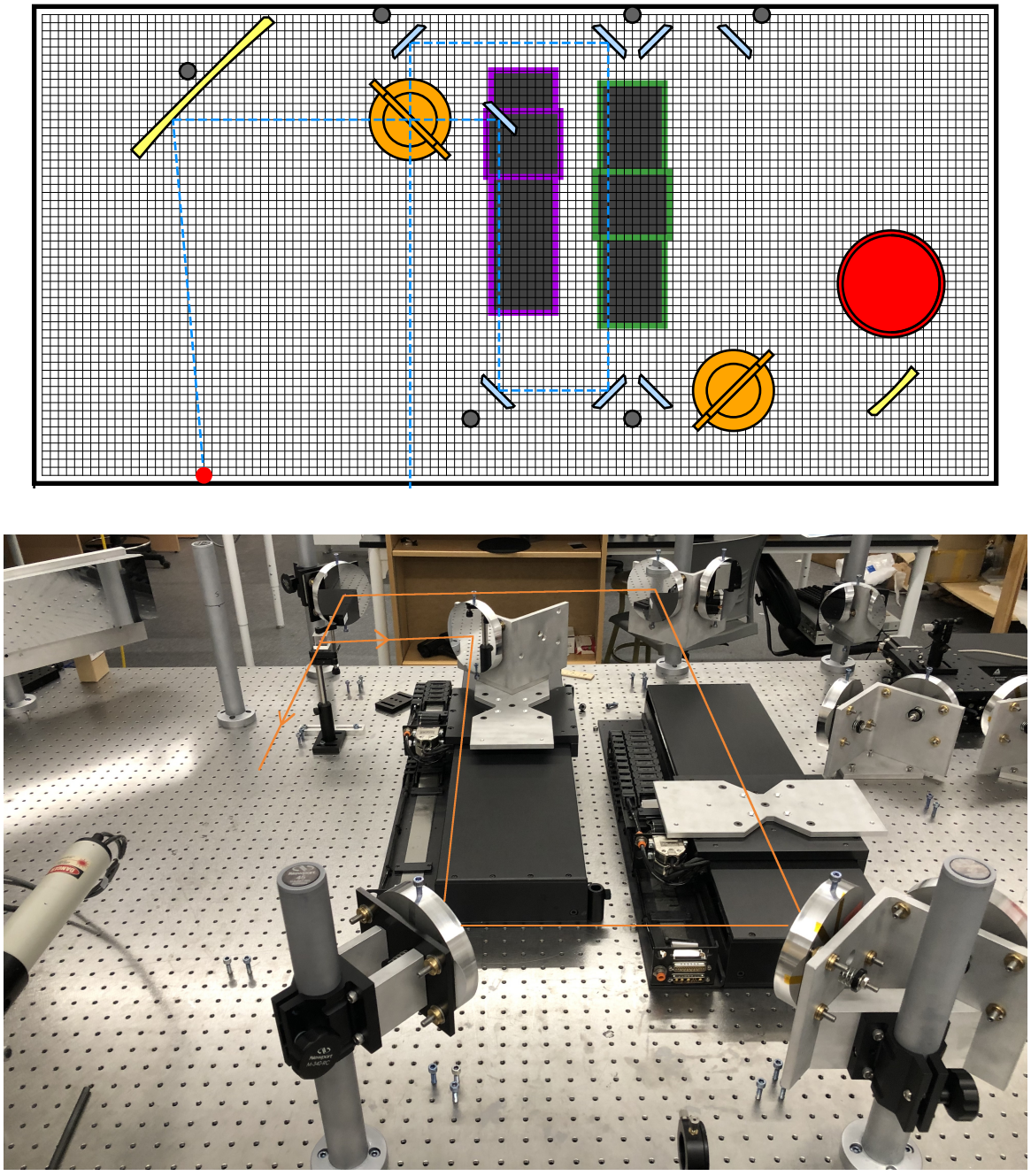


Figure B.4: An optical diagram demonstrating the alignment of the first resonant optical cavity of the DFI (top) and a corresponding photograph of the testbed (bottom). Note that a cube beamsplitter is shown in the photograph, this was later replaced with a Mylar beamsplitter.

The desired location of the beam is not always positioned in the horizontal plane so as to occur directly over grid-line of breadboard holes. To illustrate the desired beam location with respect to the breadboard grid, all subsequent optical diagrams will include grid lines marking the table breadboard (see Figure B.4).

B.4 Refining the alignment of the first cavity

Once the cavity flats were aligned to the table using the pinhole, I incorporated the first beamsplitter. Note that the smaller optical flats that relay the beam to the second cavity were not yet positioned allowing for cavity output and beamsplitter reflection to be well aligned with the table. Blocking the beam from the cavity, I ensured the beamsplitter was properly positioned and rotated such that its reflected beam was well aligned with the table using the pinhole method (see Figure B.4).

Once the beamplitter is well-positioned, the alignment of the cavity is easily seen by the spot pattern from the cavity output when viewed on a distant screen or wall. Figure B.5 shows a photograph of the spot pattern output from the cavity when it is poorly aligned. When the cavity is well aligned, the beams from subsequent passes of the cavity will be co-aligned and interference fringes will be seen.

B.5 Aligning the second cavity

The output from the first cavity and the reflected beam from the beamsplitter can be relayed to the second cavity on the detector side of the interferometer using a pair of small optical flats. These flats, which are not a part of the interferometer assembly, do not have to be well-aligned with the coordinate axes defined by the table; however, they do need to be aligned with respect to each other such that the input into the second cavity is well-aligned with the table axes.

Once the beam is input into the second cavity, the output from the first cavity can be blocked (to increase visual clarity) and the second cavity can be aligned following the same process as the first.

B.6 Introducing the double-rooftop assembly

The double-rooftop mirror arrangement is composed of two separable single-rooftop parts (left and right). Dividing the mirrors in this way allows for the alignment of the reflections from each section to be verified over a long optical path (see Figure B.6).

Once both cavities were sufficiently aligned, I placed a second alignment laser at the output of the second cavity (along the optical axis to the secondary focusing mirror) and co-aligned it with the input HeNe beam by adjusting both the position and rotation of this second beam. This ensured that the reverse path through the interferometer was well-aligned. This step is needed since the introduction of the double-rooftop mirror arrangement blocks the resonant cavity and only one side of each rooftop pair is in the optical path of the input HeNe (see Figure B.6). Using a pinhole, I aligned the right side of the double-roof assembly to the coordinate axes of the table using the long path to the left of the table. To ensure that the second cavity is well-aligned with the axis of the spectral stage, the separation of the reflected beams from each mirror in the single-rooftop portion can be monitored as the

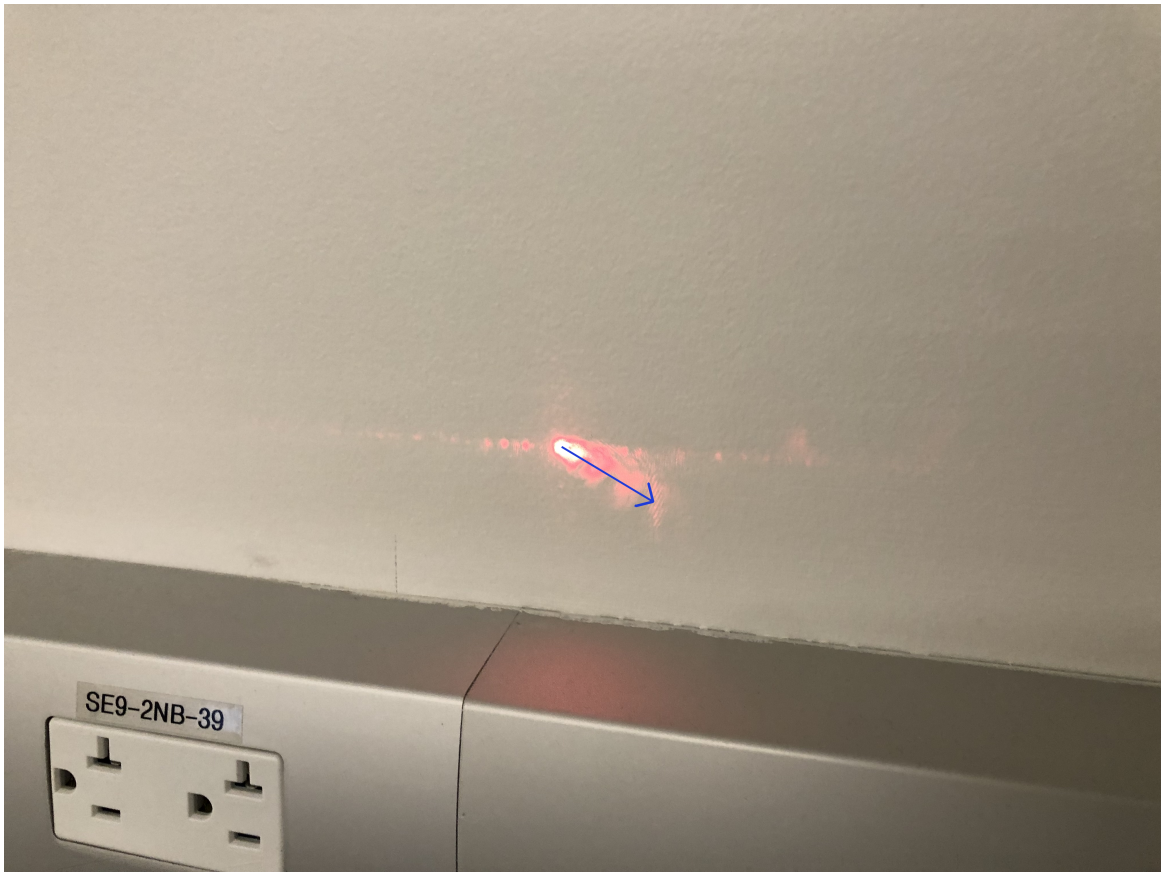


Figure B.5: The spot pattern from the output of the first resonant cavity while it is poorly aligned. The arrow demonstrates that subsequent passes of the beam through the cavity move down and to the right.

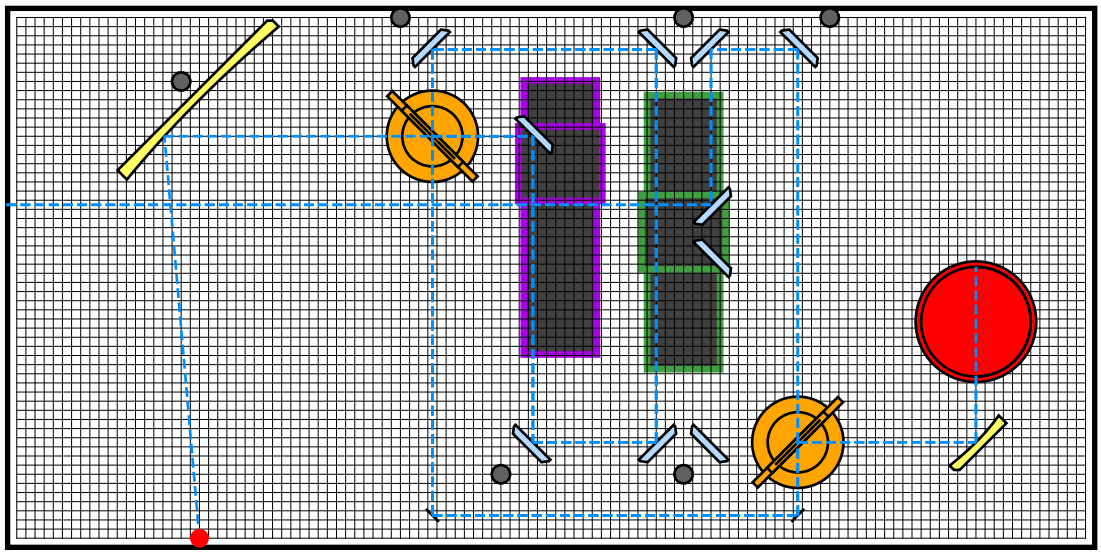


Figure B.6: The introduction of the right single-rooftop portion of the double-rooftop assembly. In this diagram there is no reverse beam passing through the interferometer and bottom mirror does not receive an alignment beam.

spatial stage moves. If the system is well aligned, the separation between each beam should not change throughout the motion.

Repeating this process with the left portion of the double-rooftop assembly would require the removal of the right portion from the spectral stage. As the removal and reintroduction of one of the single-rooftop portions of the double-rooftop assembly would result in misalignment, I did not do this. With that in mind, this process may provide a useful "coarse" alignment for the left portion of the assembly before again removing it and repeating the alignment of the right portion.

Once I introduced the left portion of the double-rooftop beam, both resonant cavities were severed and fine alignment of the left part of the double-rooftop assembly cannot be achieved using resonant cavities or the pinhole. Instead, with the assumption that the left portion of the double-rooftop assembly has the only two misaligned mirrors in the system, I adjusted both mirrors such that the incoming HeNe and reverse alignment beam are co-aligned.

B.7 Rotating the beamsplitters

With the optical flats and primary mirror aligned, the beamsplitters can be rotated and the testbed should operate as an FTS. As the rotation of the beamsplitters requires their removal, I have had to adjust them with the assumption that they are the only misaligned components when they are reintroduced. Due to the degradation of the optical beam after multiple reflections, the interference pattern at the output of the assembly can be difficult to see and turning off the main laboratory lights may be necessary.

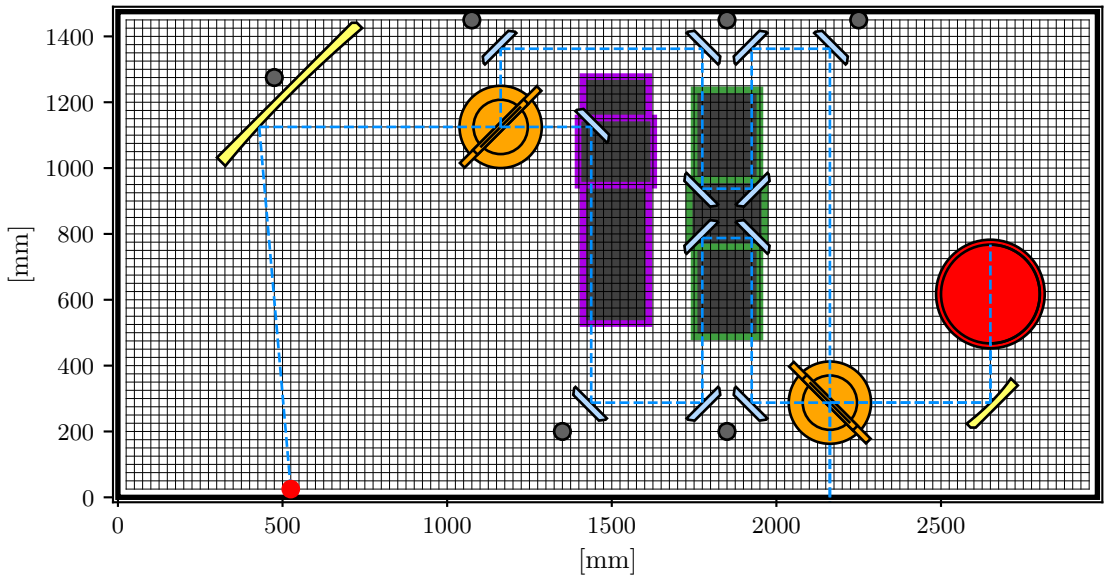


Figure B.7: The DFI in its final alignment phase in which it operated a single FTS. See Figure 2.8 for additional details.

Figure B.7 shows the DFI optical assembly in its completed single-FTS operational configuration. The grid of the table is shown to provide a reference for the beam path through the interferometer. Note that position in the horizontal plane at which the reflected beam from the primary mirror is somewhat subjective provided the optical flat mounted to the spatial stage and beamsplitter are positioned to have the same optical axis. A position that is easy to reference with the breadboard grid of the table should be chosen.

Appendix C

Alternate Beamsplitter Construction

C.1 Introduction

During the second alignment of the Double Fourier Interferometery (DFI) testbed (see Appendix B), I discovered that the ThorLabs cube beamsplitters that were employed in the first alignment of the DFI testbed introduced a vertical tilt to the transmitted beam of a few fractions of a degree. Six beamsplitters were tested and each was found to introduce the angular tilt to varying degrees. To provide better optical beamsplitters for the alignment process, I constructed optical beamsplitters that leverage the existing mounts for the nominal terahertz beamsplitters. Aluminised polyester and non-aluminised Mylar were the chosen materials for these beamsplitters as they are also functional as beamsplitters within the nominal terahertz spectral band of the DFI testbed (though they were not optimised for this purpose).

Aluminised polyester from emergency blankets purchased from a local hardware store and sheets of Mylar that were already on hand were used. These beamsplitters make use of aluminum copies of the membrane mounting rings employed by the terahertz beamsplitters that were purchased from QMC Instruments in Cardiff (Figure C.1). I designed aluminum copies of the rings and they were manufactured by a third party.

All beamsplitter manufacturing methods discussed are based upon the same principles: a larger-diameter apparatus ring is used to hold the membrane taut over the bottom piece of the smaller-diameter beamsplitter ring (with nuts in place), holes in the membrane are punctured for each of the 20 bolts that clamp the rings together using a hot soldering iron. The top piece of the ring is then put in place and the bolts are driven through the membrane holes into the nuts on the bottom piece. The bolts are then tightened in a pattern of rotating near-equilateral triangles to minimise the effects of preferentially tightening one side of the mount (similar to the pattern of torquing the lug nuts on the wheel of a vehicle).

Methods two and three make use of a scissor jack to push up against the membrane to better tension it against the bottom piece of the ring mount and prior to clamping the top and bottom pieces together. The tension in the membrane after each construction was measured by striking it and using a mobile phone speaker and audio spectrum analyser software to measure the fundamental frequency of the vibration. The tension in the membrane, T, is then determined as,

$$T = \left(\frac{fD}{0.755}\right)^2 \lambda \quad [N], \tag{C.1}$$

where f is the peak frequency measured by the spectrum analyser, D is the inner diameter

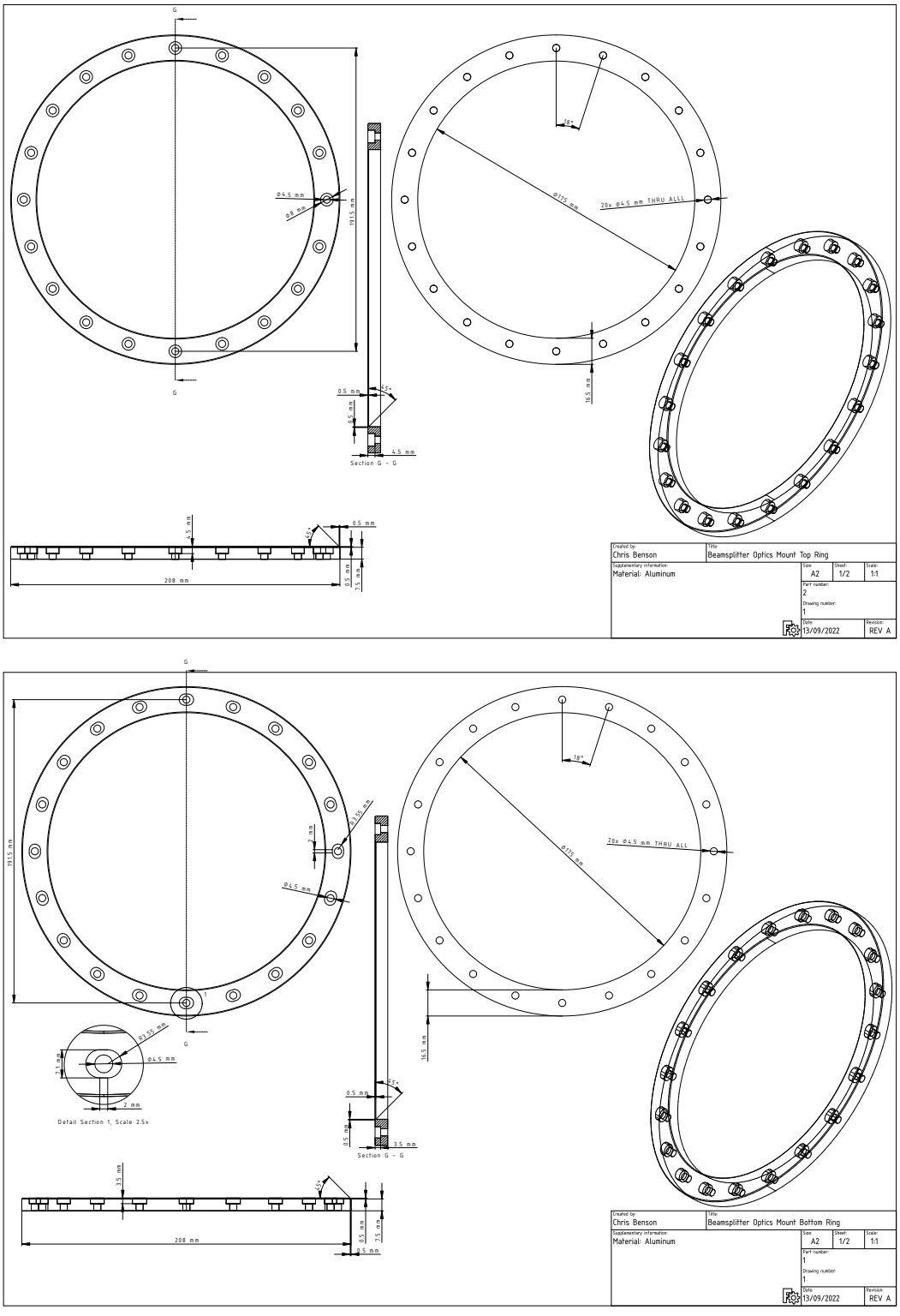


Figure C.1: Technical diagram of the top (upper panel) and bottom (lower panel) pieces of the ring mounts that clamp the beamsplitter membrane. The non-circular holes on the bottom piece allow self-wrenching of the M4 nuts.

of the ring clamp, and λ is the linear mass density of the membrane, which assumed to be approximately equal to the volume density of the membrane.

C.2 Method 1

For this method, I employed only a large diameter embroidery hoop to hand-tighten the membrane against the bottom piece of the ring mount (Figure C.2). Only aluminised polyester beamsplitters were constructed with this method. Using this method, the membrane could be tuned to a maximum frequency of $\sim$123 Hz corresponding to a tension of $\sim$124 N taking the density of the material to be 1.52 g/cm^3. At this tension, creases from the fold of the blanket are clearly visible. The quality of the reflected beam from the beamsplitter was deemed insufficient for use with the long path lengths of the interferometer.

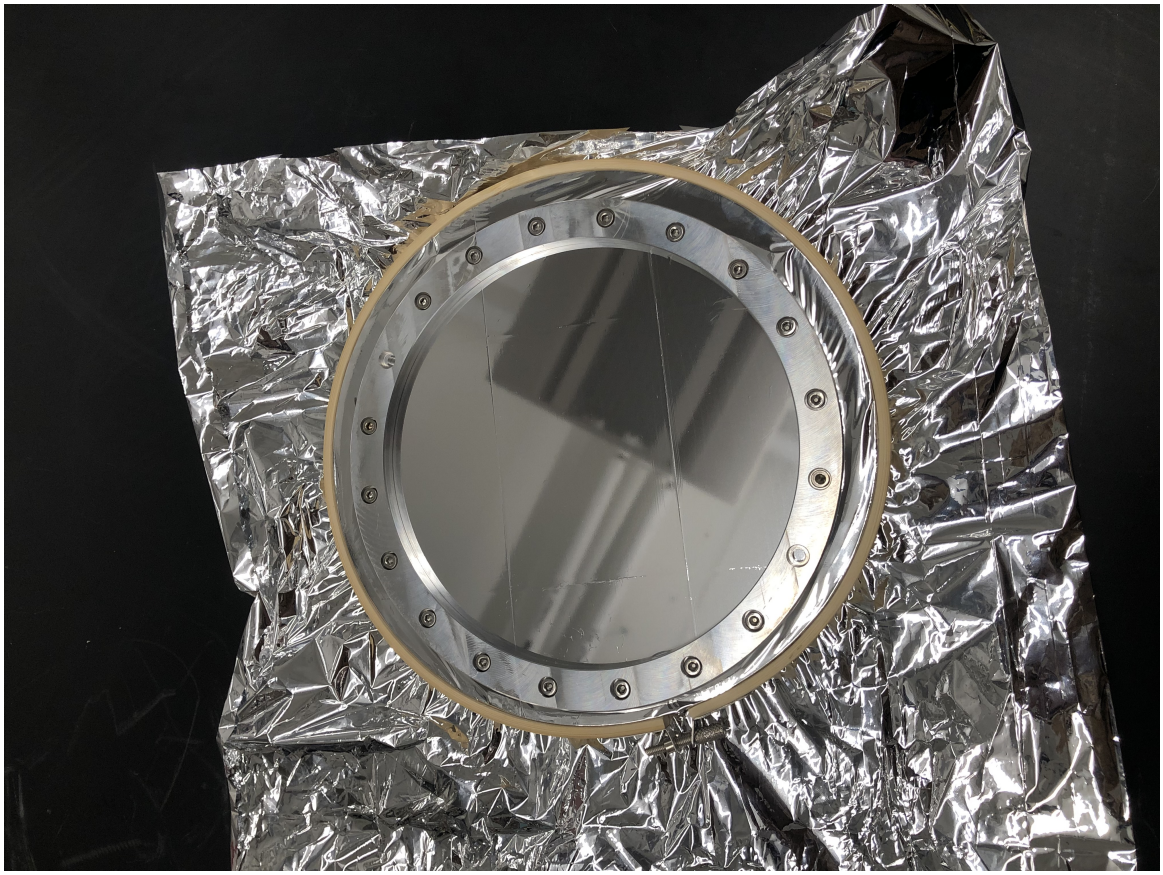


Figure C.2: The first method employed to make beamsplitters. In this method an embroidery hoop was used to tighten the aluminised polyester.

C.3 Method 2

In this and the following method, I made use of a PT-GD401 motorised lab jack to push up against the membrane once it is held tight over the base ring. In this method the membrane has been tightened against the embroidery hoop which is fixed to three optical

posts via clamps (see Figure C.3). A large diameter rigid metal ring and polymer gasket are used to facilitate clamping the embroidery ring to the optical posts. The stack of material (consisting of the large rigid metal ring, the membrane, and the embroidery ring) was also held together with intermediate clamps which provided additional friction on the membrane to hold against the upward force of the lab jack (see Figure C.4). Once the stack of materials was clamped in place, the bottom piece of the beamsplitter ring mount was pushed up against the membrane to tighten it across the surface of the ring. Only aluminised polyester membranes were used with this method.

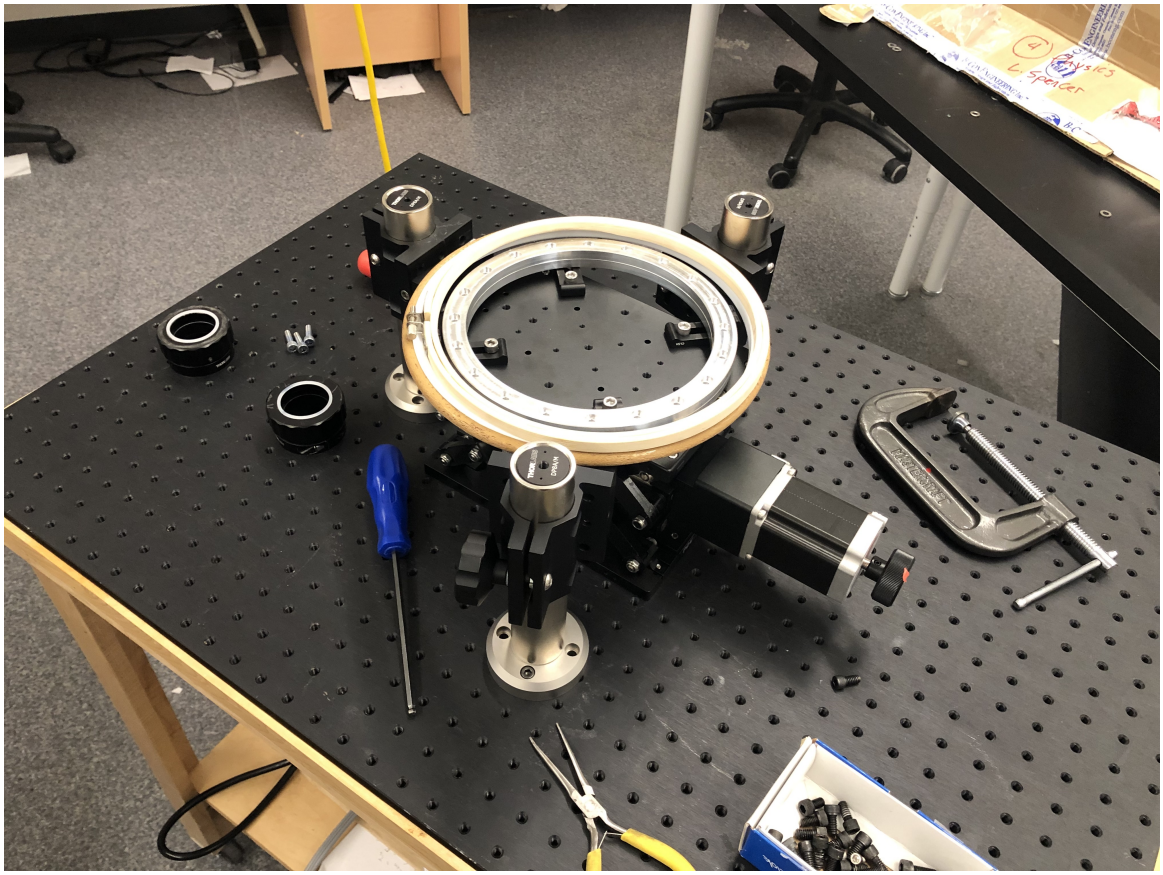


Figure C.3: Significant modifications are employed in the second method. The three optical posts and lab jack are clearly seen. The wooden embroidery hoop shown in this image was replaced by the metal ring shown in Figure C.5.

Through this method, I was able to tune the aluminised Mylar membrane to 277 Hz corresponding to a tension of ~ 632 N. The creases from the folds of the blanket were no longer visible and the improvement to reflection quality from the increased tension was evident. Figure C.5 shows a picture of the beam quality after $\sim$3 m of optical path after reflecting from this beamsplitter. This was also deemed to be of insufficient quality for use in the alignment of the interferometer.

Some design challenges occurred using this method which are summarised here. The gasket which was cut from some thick scrap polymer found in the machine shop does not survive the process. The rigid metal ring bites into the gasket when clamped down

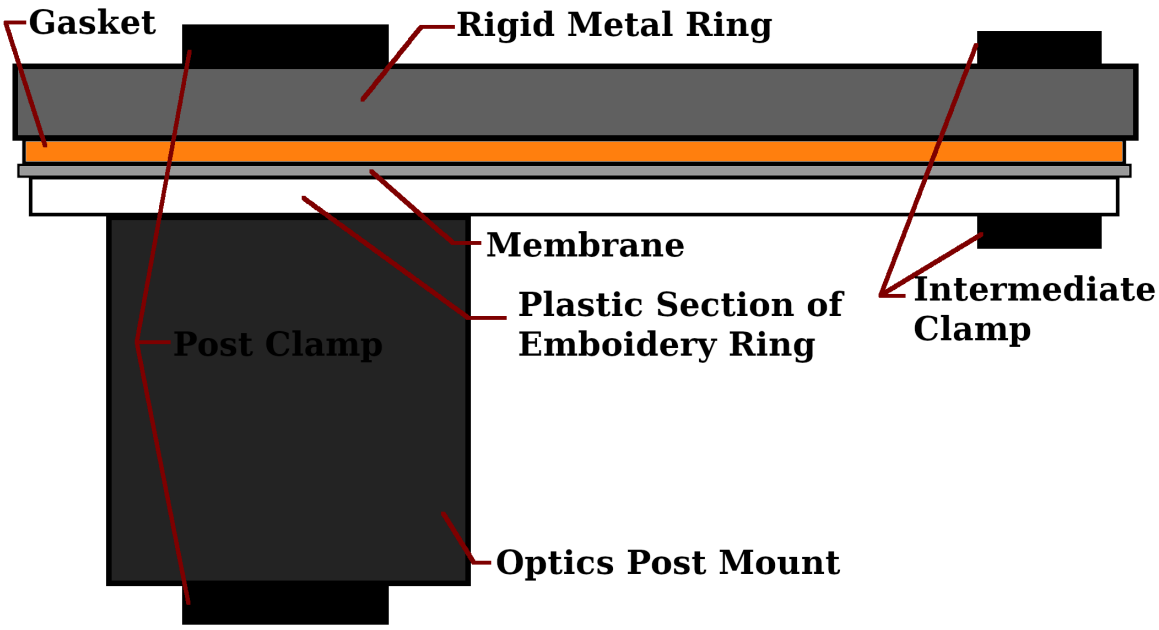


Figure C.4: A diagram of the layers of different parts of the mounting apparatus that are clamped together.

causing the gasket to tear. The rigid metal ring is the same diameter as the plastic portion of the embroidery hoop and is quite thin requiring it to be placed almost exactly on top of the plastic hoop to clamp the stack of materials together. When obscured by all of the other layers of material, particularly the membrane, this is quite difficult and improper positioning risks tearing the membrane. Another major issue with this second design is that there is insufficient resistance to the upward motion of the lab jack provided by the clamping points on the optics posts. These clamping points were collar clamps fixed by tightening the collars on the posts and the resistive force provided by the friction between the posts and the collar clamps was the limiting element of this design.

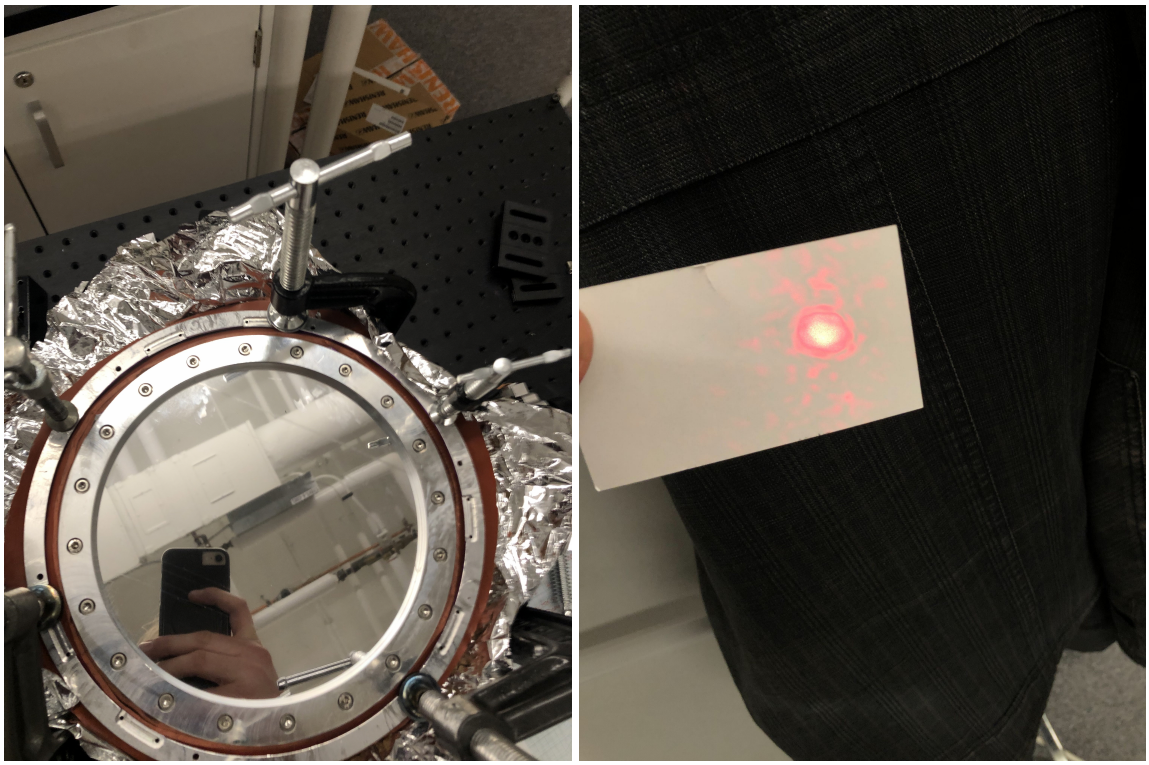


Figure C.5: The beamsplitter manufactured using the second method (left) and the beam quality after 3 m of optical path once it has reflected from the membrane surface (right).

C.4 Method 3

This method improves upon the previous method by increasing the number of optics post clamps from 3 to 4 and replacing the embroidery ring and thin rigid metal ring with two larger outer diameter rings to hold the membrane (see Figure C.6). Additionally, varnish was employed as an adhesive between the membrane and top mounting ring to further ensure the long-term tensioning of the membrane. The varnish was allowed half an hour to cure while the membrane was held under tension. This method was used for both Mylar and aluminised polyester membranes.

I found the upward force provided by the electric stepper motor on the PT-GD401 lab jack to be insufficient to improve on tensioning the membrane by hand-cranking the lab jack. However, the stepper motor on the jack was used to keep it in place and maintain the tension on the membrane while the varnish cured.

Figure C.7 shows the beam quality of the reflected beam through a Mylar beamsplitter made with this technique after $\sim$3 metres of optical travel. This surface provides beam reflections of acceptable quality for the alignment of the DFI.

This technique was effective at tensioning the Mylar membrane to ~ 380 Hz, which with a density of $1.390\,\mathrm{g/cm^3}$, corresponds to a tension of $\sim 1\,078$ N. The aluminised polyester stretched with this technique was able to reach a similar tension to the second method. Attempts to reach a higher tension with the aluminised polyester often resulted in tearing of the membrane from the hard edges of the beamsplitter mounting rings.

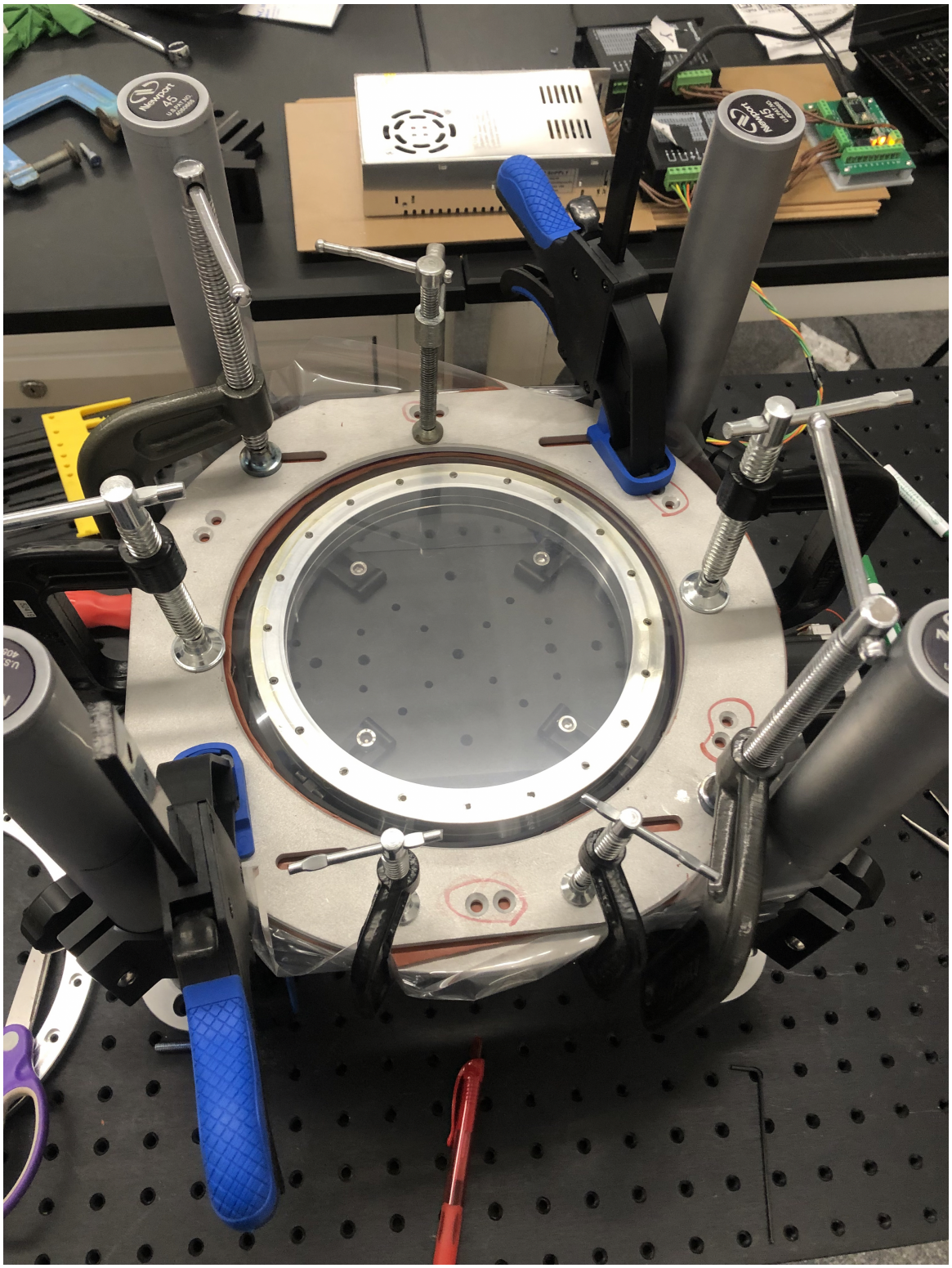


Figure C.6: In method 3, four optics posts are used as clamping points and the membrane is held between two larger outer diameter rings.

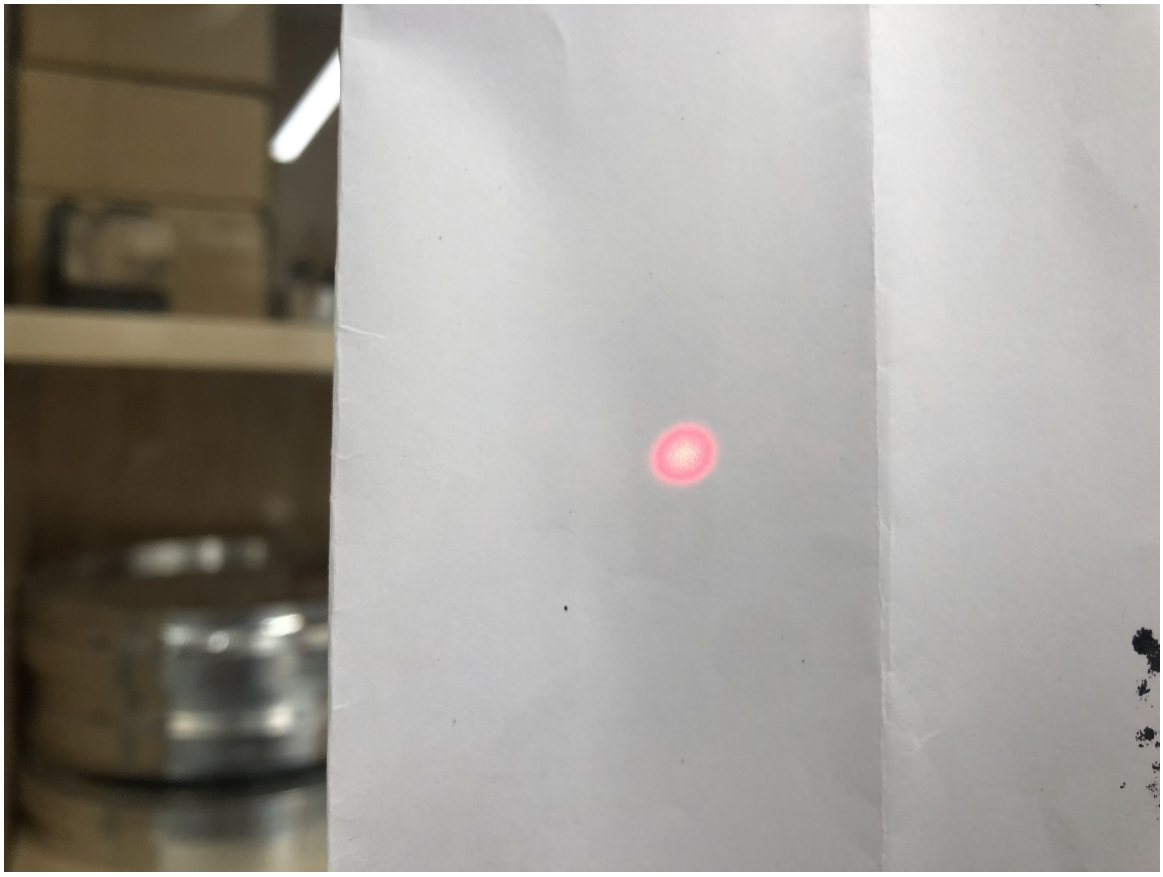


Figure C.7: The beam quality after 3 m of optical path after it has reflected from the membrane surface of a Mylar beamsplitter manufactured with the third method.

Appendix D

Additional Software Information

Unpacking the data reported from the detector array requires an understanding of how data is reported to the Direct Memory Access (DMA) space on the local computer and how this changes in the custom readout modes described in §3.3.2.

D.1 Custom readout modes

Under nominal operation, the First In, First Out (FIFO) is first filled by 32-bit integers corresponding to the heater value calculated by the Proportional-Integral-Derivative (PID) loop for channels A through D (4 integers). This is then followed by a 32-bit integer that counts the number of full frames measured by the detector which increments after every 7 occurrences, having measured channels A–D seven times (making a full frame) (1 integer). Finally, a 32-bit integer containing housekeeping data and metadata corresponding to the measurements of the four channels in the current row (1 integer). This sequence is demonstrated in the block diagram in Figure D.1. Each box represents a 32-bit integer and data is only reported from the system on the final loop count of the measurement pulse (i.e. at a loop count $n-1$, where n is the chose pulse width).

Both of the custom readout modes for the detector array described in §3.3.2 change how data are reported to the DMA FIFO on the local computer. The first modified readout mode is coded on the Field-Programmable Gate Array (FPGA) as a "Normal Readout" switch which causes the FPGA to report internal TES voltage (process variable) measurements on each loop count of a detector measurement pulse when set to false. On each loop count, the 16-bit process variables for channels A and B are reported together as a single 32-bit integer as are the process variable measurements from channels C and D. These are then followed by the 32-bit metadata/housekeeping integer. On the final loop count within the pulse, the process variables are reported alongside the end-of-pulse data reported by the detector array in its nominal readout mode. This sequence is shown in Figure D.2. To provide a clearer reference to this mode than "Abnormal/full readout" this readout mode has been referred to as "TES profiling mode" in this thesis.

The second custom readout mode is coded on the FPGA as a "Normal Output" switch that when inactive causes the detector to report the process variable value at the read index at the end of each measurement pulse. Effectively, this mode reports only the data corresponding to the final loop count of TES profiling readout mode (see Figure D.3).

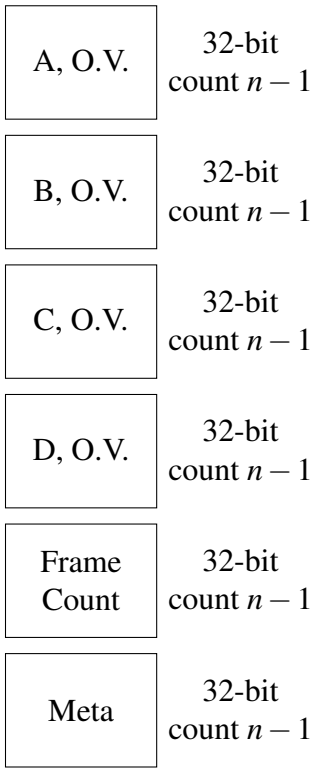


Figure D.1: The output of the detector array to the DMA FIFO when operating in the default readout mode for a measurement pulse width of n. On the last loop count in the measurement pulse (loop count $n-1$), the heater power calculated by the PID loop, represented by the output variable (O.V.), is reported with the frame counter and a metadata integer. Each 32-bit integer in the reported data structure is represented by a block.

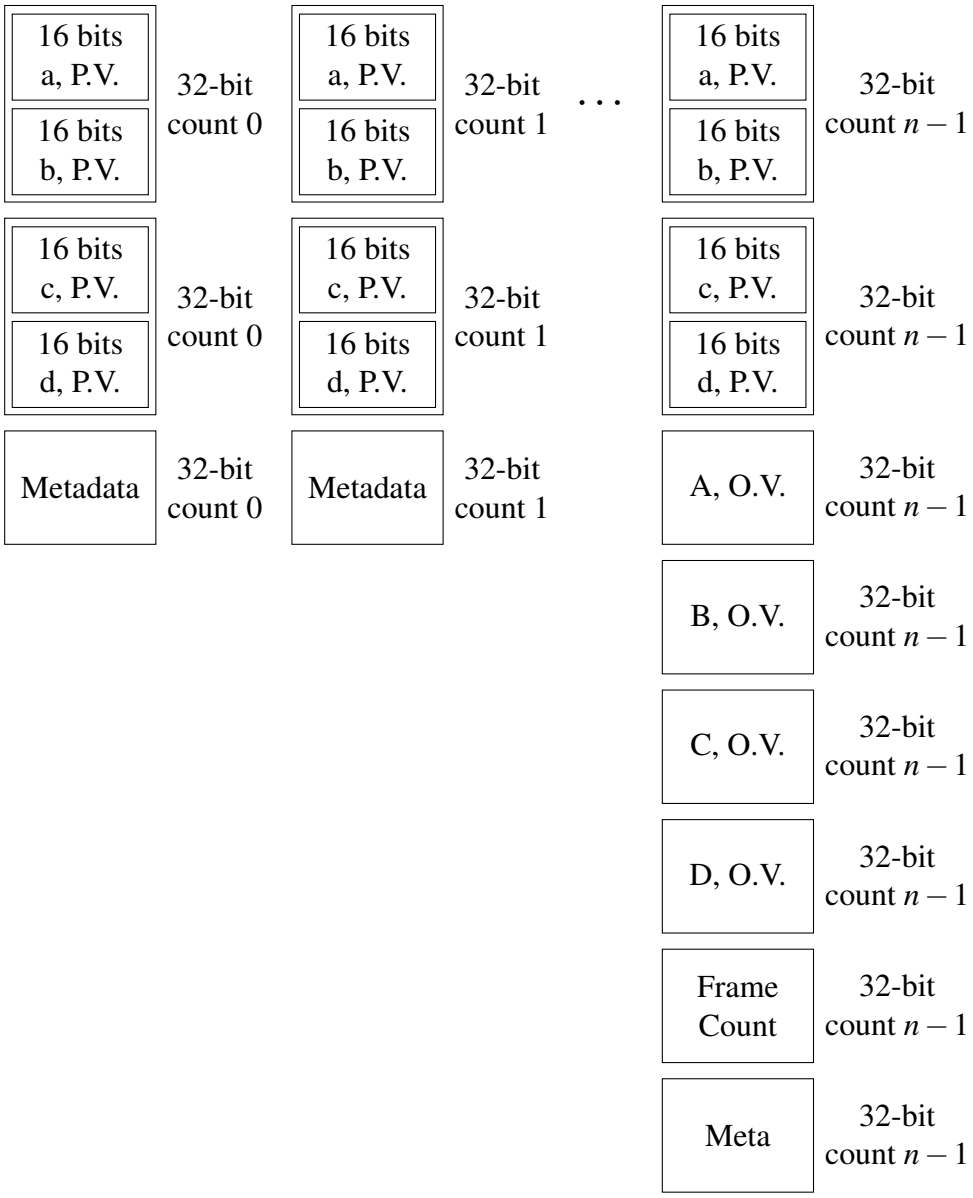


Figure D.2: The output of the detector array to the DMA FIFO when operating in the custom Transition Edge Sensor (TES) profiling readout mode for a measurement pulse width of n. At loop counts within the pulse, the TES voltage represented by the process variable (P.V.) is reported with a metadata integer. As in Figure D.1, each large block represents a 32-bit integer. The 32-bit integers that contain process variable data are further divided into two 16-bit integers, each containing the 16-bit process variable value for two channels. Each column within the block diagram represents the data output at a given loop count in the measurement pulse. On the last loop count in the measurement pulse (loop count $n-1$), the heater power calculated by the PID loop represented by the output variable (O.V.) is also reported with the frame counter and a metadata integer. P.V. (TES) measurements use a lowercase letter to represent the channel, while O.V. (heater) measurements use uppercase.

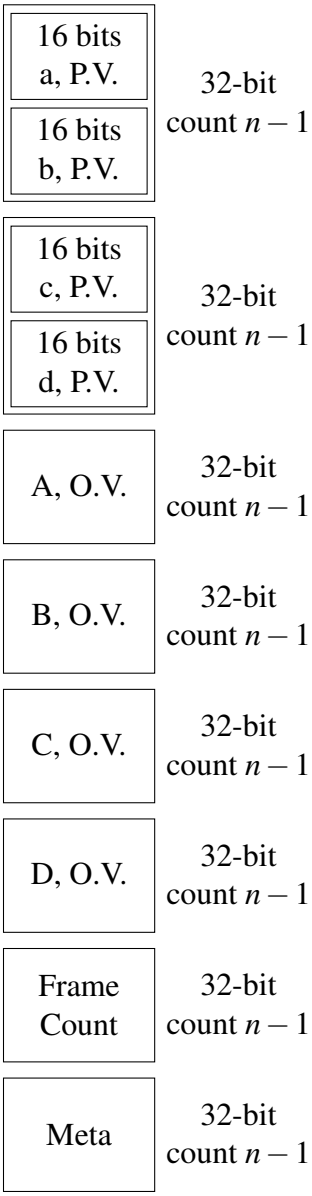


Figure D.3: The output of the detector array to the DMA memory space when operating in additional TES output mode for a measurement pulse width of n. TES voltage measurements represented by the 16-bit process variable (P.V.) are combined into 32-bit integers and reported prior to reporting detector measurements, the frame counter, and the metadata integer at the end of the measurement pulse. This arrangement follows similar conventions to the TES profiling readout mode which are detailed in Figure D.2.

D.2 Metadata encoding

Throughout the studies presented in this thesis, the structure of the 32-bit metadata integer has undergone modifications to report information internal to a detector measurement pulse when operating in custom readout modes. This shown in Figure D.4.

D.3 Detector control software

To control and monitor the detector array, host programs were designed in both Labview and Python. In both cases, the host program initialises by setting up the DMA space and FIFO communication with a specified size given in bits by a DMA request size. The desired parameters on the FPGA that define the control and readout of the detector array are then set by the program. The number of frames to be contained in a packet saved on the local disk is also determined alongside the number of 32-bit integers that constitute a full frame of detector data for the chosen detector settings. The program then proceeds to check the size of the FIFO in a loop. When the FIFO reaches a size that is greater than or equal to the size of a full data packet, a full packet is pulled from the FIFO and saved to the local hard drive.

The LabView host program was initially written in collaboration with QMC Instruments and makes use of Graphical User Interface (GUI) elements to set the control parameters on the FPGA, display detector data and metadata unpacked from the DMA FIFO in real-time, and specify the location data is to be saved.

The Python TES interface software relies on the National Instruments (NI) FPGA Interface Python API, `nifpga` [175]. This publicly available Python package enables communication between a Python session running on a host computer and an NI FPGA. This communication is achieved through session objects which are temporary connections to the FPGA. The session allows users to access controls, indicators, and FIFOs on the FPGA by the names that are assigned to them in the bitfiles that program the FPGA hardware.

The parameter space settings outlined in § 3.3.1 are managed by a `Params` class written in Python. The `Params` object can be saved to a Python serialised object (Python `pickle`) and can load a saved set of parameters from a `pickle`. When detector measurements are saved to a local computer, the `Params` object is saved automatically within the same directory as the data packets. The getters and setters that modify the registers on the FPGA are held within the Python `TES` class which can be passed a `Params` object.

The Python control software allows for the TES to be run directly within an active Python session or to be run in a dedicated thread within the Python session. Using a dedicated thread to monitor the DMA FIFO, many of the detector controlling parameters can be modified "on the fly" in a similar manner to the LabView control software.

D.4 LabVIEW PID implementation

The PID feedback of the detector array is implemented with LabVIEW's PID virtual instrument [176]. This virtual instrument provides the FPGA implementation of Equation 3.19. The controller operates on 32-bit single precision floating point numbers. A summary of the controller inputs follows.

- **reset?**: Can be used to manually reset the internal state of the PID controller.

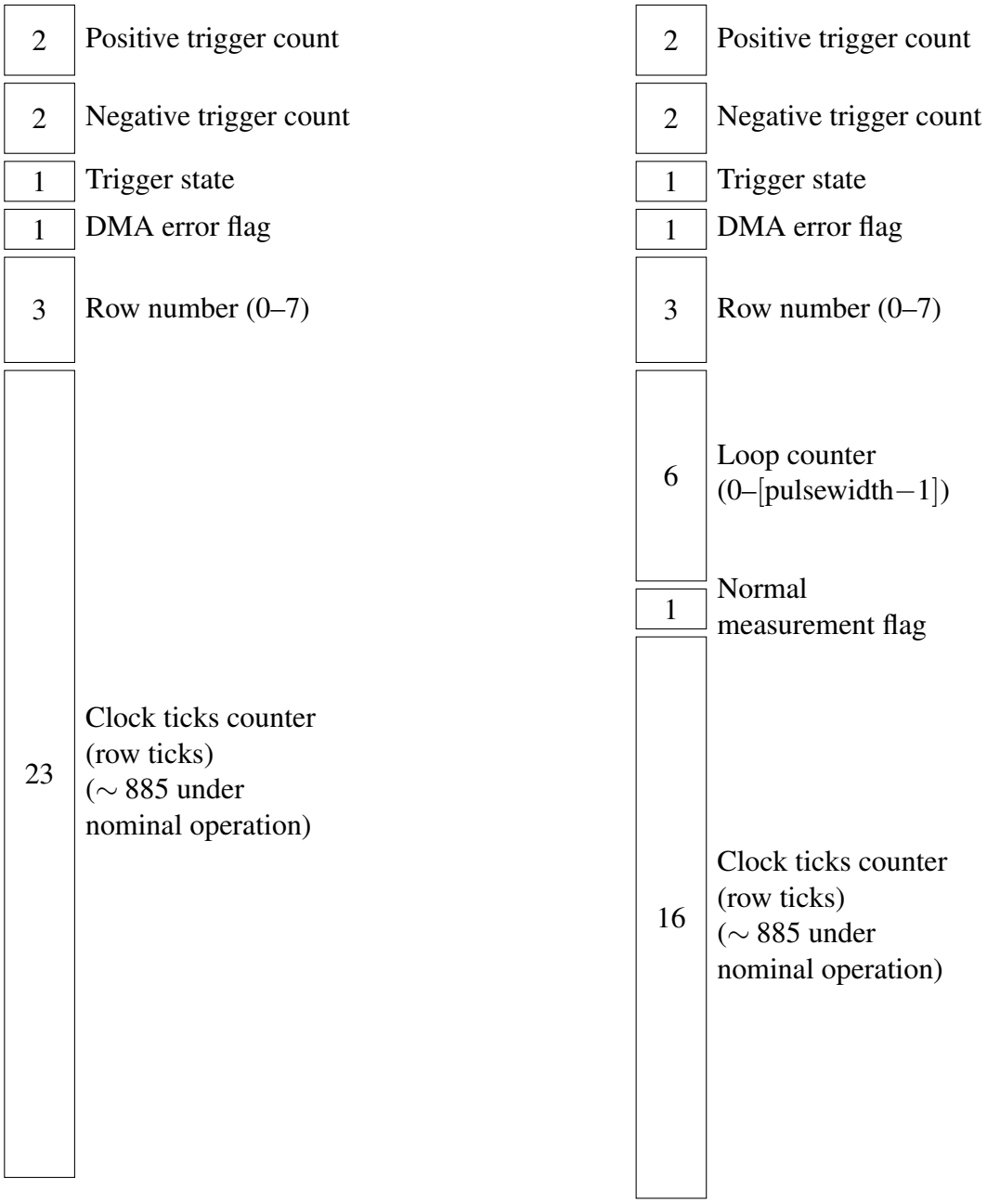


Figure D.4: The bit structure of the 32-bit metadata integer prior to modifications in April 2022 (left) and after (right). The number of bits dedicated to each block of metadata is given by the number within the block diagram. The timing of the process internal to a detector measurement is given by a counter which tracks the ticks of the 80 MHz clock on the FPGA (see §4.1.4). The more recent bit structure on the right is currently employed by the detector system.

- **setpoint**: The TES state the PID loop attempts to maintain. This is represented by the variable, s, in the equations that follow.
- **process variable**: the current state measurement of the TES. This is the primary data input to the PID controller and is represented by the variable, p.
- **manual control**: The PID controller can be coerced to output a manually set value.
- **gains**: The proportional, integral, and derivative weights are given as inputs to the controller. These are represented by the variables K_P, K_I, and K_D, respectively.
- **filter coefficient**: A low-pass filter can be employed in association with the derivative term of the PID control. It is given as $\in [0,1]$ with an increased value increasing the damping of derivative action. This is represented by the variable, a.
- **output range**: The output value from the PID control can be coerced to fall between the specified high and low bounds.
- **setpoint weighting**: Setpoint weighting can be employed to tune the proportional and derivative action by modifying the weight of the error term in each. Proportional weighting is given as $\in [0,1]$ and is represented by the variable, β. Derivative weighting is given as $\in [0,1]$ and is represented by the variable, γ.

The calculation of the PID output, $u(n)$, is given by the sum of each action term of the PID controller. All equations are presented in arbitrary data units. Proportional action is given as,

$$u_P(n) = K_P e'(n), \quad \text{where } e'(n) = \beta s - p(n). \tag{D.1}$$

Integral action is calculated as,

$$u_I(n) = K_I \left(\frac{1}{2}\right) \sum_{i}^{n} e(i) + e(i-1), \quad \text{where } e(n) = s - p(n). \tag{D.2}$$

Derivative action is determined as,

$$u_D(n) = K_D[e''(n) - e''(n-1)] + a u_D(n-1), \quad \text{where } e''(n) = \gamma s - p(n). \tag{D.3}$$

The output variable of the controller, $u(n)$, is then given as,

$$u(n) = u_P(n) + u_I(n) + u_D(n). \tag{D.4}$$

Note that in this work, β, a, and γ, are all given a value of zero.

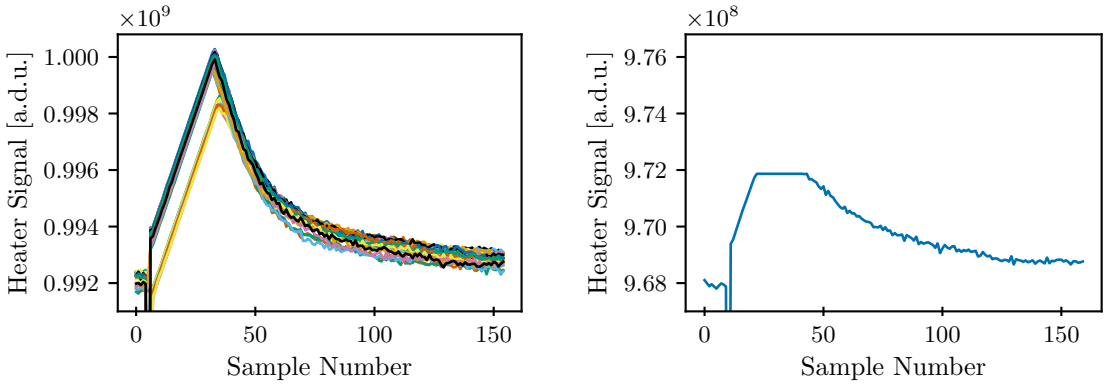


Figure D.5: The response of the central detector to 24 separate DMA errors under nominal operation (left) and a single DMA error with PID control limiting operation (right). The DMA error occurs at the discontinuity seen at detector sample 10 during which the heater is inactive for a variable time depending on the speed of recovery and acknowledgement of the FPGA Interrupt Request (IRQ).

D.5 DMA mitigation routine

To limit the effects of DMA errors on the detector signal, I developed an operational mode that limits the maximum heater power calculated by the PID feedback. When a packet is saved to the local computer, the mean value of that packet is determined and an upper limit on PID output is set to be a user-defined value above the calculated mean (using the PID output range limiting). Operating in this way is not affected by low-frequency drifts in detector signal or changes in steady-state optical loading (see §4.1.5). The detector response when operating in this mode is shown in Figure D.5 in which the output variable from the PID has been limited to 4 million data units above the mean value of the previous packet. While operating in this mode is successful at limiting the maximum heater value after a DMA error occurs, the decay after responding to detector inactivity following the error is not significantly reduced.

Appendix E

Additional Detector Response Measurement Techniques

Early measurements to determine detector time constants from their response to optical modulation proved to be unrepresentative of the actual detector response discussed in Chapter 4. Here, I discuss each of these early measurement techniques and their failings.

Early in my studies when only broadband sources were available, I employed a blackbody source, focusing optics, and a small aperture in an attempt to obtain a small enough source to be chopped by a 32-hole chopper wheel. Due to a lack of quality focusing optics at the time, I was unable to obtain a throughput of the chopped signal sufficient to exceed a detector signal Signal-to-Noise Ratio (SNR) of 1.5. Though frequency response curves were obtained with this technique (see Figure E.1), the poor quality of the data is such that they should not be considered to be precisely representative of the actual frequency response of the detector array.

Later in my studies, the Toptica TERASCAN photomixer source was obtained [129, 130, 131, 132, 133]. This source provided additional avenues to measure the frequency response of the detector array. As part of the lock-in operation with the receiving unit, the internal bias of the photomixer antenna can be modulated to chop the output optical signal. Though the antenna bias nominally operates at frequencies of $\sim$40 kHz, it can be safely adjusted to the frequencies necessary to measure the frequency response of the detectors in the array. The left panel of Figure E.2 shows example results from two frequency response measurement attempts with the photomixer chopped by both a square-wave and sinusoidal antenna bias. To avoid higher-order harmonics in each measurement, the power spectrum of the detector signal was integrated over a 5 Hz bandwidth centered on the antennae bias frequency. Both measurements show substantial deviations from the expected profile of a typical bolometer. These measurements suggest that the photomixer modulation has an internal power response to its antennae bias modulation frequency as they do not agree with other independent measurements (see Chapter 4).

Due to the low SNR of measurements of the chopped aperture and the internal response of the photomixer to its bias frequency, both of these methods were unsuccessful in accurately determining the detector frequency response. Figure E.3 shows the chopped signal from each of the methods discussed in this work. It is quite apparent that the spectral peak obtained from the chopped aperture is not well localised in frequency space and has low SNR. If not for the inability to decouple the internal response of the photomixer from the response of the detector, measurements of this type would be successful. Modulation from

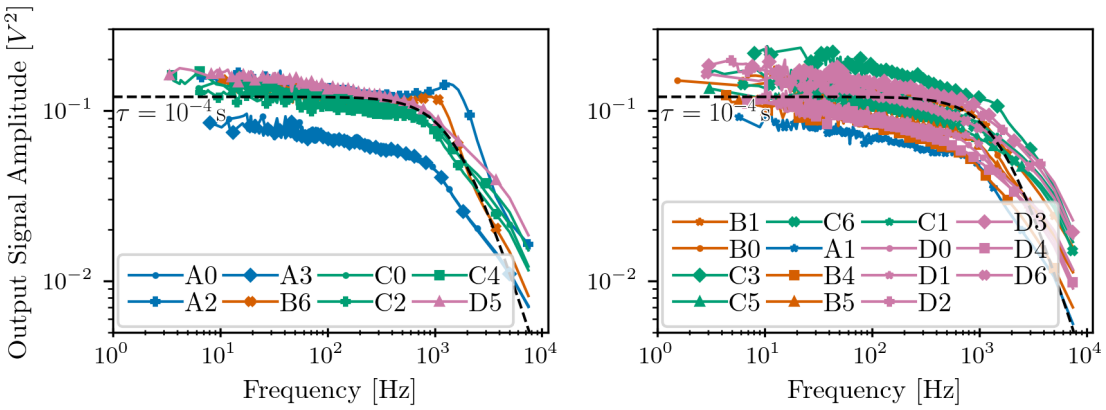


Figure E.1: The signal amplitude from the central cluster (left) and outer ring (right) of detectors measured using an illuminated small aperture and a chopper. A model response from a typical bolometer arrangement with a time constant of 0.1 ms is shown on each panel by a dashed black line. Optical throughput was poor for these measurements and they are not representative of the frequency response of the detector array.

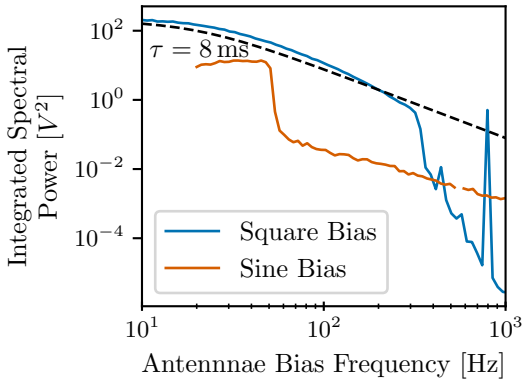


Figure E.2: The signal amplitude from the central detector while the photomixer antenna bias frequency was changed.

a physical chopper and the photomixer source is seen to have higher order harmonics from the quasi-square wave of the chopper. Response measurements using this technique must be sufficiently long to have the necessary resolution to distinguish the signal corresponding to the modulation frequency. Of all these techniques, measurements made with modulation from the DFI testbed operating as an Fourier Transform Spectrometer (FTS) provides the best data quality to measure the response of a detector array.

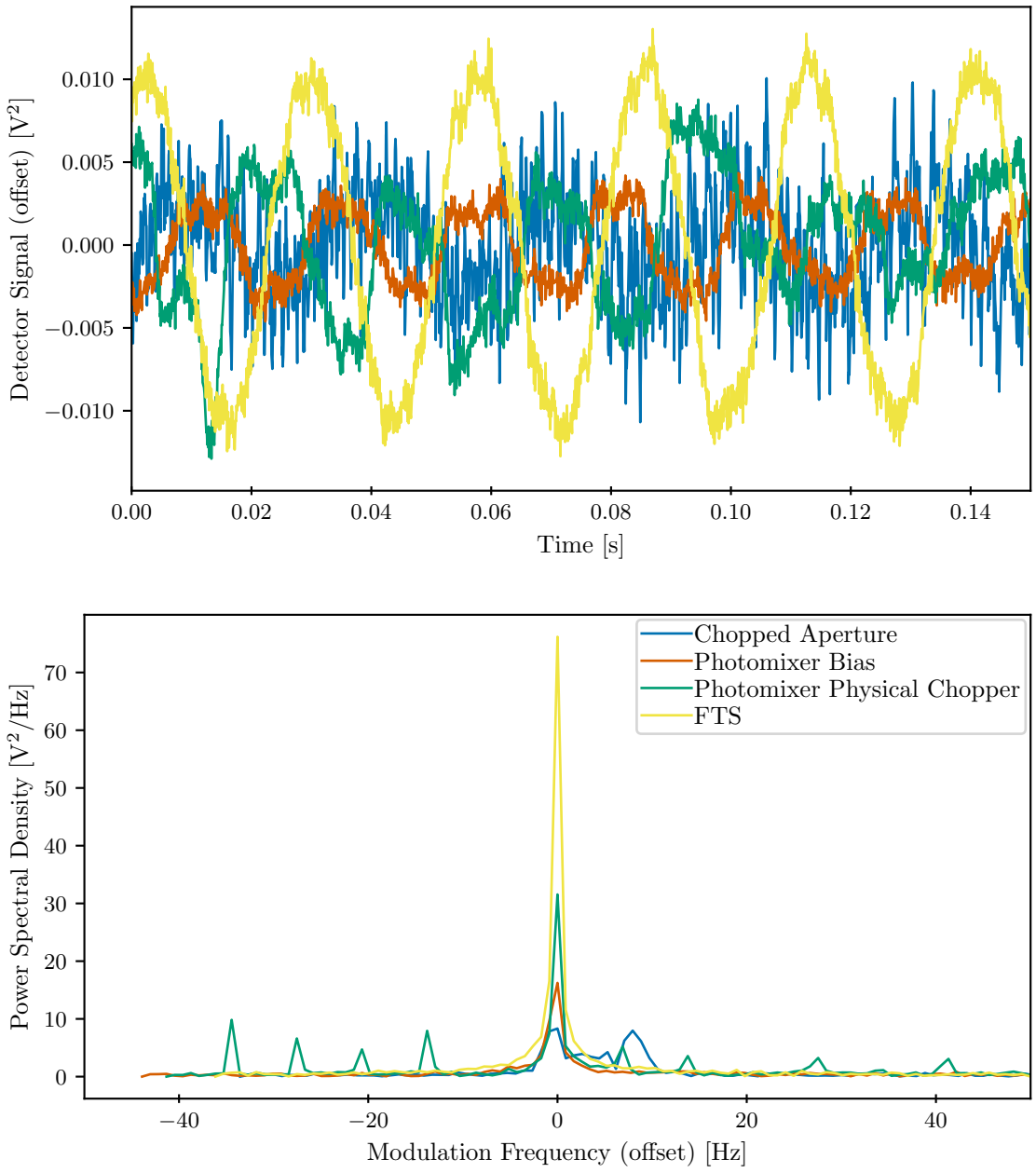


Figure E.3: The chopped signals measured by the central detector corresponding to all four techniques included in this work is shown in the top panel. The spectral peak corresponding to the optical modulation is shown in the bottom panel. The detector data shown correspond to one full data packet (see §3.3.2).